Variations in surface and thermocline conditions of the Western Pacific Warm Pool - Insights from Mg/Ca and stable isotopes in foraminifera tests

Dissertation zur Erlangung des

Doktorgrades der Naturwissenschaften

Dr. rer. nat.

am Fachbereich Geowissenschaften

der Universität Bremen

vorgelegt von

Martina Hollstein

Bremen, Dezember 2017

Gutachter

1. Gutachter: Prof. Dr. Dierk Hebbeln, Universität Bremen

2. Gutachter: Prof. Dr. Gerhard Schmiedl, Universität Hamburg

Datum des Promotionskolloquiums

16. März 2018

Abstract

The Western Pacific Warm Pool (WPWP) plays a key role within the global climate and ocean system. Keeping the highest surface ocean temperatures on Earth the region is a major source of heat and moisture to the global atmosphere and thus has a substantial influence on the regional and global climate. Despite this significance our knowledge about WPWP ocean and climate dynamics is still constrained. Thermocline reconstructions are particularly sparse, even though the thermocline is important for the regional ocean and climate conditions. For instance, WPWP thermocline waters link the extratropical Pacific Ocean to the WPWP. Subsequently, thermocline reconstructions provide the opportunity to investigate the influence of the extratropical climate on the WPWP. Besides the state of the thermocline is tightly coupled to the prevailing climate conditions and the atmospheric circulation. Thermocline reconstructions thus allow to draw clues on variations in the atmospheric circulation system.

This thesis focuses on the reconstruction of WPWP surface and thermocline conditions with the overarching aim to better understand the regional ocean and climate variability over the last (two) glacial–interglacial cycle(s). The reconstruction is based on records of marine sediment cores retrieved from the Bismarck Sea (GeoB 17419-1), and east of the Bismarck Archipelago (GeoB 17426-3) off Papua New Guinea (PNG; southern WPWP) that cover the past 110 and 210 kyr BP, respectively. To monitor the variability of the WPWP over the last glacial-interglacial cycle, the southern WPWP records are compared to published records from a northern WPWP site. Primarily, Mg/Ca and stable oxygen isotopes ($\delta^{18}O$) measured on tests of planktic foraminifera are used as proxies to reconstruct surface and thermocline temperatures, the oxygen isotope composition of seawater ($\delta^{18}O_{SW}$) and the thermal stratification of the upper water column. Mg/Ca and $\delta^{18}O$ of planktic foraminifera tests are commonly used, robust proxies to reconstruct past surface and thermocline ocean conditions. Nonetheless, their accurate calibration requires thorough regional studies, since parameters, such as calcification depth and temperature of planktic foraminifera depend on local environmental conditions. So far, the regional calcification depths and Mg/Ca-temperature dependencies of planktic foraminifera in the WPWP are fairly unknown. Here, $\delta^{18}O$ and Mg/Ca measured on planktic foraminifera tests of modern surface sediments from different stations within the WPWP are combined with water column data (temperature, salinity, and seawater $\delta^{18}O$) to estimate calcification depths and temperatures of various planktic foraminifera species in the WPWP and to establish regional multispecies and species-specific Mg/Ca-temperature calibrations.

Globigerinoides ruber and *Globigerinoides elongatus* generally reflect mixed layer conditions (~0–80 m), while *Globigerinoides sacculifer* mirrors the conditions at the bottom of the mixed layer (~45–85 m). *Pulleniatina obliquiloculata* and *Neogloboquadrina dutertrei* record upper (~90–160 m), and

Globorotalia tumida lower (~230–265 m) thermocline conditions. The newly established multispecies Mg/Ca-temperature calibration (Mg/Ca = 0.24 exp 0.097 * T) is in agreement with published regressions from other areas. The species-specific Mg/Ca-temperature relations of *G. ruber, G. elongatus* and *G. tumida* are consistent with previously published equations. However, in comparison to other areas, the calcification temperatures of *G. sacculifer*, *P. obliquiloculata* and *N. dutertrei* are exceptionally warm in the WPWP and underestimated by available calibrations. Their regional Mg/Ca-temperature relations are best described by Mg/Ca = 0.24 exp 0.097 * T for *G. sacculifer* and by Mg/Ca = 0.21 exp 0.097 * T for *P. obliquiloculata* and *N. dutertrei*. The results are of major importance aiming at the reconstruction of the paleoconditions in the WPWP. *G. ruber* and *P. obliquiloculata* are chosen as suitable indicators for surface and thermocline conditions, respectively and the regional, species-specific Mg/Ca-temperature calibrations set the basis for accurate paleotemperature estimates.

The sediment core records reflect a complex pattern of astronomically driven and glacial–interglacial variations in surface and thermocline temperature, $\delta^{18}O_{SW}$ (salinity) and the water column structure and illustrate the interplay of local and remote forcings on the WPWP. The surface $\delta^{18}O_{SW}$ records from both, the southern and the northern WPWP sites depict cyclic variations of precessional duration that likely reflect variations in precipitaton, with enhanced (reduced) precipitation when precession is high (low). The precipitation variability is most likely related to latitudinal migrations of the Intertropical Convergence Zone (ITCZ) with a more southward (northward) position of the ITCZ under high (low) precession.

The thermocline temperature record of core GeoB 17419-1 exhibits a close connection to variations in the Earth's obliquity with warmer temperatures when obliquity is high. This is attributed to obliquity-driven variations in the subduction and lateral advection of the subtropical source waters, namely the South Pacific Tropical Water (SPTW). The obliquity-relation is less apparent in the thermocline temperature records of core GeoB 17426-3 and the northern WPWP site. Instead, these records are influenced by precession. The difference in the pacing of the thermocline temperature records is likely attributed to the differing influence of astronomical forcing on the thermocline water masses that influence the individual sites. The thermocline $\delta^{18}O_{SW}$ records also show cyclic variations on the precession band, with depleted (enriched) $\delta^{18}O_{SW}$ under high (low) precession. It remains unclear whether these precession-related variations are related to shifts in the source regions of the thermocline waters and/or to variations in the vertical structure of the water column.

The difference between surface and thermocline temperatures (ΔT) of GeoB 17419-1 is used to assess variations in the relative thermocline depth. A decreased temperature gradient indicates a thermocline deepening during the Last Glacial Maximum (LGM). A compilation of hitherto available ΔT records from

the WPWP illustrates a dipole-like pattern of LGM thermocline depth anomalies, with a shoaling in the northern, and a deepening in the southern WPWP. Output of Paleoclimate Model Intercomparison Project (PMIP) LGM climate model simulations reveals that this spatial pattern of thermocline depth anomalies can be mainly attributed to glacial wind-field anomalies and Sverdrup dynamics, and ultimately associated with a contraction of the Pacific Walker cell during the LGM.

Kurzfassung

Das Westpazifische Wärmebecken (WPWP) spielt eine zentrale Rolle innerhalb des globalen Klima- und Ozeansystems. Die Region ist durch die höchsten Meeresoberflächentemperaturen der Erde gekennzeichnet. Sie bildet daher eine wichtige Quelle latenter und sensibler Wärme für die Atmosphäre und beeinflusst das regionale und globale Klima. Nichtsdestotrotz ist unser Wissen über die Klima- und Ozeandynamik des WPWP noch immer limitiert. Insbesonders gibt es nur sehr wenige Thermoklinenrekonstruktionen, obwohl die Thermokline von großer Bedeutung für die regionalen klimatischen und ozeanischen Bedingungen ist. Die Thermoklinenwasser des WPWP verbinden beispielsweise den außertropischen Pazifik mit dem WPWP. Thermoklinenrekonstruktionen ermöglichen daher ein besseres Verständnis überregionaler Einflussfaktoren auf den WPWP. Darüber hinaus ist der Zustand der Thermokline eng an die vorherrschenden klimatischen Bedingungen geknüpft. Thermoklinenrekonstruktionen erlauben somit Rückschlüsse auf Veränderungen in der atmosphärischen Zirkulation.

Der Schwerpunkt dieser Arbeit liegt auf der Rekonstruktion von Variationen in den Oberflächen- und Thermoklinen-Bedingungen des WPWP mit dem übergeordneten Ziel, die regionale Ozean- und Klimavariabilität über den(die) letzten (zwei) glazial-interglazialen Zyklus(en) besser zu verstehen. Die Rekonstruktionen basieren auf marinen Sedimentkernen, die innerhalb (GeoB 17419-1) und östlich (GeoB 17426-3) der Bismarck See vor Papua Neu Guinea (PNG; südlicher WPWP) genommen worden sind, und welche die letzten 110.000 bzw. 210.000 Jahre umfassen. Um die Variabilität des WPWP über den letzten glazialen und interglazialen Zyklus zu untersuchen, werden die Ergebnisse außerdem mit publizierten Daten einer Lokation im nördlichen WPWP verglichen. In erster Linie werden an Schalen planktischer Foraminiferen gemessene Mg/Ca Verhältnisse und stabile Sauerstoffisotope ($\delta^{18}O$) verwendet, um Oberflächen- und Thermoklinentemperaturen, die vertikale Stratifizierung der oberen Wassersäule, und die Sauerstoffisotopenzusammensetzung des Meerwassers ($\delta^{18}O_{SW}$) zu rekonstruieren. Mg/Ca und $\delta^{18}O$ stellen gebräuchliche und robuste Proxies zur Rekonstruktion von Oberflächen- und Thermoklinenbedingungen dar. Ihre Kalibrierung erfordert jedoch sorgfältige, regionale Studien zur Abschätzung der Kalzifizierungstiefe und -temperatur von Foraminiferen in Abhängigkeit von lokalen Umweltbedingungen. Die Kalzifizierungstiefen planktischer Foraminiferen im WPWP sowie regionale Mg/Ca-Temperatur-Relationen wurden bislang noch nicht untersucht. Innerhalb dieser Arbeit wurden $\delta^{18}O$ und Mg/Ca, die an Schalen planktischer Foraminiferen aus rezenten Oberflächensedimenten von verschiedenen Lokationen innerhalb des WPWPs gemessen worden sind, mit Messdaten aus der Wassersäule (Temperatur, Salzgehalt und $\delta^{18}O_{SW}$) kombiniert, um regionale Kalzifizierungstiefen und -

temperaturen mehrerer planktischer Foraminiferenarten abzuschätzen und regionale, artenübergreifende und -spezifische Mg/Ca-Temperaturkalibrierungen zu erstellen.

Die Ergebnisse zeigen, dass *Globigerinoides ruber*, *Globigerinoides elongatus* (~0–80 m) und *Globigerinoides sacculifer* (~45–85 m) die Bedingungen der Mischungsschicht aufzeichnen, während *Pulleniatina obliquiloculata* und *Neogloboquadrina dutertrei* die Bedingungen der oberen (~90–160 m), und *Globorotalia tumida* die Bedingungen der unteren (~230–265 m) Thermkcline widerspiegeln. Die neu erstellte, artenübergreifende Mg/Ca-Temperatur Kalibrierung (Mg/Ca = 0.24 exp 0.097 * T) zeigt eine gute Übereinstimmung mit zuvor publizierten Regressionen anderer Regionen. Die artenspezifischen Mg/Ca-Temperatur Beziehungen von *G. ruber*, *G. elongatus* und *G. tumida* sind ähnlich zu publizierten Gleichungen. Der neue Datensatz impliziert jedoch außergewöhnlich hohe Kalzifizierungstemperaturen von *G. sacculifer*, *P. obliquiloculata* und *N. dutertrei* im WPWP, die durch bisher existierende Kalibrierungen unterschätzt wurden. Die regionalen Mg/Ca-Temperatur Beziehung ist am besten über die Gleichungen Mg/Ca = 0,24 exp 0,097 * T für *G. sacculifer*, und Mg/Ca = 0,21 exp 0,097 * T für *P. obliquiloculata* und *N. dutertrei* beschrieben.

Die Paläo-Umweltrekonstruktionen reflektieren ein komplexes Muster orbital und glazial-interglazial beeinflusster Variationen in der Oberflächen- und Thermoklinentemperatur, $\delta^{18}O_{SW}$ und der Wassersäulenstruktur und verdeutlichen das Zusammenspiel lokaler und überregionaler Einflussfaktoren auf die Klima- und Ozeanbedingungen des WPWP. Die $\delta^{18}O_{SW}$ Werte der Oberfläche zeigen zyklische Variationen im Frequenzbereich der Präzession, die wahrscheinlich Niederschlagsvariationen widerspiegeln, mit erhöhtem (verringertem) Niederschlag, wenn die Präzession hoch (niedrig) ist. Die Niederschlagsvariabilität ist vermutlich in der meridionalen Verschiebung der intertropischen Konvergenzzone (ITCZ), mit einer südlicheren (nördlicheren) Position der ITCZ bei hoher (niedriger) Präzession, begründet.

Die anhand des Kerns GeoB 17419-1 rekonstruierte Thermoklinentemperatur weist eine enge Verbindung zu Variationen der Obliquität der Erde auf, mit wärmeren Temperaturen bei hoher Obliquität. Dies ist vermutlich durch Variationen in der Subduktion und Advektion des subtropischen Quellwassers, dem Südpazifisch Tropischen Wasser (SPTW), verursacht. An den Lokationen GeoB 17426-3 und im nördlichen WPWP ist die Thermoklinentemperatur deutlich weniger von Obliquität geprägt. Vielmehr ist die Temperaturvariabilität an diesen Lokationen durch Präzession beeinflusst. Dies lässt sich auf den unterschiedlichen Einfluss astronomischer Forcings auf die verschiedenen Wassermassen zurückführen, die die einzelnen Lokationen beeinflussen. Die Variabilität im $\delta^{18}O_{SW}$ der Thermokline deutet ebenfalls auf einen Präzessionseinfluss hin, mit niedrigerem (höherem) $\delta^{18}O_{SW}$ bei hoher (niedriger) Präzession. Es

bleibt unklar, ob diese Variationen mit Verschiebungen in den Quellregionen der Thermoklinenwasser und/oder Veränderungen in der vertikalen Stratifizierung der Wassersäule zusammenhängen.

Der Gradient zwischen Oberflächen und Thermoklinentemperatur (ΔT) in Kern GeoB 17419-1 wird verwendet, um Variationen in der relativen Tiefe der Thermokline zu bestimmen. Ein verringerter Temperaturgradient zeigt eine Vertiefung der Thermokline während des letzten glazialen Maximums (LGM) an. Eine Zusammenstellung von bisher verfügbaren ΔT-Aufzeichnungen aus dem WPWP zeigt ein Dipol-ähnliches Muster von LGM-Thermoklinen-Tiefenanomalien, mit einer Verflachung der Thermokline im nördlichen, und einer Vertiefung im südlichen WPWP. Ergebnisse von 'Paleoclimate Model Intercomparison Projects' (PMIP) LGM-Klimamodellsimulationen zeigen, dass dieses räumliche Muster von Thermoklinen-Tiefenanomalien hauptsächlich auf Anomalien im glazialen Windfeld, Sverdrup-Dynamik, und letztendlich auf eine Kontraktion der pazifischen Walker-Zirkulation während des LGM zurückzuführen ist.

Acknowledgements

I am obliged for the last three years, during which I have been working on my PhD project. Many people accompanied me throughout that time.

First of all, I thank Dierk Hebbeln, and especially Mahyar Mohtadi, who offered me the PhD position and guided me throughout, sharing their knowledge and experience in science. Mahyar has always challenged, but also encouraged me to trust myself, and gave support whenever needed. He taught me a critical, process-oriented way of thinking. Mahyar, I couldn't have asked for a better supervisor and I am grateful to work with you.

I also thank Gerhard Schmiedl who is the second reviewer of my thesis.

I am grateful to Yair Rosenthal who supervised me during my research stay at the IMCS. His enthusiasm for science is inspiring. Yair was always ready to give advice, but let me do the things my way. I also thank Paola Moffa Sanchez for her support during and after my stay at the IMCS. I had an amazing time in New Brunswick and Highland Park, and thank all the people who welcomed me there, and who shared lunch breaks, long nights and weekends with me.

Many thanks are owed to all my co-authors, namely Mahyar Mohtadi, Yair Rosenthal, Delia Oppo, Gema Martínez Méndez, Paola Moffa-Sanchez, Stephan Steinke, Matthias Prange, Kazuyo Tachikawa, Jeroen Groeneveld, Markus Kienast and Dierk Hebbeln. I am extremely grateful for your constructive, challenging and encouraging comments on my posters and manuscripts. My co-authors, especially Yair and Delia, were always willing to have a glance on my work, even though analyses were not finished yet and contributed with input, discussions and wise comments on the science. Matthias supported me at the very end of my thesis. He provided and interpreted the output of climate model simulations used within my second manuscript. I wish I had asked him for a lecture in atmosphere and ocean physics much earlier.

For laboratory support and sample processing, I would like to thank Kaixuan Bu, Stephan Steinke, Gema Martínez Méndez, Jeroen Groeneveld, Heather Johnstone, Silvana Pape, Christina Gnade, Vera Bender, Vera Lukies and Volker Diekamp. My student helpers, particularly Marco Wolsza, Vera Rodehutscort and Clara Lange are thanked for sample preparation. In addition, I thank Jutta Bülten for IT and Carmen Murken, Nico Dittert and Birgit Volkmann for any administrative support. Stefan Mulitza, Thomas Westerhold and Michael Schulz are acknowledged for helpful discussions and lectures about age modeling and time series analysis. I also acknowledge Heiko Pälike and Ute Merkel, who were, along with Mahyar and Dierk, members of my thesis committee, for their support during the committee

meetings, especially during the first two years of my thesis. Furthermore, I thank my graduate school GLOMAR for offering a wide range of courses, and especially for providing a platform to exchange with other PhD students. I really appreciated the opportunity to study in such a friendly, comfortable environment. GLOMAR also provided financial support, which enabled me to spend three months at the Rutgers University in the US.

My working goup 'AG Hebbeln' let me feel comfortable right from the beginning. I thank you for the pleasant working atmosphere with joint coffee and lunch breaks, serious discussions and laughter, moral and, needless to say, scientific support. Here, I would like to especially mention Mahyar, Jürgen Titschack, Claudia Wienberg, Gema and Stephan as well as my fellow PhDs. I am especially grateful to Martin Bartels and Yusuf Awaluddin, who were my office mates over the past three years. Martin is also thanked for the proof reading of my thesis.

This summer, I was lucky to get the chance to sail on the SO-256 expedition. It was my first expedition and an amazing experience, for which I am grateful.

My project was funded by the DFG-Research Center / Cluster of Excellence ‚The Ocean in the Earth System' and supported by the BMBF Project 03G0228A. Laboratory facilities were provided by the MARUM - Center for Marine Environmental Sciences.

My deepest thank goes to my family and friends. Without you, I would not be where I am. My parents have always supported me, not only during my PhD, but way earlier, encouraging me to get a good education and enabled me to study at the university. My friends, especially Conny, Hauke, Maria, Anna and Astrid supported me in many ways during the past years. Finally, I am deeply thankful to Martin, who has been at my side since the beginning of my studies and shared his life with me for almost ten years.

Table of Contents

Chapter 1.
Introduction

1.1. General motivation

Nowadays, we are facing rapid changes in global climate, which potentially have far-reaching and disastrous consequences for life on Earth. Not solely, but also in this regard, understanding the forcings and dynamics that control the climate variability is a major motivation for climate sciences and of paramount importance for humankind. Along with observational data and numerical models, proxy-based reconstructions are indispensable to improve our knowledge about past climate variations and ultimately our understanding about climate dynamics. They provide the opportunity to study how the climate system in the past responded to different forcings (e.g. astronomical forcing) and boundary conditions (e.g. sea level, extension of ice sheets, CO_2). The climate system consists of five major components, namely atmosphere, hydrosphere (including oceans), land surface, biosphere, and cryosphere, which interact in a complex way. The ocean plays a pivotal role in the climate system, inter alia, as it stores and transports vast amounts of heat, freshwater and carbon [*Rhein et al.*, 2013]. Ocean and atmosphere are inherently coupled. To better understand climate (and ocean) dynamics it is thus inevitably to decipher how these components interact and how the ocean responds to climate variations.

The western tropical Pacific Ocean, known as Western Pacific Warm Pool (WPWP) plays a key role within the global climate and ocean system. With annual mean sea surface temperatures (SST) exceeding 28°C [e.g. *Locarnini et al.*, 2013] (Figure 1.1) it holds the largest warm water body on Earth. Due to these high temperatures, the WPWP is a major source area of heat and water vapour to the global atmosphere [e.g. *Gagan et al.*, 2004] and has therefore a substantial influence on the regional and global climate. The area is, for example, home to large-scale climate phenomena, such as the El Niño–Southern Oscillation (ENSO) which affects climate worldwide and can have widespread and severe consequences for our ecological and socioeconomic systems, which are difficult to quantify. The ocean currents of the WPWP link the extratropical Pacific to the equatorial Pacific Ocean and the Indonesian Throughflow (ITF), which builds an important component of the global overturning circulation [e.g. *Gordon*, 1986]. For these reasons, it is of high interest to better understand WPWP climate and ocean variations and dynamics

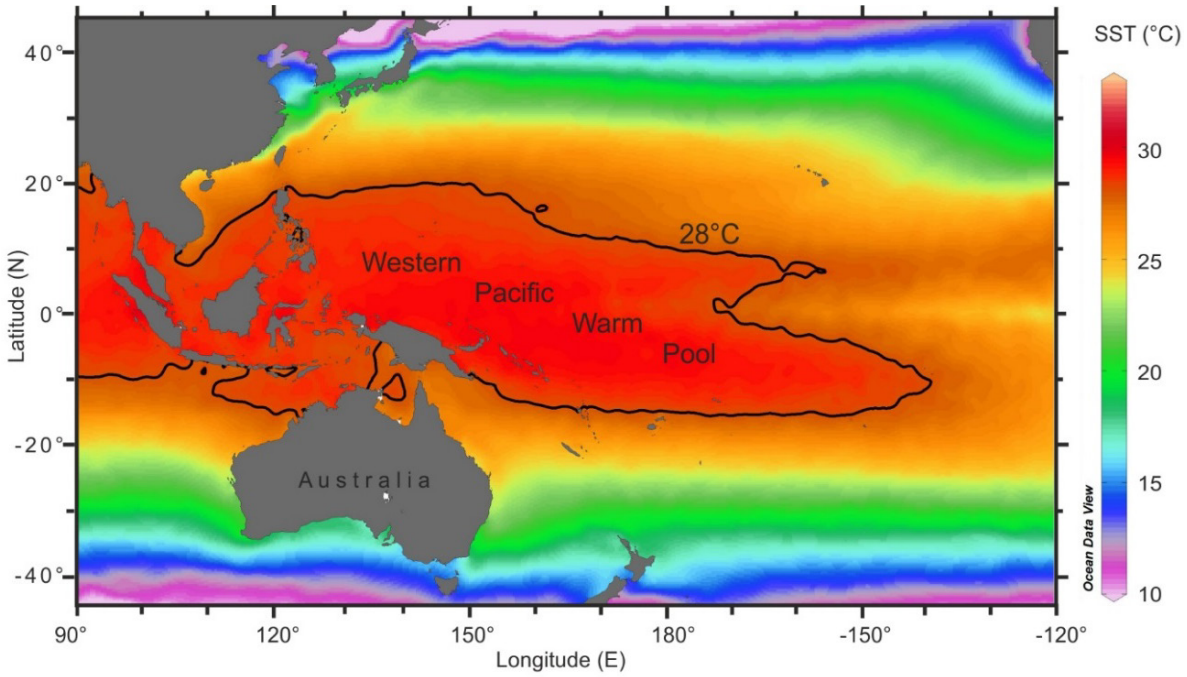

Figure 1.1. Annual mean sea surface temperatures (SSTs) across the Pacific Ocean. The contour line denotes the 28°C isotherm and defines the boundary of the Western Pacific Warm Pool (WPWP). Temperature data are derived from the World Ocean Atlas 2013 [*Locarnini et al.*, 2013]. The map was created with the Ocean Data View (ODV) software [*Schlitzer*, 2014].

1.2. State of WPWP paleoclimate and paleoceanography reconstructions

Over the past decades numerous studies have addressed the climate and ocean evolution and dynamics of the tropical Pacific and Indo-Pacific region on various timescales including millennial, orbital and glacial–interglacial cycles. These studies reveal that the long-term climate and ocean variability of the WPWP is associated with a range of factors and mechanisms, such as variations in the Walker circulation and/or the state and activity of ENSO [e.g. *Bolliet et al.*, 2011; *Sagawa et al.*, 2012], changes in the Austral-Asian monsoon system and the Hadley circulation [e.g. *Dang et al.*, 2012; *Tachikawa et al.*, 2011] as well as a remote influence of mid- and high latitude climate variations, in response to astronomical forcing and glacial–interglacial varying boundary conditions.

Astronomical forcing that include variations in the Earth's orbital eccentricity (deviation of the Earth's orbit from a circular line that varies on 100 and 400 kyr cycles), obliquity (the Earth's axial tilt that varies between 22.5 and 24.5° with a periodicity of 41 kyr) and precession (wobbling of the Earth's axis and rotation of the orbital ellipse that varies on 19 and 23 kyr cycles) control the insolation strength and (temporal and spatial) distribution on Earth and therefore have manifold impacts on ocean and climate dynamics. The Earth's orbital precession controls the seasonal and interhemispheric distribution of insolation with increased (decreased) insolation during northern summer coupled to decreased (increased)

insolation during southern summer when precession is low (high). The interhemispheric alternating strength of insolation strongly affects the distribution of rainfall in the tropics. Broadly speaking, phases of high summer insolation coincide with enhanced rainfall amounts on the same hemisphere [e.g. *Cheng et al.*, 2012; *Wang et al.*, 2014]. Accordingly, proxy records from around the WPWP generally indicate that the rainfall over southern China is stronger (weaker) when precession is low (high), while it is weaker (stronger) over Papua New Guinea (PNG) [e.g. *Tachikawa et al.*, 2011; *Wang et al.*, 2001]. This pattern has been attributed mainly to meridional shifts of the ITCZ, changes in its rainfall intensity, and changes in the intensity of the Austral-Asian monsoon, which react sensitively to the precession-induced variations in seasonal temperature gradients and varying land–ocean thermal contrasts (see chapter 2.2.1 for details on the ITCZ and the Austral-Asian monsoon system) [e.g. *Mohtadi et al.*, 2016; *Schneider et al.*, 2014]. However, other records reveal that the spatial rainfall structure is more complicated and not fully understood yet. For instance, speleothem records from the northern (~4°N) [*Partin et al.*, 2007] and southern (~8.5 °S) [*Griffiths et al.*, 2009] WPWP bear some similarities over the last precession cycle [*Cheng et al.*, 2012]. Likewise, a marine proxy record from offshore Mindanao (northern WPWP) indicates an antiphased relationship between local precipitation and northern hemisphere summer insolation [*Fraser et al.*, 2014]. Based on these records, it was proposed that complex variations in the Walker circulation (a zonal atmospheric circulation cell spanning over the tropical Pacific Ocean, see chapter 2.2.2 for details) exert an additional control on WPWP precipitation on the precession band[*Cheng et al.*, 2012; *Fraser et al.*, 2014]. A dependence of the Walker circulation on precession-controlled insolation variations has also been suggested on the basis of other climate indices [e.g. *Tudhope et al.*, 2001; *Turney et al.*, 2004] and by model simulations [*Clement et al.*, 1999; *Liu et al.*, 2000], though more recent models do not show a clear link of ENSO to Earth's orbital variations [*Emile-Geay et al.*, 2015].

The impact of obliquity on the tropical Pacific is still unclear. Obliquity controls the seasonality of insolation on both hemispheres, with high (low) obliquity causing a stronger (weaker) seasonality on both hemispheres. The influence of obliquity on low-latitude insolation is very small. Despite this fact, several records from the tropical Pacific Ocean provide evidence that obliquity influences the regional climate. For instance, some temperature records show a significant 41-kyr signal [*de Garidel-Thoron et al.*, 2005; *Lea et al.*, 2000; *Pena et al.*, 2008]. In addition, high-resolution temperature records from both hemispheres of the Indo-Pacific region show a cooling trend during the Holocene [*Rosenthal et al.*, 2013]. It was hypothesized that this cooling trend is caused by a remote influence of obliquity-driven climate variations in mid- and high latitudes [*Rosenthal et al.*, 2013; *Rosenthal et al.*, 2017]. Besides, a proxy record from offshore PNG indicate enhanced (decreased) rainfall over PNG when obliquity is low (high) [*Liu et al.*, 2015] suggesting that obliquity impacts the atmospheric circulation in the tropics. This is also supported by modeling studies that indicate an obliquity influences on the tropical Pacific climate by

enforcing reorganizations of the Hadley circulation, which could be linked to obliquity-induced alterations in the meridional (equator–pole) insolation gradient with smaller (larger) gradients when obliquity is high (low). [*Bosmans et al.*, 2015; *Mantsis et al.*, 2011; *Mantsis et al.*, 2014]. Obliquity-related variations in the meridional insolation and surface pressure gradients could also affect the Pacific subtropical gyre circulation, which is suggested to weaken (strengthen) when obliquity is high (low) [*Lee and Poulsen*, 2005; *Mantsis et al.*, 2011; *Timmermann et al.*, 2014].

In addition, changing boundary conditions, such as atmospheric CO_2, the extent of ice sheets and sea level, control the climatic and oceanic conditions over glacial–interglacial cycles. Many reconstructions focused on the climatic evolution from the Last Glacial Maximum (LGM) to the Holocene. These reconstructions reveal that the WPWP surface ocean warmed by ~2.5 to 5.0 °C from the LGM to the Holocene [*Bolliet et al.*, 2011; *de Garidel-Thoron et al.*, 2007; *Fraser et al.*, 2014; *Lea et al.*, 2000; *Regoli et al.*, 2015; *Sagawa et al.*, 2012; *Tachikawa et al.*, 2014]. The few available thermocline reconstructions indicate a thermocline warming of ~4.0 to 5.0 °C during the same period [*Bolliet et al.*, 2011; *Sagawa et al.*, 2012]. Proxy-based and numerical modeling studies indicate that changing boundary conditions over glacial–interglacial cycles affected both the Hadley circulation with the Austral-Asian monsoon system and the ITCZ [e.g. *Leech et al.*, 2013; *Rosenthal et al.*, 2003], and the Walker circulation [e.g. *DiNezio and Tierney*, 2013] and/or the state and activity of ENSO [e.g. *Andreasen and Ravelo*, 1997; *Koutavas et al.*, 2002]. Due to its large-scale effects, the reconstruction of past variations in the Walker circulation and ENSO has drawn particular attention. However, published studies from the western and eastern tropical Pacific Ocean that use a wide range of proxies and indications as well as climate model simulations provide contrasting results, pointing to both, either a weaker Walker circulation and/or more El Niño-like conditions (or an enhanced ENSO activity) [e.g. *Koutavas et al.*, 2002; *Sadekov et al.*, 2013; *Sagawa et al.*, 2012] or a stronger Walker circulation and/or more La Niña-like conditions (or a reduced ENSO activity) [e.g. *Andreasen and Ravelo*, 1997; *Ford et al.*, 2015; *Zhu et al.*, 2017] during glacial periods as the LGM (see chapter 2 for details about the Hadley and Walker circulations).

1.3. Scientific objectives

As introduced, proxy-based paleo-reconstructions and climate model simulations reveal that the long-term climate variability and ocean dynamics of the WPWP are controlled by many different forcings and mechanisms on various timescales. However, the results only provide an incomplete picture on WPWP ocean and climate dynamics and are partly contradicting. For instance, many hitherto available records from the Indo-Pacific region focus on the period since the LGM. However, this timeframe is not sufficiently long to entangle different driving forces and mechanisms. Besides, they provide conflicting

results, for instance, about the state of the WPWP, suggesting both, a stronger Pacific Walker circulation and/or more La Niña-like conditions as well as a weaker Walker circulation and more El Niño-like conditions during the LGM.

Especially thermocline reconstructions are sparse, despite the important role of thermocline waters and conditions for the WPWP ocean and climate dynamics: (i) The WPWP thermocline waters originate in the extratropical Pacific Ocean (see chapter 2.3 for details). Thermocline reconstructions thus provide the opportunity to investigate the influence of extratropical Pacific climate variability on the WPWP thermocline and on the equatorial Pacific climate. (ii) The depth and state of the thermocline are closely linked to the prevailing climate conditions. Subsequently, records of thermocline depth variations allow to draw clues on variations in the atmospheric circulation system. Modern observations for instance show that the state of ENSO and associated variations in the Pacific Walker circulation have a strong influence on the depth of the thermocline with a shallower (deeper) thermocline during El Niño (La Niña). In turn, the thermocline depth is also involved in several feedback mechanisms that damp or amplify ENSO [e.g. *Gasparin et al.*, 2012; *Gu and Philander*, 1997] and might therefore have a direct impact on the WPWP climate. (iii) WPWP thermocline waters feed the ITF. Numerous studies focused on the evolution of the ITF [e.g. *Ding et al.*, 2013; *Xu et al.*, 2008]. However, knowledge on the evolution of the WPWP source water masses is very limited. Especially records from the southern WPWP are sparse and it is fairly unknown how the source waters of South Pacific origin influenced the ITF and the climate of the maritime continent throughout the past.

Ideal tools to reconstruct both, surface and thermocline conditions are provided by geochemical proxies as stable oxygen isotopes and Mg/Ca ratios measured on the calcite tests of surface and thermocline-dwelling planktic foraminifera from marine sediments (see chapter 3 for details). However, an accurate calibration and application of these proxies require thorough regional studies, because parameters such as calcification depth and temperature of planktic foraminifera strongly depend on local environmental conditions. To date, estimates of calcification depths are limited to plankton tow and sediment trap studies from the central equatorial Pacific, North Pacific or Indian Ocean [*Kawahata et al.*, 2002; *Kuroyanagi and Kawahata*, 2004; *Mohtadi et al.*, 2011; *Peeters et al.*, 2002; *Rippert et al.*, 2016; *Watkins et al.*, 1996]. Since regional calcification depths estimates are lacking, regional thermocline reconstructions, so far, are based on many different planktic foraminifera species, such as *Globigerinoides elongatus* (previously referred to as *G. ruber* s.l.) [*Regoli et al.*, 2015], *Globigerinoides sacculifer* [*de Garidel-Thoron et al.*, 2007], *Pulleniatina obliquiloculata* [*Bolliet et al.*, 2011] and *Globorotalia tumida* [*Leech et al.*, 2013]. Besides, the regional Mg/Ca-temperature dependencies of the commonly used planktic foraminifera species are fairly unknown. Particularly, species-specific Mg/Ca-temperature calibrations for presumably

thermocline-dwelling planktic foraminifera do not exist and the adequacy of calibrations from other areas [e.g. *Anand et al.*, 2003], so far, has not yet been tested for the WPWP.

This thesis aims at reconstructing the evolution of WPWP surface and thermocline conditions over the last (two) glacial–interglacial cycle(s) with the overarching goal to better understand the ocean and climate variability and dynamics within the WPWP. Due to the striking gap of knowledge concerning the evolution of the southern WPWP, a special focus lies on the southern WPWP offshore PNG. Mg/Ca ratios and stable oxygen isotopes measured on tests of planktic foraminifera from marine sediment cores are used as the main proxies to reconstruct (sub)surface ocean temperatures and the oxygen isotope composition of seawater throughout the thesis. Where appropriate other proxies and the output of PMIP (Paleoclimate Model Intercomparison Project) climate model simulations are additionally used.

The following scientific questions are addressed in the frame of this thesis:

1) At which depths do planktic foraminifera species commonly used in paleo-reconstructions calcify in the WPWP and consequently, which foraminifera species are most appropriate to reconstruct the regional surface and thermocline conditions? Which equations do best describe the regional Mg/Ca-temperature dependencies of the individual species in the WPWP?
2) How did the WPWP thermocline respond to various forcings over the past (two) glacial–interglacial cycle(s)? What mechanisms controlled WPWP thermocline conditions and dynamics?
3) How did climate and ocean conditions vary across the WPWP?

1.4. Thesis outline, overview of own research and authors contributions

The thesis is written in a cumulative form. In chapter 2 the WPWP with its prevailing climate and ocean conditions is introduced. In chapter 3 the material and methods used are presented in a comprehensive way. Chapters 4-6 build the main part of the thesis and consist of three individual manuscripts, which address the scientific questions raised above. The individual manuscripts are published, submitted, or in preparation for submission in peer-reviewed international scientific journals. They were prepared and written in collaboration with other scientists. An outline of the individual manuscripts and the author's contribution is given below. Chapter 7 provides a synthesis and an outlook on connection points for potential future research projects.

Manuscript 1 (Chapter 4):

"Stable oxygen isotopes and Mg/Ca in planktic foraminifera from modern surface sediments of the Western Pacific Warm Pool: Implications for thermocline reconstructions"

Martina Hollstein, Mahyar Mohtadi, Yair Rosenthal, Paola Moffa Sanchez, Delia Oppo, Gema Martínez Méndez, Stephan Steinke, Dierk Hebbeln

Published in *Paleoceanography*, doi:10.1002/2017PA003122

The manuscript aims to determine how modern hydrographic conditions of the WPWP are recorded in planktic foraminifera shells. A set of 12 modern core top samples from different stations within the WPWP was selected to estimate calcification depths and temperatures of various planktic foraminifera species in the WPWP and to establish regional multispecies and species-specific Mg/Ca-temperature calibrations. The results are of key importance to the rest of the thesis because they reveal which foraminifera species can be used as suitable indicators of WPWP surface and thermocline conditions and which equations best describe the regional Mg/Ca-temperature dependencies.

M. Mohtadi, Y. Rosenthal and M. Hollstein designed the study. The sample material was provided by M. Mohtadi and Y. Rosenthal. The preparation of samples for radiocarbon measurements was largely done by student helpers under the guidance of G. Martínez Méndez. Apart from that, M. Hollstein was responsible for sample processing. She prepared the samples for stable isotope and Mg/Ca analysis and performed the Mg/Ca measurements on the ICP-MS. Y. Rosenthal and P. Moffa-Sanchez provided support in sample preparation and processing. M. Hollstein interpreted the data with contributions of M. Mohtadi, Y. Rosenthal and D. Oppo, and wrote the manuscript with contributions of all co-authors.

Manuscript 2 (Chapter 5):

"Variations in Western Pacific Warm Pool surface and thermocline conditions over the past 110,000 years: Forcing mechanisms and implications for the glacial Walker circulation"

Martina Hollstein, Mahyar Mohtadi, Yair Rosenthal, Matthias Prange, Delia Oppo, Gema Martínez Méndez, Kazuyo Tachikawa, Paola Moffa Sanchez, Stephan Steinke, Dierk Hebbeln,

Submitted to *Quaternary Science Reviews*

This manuscript aims to improve our understanding about the driving forces and mechanisms that control climate and ocean conditions in the WPWP. New and published Mg/Ca and $\delta^{18}O$ records of planktic foraminifera from sediment cores retrieved offshore PNG are combined to reconstruct variations in WPWP surface and thermocline conditions and the vertical stratification of the upper water column over the past 110 kyr. In addition, available Paleoclimate Model Intercomparison Project (PMIP) climate model

simulations are used to discuss potential forcing mechanisms for changes in WPWP thermocline depth. The records reflect a complex pattern of glacial–interglacial and astronomically driven variations in (sub)surface temperature, salinity and the water column structure and illustrate the role of local and remote forcings on the WPWP surface and thermocline conditions.

M. Hollstein, M. Mohtadi and M. Prange designed the story. Under the guidance of G. Martínez Méndez and M. Hollstein student helpers prepared the samples and selected foraminifera for geochemical analyses. M. Hollstein cleaned the samples for Mg/Ca analyses and performed the measurements under supervision of Y. Rosenthal and P. Moffa Sanchez. S. Steinke performed the XRF core scanning. M. Hollstein interpreted the proxy data with contributions of M. Mohtadi, Y. Rosenthal, D. Oppo, and K. Tachikawa and led the write-up of the manuscript. M. Prange performed the climate model simulations, interpreted the results and provided the corresponding text. All authors contributed to the final version of the manuscript.

Manuscript 3 (Chapter 6):

"The impact of astronomical forcing on the surface and thermocline variability across the Western Pacific Warm Pool over the past 160 kyr"

Martina Hollstein, Mahyar Mohtadi, Jeroen Groeneveld, Delia Oppo, Markus Kienast, Gema Martínez Méndez, Dierk Hebbeln

In preparation

This manuscript aims to monitor the climate and ocean variability across the WPWP during the last glacial–interglacial cycle. For this purpose, surface and thermocline Mg/Ca and $\delta^{18}O$ records from offshore PNG are compared with previously published records from the northern WPWP. The comparison indicates that the spatial structure across the WPWP remained relatively constant over the last glacial–interglacial cycle. Differences between records from the individual core sites are linked to astronomical forcing.

M. Hollstein and M. Mohtadi conceived the study. The sample preparation for stable isotope and Mg/Ca measurements was largely done by M. Hollstein with the help of student assistants, supervised by M. Hollstein and G. Martínez Méndez. Mg/Ca analyses were done by J. Groeneveld and M. Hollstein. M. Hollstein interpreted the results and wrote the manuscript with contributions of M. Mohtadi, D. Oppo and M. Kienast.

Chapter 2.

The Western Pacific Warm Pool

2.1. Modern setting

By definition, the WPWP comprises the area of the equatorial western Pacific Ocean where sea surface temperatures (SST) exceed 28 °C year-round (Figure 2.1) [*Carton and Giese*, 2008; *Locarnini et al.*, 2013]. To the west it is bordered by the Philippine archipelago, the Maluku Islands, New Guinea and the Indonesian Seas. The WPWP includes several deep ocean basins, such as the Philippine Sea, Caroline Basin, Bismarck Sea, Solomon Sea, Mariana Basin and the Marshall Basin (Figure 2.1) [e.g. *Tomczak and Godfrey*, 2003].

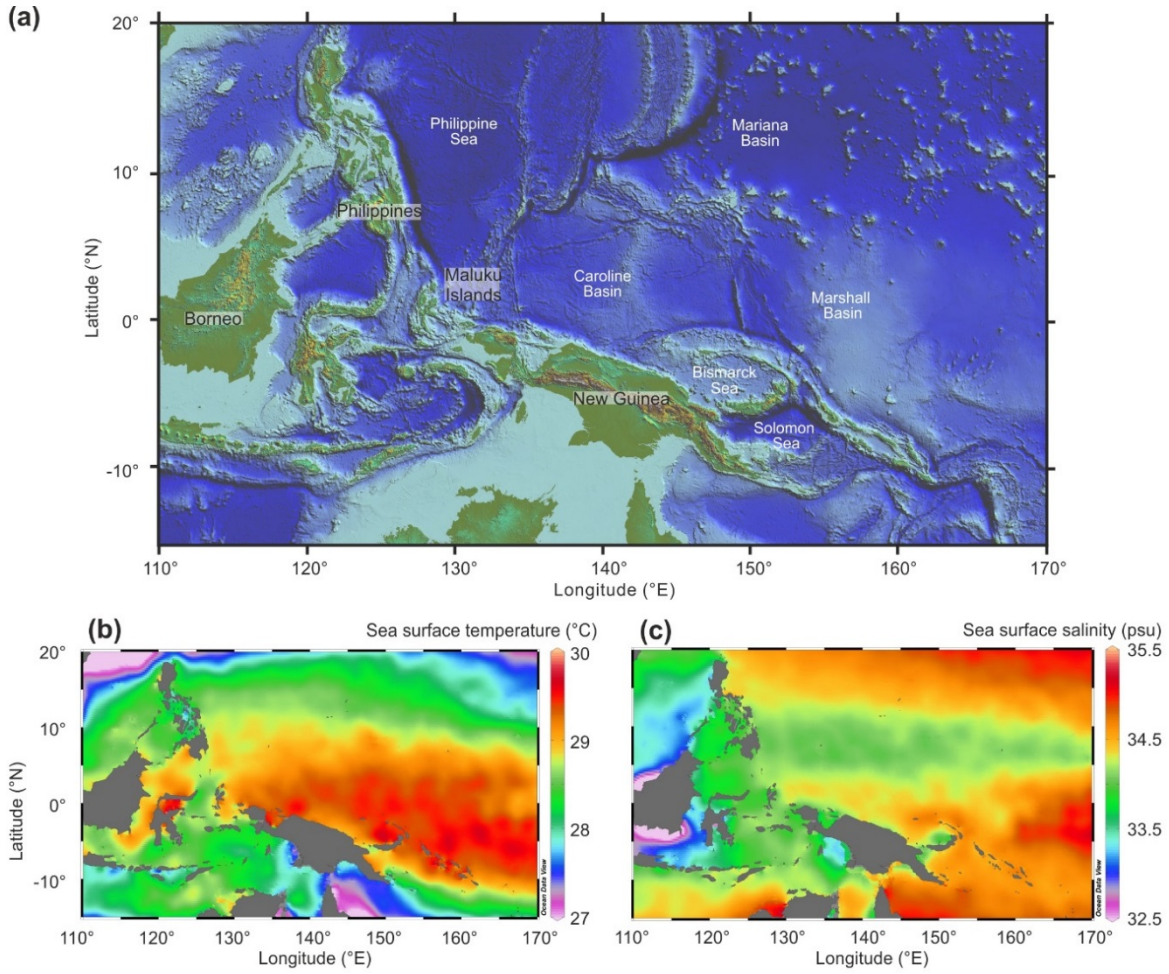

Figure 2.1. (a) Bathymetric map of the WPWP. (b and c) Mean annual sea surface temperature and salinity in the WPWP. Data are derived from the World Ocean Atlas 2013 [*Locarnini et al.*, 2013; *Zweng et al.*, 2013]. The maps in (b) and (c) were created with the Ocean Data View software [*Schlitzer*, 2014].

The WPWP builds the largest body of warm water on Earth. The pool of warm waters is created and maintained by constantly blowing trade winds that push warm surface waters towards the western part of the Pacific Ocean. The exceptionally warm mean annual temperatures cause deep convection and year-round heavy rainfall. Consequently, sea surface salinity (SSS) is relatively low, varying around 34.0–34.5 psu (Figure 2.1) [*Carton and Giese*, 2008; *Zweng et al.*, 2013]. The average mixed layer depth in the area is about 50–100 m [*Locarnini et al.*, 2013].

The regional climate and oceanography of the WPWP is complex and determined by various ocean–atmosphere couplings. On a seasonal scale, the climate is mainly determined by variations in the Hadley circulation, associated migrations of the ITCZ and the Austral-Asian monsoon system (chapter 2.2). On interannual timescales the Walker circulation and ENSO exert an additional control on the regional climate and ocean conditions (see chapter 2.3). During the southeast monsoon season in boreal summer, southeasterly winds prevail, the ITCZ is located to the north of the equator and precipitation in the northern hemisphere WPWP is strongest (Figure 2.2). During the northwest monsoon season in austral summer, trade winds reverse and the ITCZ is located to the south of the equator, which leads to increased precipitation over the study area and PNG. Seasonal variations in climate mainly affect the surface ocean hydrography. However, available climatological studies indicate that even average variations in surface temperature and salinity are relatively small, they do not exceed 1–2 °C and 1 psu, respectively [*Carton and Giese*, 2008; *Locarnini et al.*, 2013; *Zweng et al.*, 2013]. The thermocline remains almost unaffected by seasonal variations. Besides, seasonal variations in trade winds lead to only minor changes in mixed layer depths.

The Walker circulation and ENSO affect surface and thermocline ocean conditions and the mixed layer depths. El Niño (La Niña) is characterized by drier (wetter) conditions, cooler (warmer) sub(surface) temperatures and a shallower (deeper) thermocline across the WPWP. Interannual variations in surface temperatures are below 2–3 °C. Thermocline temperatures vary up to 7–8 °C in response to ENSO [*Carton and Giese*, 2008]. Anomalies in mixed layer or thermocline depth are in the order of several tens of meters. For instance, for the period between 1986 and 1998 observations indicate that the 20 °C isotherm, which is often used as an indicator for the thermocline depth in the WPWP, varied up to 40 m in relation to ENSO [*Harrison and Vecchi*, 2001].

2.2. Atmospheric circulation

2.2.1. Hadley circulation, ITCZ, and the Austral-Asian monsoon

The atmospheric circulation system over the tropical Pacific Ocean includes two major components: The meridional overturning Hadley cells and the zonal overturning Walker cells. The Hadley circulation

controls the spatial distribution of precipitation and the meridional transport of heat and energy within the atmosphere [e.g. *Donohoe et al.*, 2013]. It is basically driven by meridional temperature gradients between tropics and subtropics. Exceptional warm temperatures across the equator cause ascend of air. Near the tropopause, the rising air diverges into a northern and a southern branch that flow poleward, descend in the subtropics and then flow back within easterly trades towards the equator, where the branches converge creating a trough of deep atmospheric convection and heavy rainfall, known as the ITCZ. The ITCZ is thus mainly allocated with the ascending branch of the Hadley circulation. The atmospheric near surface flow is characterized by warm and moist easterly trades that also feed the ITCZ [e.g. *Schneider et al.*, 2014]. The position of the ascending branch of the Hadley cells and the ITCZ mainly depends on the thermal conditions near the surface which are primarily modulated by insolation and ocean currents that transport huge amounts of heat. In accordance with this, the rising Hadley branch and the ITCZ seasonally migrate between the hemispheres [e.g. *Schneider et al.*, 2014]. During boreal summer (austral winter), the rising Hadley branch, the ITCZ and therewith maximal precipitation are located to the north of the equator (over the northern WPWP) and southeasterly trade winds prevail. During boreal winter (austral summer), the rising Hadley branch and the ITCZ shift to the south, maximal rainfall is located to the south of the equator (over the southern WPWP) and northeasterly winds prevail (Figure 2.2).

The WPWP is partly also affected by the Austral-Asian monsoon. The Austral-Asian monsoon system includes the Indian and south-east Asian monsoon as well as the Australian-Indonesian monsoon [*Jourdain et al.*, 2013]. Basically responding to the seasonal cycling of insolation, meridional temperature gradients and land–sea thermal contrasts the Austral-Asian monsoon system is closely related to the Hadley circulation and the ITCZ. Heating of the Asia continent during boreal spring (austral autumn) initiates the Asian summer monsoon, which transports moisture and heat from Australia across the WPWP to the Asian continent. The boreal winter monsoon is characterized by cold, dry Siberian air flowing southward across eastern China, ultimately contributing to the wet Indonesian-Australian summer monsoon, that affects Indonesia, PNG and northern Australia [*An*, 2000]. The maritime continent forms a land-bridge along which the monsoon marches gradually from boreal summer to winter and vice versa [*Chang et al*., 2005]. As typical for tropical monsoons, rainfall occurs almost entirely within the ITCZ [*Mohtadi et al.,* 2016 and references therein]. Summarized, during boreal summer, when the ITCZ is located over the northern WPWP, southeast trades prevail (southeast monsoon). During boreal winter, the winds reverse and northwest trades prevails (northwest monsoon) and the ITCZ is located over the southern WPWP (Figure 2.2).

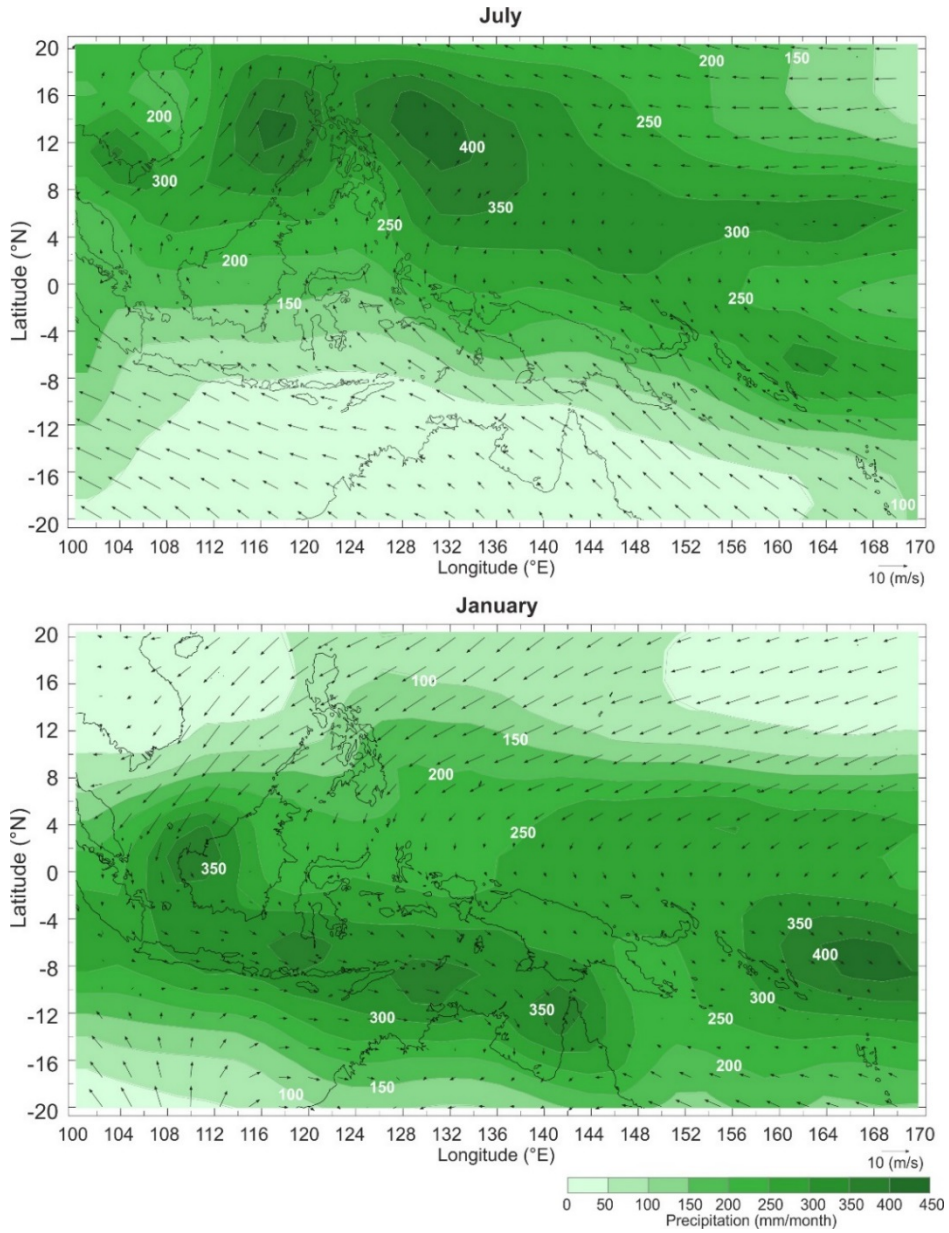

Figure 2.2. Monthly precipitation and wind across the WPWP for austral winter (July; top) and summer (January; bottom) during the 1981−2010 base period. The precipitation rate is indicated by green shading. Average wind speed and direction at a pressure level of 1000 hPa are indicated by black arrows. The data are provided by the U.S. National Centers for Environmental Prediction (NCEP). Figures are modified from iridl.ldeo.columbia.edu.

2.2.2. Pacific Walker circulation and the El Niño–Southern Oscillation

The Pacific Walker circulation is a zonal equatorial circulation cell, which is set up between the warm western and cool eastern Pacific Ocean. As described further above, easterly trades push warm waters across the Pacific Ocean creating a warm pool in the tropical western Pacific Ocean. Warm air ascends over the WPWP and flows towards the east, where it descends over the eastern equatorial Pacific and flows back towards the WPWP near the ocean surface (Figure 2.3). The ascend of air is associated with convection and precipitation above the WPWP. Concomitantly, the thermocline in the WPWP is rather

deep, while the eastern Pacific Ocean is characterized by upwelling of cold subsurface waters and a rather shallow thermocline [*Carton and Giese*, 2008; *Locarnini et al.*, 2013; *Zweng et al.*, 2013].

The ENSO describes an instability in this coupled atmosphere–ocean system: La Niña events (ENSO cold phases) are characterized by a stronger than normal Walker circulation that goes along with enhanced precipitation over the western and decreased precipitation over the eastern equatorial Pacific Ocean. The strengthening of the Walker circulation is coupled to a thermocline deepening in the WPWP and stronger upwelling in the eastern equatorial Pacific, which leads to anomalously cool temperatures off South America. By contrast, El Niño events (ENSO warm phases) are characterized by a weakening and eastward displacement of the Pacific Walker cell. The weakening of the trade winds goes along with a cooling of surface ocean temperature, a thermocline shoaling in the WPWP, and with a reduction in upwelling of cold waters in the eastern Pacific Ocean (thermocline deepening), which leads to a warming of the surface ocean offshore South America. Anomalously dry conditions occur in the western (central) tropical Pacific and wet conditions in the eastern equatorial Pacific (Figure 2.3) [e.g. *Philander*, 1985]. With periods between two and seven years, the state of ENSO varies irregularly on interannual timescales, but its evolution is phase-locked within the annual cycle, whereby the El Niño/La Niña events peak during boreal winter (austral summer) [e.g. *Rasmussen and Carpenter*, 1982].

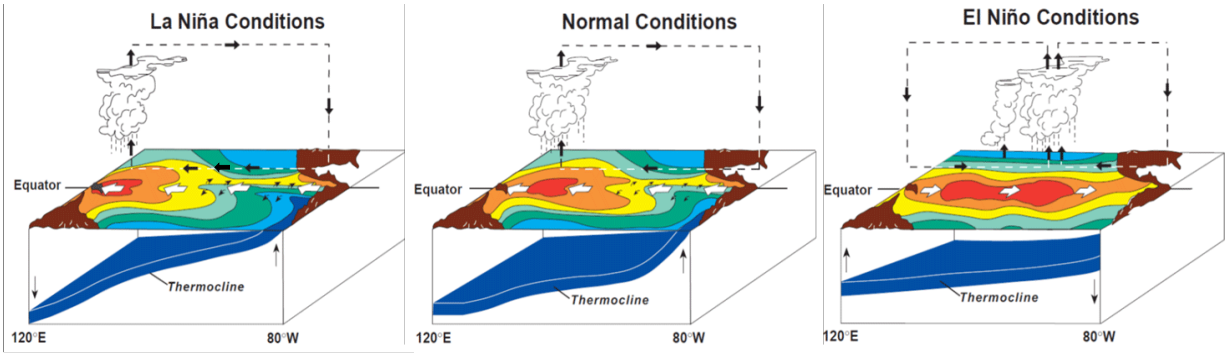

Figure 2.3. Sketch that illustrates the characteristic changes in climate and ocean conditions that are associated with ENSO [NOAA; https://www.pmel.noaa.gov].

The forcings and mechanisms controlling ENSO are not completely understood yet. Apparently, the oscillation between El Niño and La Niña conditions is driven by various positive and negative coupled ocean–atmosphere feedbacks that amplify or reduce the ENSO states. A positive feedback loop that contributes to the amplification of warm and cold ENSO phases is, for instance, the so-called Bjerknes feedback [*Bjerknes*, 1969]: A warming of surface ocean temperatures in the eastern equatorial Pacific decreases the zonal SST gradient causing a weakening of the Walker circulation and trade winds. Weaker trades further reduce the upwelling of cold waters in the eastern equatorial Pacific Ocean, which causes a

warming of surface ocean temperatures. By now, different other feedback loops that amplify or reduce the development of warm and cold ENSO phases are known [see e.g. *Collins et al.*, 2010]. However, the transition from warm to cold ENSO phases and vice versa still remains unclear.

2.3. Ocean circulation and water masses

The surface ocean circulation is driven by the atmospheric circulation. In the Pacific Ocean low latitude trades and mid-latitude westerlies set up two large gyres, namely the North and South Pacific Subtropical Gyres (Figure 2.4). The WPWP is mainly influenced by the westward flowing North Equatorial Current (NEC) in the North Pacific and South Equatorial Current (SEC) in the South Pacific Ocean and by tropical western boundary currents (WBCs) that are formed by bifurcation of the North and South Equatorial Currents at the Philippine and Australian coasts, respectively. More specifically, in the North Pacific, the NEC bifurcates at the Philippine coast into the poleward flowing Kuroshio Current and the equatorward flowing Mindanao Current (MC) [e.g. *Gordon et al.*, 2014; *Qiu and Chen*, 2010; *Toole et al.*, 1990]. In the South Pacific Ocean, the westward flowing SEC bifurcates into the northward directed New Queensland and Gulf of Papua Currents (NQC and GPC) and the southward directed East Australian Current (EAC) as it reaches the Australian coast [e.g. *Kessler and Gourdeau*, 2007]. The NQC and GPC flow equatorward along the east coast of Australia and through the Gulf of Papua and then feed the New Guinea Coastal Undercurrent (NGCUC) and the New Guinea Coastal Current (NGCC), which flow through the Bismarck Sea along the coast of New Guinea [*Fine et al.,* 1994]. A part of the SEC retroflects and forms the South Equatorial Counter Current. A branch of the GPC does not enter the Bismarck Sea but is deflected eastward and flows into the New Ireland Coastal Undercurrent (NICU). At the confluence zone of the MC and the SEC and NGCC/NGCUC near the equator, the currents feed the eastward flowing Equatorial Undercurrent (EUC), the North Equatorial Countercurrent (NECC) and the ITF [e.g. *Fine et al.*, 1994; *Goodman et al.*, 2005; *Gordon*, 1986; *Grenier et al.*, 2011; *Tsuchiya et al.*, 1989; *Wyrtki*, 1961]. The retroflection of the currents is also associated with the formation of the Mindanao Eddy (ME) and the Halmahera Eddy (HE) (Figure 2.4) [e.g. *Firing et al.*, 2005; *Lukas et al.*, 1991].

Driven by the atmospheric circulation, regional surface currents underlie seasonal and interannual alterations. Noteworthy, in the context of this thesis, during the SE monsoon season (austral winter) the NGCC flows westwards. During the NE monsoon (austral summer), when the trades reverse, the NGCC flows eastwards. The NCGUC does not reverse, but it weakens during the NE monsoon season [e.g. *Cresswell*, 2000; *Kuroda*, 2000].

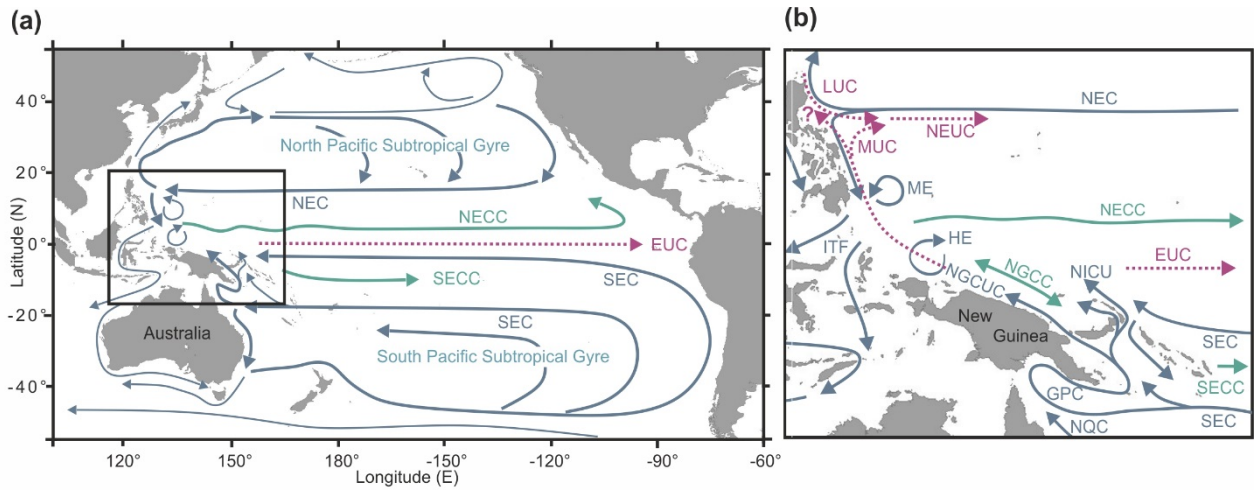

Figure 2.4. (Sub)surface circulation of the Pacific Ocean [modified from *Hu et al.*, 2015]. (a) Schematic of main (sub)surface currents. (b) Regional circulation in the WPWP. Blue arrows indicate (sub)surface currents; green arrows indicate surface-trapped currents; dashed violet arrows indicate undercurrents. The question mark indicates uncertainty in the flow path of the current. NEC – North Equatorial Current, NECC – North Equatorial Countercurrent, SEC – South Equatorial Current, SECC – South Equatorial Countercurrent, LUC – Luzon Undercurrent, MUC – Mindanao Undercurrent, NGCC – New Guinea Coastal Current, NGCUC, New Guinea Coastal Undercurrent, NEUC - North Equatorial Undercurrent, NICU - New Ireland Coastal Current, NQC – North Queensland Current, GPC – Gulf of Papua Current, ME – Mindanao Eddy, HE – Halmahera Eddy.

The upper ocean is influenced by different water masses with unique signatures. The upper thermocline is influenced by the North Pacific Tropical Water (NPTW) offshore the Philippines and South Pacific Tropical Water (SPTW) offshore PNG (Figure 2.5a).

- The **NPTW** is characterized by relatively high salinity with a maximum around 34.5 psu. It is formed within the North Pacific Subtropical Gyre by subduction of saline surface water and then transported into the WPWP by the NEC and MC [Fine et al., 1994].
- The **SPTW** is marked by high salinity with a maximum around 35.5–35.8 psu. It is produced by subduction of highly saline surface waters within the South Pacific Subtropical Gyre [e.g. *Qu et al.*, 2013; *Tsuchiya et al.*, 1989] and transported into the WPWP by the SEC and WBCs. There are two SPTW branches: The South Pacific Equatorial Water (SPEW), is produced in the subtropical central South Pacific Ocean near the Polynesian islands (~20 °S) [see *Grenier et al.*, 2013 and references therein] and enters the WPWP from the east. The second SPTW branch is probably formed within the subtropical Pacific around 30 °S (Figure 1) [see *Grenier et al.*, 2013 and references therein] and enters the WPWP from the south. The core of this SPTW branch is marked by salinity of ~35.5 psu, the core of the SPEW is marked by slightly higher salinity of ~35.6–35.8 psu [*Qu and Lindstrom*, 2002].

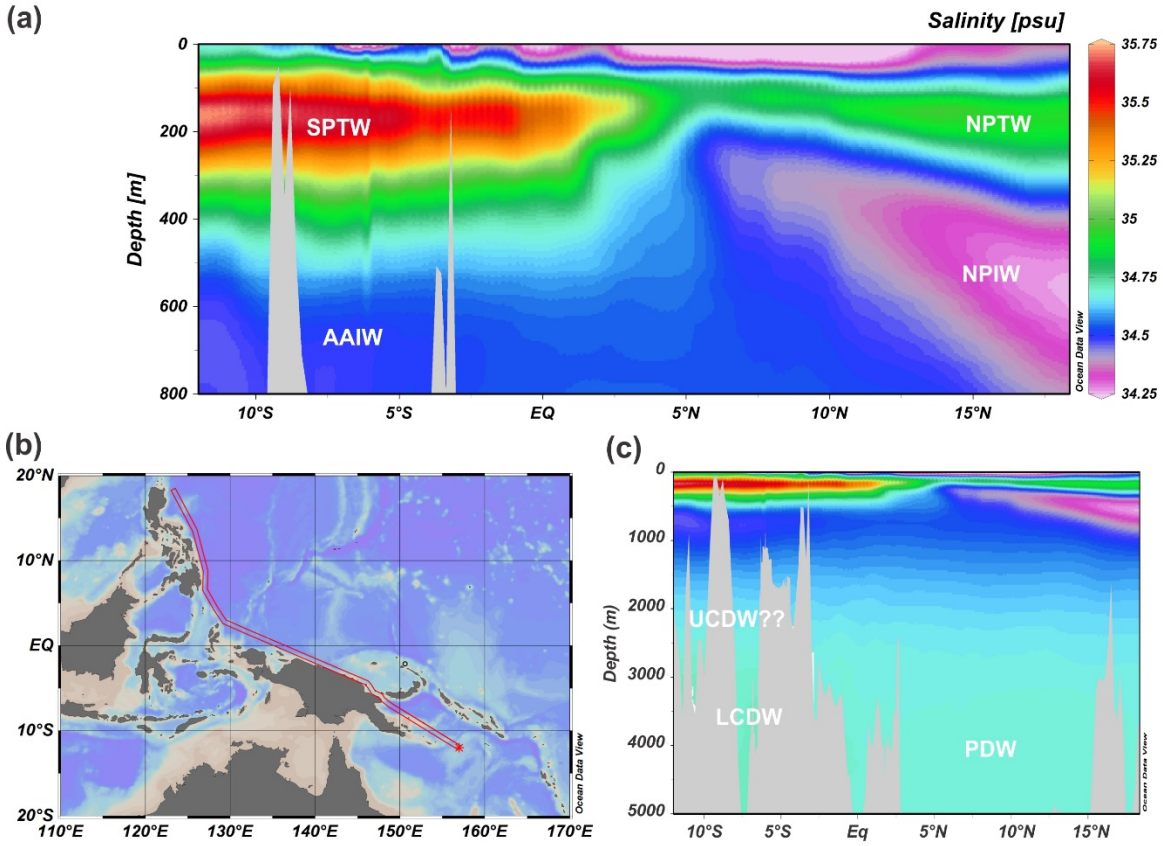

Figure 2.5. Main water masses influencing the WPWP. (a) Salinity section showing the upper 800 m of the water column along the profile indicated in (b). Salinity data are from WOA13 [*Zweng et al.*, 2013]. (b) Bathymetric map of the study area. The red line indicates the salinity profile shown in (a) and (c). (c) Same as (a) but for the upper 5000 m of the water column. The main water masses as labelled as follows: SPTW – South Pacific Tropical Water, NPTW – North Pacific Tropical Water, AAIW – Antarctic Intermediate Water, NPIW – North Pacific Intermediate Water, UCDW – Upper Circumpolar Deep Water, LCDW – Lower Circumpolar Deep Water, PDW – Pacific Deep Water.

Below the SPTW/NPTW, the WPWP is potentially influenced by cooler, less saline central and intermediate water masses. Central waters include the North Pacific Central Mode Water (NPCMW) [*Hanawa and Talley*, 2001], the Western South Pacific Central Water (WSPCW) and Pacific Equatorial Water (PEW) [*Gasparin et al.*, 2014] that influences the northern and southern WPWP, respectively. In the southern WPWP, the Subantarctic Mode Water (SAMW) further influences the hydrography [*Hanawa and Talley*, 2001]. At intermediate depth the western tropical Pacific Ocean is dominated by the North Pacific Intermediate Water (NPIW) and/or the Antarctic Intermediate Water (AAIW) with a prevalence of NPIW offshore the Philippines and AAIW offshore PNG [*Fine et al.*, 1994; *Zenk et al.*, 2005]. Modification and mixing of these water masses with Pacific Deep Water (PDW) generates the Equatorial Pacific Intermediate Waters (EqPIWs), which influences the central WPWP [*Bostock et al.*, 2013].

- The **SAMW** is characterized by low salinity (34.0–34.5 psu) and high oxygen. It is mainly formed in the southeastern Pacific Ocean by winter mixing and subduction of surface waters and transported to the South Pacific Subtropical Gyre, where it ventilates the lower thermocline [e.g. *Hartin et al.*, 2011; *Qu et al.*, 2009; *Sarmiento et al.*, 2004 and references therein].
- The **NPIW** is characterized by low salinity with a minimum around 34 psu. It originates in the Northwest Pacific Ocean where it forms by brine rejection in the Okhostk Sea and Oyashio region [*Shcherbina et al.*, 2003; *Talley*, 1993]. It flows southwards at water depths between ~300 and 600 m (core around 500 m) [*Bostock et al.*, 2010].
- The **AAIW** is reported to range from about 600 to 1100 m water depth [*Bostock et al.*, 2010]. It is characterized by a salinity minimum of about 34.4 psu. It is produced at the northern edge of the Southern Ocean by modification of upwelled Circumpolar Deep Water at the air–sea interface and subsequent winter subduction [*McCartney*, 1977].
- The **EqPIW** flows at depth around 900 m (700–1000 m). It displays higher salinity than the NPIW and AAIW with minimum around 34.5–34.6 psu. It is mainly sourced by mixing of AAIW with Pacific Deep Water (PDW), a minor proportion can also be attributed to the NPIW [*Bostock et al.*, 2010].

The deep WPWP is bathed by the PDW, the Lower Circumpolar Deep Water (LCDW), and potentially by the Upper Circumpolar Deep Water (UCDW):

- The **PDW** is formed by mixing of modified North Atlantic Deep Water (NADW), LCDW and AAIW. It is the oldest water of the Pacific Ocean and bathed the deep layers of the WPWP [e.g. *Tomczak and Godfrey*, 2003].

- The **LCDW**, which forms as a mixture between Antarctic Bottom Water (AABW) and modified NADW [*Wijffels et al.*, 1996] bathes the abyssal depths of the southern WPWP.

Chapter 3.

Material and methods

The studies presented in this thesis are based on water column data and geochemical proxies measured on foraminifera shells from marine sediment cores (multi- and gravity cores). The sample material was collected offshore the Philippines and PNG during the R/V *Sonne* expedition SO-228 [*Mohtadi et al.*, 2013] in May–June 2013 and during the R/V *Revelle* expedition RR-1313 [*Rosenthal*, unpublished] in August 2013 (Figure 3.1, Tables 3.1 and 3.2). In total, the material comprises surface sediment samples from 12 sites, two gravity cores, and water column data collected at 21 different stations.

All sampling sites are located in the heart of the WPWP. The multi cores (surface sediments) were exclusively sampled in the coastal WPWP where sedimentation rates are higher than in the open Pacific Ocean. For this reason, all surface sediment samples are of modern age. This allows a direct comparison of the sample material to modern ocean conditions. Besides, water column data were collected in close proximity to sediment samples. Proxy and water column data can therefore be directly combined.

The gravity core GeoB 17419-1 was retrieved offshore PNG within the Bismarck Sea. Since the site is located close to the Sepik River mouth (100–150 km) (Figure 3.1b), it is influenced by continental climate and suitable to record variations in river runoff and continental precipitation over PNG. Gravity core GeoB 17426-3 was retrieved east of the Bismarck Archipelago offshore New Hannover (Figure 3.1). In contrast to GeoB 17419-1 the site is not influenced by continental climate and thus well-suited to study the climatic evolution of the open western Pacific Ocean. The core covers the last 210 kyr and hence provides the opportunity to study surface and thermocline variations over the past two glacial–interglacial cycles. The thermocline at the two core sites is influenced by different water masses. While site GeoB 17419-1 is influenced by the SPTW that enters the WPWP from the south, site GeoB 17426-3 is influenced by the SPEW that enters the WPWP from the east. This provides the opportunity to study the differing impact of both thermocline water masses on the WPWP.

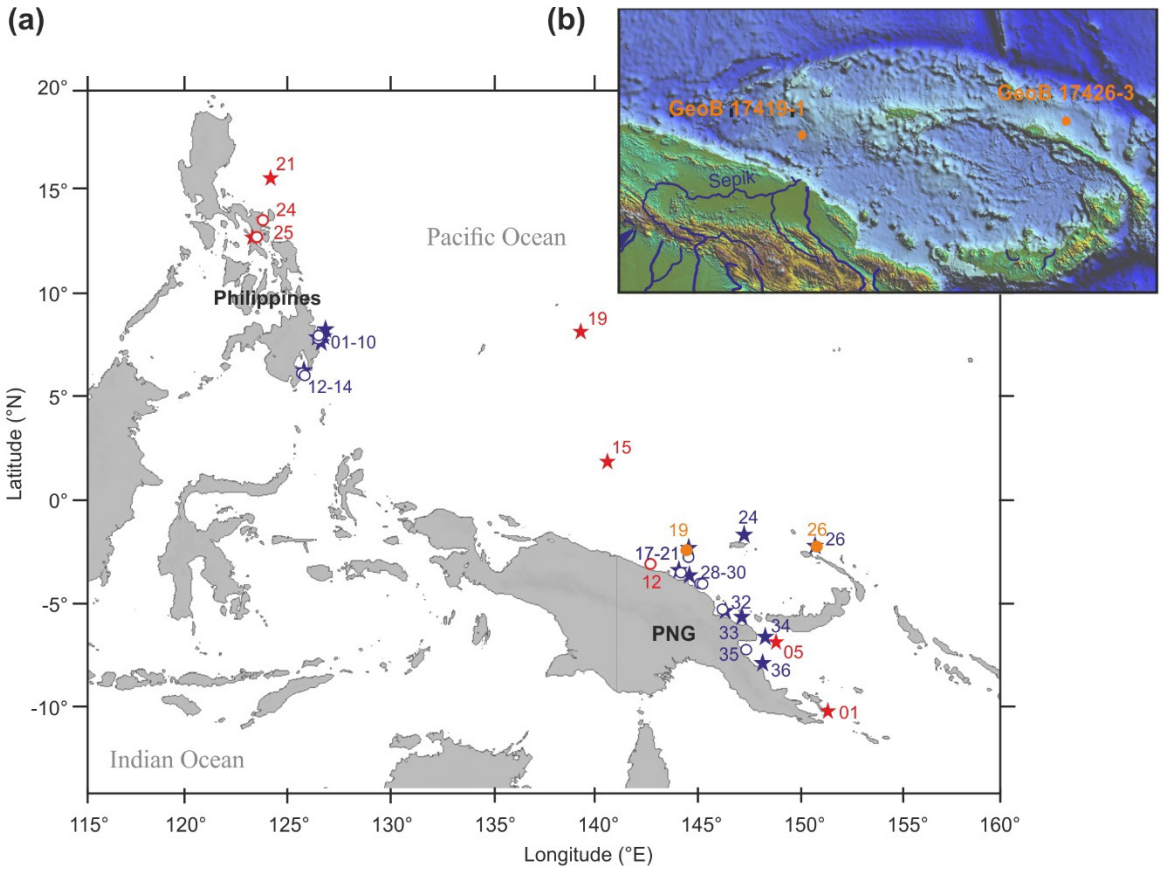

Figure 3.1. (a) Schematic map of the study area showing the stations, where water column data (stars) and sediment cores (dots) were collected during expeditions SO-228 (blue) and RR-1313 (red). Sites are labelled with station numbers. The core sites of the gravity cores GeoB17419-1 and GeoB 17426-3 are marked with orange dots. (b) Bathymetric map of the study area off PNG. Orange dots denote the positions of the gravity cores GeoB 17419-1 and GeoB 17426-3.

3.1. Material

3.1.1. Water column data

Water column data provide information about the present physical and chemical conditions at chosen sites and measuring periods. Available data sets from ocean observatory programs, such as the World Ocean Atlas (WOA) or the Simple Ocean Data Assimilation (SODA) are used to get an overview about the modern climatology and how the hydrography within the study area varies in response to seasonal and interannual climate variability. However, such data sets have certain limitations. For instance, stations do not directly correspond to the sediment sampling sites, different water column data were not necessarily measured at the same time, and particularly $\delta^{18}O_{SW}$ measurements are very sparse.

To get detailed information about the current hydrographic conditions within the study area, different parameters, such as temperature, salinity and the oxygen isotope composition of seawater were measured

simultaneously at sites in close proximity to the sediment sampling sites during the expeditions SO-228 and RR-1313. The great advantage of the newly generated dataset is that it provides simultaneous measurements of surface and subsurface temperature, salinity and $\delta^{18}O_{SW}$ from the WPWP in close proximity to the sediment sampling sites (Figure 3.1). A possible disadvantage is that the data only show a snapshot of hydrographic conditions and therefore, do not necessarily represent mean annual hydrography. However, as described in chapter 2.1, the seasonal variability in temperature and salinity is very small in the WPWP. Interannual variations in ocean hydrography are mainly associated with ENSO. The expeditions SO-228 and RR-1313 took place during a normal year (2013). Water column data collected during these expeditions are therefore expected not to be biased to El Niño or La Niña conditions.

Table 3.1. Sampling stations of CTD data and water samples used in this thesis (chapter 4)

Station	Expedition	Latitude (°N)	Longitude (°E)	Device
RR1313-21 45CTD	RR-1313	15.4	124	CTD
RR1313-25 56CTD	RR-1313	12.78	123.48	CTD
GeoB 17401-1	SO-228	8.33	126.91	CTD
GeoB 17403-1	SO-228	7.82	126.68	CTD
GeoB 17404-1	SO-228	7.9	126.54	CTD
RR1313-19 42CTD	RR-1313	8	139.5	CTD
GeoB 17407-1	SO-228	7.94	126.76	CTD,
GeoB 17412-1	SO-228	5.93	126.07	CTD
GeoB 17413-2	SO-228	6.35	125.85	CTD
RR1313-15 38CTD	RR-1313	2.22	141.14	CTD
GeoB 17417-1	SO-228	-1.58	144.5	CTD
GeoB 17420-1	SO-228	-2.36	144.48	CTD
GeoB 17424-1	SO-228	-0.62	147.17	CTD
GeoB 17426-1	SO-228	-1.81	150.86	CTD
GeoB 17428-2	SO-228	-2.54	144.15	CTD
GeoB 17432-1	SO-228	-4.66	146.2	CTD
GeoB 17433-1	SO-228	-4.38	147.13	CTD
GeoB 17434-1	SO-228	-5.41	148.27	CTD
GeoB 17436-2	SO-228	-6.11	148.2	CTD
RR1313-05 13CTD	RR-1313	-6.82	148.91	CTD
RR1313-01 01CTD	RR-1313	-10.25	151.31	CTD

Temperature and salinity data were measured along vertical profiles at individual stations using Seabird SBE911 (plus) CTD (Conductivity, Temperature and Depth) profilers during both expeditions. At some stations water samples for geochemical analyses (e.g. stable isotope analyses, see chapter 3.4 for details)

were taken, at water depths that represent the characteristic water masses of the WPWP [*Mohtadi et al.*, 2013; *Rosenthal*, unpublished]. Sampling was performed with the CTD-sampling rosettes, which are equipped with 24 Niskin bottles of 10–15 L volume. The bottles were filled at chosen depth via remote control. A part of the collected water was siphoned into 100 mL glass bottles for stable isotope analyses, care was taken to avoid getting air bubbles into the samples. The samples were sealed with wax and stored at 4 °C before analysis.

3.1.2. Sediment samples

Surface sediments used here were collected with multicorer devices, which allow recovering undisturbed surface sediments. The collected sediment tubes were cut into 1 cm slices on board [*Mohtadi et al.*, 2013; *Rosenthal*, personal communication]. The upper 1–2 cm, the core tops of the individual multicores, were used for the analyses presented in this thesis.

Table 3.3. Specifications of sediment cores used in this thesis

Core	Expedition	Latitude (°N)	Longitude (°E)	Water depth (m)	Device
Surface sediment samples (Chapter 4)					
RR1313-24 50MC	RR-1313	13.57	123.73	1055	Multi corer
RR1313-25 53MC	RR-1313	12.78	123.48	559	Multi corer
GeoB 17404-2	SO-228	7.90	126.54	404	Multi corer
GeoB 17410-3	SO-228	7.87	126.59	771	Multi corer
GeoB 17414-2	SO-228	6.26	125.83	2188	Multi corer
GeoB 17419-2	SO-228	-2.81	144.50	1883	Multi corer
RR1313-12 30MC	RR-1313	-3.13	142.76	994	Multi corer
GeoB 17421-2	SO-228	-3.55	144.20	588	Multi corer
GeoB 17429-1	SO-228	-4.10	145.20	1604	Multi corer
GeoB 17430-2	SO-228	-4.22	145.03	1160	Multi corer
GeoB 17432-3	SO-228	-5.34	146.20	1388	Multi corer
GeoB 17435-2	SO-228	-7.27	147.34	1001	Multi corer
Sediment sequences for paleo-reconstructions (Chapters 5 and 6)					
GeoB 17419-1	SO-228	-2.81	144.50	1883	Gravity corer
GeoB 17426-3	SO-228	-2.19	150.86	1368	Gravity corer

The longer sediment sequences of GeoB 17419-1 and GeoB 17426-3 were taken with a gravity corer. The core was split lengthwise on board into working and archive halves. The gravity core GeoB 17419-1 has a length of 9.14 m, GeoB 17426-3 a length of 10.31 m. The sediments of both cores are composed of nannofossil ooze rich in planktic foraminifera. The sediment of GeoB 17426-3 is additionally intercalated by ash layers. Samples for downcore analyses were taken with syringes of 10 cm^3 volume in depth

intervals of 4 cm throughout the cores. The sample material was stored at 4 °C before preparing them for geochemical analysis. Then, the gravity core samples were freeze-dried. All samples were washed over sieves with mesh sizes of 63 µm and 150 µm to eliminate the finer fractions and dried in an oven at 40–60 °C. Planktic and benthic foraminifera were selected under a microscope for geochemical analyses.

3.2. (Planktic) foraminifera and their use as proxies

The paleoceanographic reconstructions presented in this thesis are mainly based on geochemical parameters measured on planktic foraminifera tests. Foraminifera are marine eukaryotic protists that occur globally in the world's ocean, where they either dwell within the upper water column (planktic foraminifera), or inhabit the uppermost seafloor sediments (benthic foraminifera). Most of them build calcareous shells (tests) that enclose their unicellular bodies [e.g. *Kucera*, 2007 and references therein]. Since foraminifera precipitate their calcite tests largely in equilibrium to the ambient seawater, they record the prevailing chemical and physical (isotopic) composition of the water. After the planktic foraminifera's death the tests sink to the seafloor, where they are buried in the sediments. The fossil tests can then be collected with the sediments and used for paleoceanographic reconstructions, i.e. to reconstruct past chemical and physical properties of the ocean water. The abundance, global prevalence and good preservation of foraminifera tests in marine sediments make them an excellent paleo-archive and the most common source of paleoceanographic proxy reconstructions [*Kucera*, 2007].

The taxonomic classification of fossil foraminifera is based on the structure or morphological characteristics of their (calcite) tests [e.g. *Kennett*, 1976]. There are about 40–50 known modern planktic foraminifera species, but only abound 20 of them are used for paleo-reconstructions. Benthic species are more diverse, with several thousand described living and fossil species [e.g. *Holbourn et al.*, 2013; *Sen Gupta*, 2003 and references therein]. The spatial and temporal distribution, the assemblage as well as the physiology (e.g. size and weight) and abundance of the individual species depends on the environmental conditions, influenced by numerous factors, such as ocean temperatures, salinity, pH, the availability of food, nutrients, the occurrence of predators or competition. Since some species possess algal symbionts (mainly dinoflagellates) they also depend on the availability of light [e.g. *Arnold and Parker*, 2003]. Using foraminifera tests for proxy-based paleo-reconstructions therefore requires knowledge concerning their ecological preferences and how changing environmental conditions affect the physiology of foraminifera and the chemical composition of their tests.

In this thesis, tests of several planktic foraminifera species are used for proxy calibrations and paleoceanographic reconstructions: *Globigerinoides ruber*, *Globogerinoides elongatus*, *Globigerinoides sacculifer*, *Pulleniatina obliquiloculata*, *Neogloboquadrina dutertrei and Globorotalia tumida*. These

species are commonly used for paleoceanographic reconstructions in the WPWP [e.g. *Bolliet et al.*, 2011; *de Garidel-Thoron et al.*, 2007; *Lea et al.*, 2000; *Leech et al.*, 2013; *Regoli et al.*, 2015; *Sagawa et al.*, 2012; *Tachikawa et al.*, 2014]. For these species, the calcification depths and Mg/Ca-temperature dependencies in the WPWP are estimated (chapter 4). Subsequently, the surface-dwelling species *G. ruber* and the thermocline-dwelling species *P. obliquiloculata* are used to reconstruct past surface and thermocline conditions offshore PNG (chapters 5 and 6). In addition, proxy records of the benthic foraminifera *Cibicides wuellerstorfi* are used to establish the age models of gravity cores GeoB 17419-1 and GeoB 17426-3 (see section 3.3).

Overall, sediment trap data imply that all planktic foraminifera species used calcify perennially in the WPWP [*Kawahata et al.*, 2002; *Yamasaki et al.*, 2008]. More specifically, flux data show large (small) peaks during boreal summer (winter) under El Niño conditions and an increased shell flux during the first half of the year under La Niña conditions. However, there are only two studies that investigate the seasonal distribution of planktic foraminifera in the WPWP [*Kawahata et al.*, 2002; *Yamasaki et al.*, 2008]. Further studies are needed to verify previous results and to get an improved understanding about the (intra-)seasonal preferences of planktic foraminifera in the WPWP.

3.3. Dating of samples and the construction of age models

Precise age estimates and thorough age-depth models build the backbone of any proxy-based paleo-reconstruction. They are essentially needed to relate events unequivocally to certain periods. Commonly, only a few samples of a sediment sequence are dated. The age-depth relation between these samples is then inferred by interpolation. For the calibrations of proxies, the use of modern samples is essential to ensure that the proxies measured on the foraminifera tests can be related to present hydrographic conditions. Therefore, all samples used within a calibration study should be dated to ensure that they are of modern age.

There are numerous different tools that can be used to date samples. A powerful tool to date carbonate samples is radiocarbon dating (section 3.3.1). However, as will be explained below, this method is subject to certain limitations. Therefore, also other techniques were used, in addition to radiocarbon dating, to control the age of core top samples (section 3.3.2) and to generate the age models of the gravity cores GeoB 17419-1 and GeoB 17426-3 (section 3.3.3).

3.3.1. Radiocarbon dating

A powerful and commonly applied tool to determine the age of marine samples has been established by radiocarbon (^{14}C) dating of carbonates (e.g. foraminifera tests). The technique is based on measuring the concentration of the radiogenic carbon isotope ^{14}C in the sample material. ^{14}C is produced within the upper atmosphere. By interactions of cosmic rays with atomic nuclei neutrons are released. ^{14}C is then produced by neutron bombardment of nitrogen atoms (^{14}N). After production, ^{14}C oxidizes and becomes part of the carbon cycle as $^{14}CO_2$. It dissolves in the seawater where it is incorporated into marine carbonates (e.g. foraminifera tests) [e.g. *Hughen*, 2007 and references therein]. When organisms die the ^{14}C content incorporated in their bodies decreases gradually due to radioactive decay, with a half-life of 5.730 ± 40 years [see *Godwin*, 1962]. By determining the relative ^{14}C content of fossil samples (reference is usually ^{12}C, which is the most abundant carbon isotope) in comparison to a modern standard it is possible to estimate the radiocarbon age of the sample. A common way to determine the ^{14}C content of a sample is by counting the carbon ions using accelerator mass spectrometry (AMS). It is conventionally assumed that initial ^{14}C concentrations remained constant throughout the past [*Stuiver and Polach*, 1977]. However, due to various factors the ^{14}C concentration within the atmosphere varied throughout the past. For this reason, radiocarbon ages deviate from calendar ages in the past and a correction is necessary to translate the radiocarbon into calendar ages. The calibration is based on comparing ^{14}C ages to records dated by other means (e.g. tree rings), the so called calibration curves [e.g. *Reimer et al.*, 2013 and references therein]. Additionally, radiocarbon dated ages of marine samples need to be corrected for reservoir effects [*Bard*, 1988]. Especially deep water masses do not exchange with the atmosphere and become depleted in ^{14}C. The global ocean circulation system brings old waters to the surface, where they mix with modern waters. Therefore, ocean waters are not in isotopic equilibrium with the atmosphere, but appear older than the contemporaneous atmosphere [e.g. *Bard*, 1988 and references therein]. The age difference between the atmosphere and the surface ocean, the so called reservoir effect, is estimated to be about 400 years on global average [*Reimer et al.*, 2013]. However, due to the process described, marine ^{14}C reservoir ages vary geographically. If the deviation from the global reservoir age estimate is known, local reservoir age corrections (ΔR) can be applied. In addition, reservoir ages may have changed over time. Modelled changes in the global reservoir age are considered in marine calibration curves (e.g. MARINE13) [*Reimer et al.*, 2013].

At the 1972 Radiocarbon Conference standards for reporting ^{14}C were adopted to make radiocarbon ages, that were measured in different laboratories, comparable [see *Stuiver and Polach*, 1977]. Radiocarbon ages that meet these criteria are reported as *conventional radiocarbon ages*. (I) A half-life of 5568 ± 30 years (the so called "Libby half-life") is assumed [*Libby*, 1955] to ensure consistency between records generated before and after 1962, when the value was recalculated to 5730 ± 40 years. (II) A certain

standard (the National Bureau of Standards (NBS) oxalic standard) is used as radiocarbon standard. (III) Samples are corrected for isotopic fractionation during the measurement process. (IV) Due to the testing and detonation of thermonuclear weapons during the 1950, 1950 AD is taken as the reference date for radiocarbon dates and established as the year 0 before present (BP). (V) It is assumed that atmospheric ^{14}C concentrations remained constant throughout the past.

Radiocarbon dating has several advantages [see e.g. *Hughen*, 2007]. In general, any material that contains inorganic or organic carbon can potentially be dated. Moreover, the input of ^{14}C into the ocean is spatially homogenous and the exchange rates between ocean and atmosphere are high. For these reasons, the method is widely applicable in paleoceanography. However, the method is also subject to certain limitations. For instance, it is restricted to samples younger than 40,000–50,000 years. Consequently, other stratigraphic methods have to be applied for records that exceed this age range. Although the required amount of sampling material nowadays is small (at least about 200–500 µg) the method is not suitable for very small carbonate samples.

3.3.2. Using the Suess effect as indicator for modern ages

To estimate if samples are of modern age, the $\delta^{13}C$ records from the respective sediment cores can be checked for the so-called Suess effect. The Suess effect describes a rapid decrease in seawater $\delta^{13}C$ that goes along with the depletion in ^{13}C of atmospheric CO_2, caused by an increase in deforestation and burning of ^{12}C rich fossil fuels since the industrial revolution [e.g. *Böhm et al.*, 1996; *Friedli et al.*, 1986]. Since foraminifera record the carbon isotope composition of the ambient seawater, the Suess effect can be recognized in the $\delta^{13}C$ records of surface-dwelling planktic foraminifera.

3.3.3. Isotope stratigraphy

For periods that exceed the range where radiocarbon dating is possible, age models can be generated by graphical alignment of proxy records to records from other cores that have a known stratigraphy. In principle, all kinds of proxy records can be used to establish an age model by synchronization. For quaternary samples age models are often established by graphical alignment of foraminiferal $\delta^{18}O$ records. Since $\delta^{18}O$ records globally are influenced by the waxing and waning of ice sheets over glacial–interglacial cycles (see chapter 3.4 for details) they show similar glacial–interglacial patterns that build the basis for graphical correlation between the records. Stacks that average $\delta^{18}O$ records from multiple sites and thus improve the signal-to-noise ratio of the climate signal are particularly useful reference records [*Lisiecki and Raymo*, 2005]. Commonly used reference stacks are, for example, the SPECMAP stack, which is based on globally distributed $\delta^{18}O$ records of planktic foraminifera [*Imbrie et al.*, 1984] and the global benthic foraminifera $\delta^{18}O$ stack LR04 [*Lisiecki and Raymo*, 2005].

3.3.4. Dating of surface sediments

The age estimates of most surface sediments (the GeoB samples) presented in this thesis are based on AMS radiocarbon dating of monospecific or mixed *G. ruber*, *G. elongatus* and *G. sacculifer* samples. The measurements were performed by the Keck Carbon Cycle Accelerator Mass Spectrometry Laboratory at the University of California, Irvine. Following the conventions of *Stuiver and Polach* [1977] all ages are reported as conventional ^{14}C. Fraction modern carbon ($F^{14}C$) values above one indicate that all dated samples are of modern age. However, the RR1313 samples did not contain enough foraminifera for radiocarbon dating. To check, if these samples are of modern age as well, $\delta^{13}C$ values were estimated on *G. ruber* samples (10 individuals, size fraction: 250–300 µm) from the upper 10 cm of each of the respective multicores and checked for the Suess effect. The carbon isotope measurements were performed by the isotope laboratory at Rutgers University, New Jersey. The laboratory uses a Micromass Optima mass spectrometer that is coupled to an automatic line for carbonate preparation. Measured isotope values were calibrated against the international Vienna Pee Dee Belemnite (VPDB) standard by an internal standard, which is calibrated against the National Bureau of Standards (NBS) 19 standard. Rapid drops in the $\delta^{13}C$ records of all sediment sequences indicate the Suess effect and verified the modern age of the samples. Consequently, all surface sediment samples presented in this thesis are of modern age.

3.3.5. Age models of GeoB 17419-1 and GeoB 17426-3

The age models of the gravity cores GeoB 17419-1 and GeoB 17426-3 are based on AMS ^{14}C ages and on the correlation of benthic $\delta^{18}O$ to the global benthic LR04 stack. Specifically, the age model of the upper 414 cm (206 cm) of gravity core GeoB17419-1 (GeoB 17426-3) is based on AMS ^{14}C ages of 26 (10) monospecific *G. sacculifer* or mixed *G. ruber*, *G. elongatus*, and *G. sacculifer* samples. All radiocarbon measurements were performed by the Keck Carbon Cycle Accelerator Mass Spectrometry Laboratory at the University of California, Irvine. Radiocarbon ages were converted to calendar ages using the Marine13 calibration curve [*Reimer et al.*, 2013]. To compensate for local deviations from the global reservoir age, local reservoir age corrections of $\Delta R = 70 \pm 60$ yrs [*McGregor et al.*, 2008] and $\Delta R = 141 \pm 131$ yrs [*Petchey and Ulm*, 2016] were applied to the ages of GeoB 17419-1 and GeoB 17426-3, respectively.

Between dating points the age-depth relations were modelled with a Bayesian approach using the software BACON R 2.2 [*Blaauw and Christen*, 2011]. In a Bayesian routine the accumulation of the sediment sequence through time is modelled by multiple Monte Carlo runs. These include random sampling of the probability distribution of the calibrated dates and the calculation of accumulation between the individual dating points. Specifically, the sediment sequence is divided into many, thin, vertical sections and the accumulation rate for each segment is modelled under consideration of the accumulation rate of the previous section. It thus allows a more variable accumulation of sediments than linear interpolation.

BACON allows to vary many parameters under consideration of prior information about the specific sediment sequence [*Blaauw and Christen*, 2011].

Below 414 cm (GeoB 17419-1) and 206 cm (GeoB 17426-3), the age models are established by alignment of benthic $\delta^{18}O$ values (*C. wuellerstorfi*) to the global benthic LR04 $\delta^{18}O$ stack [*Lisiecki and Raymo*, 2005]. Graphical alignment was done with the software AnalySeries [*Paillard et al.*, 1996]. Tie points were defined at maxima in $\delta^{18}O$ that were associated with individual Marine Isotopes Stages. Between the tie points, the chronology was inferred by linear interpolation. Linear interpolation was preferred over Bayesian age modeling for these parts of the records as uncertainty ranges cannot be defined around the tie points and therefore a Monte Carlo simulation with random sampling of ages from a predefined range does not appear reasonable. The age models reveal that the GeoB17419-1 and GeoB 17426-3 records cover the last 110 and 210 kyr, respectively.

3.4. Stable oxygen isotopes

Stable oxygen isotopes measured in foraminifera tests are among the most important proxies in paleoclimatology and paleoceanography and used to reconstruct past variations in temperature and the oxygen isotope composition of seawater. There are three stable oxygen isotopes that naturally occur in different proportions, ^{16}O (99.76%), ^{17}O (0.04%), ^{18}O (0.20%) [*Böhlke et al.*, 2005]. The proxy is based on the thermodynamically driven fractionation between ^{16}O and ^{18}O. For example, during evaporation, fractionation favors the removal of the lighter isotope ^{16}O from the ocean (kinetic fractionation). As a result, the ocean becomes relatively enriched and the atmosphere relatively depleted in ^{18}O. Conversely, rain drops are enriched in ^{18}O relative to the cloud's moisture, since the heavier ^{18}O is favored during condensation. Thus, the oxygen isotope composition of seawater varies in dependence on the ratio between evaporation and precipitation. Since foraminifera precipitate their calcite tests close to equilibrium with the ambient seawater, they record the prevailing isotope composition and hence changes in climate. Due to thermodynamic fractionation that occurs during calcite precipitation (equilibrium fractionation), the isotope composition of foraminiferal carbonate is additionally affected by ocean temperatures. With increasing temperature less ^{18}O is incorporated into the calcite shells.

The oxygen isotopic composition of a sample ($\delta^{18}O$) is given as a deviation of the $^{18}O/^{16}O$ ratio of the sample from the ratio of a known standard as parts per thousand (per mil):

$$\delta^{18}O\ (per\ mil) = \left[\frac{(^{18}O/^{16}O)sample - (^{18}O/^{16}O)standard}{(^{18}O/^{16}O)standard}\right] * 1000 \qquad (3.1)$$

The composition of carbonates is commonly reported relative to the Vienna Peedee Belemnite (VPDB), the composition of water samples relative to the Vienna Standard Mean Ocean Water (VSMOW) standard [*Coplen*, 1996].

As introduced, the $\delta^{18}O$ of foraminiferal carbonates is controlled by the $\delta^{18}O_{SW}$ and calcification temperature (see also Figure 3.2) with low $\delta^{18}O$ corresponding to lower $\delta^{18}O_{SW}$ and/or higher temperatures and vice versa. The oxygen isotope composition of seawater is influenced by a range of factors. Generally, $\delta^{18}O_{SW}$ varies with latitude, altitude and continentality for the following reason: Tropical oceans as the WPWP build the major source of water vapor to the global atmosphere. The water vapor is then transported to high latitudes. As described above, the atmospheric moisture is relatively depleted in ^{18}O. Due to a gradual rainout during the transport of the evaporated water within the atmospheric circulation system the water vapor that remains in the atmosphere becomes increasingly/successively depleted in ^{18}O with increasing latitude and altitude, and decreasing temperature (Raleigh fractionation/Raleigh distillation). Particularly, precipitation in high latitudes and freshwater stored in ice sheets is strongly depleted in ^{18}O [e.g. *IAEA*, 2000].

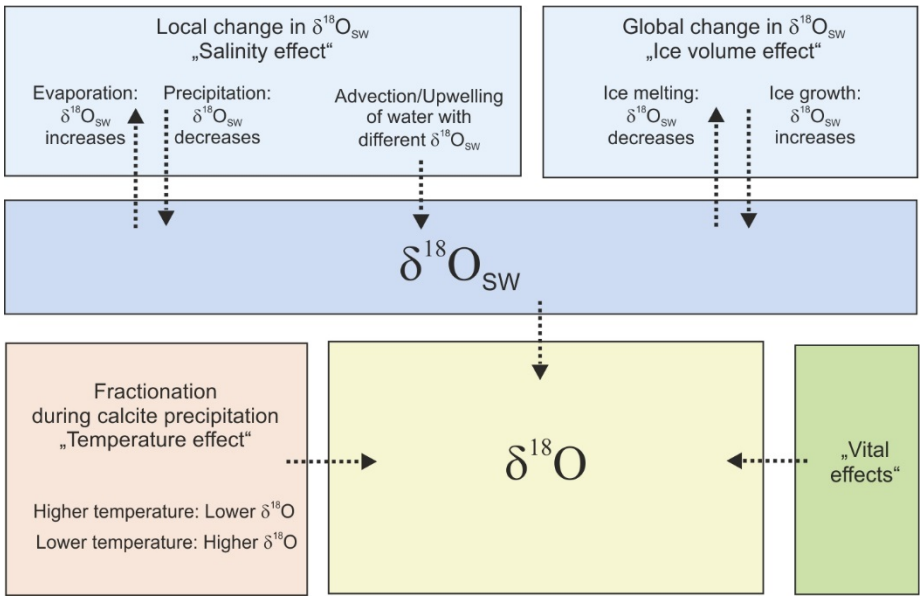

Figure 3.2. Factors that influence the $\delta^{18}O$ of foraminiferal calcite [modified from *Ravelo and Hillaire-Marcel*, 2007].

Local factors, such as (seasonal or interannual) variations in evaporation and precipitation, changes in the source of precipitation as well as advection, upwelling and subduction of water masses with a different isotopic composition control the $\delta^{18}O_{SW}$ on shorter timescales. The isotope signal is additional controlled by global variations in the $\delta^{18}O_{SW}$. The $\delta^{18}O_{SW}$ of the global ocean is primarily influenced by changes in

the amount of water stored as ice on land [*Shackleton*, 1967]. Over the course of glacial–interglacial cycles the formation and regression of extensive ice sheets has a huge impact on the global $\delta^{18}O_{SW}$. For instance a $\delta^{18}O_{SW}$ change of about 1.0–1.2‰ accounts for global changes in ice volume from LGM to Holocene [*Fairbanks*, 1989; *Peltier and Fairbanks*, 2006; *Schrag et al.*, 2002; *Waelbroeck et al.*, 2002]. To reconstruct local variations in ocean temperature or $\delta^{18}O_{SW}$ from foraminiferal calcite, the $\delta^{18}O$ records therefore have to be corrected for global changes in ice volume.

The thermodynamic fractionation during calcite precipitation (the temperature effect) causes an offset of $\delta^{18}O$ from $\delta^{18}O_{SW}$, which is inversely related to calcification temperature [*Ravelo and Hillaire-Marcel*, 2007]. Hence, foraminiferal $\delta^{18}O$ records can be used for paleothermometry if the $\delta^{18}O_{SW}$ is known. For this, numerous paleotemperature equations for various foraminifera species and ocean regions have been established over the past decades [e.g. *Bemis et al.*, 1998; *Farmer et al.*, 2007; *Shackleton*, 1974]. In turn, if the calcification temperature of the foraminifera is known from other records (e.g. from Mg/Ca paleothermometry, see chapter 3.5), foraminiferal $\delta^{18}O$ records can be used to estimate past variations in $\delta^{18}O_{SW}$. In addition, the paleotemperature equations allow to predict theoretical $\delta^{18}O$ values from temperature and $\delta^{18}O_{SW}$. This approach is commonly used to estimate the calcification depth of planktic foraminifera by comparing shell $\delta^{18}O$ to depth profiles of predicted $\delta^{18}O$ [e.g. *Mohtadi et al.*, 2011; *Ravelo and Fairbanks*, 1992].

For the application of $\delta^{18}O$ in foraminifera tests as a proxy for paleoreconstructions, it is assumed that foraminifera precipitate their shells in equilibrium to seawater. However, some species calcify out of equilibrium due to biological effects (so called vital effects) [see *Ravelo and Hillaire-Marcel*, 2007 and references therein]. Vital effects are potentially caused by the photosynthetic activity of symbionts, ontogenetic effects, species-specific calcification rates, the addition of gametogenic calcite as the foraminifera sinks at the end of its lifecycle, and possibly carbonate ion concentrations of the ambient seawater (pH effect) [*Ravelo and Hillaire-Marcel*, 2007 and references therein]. For the planktic foraminifera species used in this thesis, vital effects are estimated to range between 0.0 and -1.0‰ [see *Lončarić et al.*, 2006; *Niebler et al.*, 1999 and references therein]. Possible vital effects have to be considered when interpreting $\delta^{18}O$ signals. However, the large variety of factors that could potentially influence the isotope composition of foraminiferal calcite hampers a precise correction of $\delta^{18}O$ for disequilibrium effects.

In this thesis, $\delta^{18}O$ values of the planktic foraminifera *G. ruber*, *G. elongatus*, G. sacculifer, *P. obliquiloculata*, *N. dutertrei* and *G. tumida* from the surface sediments was combined with the water column data (CTD data and $\delta^{18}O_{SW}$) collected during the SO-228 and RR-1313 expeditions to estimate the calcification depth and temperatures of the individual species (chapter 4). More precisely, CTD data and

$\delta^{18}O_{SW}$ measured on the water samples were used to calculate depth profiles of predicted $\delta^{18}O$. Shell $\delta^{18}O$ of each foraminifera species and sample was then compared to the calculated profiles of $\delta^{18}O$ to estimate the calcification depth and temperatures. Furthermore, records of $\delta^{18}O$ in *G. ruber* and *P. obliquiloculata* from the gravity cores GeoB 17419-1 and GeoB 17426-3 were used to assess past variations $\delta^{18}O_{SW}$ (chapters 5 and 6). Benthic $\delta^{18}O$ records were used to establish the age models of the gravity cores.

The $\delta^{18}O_{SW}$ of the water samples was determined at the Department of Geography and Earth Sciences, University of Erlangen-Nuremberg, Germany on a Picarro L1102-i CRDS water analyser with vaporization module V1102-i coupled to a CTC/Leaptec PAL auto sampler. Calibration against Vienna Standard Mean Ocean Water (VSMOW) was achieved by calibration to laboratory water standards calibrated against IAEA-standards VSMOW2 and SLAP2 [*van Geldern and Barth*, 2012]. External reproducibility was 0.05‰. For the RR1313 samples, δ^{18}Osw was determined at Rutgers University, New Jersey on a FISONS OPTIMA Mass Spectrometer equipped with a MicroMass Multiprep automatic sample processing system after water sample equilibration with CO_2 using standard methods [*Epstein and Mayeda*, 1953; *Fairbanks*, 1982]. All samples were run in duplicate. Precision was estimated to be ± 0.03‰ (1 σ) as determined by multiple (n = 12) daily analyses of a laboratory standard. Replicates must measure to within 0.068‰ to be included in the final data set. Instrument linearity and accuracy was determined by comparison of the laboratory standard to NBS standard water VSMOW, GISP, and SLAP. Accuracy was estimated to be within 0.03‰ by comparison of measurements of North Atlantic Bottom Water with VSMOW.

Foraminiferal shell $\delta^{18}O$ of was measured by the isotope laboratory at MARUM, University of Bremen on a Finnigan MAT 251 mass spectrometers with Kiel I or Kiel III devices. Isotope values were calibrated against the VPDB standard. The internal carbonate standard is a Solnhofen Limestone, which is calibrated to the National Bureau of Standards (NBS) 19 standard. The long-term analytical precision was better than ± 0.07‰. Replicate measurements were performed on ten percent of the samples to control the reproducibility of the samples. The results revealed that the average standard deviation for $\delta^{18}O$ of the surface sediment samples is 0.22‰ (between 0.07 and 0.42‰ for individual foraminifera species). For the $\delta^{18}O$ records of GeoB 17419-1, the average standard deviation is 0.12‰ for *G. ruber* (n = 22) and 0.14‰ for *P. obliquiloculata* (n = 22). For the records of GeoB 17426-3, the average standard deviation is 0.15‰ for *G. ruber* (n = 25) and 0.17‰ for *P. obliquiloculata* (n = 23).

3.5. Mg/Ca paleothermometry

The ratio of Magnesium (Mg) to Calcium (Ca) in foraminiferal calcite has become one of the most commonly used proxies to reconstruct past variations in ocean temperature. The proxy is based on the fact

that foraminifera, during the formation of their tests, substitute a part of the Ca by Mg. This substitution is an endothermic reaction and therefore favored at higher temperatures [e.g. *Lea*, 2014; *Rosenthal*, 2007 and references therein]. Consequently, an increase (decrease) in ocean temperature will be associated with an increase (decrease) in the Mg/Ca ratio of foraminiferal calcite. Conversely, Mg/Ca ratios measured on foraminifera tests give information about the temperature of the ambient seawater at the time when the test was built.

Using Mg/Ca for paleothermometry has several advantages, even in comparison to other proxies: The primary temperature dependence makes it an independent temperature proxy. In addition, since both elements have a long oceanic residence times (~13 Ma for Mg, 1 Ma for Ca) Mg/Ca ratios of seawater are relatively constant over the past Ma [*Rosenthal*, 2007]. This implies that variations in Mg/Ca can be unequivocally linked to climate variability. Furthermore, in combination with $\delta^{18}O$, Mg/Ca in foraminiferal calcite can be used to isolate changes in $\delta^{18}O_{SW}$ as described in chapter 3.4. The combination of $\delta^{18}O$ and trace elements in biogenic carbonates is particularly useful as the proxies are measured on the same phase, and therefore, uncertainties that are associated with the use of different proxy carriers are being reduced.

A large number of studies revealed that the relationship between Mg/Ca in planktic foraminifera and ocean temperature is well described by an exponential fit [e.g. *Anand et al.*, 2003; *Cléroux et al.*, 2008; *Dekens et al.*, 2002; *Elderfield and Ganssen*, 2000; *McConnell and Thunell*, 2005; *Mohtadi et al.*, 2009; *Mohtadi et al.*, 2011; *Regenberg et al.*, 2009]. The choice of an exponential fit traces back to thermodynamic considerations [*Lea et al.*, 1999; *Rosenthal et al.*, 1997]. Mg/Ca to temperature dependencies are usually expressed as

$$\frac{Mg}{Ca} = B^{A*Temperature}$$

with the pre-exponential constant B describing the absolute temperature and the exponential constant A describing the sensitivity of Mg/Ca to temperature changes. Commonly used Mg/Ca-temperature equations suggest that the temperature sensitivity of planktic foraminifera is around 9% per °C [e.g. *Anand et al.*, 2003; *Lea et al.*, 1999; *Rosenthal and Lohmann*, 2002].

Despite its primary temperature dependency Mg/Ca ratios can be biased by a range of secondary effects that have to be kept in mind when working with Mg/Ca. First, contamination by phases that contain high levels of Mg, such as clay, Mn-rich carbonates ($MnCO_3$) or metal-oxide coatings (Mn- and Fe-oxides) that potentially overgrow the calcite tests after their deposition, and organic matter may potentially influence the Mg/Ca ratios [e.g. *Barker et al.*, 2003; *Martin and Lea*, 2002; *Pena et al.*, 2005]. A careful cleaning of the samples to counteract contamination is therefore inevitably. Second, post-depositional partial

dissolution can significantly alter the Mg/Ca composition causing a loss of Mg/Ca, because high Mg-calcite is more soluble than low Mg-calcite [e.g. *Regenberg et al.*, 2014; *Rosenthal et al.*, 2000]. Dissolution effects increase with water depth due to decreasing carbonate saturation levels [e.g. *Brown and Elderfield*, 1996; *Dekens et al.*, 2002; *Russell et al.*, 1994] and can critically alter the Mg/Ca ratios in foraminifera tests even above the modern lysocline [e.g. *Rosenthal and Lohmann*, 2002]. Therefore, the preservation of the samples has to be controlled carefully to exclude potential dissolution effects. Finally, seawater salinity and pH and/or [CO_3^{2-}] potentially affect Mg uptake. Several studies reported apparently positive relation between salinity and Mg/Ca [*Arbuszewski et al.*, 2010; *Ferguson et al.*, 2008; *Kısakürek et al.*, 2008; *Mathien-Blard and Bassinot*, 2009; *Nürnberg et al.*, 1996] and an inverse relation between pH and/or [CO_3^{2-}] and Mg/Ca [*Evans et al.*, 2016; *Kısakürek et al.*, 2008; *Lea et al.*, 1999; *Russell et al.*, 2004; *Spero et al.*, 2015]. Estimates on the effect of salinity on Mg/Ca ratios vary widely. Some studies that suggest a significant impact of salinity on Mg/Ca have been criticized that the sample material used might be substantially affected by dissolution, seasonality [*Arbuszewski et al.*, 2010] or diagenetic alteration [*Ferguson et al.*, 2008; *Hertzberg and Schmidt*, 2013; *Hönisch et al.*, 2013]. All in all, salinity effects appear to be negligible when salinity is below 35 psu. It is unclear, whether pH or [CO_3^{2-}] exert a dominant control on Mg/Ca [*Allen et al.*, 2016; *Evans et al.*, 2016]. However, previous studies provide confidence that the effects on Mg/Ca are negligible under ambient seawater conditions [*Kısakürek et al.*, 2008; *Russell et al.*, 2004].

The incorporation of Mg into foraminifera tests is ecologically biased. The specific Mg/Ca-temperature relations depend, inter alia, on the foraminifera species, its habitat depth, the region and the environmental conditions. To determine the Mg/Ca-temperature dependencies (e.g. of a certain area or species), Mg/Ca needs to be calibrated against temperature. In this project, regional multispecies and species-specific Mg/Ca-temperature calibrations for the WPWP are established by comparing Mg/Ca ratios of several planktic foraminifera species from modern surface sediment samples to water column temperatures measured during the CTD casts of the SO-228 and RR-1313 expeditions. Afterwards, Mg/Ca-based temperature records of the surface and thermocline-dwelling planktic foraminifera *G. ruber* and *P. obliquiloculata,* respectively, from core GeoB 17419-1 and/or GeoB 17426-3 are used to reconstruct the past temperature variability within the WPWP.

For the Mg/Ca measurements, between 10 and 30 individuals of each sample and foraminifera species were selected. The surface sediment samples and samples from gravity core GeoB 17419-1 were prepared and measured at the Rutgers University, New Jersey. The samples from gravity core GeoB 17426-3 were prepared and measured at the University of Bremen.

A so-called full trace metal cleaning was applied to clean the surface sediment samples and the GeoB 17419-1 samples. This is not inevitably necessary for Mg/Ca measurements. However, additional trace element ratios, such as Cd/Ca, B/Ca, and Ba/Ca, that require full trace metal cleaning, were measured along with Mg/Ca. These element ratios are not part of this thesis, but might be used for future studies. Prior to cleaning, all samples were gently crushed between two glass plates to crack open the chambers of the individual foraminifera in order to increase the cleaning efficiency. The crushed material was transferred to acid-cleaned 0.5 ml vials for cleaning. The full trace metal cleaning procedure followed the protocol of *Boyle and Keigwin* [1985] as modified by *Rosenthal et al.* [1997] and *Rosenthal et al.* [1999]. In total the cleaning procedure consists of 4 cleaning steps. It starts with a clay removal step that comprises three water rinses using purified, double distilled water (ddH_2O) and two methanol rinses. Then, a reductive step with an anhydrous hydrazine in ammonium hydroxide and citric acid/ammonia solution is applied to remove metal oxide coatings. An oxidative step using hydrogen peroxide buffered with 0.1 M sodium hydroxide is done to remove organic material. Afterwards, the samples are transferred into new, acid cleaned vials. A weak acid leaching step with 0.001 M nitric acid is done to remove Mn-rich carbonates. Finally, the samples are dissolved in 0.065 M nitric acid, centrifuged for 10 min at 10000 rpm to eliminate insoluble particles from the measurements and diluted with 0.5 M nitric acid. The final calcium concentration ranged between 0.2 and 9.7 mmol/mol (average 4.3 mmol/mol). Samples were eliminated if the calcium concentration was below 0.2 mmol/mol.

Trace element ratios of all core top samples and GeoB 17419-1 were measured with a Thermo Fisher/Finnigan Element XR sector-field inductively coupled plasma mass spectrometer (ICP-MS). Along with Mg/Ca several other element ratios, such as Cd/Ca, B/Ca and Ba/Ca, and Fe/Ca, Al/Ca and Mn/Ca were measured. Fe/Ca, Al/Ca and Mn/Ca are used to monitor possible clay and oxide contamination of the samples. Fe/Ca was measured in medium resolution, while all other element ratios were determined in low resolution ($\Delta m/m = 4000$ and $\Delta m/m = 300$, respectively). Measured element ratios were blank corrected with a blank solution that consists of the same acids used to dissolve and dilute the samples. Drift and matrix effects were controlled with in-house standard solutions [*Rosenthal et al.*, 1999] using a spiked gravimetric standard (SGS), which is calibrated against the international ECRM standard. It has a reference Mg/Ca composition of 6.033 mmol/mol. Both, blank and SGS standard, were measured after every fifth sample. To quantify and correct for offsets that are potentially caused by varying calcium concentrations (matrix effects), six matrix samples with Ca concentrations ranging between 1.5 and 8 mmol/mol were measured at the beginning of each measuring sequence. The matrix samples were prepared by nitric acid dilution of the SGS standard. For Mg/Ca the matrix correction was always less than 4% of the original SGS value. The long term precision of the data was controlled by replied measurements of three in house standard solutions (consistency standards) [*Rosenthal et al.*, 1999] with

Mg/Ca ratios of 1.44 (CS1), 3.49 (CS2) and 8.71 mmol/mol (CS3). For Mg/Ca the standard deviations of the individual consistency standards were 1.53% (CS1), 0.68% (CS2) and 0.72% (CS3). To calculate the reproducibility of the values, replicate measurements were performed on 10 percent of the samples of each data set. The results indicate an average standard deviation of 0.22 mmol/mol for planktic foraminifera from the surface sediment samples and 0.30 mmol/mol for *P. obliquiloculata* in samples of gravity core GeoB 17419-1.

To prepare the samples of GeoB 17426-3 for Mg/Ca measurements, the Mg/Ca cleaning procedure of *Barker et al.* [2003] was applied. In comparison to the full trace metal cleaning, this cleaning procedure does not include a reductive step. The cleaning includes five water and two methanol washes, an oxidative step with hydrogen peroxide buffered with 1% sodium hydroxide, and a weak acid leach using 0.001 M nitric acid. The cleaned samples were dissolved in 0.075 M nitric acid, centrifuged (10 min at 6000 rpm) and diluted with water. The samples were measured on an Agilent Technologies 700 Series Inductively Coupled Plasma Optical Emission Spectrophotometer (ICP-OES), which is connected to a Cetax ASX 520 autosampler. The instrumental drift and precision were controlled by using an in-house standard, which was measured after every fifth sample and the international ECRM 752-1 standard, which was typically measured after every fiftieth sample. Replicate measurements on 10% of the samples indicate an average standard deviation of 0.28 mmol/mol for *G. ruber* and 0.26 mmol/mol for *P. obliquiloculata*.

To monitor the cleaning efficacy and because contaminants, such as Al, Fe or Mn cannot always be completely removed, we measured contaminant phases Al/Ca, Fe/Ca and Mn/Ca alongside with Mg/Ca and used scatter plots to estimate the influence of these contaminants on Mg/Ca. None of these ratios showed a covariance to Mg/Ca (see Figure 3.3 and Appendix A1.3). We therefore assume that Mg/Ca is not substantially affected by contamination.

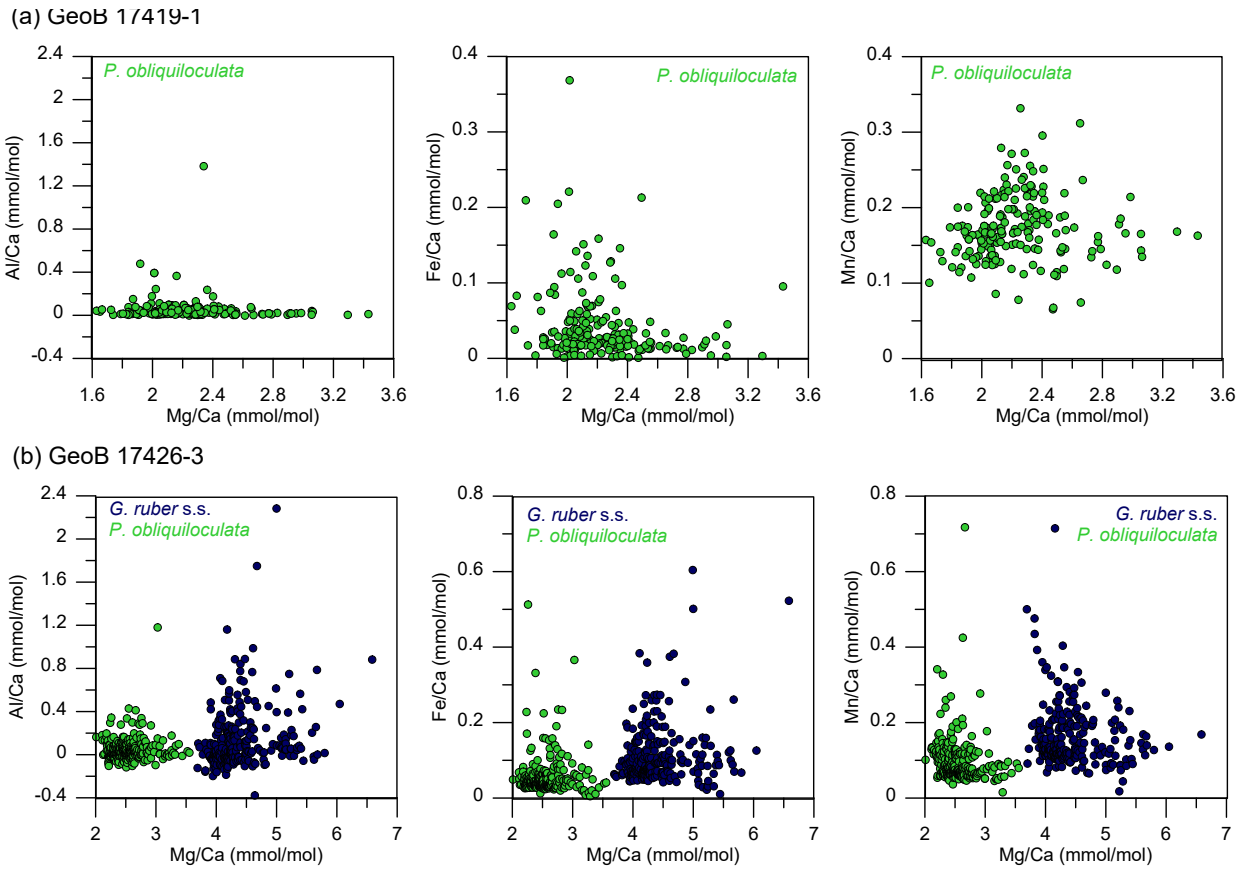

Figure 3.3. Al/Ca (left), Fe/Ca (middle) and Mn/Ca (right) in planktic foraminifera of gravity cores GeoB 17419-1 (a) and GeoB 17426-3 (b) versus Mg/Ca. Note the different scaling of the axes. Results from replicate measurements are shown separately.

Several factors indicate an overall good carbonate preservation in the samples used within the framework of this thesis: First, all sampling sites are situated well above the present lysocline, which is located at around 3300 m water depth [see *Berger et al.*, 1982 and references therein]. However, as mentioned above, some studies indicate that even samples from shallower water depths might be affected by post-depositional dissolution. For the surface sediment samples, the occurrence of aragonitic pteropods in most GeoB samples (including the core top from the deepest core site at about 2200 m water depth) implies a good carbonate preservation, because aragonite is more soluble than calcite. Moreover, the Mg/Ca ratios of the surface sediments from different sites do not show a significant correlation to water depth (Figure 3.4a). Finally, a correlation between Mg/Ca and shell normalized weight can be indicative for dissolution [e.g. *Rosenthal and Lohmann*, 2002]. Neither Mg/Ca ratios of the surface sediment samples (Figure 3.4a) nor of samples from gravity core GeoB 17419-1 show a correlation to shell normalized weight (Figure 3.4b). The samples of core GeoB 17426-3 were not weighed, but the site is located at shallower water depth than GeoB 17419-1 (Table 3.3). Therefore effects of dissolution are expected to be negligible.

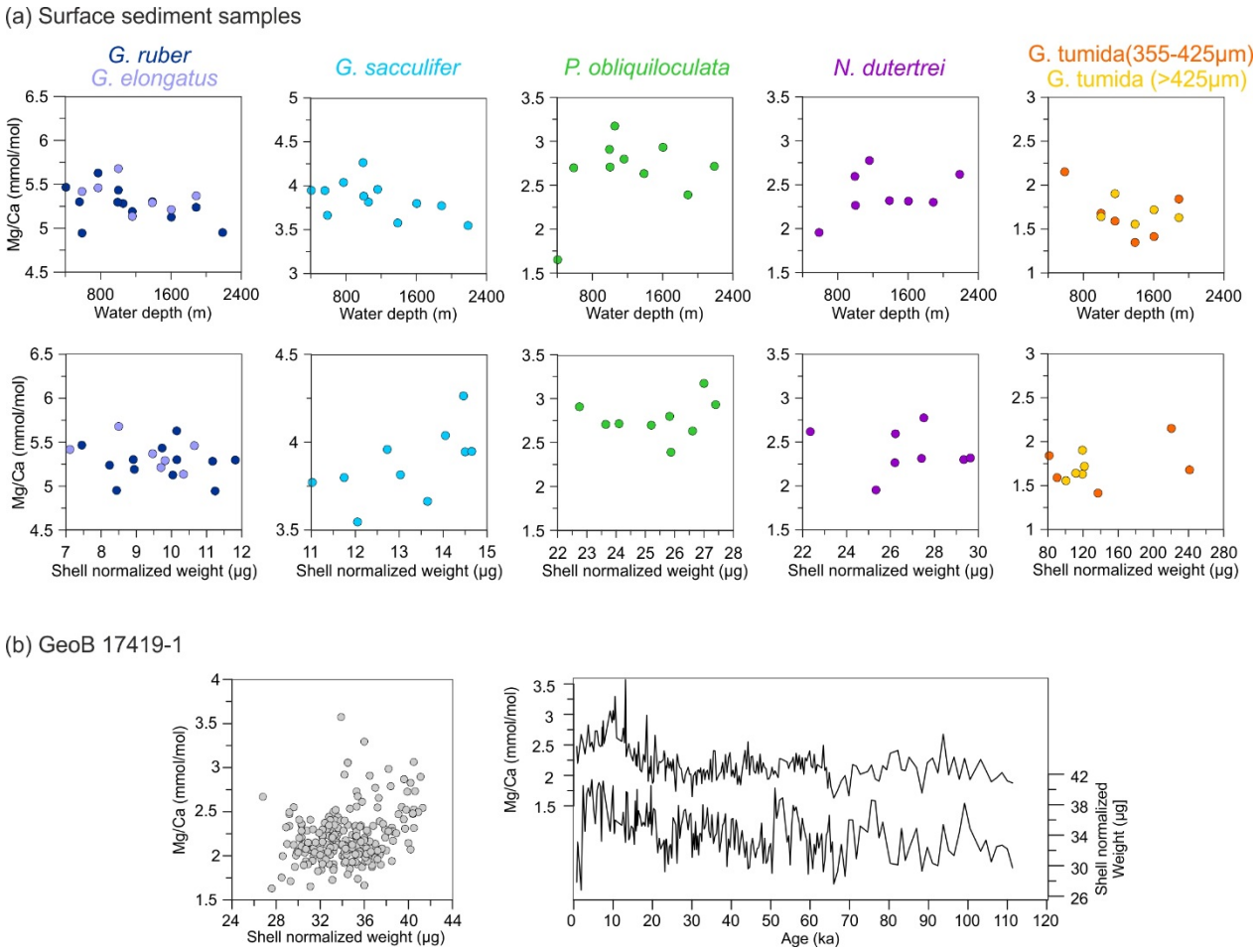

Figure 3.4. Control for potential dissolution effects on planktic foraminifera of the surface sediment samples (a) and gravity core GeoB 17419-1 (b). (a) Shell Mg/Ca of each species and sample versus water depth at the respective core sites (top) and shell normalized weight (bottom). (b) Shell Mg/Ca of *P. obliquiloculata* of GeoB 17419-1 versus shell normalized weight.

It is unlikely that the Mg/Ca ratios presented in this thesis are substantially influenced by salinity or pH and [CO_3^{2-}] for the following reasons: Nowadays, the salinity range in the sampling area is small (between 33.9 and 35.6 psu) and variations between SO-228 and RR-1313 CTD stations at water depths that correspond to the calcification depth of individual planktic foraminifera species are below 1.2 psu. Data from surface sediment samples reveal that shell Mg/Ca and salinity do not correlate (R-values range between 0.00 and 0.35 for individual species). Moreover, Mg/Ca ratios in samples from offshore the Philippines and PNG are very similar, although these areas are influenced by different water masses (NPTW and SPTW) that are marked by different salinities. Neither pH nor [CO_3^{2-}] was measured during the SO-228 and RR-1313 expeditions. Therefore, the variability of these parameters within the study area is unknown. However, as mentioned above, previously published studies show that the impact of pH and

[CO_3^{2-}] on Mg/Ca under ambient seawater conditions is very small. Nonetheless, a secondary influence of these parameters on Mg/Ca, especially on the paleo-records, cannot be fully excluded.

3.6. X-Ray Fluorescence core scanner analyses

X-Ray Fluorescence (XRF) spectrometry provides the opportunity to analyze the element composition of marine sediment cores in high resolution directly at the surface of the split core determining the intensities of several elements such as Ti, Fe, Al, K or Ca within the sediment. The strengths of XRF core scanner analyses are a fast data acquisition at relatively low consumable costs. Since it is a non-destructive method it can be performed on the archive half of the core. With XRF scanning, only the sediment surface is analyzed. The method is therefore especially useful for homogenous sediments. It can hardly be applied to hard or strongly disturbed sediments.

The element composition of marine sediment cores can, for instance, serve as a proxy for past continental hydroclimate variations [e.g. *Arz et al.*, 1998; *Lückge et al.*, 2009; *Tachikawa et al.*, 2014] for the following reason: Increased rainfall over the drainage basins of river systems enhances land erosion and river runoff and hence the supply of terrigenous particles to the oceans. Consequently, the accumulation of terrigenous particles recorded in marine sediments varies in accordance with the continental hydroclimate. Commonly, records of the relative abundance of siliciclastic components, such as Ti or Fe to Ca are used to estimate variations in the terrigenous sedimentation [e.g. *Arz et al.*, 1998; *Tachikawa et al.*, 2011]. Ca is expected to mainly reflect the marine carbonate content in the sediments. When applying this proxy, it thus has to be kept in mind that variations in the ratio between terrigenous components and Ca could also be influenced by variations in the calcareous productivity.

In this thesis, the Ti/Ca ratio of the gravity core GeoB17419-1 is used as an indicator for variations in continental rainfall over PNG. As mentioned in chapter 3.1, the core site is located in close proximity to the Sepik River mouths (Figure 3.1) and the sedimentary record is therefore influenced by terrigenous particles supplied by these river systems. The record of Ti/Ca is additionally used to verify the age model of the core by comparing the Ti/Ca record to the Ti/Ca record from the nearby core MD05-2920 [*Tachikawa et al.*, 2011].

Measurements were performed at the MARUM, University of Bremen using an XRF Core Scanner II (AVAATECH Serial No. 12). Prior to scanning, the surface of the archive half was smoothed and covered with a 4 µm thin SPEXCerti Prep Ultralene1 foil to avoid contamination of the XRF measurement unit and desiccation of the sediment. XRF data were collected in 2 cm intervals over a 1.2 cm^2 area using a down-core slit size of 10 mm, generator settings of 10 kV (excitation potential), a current of 0.02 mA, and

a sampling time of 20 seconds were used. The settings allow the analysis of light elements (Al, Si, S, K, Ca, Ti, Mn, Fe). The data were acquired by a Canberra X-PIPS Silicon Drift Detector (SDD; Model SXD 15C-150-500) with 150eV X-ray resolution, the Canberra Digital Spectrum Analyzer DAS 1000 and an Oxford Instruments 100W Neptune X-ray tube with rhodium (Rh) target material. Raw data spectra were processed by the Iterative Least square software WIN AXIL (Analysis of X-ray spectra by Iterative Least square) package from Canberra Eurisys. Results are reported as counts per second.

Chapter 4.
Stable oxygen isotopes and Mg/Ca in planktic foraminifera from modern surface sediments of the Western Pacific Warm Pool: Implications for thermocline reconstructions

Martina Hollstein[1], Mahyar Mohtadi[1], Yair Rosenthal[2], Paola Moffa Sanchez[3], Delia Oppo[4], Gema Martínez Méndez[1], Stephan Steinke[5], Dierk Hebbeln[1]

[1]MARUM – Center for Marine Environmental Sciences, University of Bremen, Bremen, Germany

[2]Institute of Marine and Coastal Sciences, Rutgers, State University of New Jersey, USA.

[3]School of Earth and Ocean Sciences, Cardiff University, Cardiff, UK

[4]Department of Geology and Geophysics, Woodshole Oceanographic Institution, Massachusetts, USA

[5]Department of Geological Oceanography, Xiamen University, Xiamen, China

Published in *Paleoceanography*, doi:10.1002/2017PA003122

Abstract

Mg/Ca and stable oxygen isotope compositions ($\delta^{18}O$) of planktic foraminifera tests are commonly used as proxies to reconstruct past ocean conditions including variations in the vertical water column structure. Accurate proxy calibrations require thorough regional studies, since parameters such as calcification depth and temperature of planktic foraminifera depend on local environmental conditions. Here we present radiocarbon-dated, modern surface sediment samples and water column data (temperature, salinity, and seawater $\delta^{18}O$) from the Western Pacific Warm Pool. Seawater $\delta^{18}O$ ($\delta^{18}O_{SW}$) and salinity are used to calculate individual regressions for western Pacific surface and thermocline waters ($\delta^{18}O_{SW}$ = 0.37*S – 12.4 and $\delta^{18}O_{SW}$ = 0.33*S – 11.0). We combine shell $\delta^{18}O$ and Mg/Ca with water column data to estimate calcification depths of several planktic foraminifera and establish regional Mg/Ca-temperature calibrations. *Globigerinoides ruber, Globigerinoides elongatus* and *Globigerinoides sacculifer* reflect mixed layer conditions. *Pulleniatina obliquiloculata* and *Neogloboquadrina dutertrei* and *Globorotalia tumida* preserve upper and lower thermocline conditions, respectively. Our multispecies Mg/Ca-temperature calibration (Mg/Ca = 0.26 exp 0.097*T) matches published regressions. Assuming the same temperature sensitivity in all species, we propose species-specific calibrations that can be used to reconstruct upper water column temperatures. The Mg/Ca-temperature dependencies of *G. ruber, G.*

elongatus and *G. tumida* are similar to published equations. However, our data imply that calcification temperatures of *G. sacculifer*, *P. obliquiloculata* and *N. dutertrei* are exceptionally warm in the western tropical Pacific and thus underestimated by previously published calibrations. Regional Mg/Ca-temperature relations are best described by Mg/Ca = 0.24 exp 0.097*T for *G. sacculifer* and by Mg/Ca = 0.21 exp 0.097*T for *P. obliquiloculata* and *N. dutertrei*.

4.1. Introduction

The Western Pacific Warm Pool (WPWP) is a major source of heat and water vapor to the global atmosphere with far-reaching climate impacts [e.g. *Gagan et al.*, 2004]. The area is also thought to play an essential role in the global overturning circulation, because it provides waters to the Pacific equatorial current system and the Indonesian Throughflow, [e.g. *Gordon*, 1986]. Present climate in the WPWP is mainly controlled by the Austral-Asian monsoon system and large-scale climate phenomena such as the El Niño–Southern Oscillation (ENSO). The regional climate is strongly coupled to ocean conditions. Changes in the prevailing climate conditions affect, for example, mixed layer depth and the thermocline structure [e.g. *DiNezio et al.*, 2011; *Vecchi et al.*, 2006]. Thus, reconstructing past hydrographic conditions and variations in the vertical structure of the water column allows to draw conclusions on the regional WPWP climate evolution.

There is an ongoing debate how the thermocline depth varied throughout the past. For example, some records indicate a thermocline deepening during the Last Glacial Maximum [e.g. *Bolliet et al.*, 2011], others indicate a thermocline shoaling during the same period [*Andreasen and Ravelo*, 1997; *Beaufort et al.*, 2001; *de Garidel-Thoron et al.*, 2007; *Regoli et al.*, 2015; *Sagawa et al.*, 2012], and yet others indicate no change compared to the modern ocean [*Patrick and Thunell*, 1997]. Many of these reconstructions are based on the calculation of differences between shell Mg/Ca-derived temperature and/or $\delta^{18}O$ of planktic foraminifera calcifying at different depth levels to estimate vertical temperature gradients within the upper water column [e.g. *Bolliet et al.*, 2011; *de Garidel-Thoron et al.*, 2007; *Regoli et al.*, 2015]. Previous studies used, for example, the difference between shell Mg/Ca in *G. ruber* as surface indicator and *P. obliquiloculata* or *N. dutertrei* as thermocline depth indicators [e.g. *Bolliet et al.*, 2011], or the difference between *G. ruber* sensu stricto and *G. ruber* sensu lato (here referred to as *G. ruber* and *G. elongatus* following *Aurahs et al.* [2011]) [*Regoli et al.*, 2015]. However, to choose species and interpret such proxy records correctly, it is essential to understand how modern hydrographic conditions are reflected in foraminiferal calcite.

The choice of species to use depends on regional calcification depths, which are determined by the species preferences and local environmental conditions. However, although many paleoclimate reconstructions for

the WPWP exist, precise estimates of calcification depths are sparse in this area. Published reconstructions rely on plankton tow and sediment trap studies in the central equatorial Pacific, North Pacific, or Indian Ocean [*Kawahata et al.*, 2002; *Kuroyanagi and Kawahata*, 2004; *Mohtadi et al.*, 2011; *Peeters et al.*, 2002; *Rippert et al.*, 2016; *Watkins et al.*, 1996]. In addition, precise Mg/Ca-temperature calibrations are a prerequisite to convert Mg/Ca into temperature. For the WPWP there are only two regional Mg/Ca-temperature calibrations [*Lea et al.*, 2000; *Sagawa et al.*, 2012]. *Lea et al.* [2000] provide a species-specific calibration for *G. ruber,* and *Sagawa et al.* [2012] present a multispecies calibration. Both calibrations are exposed to certain limitations. While the species-specific calibration might be biased by postdepositional effects on the core top planktic foraminifera sample material [*Lea et al.*, 2000], the multispecies equation of *Sagawa et al.* [2012] bases only on data from a single station. Besides, both calibrations base on late Holocene sediments and therefore, might lack comparability to present hydrography. Regional species-specific calibrations for subsurface planktic foraminifera species do not exist for the WPWP. Subsequently, most proxy studies use Mg/Ca-temperature calibrations from other areas [e.g. *Bolliet et al.*, 2011; *de Garidel-Thoron et al.*, 2007; *Regoli et al.*, 2015; *Tachikawa et al.*, 2014]. However, the adequacy of previously published Mg/Ca-temperature calibrations for the WPWP has not yet been tested.

Here we present paired Mg/Ca and $\delta^{18}O$ measurements on planktic foraminifera tests from radiocarbon-dated, modern surface sediments in combination with water column data from stations offshore the Philippines and Papua New Guinea (PNG) (Figure 4.1a and Table 4.1). Together, these areas represent a major part of the WPWP. We estimate species-specific calcification depths and temperatures of various planktic foraminifera species and establish regional Mg/Ca-temperature calibrations for the WPWP. In order to estimate calcification depths, we compare shell $\delta^{18}O$ with depth profiles of expected equilibrium $\delta^{18}O$ of calcite ($\delta^{18}O_C$) at the respective locations. While this is a common approach, an advantage of our study is the availability of concurrently measured salinity and seawater $\delta^{18}O$ ($\delta^{18}O_{SW}$) data, upon which the calculated depth profiles of $\delta^{18}O_C$ are based on. In this framework, we also calculate and provide regional $\delta^{18}O_{SW}$-salinity regressions for surface and subsurface water masses in the WPWP. Finally, we relate Mg/Ca to calcification temperatures to find the most appropriate Mg/Ca calibration for each species and establish a regional multispecies as well as monospecific Mg/Ca-temperature calibrations. We identify the appropriate species to reconstruct past variations in mixed layer depth and thermocline structure as well as the appropriate calibrations to convert Mg/Ca into temperature.

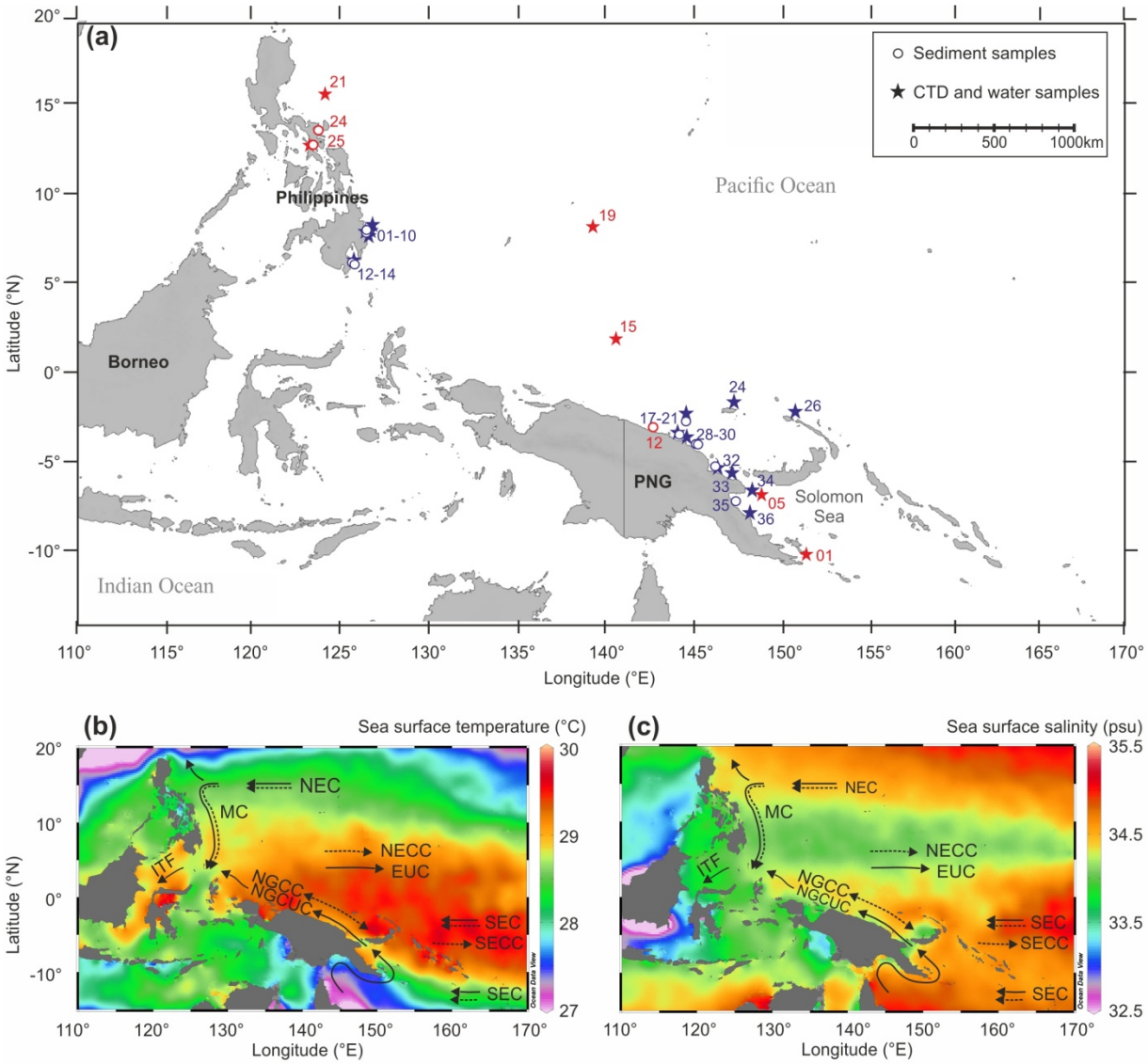

Figure 4.1. (a) Schematic map of the study area showing the stations, where water column data (stars) and surface sediments (dots) were collected during expeditions SO-228 (blue) and RR-1313 (red). Sites are labeled with station numbers. (b) Mean annual sea surface temperature and (c) sea surface salinity derived from WOA13 [*Locarnini et al.*, 2013; *Zweng et al.*, 2013]. Temperature and salinity maps were created with the Ocean data view software [*Schlitzer*, 2014]. Dashed and solid arrows indicate main surface and (sub)surface currents influencing the study sites. MC – Mindanao Current, NEC – North Equatorial Current, NECC – North Equatorial Counter Current, EUC – Equatorial Undercurrent, NGCC – New Guinea Coastal Current, NGCUC – New Guinea Coastal Undercurrent, SEC – South Equatorial Current, SECC – South Equatorial Countercurrent, ITF – Indonesian Throughflow.

We note that the study is subject to certain limitations. First, it is based on surface sediments. This bears the disadvantages that we do not have direct information about hydrographic parameters at periods, when the calcite shells were built. Besides, we cannot fully exclude secondary influences (e.g. dissolution) on our data and, we cannot resolve (intra)seasonal changes in hydrography. Second, our study includes water column data measured during two expeditions. These data provide only snapshots of the WPWP

hydrography. Moreover, we did not measure pH or [CO_3^{2-}] and therefore, cannot fully exclude an effect of pH or [CO_3^{2-}] on shell Mg/Ca, although it appears negligible under ambient seawater conditions [*Kısakürek et al.*, 2008; *Russell et al.*, 2004]. Third, since the availability of modern sample material is a prerequisite for calibration studies, our sites are exclusively located in the coastal WPWP, where sedimentation rates are higher than in the open Pacific Ocean. The applicability of our calibrations for the open ocean WPWP needs to be tested in future studies. Finally, especially species-specific calibrations are restricted by the fact, that the temperature range within the study area is rather small. Where necessary, we discuss the limitations of the data in more detail (see section 4.4.5). Overall, the strengths of this study outweigh the mentioned limitations. Sediment-based studies have the great advantage that they are performed on the same material used for paleostudies. In relation to this, a great advantage of our study is the availability of (radiocarbon) dated, modern surface sediments. In addition, as mentioned above, our study greatly benefits from concurrent measurements of temperature, salinity and $\delta^{18}O_{SW}$.

Table 4.1. Shell stable oxygen isotopes and Mg/Ca ratios of various planktic foraminifera species in surface sediments from the Western Pacific Ocean.

Core	Latitude (°N)	Longitude (°E)	Water depth (m)	*G. ruber* $\delta^{18}O$ (‰ VPDB)	*G. ruber* Mg/Ca (mmol/mol)	*G. elongatus* $\delta^{18}O$ (‰ VPDB)	*G. elongatus* Mg/Ca (mmol/mol)	*G. sacc.* $\delta^{18}O$ (‰ VPDB)	*G. sacc.* Mg/Ca (mmol/mol)	*P. obliq.* $\delta^{18}O$ (‰ VPDB)	*P. obliq.* Mg/Ca (mmol/mol)	*N. dutertrei* $\delta^{18}O$ (‰ VPDB)	*N. dutertrei* Mg/Ca (mmol/mol)	*G. tumida* (355-425 µm) $\delta^{18}O$ (‰ VPDB)	*G. tumida* (355-425 µm) Mg/Ca (mmol/mol)	*G. tumida* (>425 µm) $\delta^{18}O$ (‰ VPDB)	*G. tumida* (>425 µm) Mg/Ca (mmol/mol)
Philippines																	
RR1313-24 50MC	13.57	123.73	1055	-3.25 -3.15	5.28	-3.24	-	-2.78	3.81	-3.47	3.17	-1.84	-	-	-	-	-
RR1313-25 53MC	12.78	123.48	559	-2.95	5.30	-3.30	-	-	3.95	-	-	-	4.23	-	-	-	-
GeoB 17404-2	7.90	126.54	404	-3.03	5.47	-2.91	-	-2.69	3.95	-	-	-	-	-	-	-	-
GeoB 17410-3	7.87	126.59	771	-3.08	5.44 5.82	-3.79	5.46	-3.16 -2.89 -2.94 -2.55 -2.47	4.04	-	-	-	2.68	-	3.27	-	-
GeoB 17414-2	6.26	125.83	2188	-3.13	4.95	-3.01	-	-2.90	3.55	-2.34	2.69 2.74	-2.31 -2.23 -2.23 -2.12 -2.07	2.62	-	-	-	-
Papua New Guinea																	
GeoB 17419-2	-2.81	144.50	1887	-3.18 -3.14 -3.10 -3.15 -2.90	5.17 5.30	-3.05	5.37	-2.95	3.77	-2.15 -1.80 -1.69 -1.59 -1.57	2.27 2.51	-1.64	2.30	-0.70 -0.64 -0.16	1.79 1.89	-0.94	1.63
RR1313-12 30MC	-3.13	142.76	994	-3.74	5.30	-3.01	-	-3.39	4.26	-2.40	2.91	-	2.59	-	-	-	-
GeoB 17421-2	-3.55	144.20	588	-3.45	4.94	-3.43	5.42	-2.64	3.66	-2.20	2.70	-1.52 -1.42 -1.35 -1.27	1.95	-0.31	2.15	-	-
GeoB 17429-1	-4.10	145.20	1604	-3.02	5.13	-3.04 -2.81 -2.77 -2.73 -2.59	5.21	-2.62	3.74 3.85	-2.00	2.93	-2.01	2.24 2.39	-0.07	1.41	-0.08	1.72
GeoB 17430-2	-4.22	145.03	1160	-3.38 -3.31 -3.02 -2.98 -2.78	5.19	-2.98	5.14	-2.73	3.89 4.03	-2.15	2.80	-1.75	2.78	-0.01	1.43 1.76	-0.31	1.90
GeoB 17432-3	-5.34	146.20	1388	-3.24	5.30	-2.86	5.14 5.44	-2.62 -2.60 -2.60 -2.47 -1.72	3.58	-2.13	2.63	-2.09	1.54 3.09	-	1.35	0.06	1.56
GeoB 17435-2	-7.27	147.34	1001	-3.29	5.10 5.77	-3.24 -3.02 -2.89 -2.24	5.68	-2.81	3.88	-2.23	2.70 2.71	-2.09	2.26	-0.15	1.68	-0.45 -0.35 -0.08	1.43 1.85

4.2. Study area

The WPWP is characterized by exceptionally high ocean temperatures with sea surface temperatures exceeding 28°C (Figure 4.1b) [*Locarnini et al.*, 2013]. Sea surface salinity is about 34 psu (Figure 4.1c) [*Zweng et al.*, 2013]. The average mixed layer depth is about 50–100 m [*Locarnini et al.*, 2013]. The upper thermocline waters are characterized by higher salinities with maxima of around 34.5–35.0 psu off the Philippines and 35.5 psu off PNG. Salinity maxima correspond to the North and South Pacific Tropical Waters (NPTW and SPTW). The NPTW is formed within the western North Pacific Subtropical Gyre and transported along the Philippines toward the equator by the Mindanao Current (MC) [*Fine et al.*, 1994]. The SPTW originates in the South Pacific Suptropical Gyre [*Tsuchiya et al.*, 1989]. It is transported westward by the SEC and along the coast of PNG by the New Guinea Coastal Current (NGCC) and Undercurrent (NGCUC) systems. Below the NPTW and SPTW waters are characterized by lower salinities and are influenced by the Antarctic Intermediate Water (AAIW) originating in the Southern Ocean and/or the North Pacific Intermediate water (NPIW) with stronger predominance of AAIW offshore PNG and of NPIW offshore the Philippines [*Fine et al.*, 1994; *Zenk et al.*, 2005].

The seasonal climate variability is mainly controlled by the Austral-Asian monsoon and leads to only minor changes in the WPWP hydrography. Temperature and salinity variations are smaller than 1–2 °C and 1 psu [*Locarnini et al.*, 2013; *Zweng et al.*, 2013]. On interannual timescales, El Niño–Southern Oscillation (ENSO) affects surface ocean conditions as well as the vertical structure of the water column in the WPWP with drier (wetter) conditions and a shallower (deeper) thermocline during El Niño (La Niña) years.

Generally, the northern part of the study area is characterized by oligotrophic surface conditions and a deep chlorophyll maximum at the top of the thermocline [*Radenac and Rodier*, 1996]. North of PNG nutrient concentrations and biological productivity are higher than elsewhere in the WPWP [*Radenac et al.*, 2016]. However, the (vertical) distribution of nutrients and chlorophyll is variable on (intra-)seasonal timescales [e.g. *Higgins et al.*, 2006; *Radenac and Rodier*, 1996; *Radenac et al.*, 2016].

The (intra-)seasonal distribution of planktic foraminifera is controlled by different factors, such as temperature, salinity and the availability of light and nutrients. Sediment trap data do not reveal a clear picture of (intra)seasonal preferences of planktic foraminifera in the study area [*Kawahata et al.*, 2002; *Yamasaki et al.*, 2008]. Flux data from the equatorial Pacific showed large (small) peaks during boreal summer (winter) under El Niño conditions and an increased shell flux during the first half of the year under La Niña conditions [*Kawahata et al.*, 2002; *Yamasaki et al.*, 2008]. Since no clear (intra)seasonal pattern is indicated by these data we assume that planktic foraminifera calcify perennially in the WPWP.

4.3. Materials and methods

4.3.1. Water column data and $\delta^{18}O_{SW}$–salinity regressions

For this study, we used profiles of water column data, measured at 15 stations offshore the Philippines and PNG in May–June 2013 during RV *Sonne* expedition SO-228 [*Mohtadi et al.*, 2013] and at six stations in August 2013 during RV *Revelle* expedition RR-1313 (Figure 4.2) [*Rosenthal,* unpublished]. Temperature and salinity profiles are based on CTD (conductivity, temperature and depth) data. CTD data were measured using Seabird SBE911 (plus) CTD profilers during both expeditions. During CTD casts, water samples for stable isotope analyses were collected from several water depths (Appendix, Table A1.1). Sampling was performed with CTD-sampling rosettes equipped with 24 Niskin bottles of 10–15 L volume. A part of the collected water was siphoned into 100 mL glass bottles for stable isotope analyses, care was taken to avoid getting bubbles in the samples [*Mohtadi et al*., 2013; *Rosenthal,* unpublished]. All SO-228 samples (labeled as GeoB-samples in Table 4.1) were sealed with wax and stored at 4°C before analysis. $\delta^{18}O_{SW}$ was determined with a Picarro L1102-i CRDS water analyzer with vaporization module V1102-i coupled to a CTC/Leaptec PAL auto sampler at the Department of Geography and Earth Sciences, University of Erlangen-Nuremberg. Calibration against Vienna Standard Mean Ocean Water (VSMOW) was achieved by calibration to laboratory water standards calibrated against International Atomic Energy Agency (IAEA)-standards VSMOW2 and SLAP2 [*van Geldern and Barth*, 2012]. External reproducibility was 0.05‰. For the RR1313 samples, δ^{18}Osw measurements were made at Rutgers University, New Jersey on a FISONS OPTIMA Mass Spectrometer equipped with a MicroMass Multiprep automatic sample processing system after water sample equilibration with CO_2 using standard methods [*Epstein and Mayeda*, 1953; *Fairbanks*, 1982]. All samples were run in duplicate. Precision was estimated to be ± 0.03‰ (1 σ) as determined by multiple (n = 12) daily analyses of a laboratory standard. Replicates must measure to within 0.068‰ to be included in the final data set. Instrument linearity and accuracy were determined by comparison of the laboratory standard to National Bureau of Standards (NBS) standard water VSMOW, GISP, and SLAP. Accuracy was estimated to be within 0.03‰ by comparison of measurements of North Atlantic Bottom Water with VSMOW.

Generally, $\delta^{18}O_{SW}$ is linearly related to salinity [*Craig and Gordon*, 1965; *Fairbanks et al.*, 1992]. However, since both parameters are controlled by a number of factors, intercept and slope of their relation are not the same for all ocean regions. Therefore, regional calibrations are required [*LeGrande and Schmidt*, 2006]. Because the $\delta^{18}O_{SW}$–salinity relation is not constant over depth, we generated separate equations for surface and subsurface (SPTW and NPTW) waters. For both, we investigated individual relations for the areas offshore the Philippines and PNG as well as combined, more general, relations representing the entire study area. We do not necessarily consider water samples from all stations and depth intervals. Rather, for each equation we include samples that best characterize the relevant water

masses (Appendix 1, Figure A1.1). The SPTW and NPTW regressions include only samples that represent the core of these water masses; the WPWP wide subsurface regression is more general and covers a slightly wider depth range.

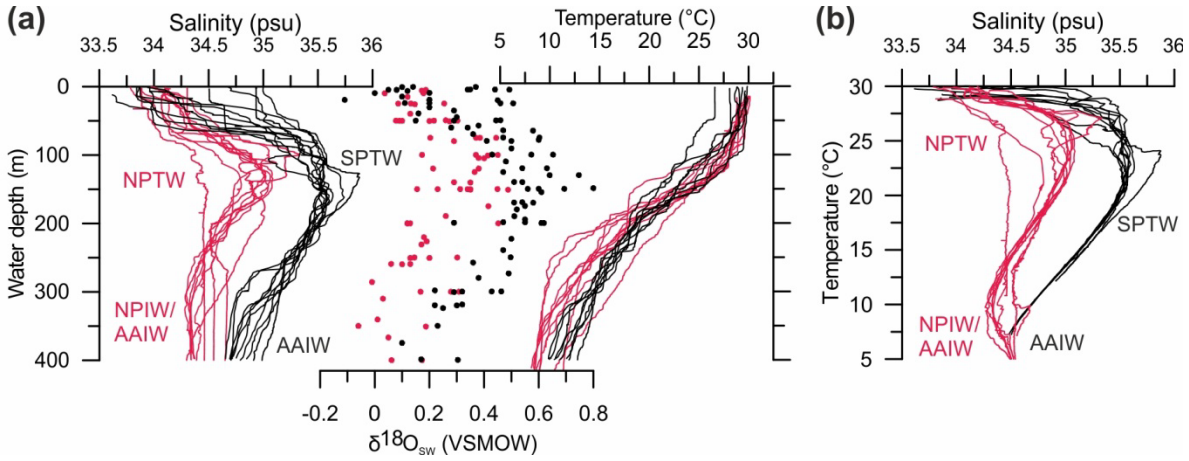

Figure 4.2. (a) Salinity, $\delta^{18}O_{SW}$ and temperature profiles and (b) Temperature-salinity relations at stations offshore the Philippines (red) and Papua New Guinea (black). Water masses are labeled as follows: NPTW – North Pacific Tropical Water, SPTW – South Pacific Tropical Water, NPIW – North Pacific Intermediate Water, AAIW – Antarctic Intermediate Water.

4.3.2. Sediment samples

Surface sediments were collected with multicorer devices during expedition SO-228 (nine sampling sites) [*Mohtadi et al.*, 2013] and during expedition RR-1313 (three sampling sites) [*Rosenthal et al.*, unpublished]. The upper one or two cm of each multicore were washed over 63 µm sieves and dried.

All core sites are situated well above the present lysocline depth of 3300 m where carbonate preservation is expected to be good [see *Berger et al.*, 1982 and references therein]. The presence of aragonitic pteropod shells in most SO-228/GeoB core tops (including the core top from our deepest site) further indicate a good carbonate preservation in our samples.

4.3.3. Dating

Age estimates of all GeoB sediment samples are based on accelerator mass spectrometry (AMS) ^{14}C ages (Table 4.2). All ^{14}C ages were measured on monospecific *Globigerinoides sacculifer* or on mixed *Globigerinoides ruber, G. elongatus* and *G. sacculifer* samples. The measurements were carried out at the Keck Carbon Cycle Accelerator Mass Spectrometry Laboratory, University of California, Irvine . Fraction modern carbon ($F^{14}C$) values above 1 indicate modern ages for all ^{14}C dated samples (Table 4.2). In addition, a few GeoB samples were treated with Rose Bengal and contained stained individuals, indicating that these individuals died only very recently.

The RR-1313 samples did not contain enough foraminifera for radiocarbon dating. For age control of these samples, we measured the carbon isotopic composition ($\delta^{13}C$) on about 10 specimens of *G. ruber* from the 250–300 µm size fraction from the upper 10 cm of each multicore to check for the Suess effect (Figure A1.2). The Suess effect describes a rapid decrease in seawater $\delta^{13}C$ going along with the depletion in ^{13}C of atmospheric CO_2, which has been caused by an increase in deforestation and burning of ^{12}C rich fossil fuels since the industrial revolution [e.g. *Böhm et al.*, 1996; *Friedli et al.*, 1986]. The $\delta^{13}C$ measurements were performed at Rutgers University, New Jersey using a Micromass Optima mass spectrometer, coupled to an automatic line for carbonate preparation. The stable isotope values were calibrated against the international Vienna Peedee belemnite (VPDB) standard using an internal standard, which is calibrated against the National Bureau of Standards (NBS) 19 standard. The long-term standard deviation for $\delta^{13}C$ was 0.06‰. Rapid drops in $\delta^{13}C$ from our RR-1313 multicores are indicative for Suess effect and hence, modern ages of these surface sediments (Figure A1.2). Thus, all samples used in this study reflect modern hydrographic conditions of the WPWP.

Table 4.2. Radiocarbon dating of surface sediments from the Western Pacific Warm Pool. Results are expressed as fraction modern carbon ($F^{14}C$) and conventional ^{14}C ages.

Core	Lab-ID	Depth (cm)	Species	$F^{14}C$ ± error	^{14}C age ± error (years)	Cal. Age
GeoB 17404-2	142715	1–2	*G. ruber*, *G. elongatus*, *G. sacculifer*	1.042 ± 0.002	-325 ± 20	>1950 AD
GeoB 17410-3	158806	1–2	*G. ruber*, *G. elongatus*, *G. sacculifer*	1.064 ± 0.002	-490 ± 20	>1950 AD
GeoB 17414-2	158804	0–1	*G. ruber*, *G. elongatus*, *G. sacculifer*	1.058 ± 0.002	-445 ± 20	>1950 AD
GeoB 17419-2	142718	0–1	*G. sacculifer*	1.072 ± 0.002	-550 ± 20	>1950 AD
	142719	0–1	*G. sacculifer*	1.068 ± 0.003	-515 ± 20	>1950 AD
GeoB 17421-2	158805	0–1	*G. ruber*, *G. elongatus*, *G. sacculifer*	1.054 ± 0.002	-420 ± 15	>1950 AD
GeoB 17429-1	142725	0–1	*G. sacculifer*	1.054 ± 0.002	-415 ± 20	>1950 AD
GeoB 17430-2	142717	0–1	*G. ruber*, *G. elongatus*, *G. sacculifer*	1.058 ± 0.002	-445 ± 20	>1950 AD
GeoB 17432-3	142716	0–1	*G. sacculifer*	1.049 ± 0.002	-375 ± 20	>1950 AD
GeoB 17435-2	158803	0–1	*G. sacculifer*	1.066 ± 0.002	-500 ± 20	>1950 AD

4.3.4. Isotope and trace element analyses

Tests from the foraminiferal species *G. ruber*, *G. elongatus* and *G. sacculifer* (without sac-like final chamber) (all taken from the 250–355 µm size fraction), *Neogloboquadrina dutertrei* and *Pulleniatina obliquiloculata* (355–425 µm), and *Globorotalia tumida* (355–425 µm and >425 µm) were picked under a binocular for $\delta^{18}O$ and Mg/Ca analyses. For all species but *G. tumida*, specimens were separately picked for isotope and Mg/Ca analyses. *G. tumida* specimens were very rare in most of the samples. In order to ensure that fragments of several individuals were used for each measurement, 10 (where available) individuals were picked, crushed, homogenized and then separated for isotope and trace element analyses. Around 40–120 µg carbonate (around 3–10 specimens) were used for stable isotope analyses. The isotopic composition of all samples was measured at the MARUM-isotope laboratory, University of Bremen, Germany, using a Finnigan MAT 251 mass spectrometer, connected to an automatic line for carbonate preparation (type "Kiel III"). All isotope values were calibrated against the international VPDB standard. The internal carbonate standard is a Solnhofen Limestone, which is calibrated to the NBS 19 standard. The analytical standard deviation for $\delta^{18}O$ is below ± 0.07‰. To check the reproducibility of the data we performed up to four (depending on the available material) replicate measurements on 11 samples (Table 4.1). The results indicate an average standard deviation of 0.22‰ for $\delta^{18}O$.

For Mg/Ca analyses we used 30 (where available) well-preserved specimens of *G. ruber* and *G. elongatus*, 25 specimens of *G. sacculifer*, 15 specimens of *P. obliquiloculata* and *N. dutertrei* and between 2 and 10 individuals of *G. tumida*. Although the presence of pteropods indicates negligible effect of carbonate dissolution, all samples were weighed to estimate a potential influence of dissolution on the Mg/Ca records. Samples were gently crushed between two glass plates to open the chambers. The full trace metal cleaning procedure followed the protocol described by *Barker et al.* [2003] with an additional reductive step [*Boyle and Keigwin*, 1985; *Rosenthal et al.*, 1997; *Rosenthal et al.*, 1999]. Samples were dissolved in 0.0065 M HNO_3, centrifuged for 10 min at 10000 rpm and diluted with 0.5 N HNO_3. The final calcium concentration of the samples was on average 3.2 mM. Trace metal ratios were measured at Rutgers University, New Jersey with a Thermo Fisher/Finnigan Element XR sector-field inductively coupled plasma mass spectrometer (ICP-MS). Mg/Ca measurements were performed in low resolution ($\Delta m/m$ = 300). Measured ratios were blank corrected. Mass drift and matrix effects and the long term precision of the data were controlled with in house standard solutions [*Rosenthal et al.*, 1999]. All Mg/Ca values are given in mmol/mol. Replicate measurements on 14 samples revealed an average standard deviation of 0.23 mmol/mol (Table 4.1). To monitor the cleaning efficacy Al/Ca, Fe/Ca and Mn/Ca were measured alongside Mg/Ca. None of these ratios showed a covariance with Mg/Ca (Figure A1.3). Mg/Ca ratios of individual species do not show a correlation to water depth or shell normalized weights (Figure A1.4). Thus, we exclude any substantial effect of carbonate dissolution on shell Mg/Ca values.

4.3.5. Estimation of calcification depths and temperatures

In order to estimate species-specific calcification depths we compare shell $\delta^{18}O$ of individual species with depth-profiles of $\delta^{18}O_C$, assuming that all species calcified in isotopic equilibrium with seawater. The water depth where shell $\delta^{18}O$ matches the expected $\delta^{18}O_C$ is considered to reflect the calcification depth of the respective species at the site.

Depth-profiles of expected $\delta^{18}O_C$ were calculated from SO-228 and RR-1313 CTD salinity profiles as follows. First, $\delta^{18}O_{SW}$ was calculated from salinity using here established regional (WPWP) $\delta^{18}O_{SW}$-salinity equations (equations (4.1) and (4.2) in section 4.4.1). The average uncertainty in the calculated $\delta^{18}O_{SW}$ given as the average standard deviation between measured and calculated $\delta^{18}O_{SW}$ is 0.05‰. It was necessary to calculate $\delta^{18}O_{SW}$ from CTD salinity instead of using the measured $\delta^{18}O_{SW}$ to obtain continuous profiles. Results were converted from VSMOW to the VPDB scale by subtracting 0.27‰ [*Hut*, 1987]. Then, we applied a set of commonly used $\delta^{18}O$-temperature equations (Table 4.3) to predict equilibrium $\delta^{18}O_C$ using CTD temperature and the previously calculated $\delta^{18}O_{SW}$. Finally, we matched shell $\delta^{18}O$ to the $\delta^{18}O_C$ profiles. Since surface sediments were not always taken at the same positions as CTD, we matched shell $\delta^{18}O$ to profile(s) from those station(s), which are nearest to the core sites. To determine uncertainties of the calcification depth of each species and core site we estimated the calcification depths based on shell $\delta^{18}O$ with added/subtracted species-specific standard deviations. Depending on the standard deviation and the shape of the profiles, average uncertainties range between ± 10 and 30 m.

Table 4.3. General and species-specific $\delta^{18}O$-temperature equations used in this study

Reference	Species	Linear equations $T\ (°C) = a - b\ (\delta^{18}O_C - \delta^{18}O_{SW})$		
		a	b	
Bemis et al. [1998]	*O. universa (HL)*	14.9	-4.8	
Bouvier-Soumacnac and Duplessy [1985]	*N. dutertrei*	10.5	-6.58	
Farmer et al. [2007]	*G. ruber*	15.4	-4.78	
	G. sacculifer	16.2	-4.94	
	N. dutertrei	14.6	-5.09	
	P. obliquiloculata	16.8	-5.22	
	G. tumida	13.1	-4.95	
Mulitza et al. [2003]	*G. ruber*	14.2	-4.44	
	G. sacculifer	14.91	-4.35	
Shackleton [1974]	*Uvigerina sp.*	16.9	-4.0	
Spero et al. [2003]	*G. sacculifer*	12.0	-5.67	
		Quadratic equations $T(°C) = a - b\ (\delta^{18}O_C - \delta^{18}O_{SW}) + c\ (\delta^{18}O_C - \delta^{18}O_{SW})^2$		
		a	b	c
Kim and O'Neil [1997]	inorganic	16.1	-4.64	0.09

CTD temperatures at depths corresponding to the estimated calcification depths give an estimate of the calcification temperatures for each species and core site. For *G. elongatus*, *P. obliquiloculata and N. dutertrei* only a few samples from the Philippines contained enough individuals to perform isotope analyses. For *G. tumida* none of the Philippines samples contained enough specimens and therefore depth and temperature estimates for this species are only representative for the area offshore PNG.

4.4. Results

4.4.1. Water column data and $\delta^{18}O_{SW}$-salinity regressions

The $\delta^{18}O_{SW}$-salinity relations for the study area during summer 2013 reveal that a $\delta^{18}O_{SW}$ increase of about 0.3 to 0.4‰ corresponds to a salinity increase of 1 psu (Figure 4.3). Regressions for surface waters offshore the Philippines and PNG (considering only samples from the Bismarck and Solomon Seas) are very similar (Figure 4.3a, blue and red dots, respectively). The regression line for surface waters offshore PNG shows only a slightly steeper slope and consequently, a smaller intercept.

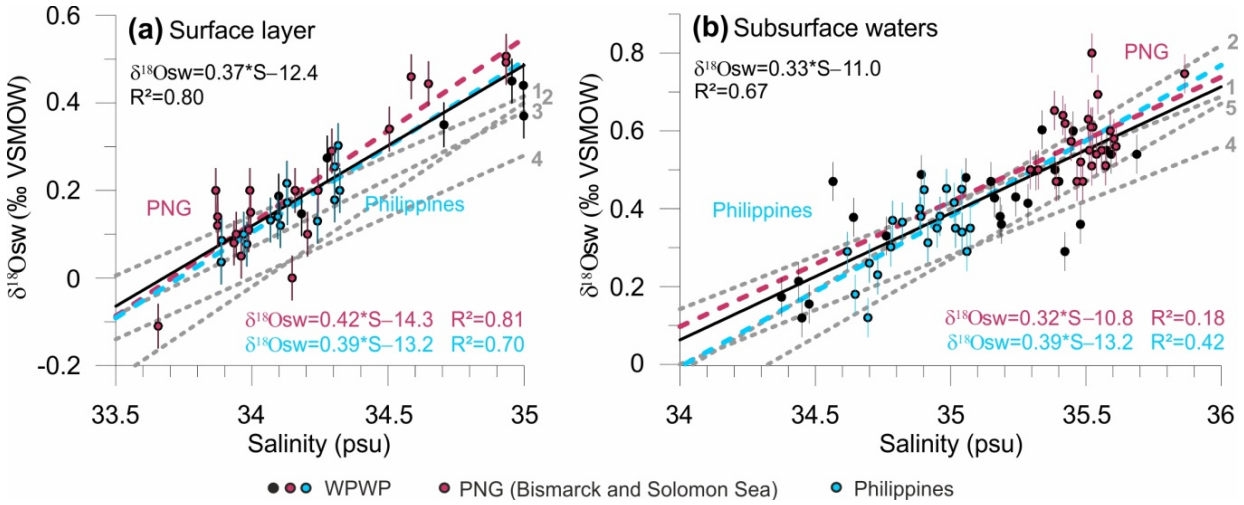

Figure 4.3. Regional $\delta^{18}O_{SW}$–salinity relations for (a) surface and (b) subsurface waters in the Western Pacific Warm Pool. Dots indicate individual samples included in the regressions. Red and blue colors indicate subsets of samples included in the regional regressions off Papua New Guinea (PNG) and the Philippines, respectively. Black dots indicate samples from sites that are not included in the regional regressions. Black lines indicate regression lines for the entire study area and colored lines for the subareas. Gray stippled lines show regional $\delta^{18}O_{SW}$–salinity equations published by 1. *Fairbanks et al.* [1997], 2. *Morimoto* [2002], 3/5. *Leech et al.* [2013], 4. [*LeGrande and Schmidt*, 2011]. Bars indicate laboratory standard deviations for oxygen isotope measurements.

Taking all SO-228 and RR-1313 stations across the WPWP into account (Figure 4.3a, all black and colored dots) the surface $\delta^{18}O_{SW}$-salinity relation can be described as

$$\delta^{18}O_{SW} = 0.37\ (\pm\ 0.03) * S - 12.4\ (\pm\ 1.0) \qquad (R^2 = 0.80) \qquad (4.1)$$

Regression lines describing the $\delta^{18}O_{SW}$-salinity relations for subsurface waters (NPTW and SPTW) show a shallower slope than for surface waters with slightly higher intercepts (Figure 4.3b). Due to the very small salinity ranges within the NPTW and SPTW it is difficult to assess a robust relationship for each of these water masses. The regressions also greatly depend on the depths and number of stations included in each equation. However, although NPTW and SPTW have different characteristics (see Figure 4.2), their $\delta^{18}O_{SW}$-salinity regressions are very similar to each other. Therefore, we also provide one equation for WPWP subsurface waters that includes all SO-228 and RR-1313 sample stations (Figure 4.3b, all black and colored dots).

$$\delta^{18}O_{SW} = 0.33\ (\pm\ 0.03) * S - 11.0\ (\pm\ 1.1) \qquad (R^2 = 0.67) \qquad (4.2)$$

4.4.2. Calcification depth

In general, shell $\delta^{18}O$ increases with increasing calcification depth of the species. *G. ruber* and *G. elongatus* record the lowest $\delta^{18}O$ values and *G. tumida* records the highest $\delta^{18}O$ values. *G. sacculifer*, *P. obliquiloculata* and *N. dutertrei* calcify in between. Shell $\delta^{18}O$ and our derived mean calcification depths of the species used are very similar offshore the Philippines and PNG. Therefore, in our discussion we do not distinguish between samples from the Philippines and PNG. Figure 4.4 and Table 4.4 give $\delta^{18}O$-derived depths for all species as estimated by applying the $\delta^{18}O$-temperature equation of *Bemis et al.* [1998]. Depth estimates for each species applying different $\delta^{18}O$-temperature equations in comparison are provided in the appendix (Figures A1.4–1.6).

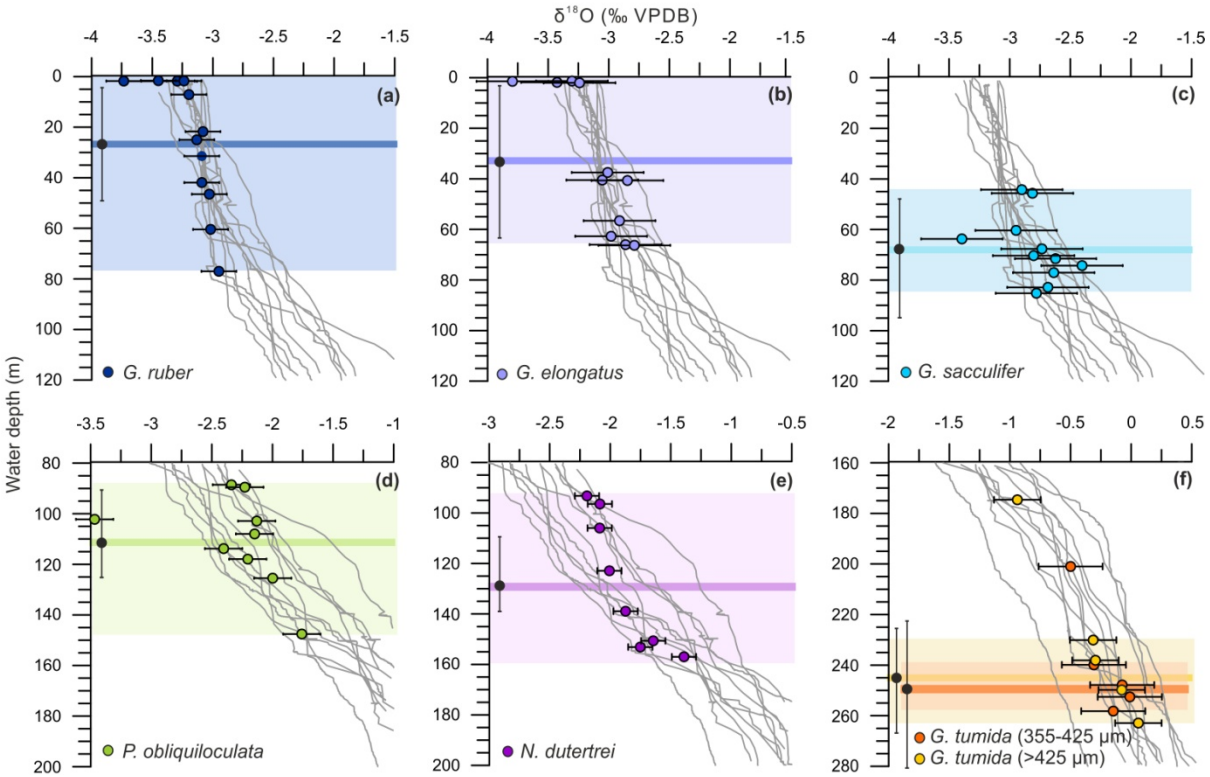

Figure 4.4. Shell $\delta^{18}O$ derived calcification depth estimates for several planktic foraminifera (colored dots) in the Western Pacific Warm Pool. Gray lines indicate depth profiles of predicted $\delta^{18}Oc$ calculated from individual CTD casts (see section 4.3.5 for details). The average calcification depth at each core site is determined by matching shell $\delta^{18}O$ to $\delta^{18}O_C$ of the profile(s) nearest to the respective core site. Horizontal bars indicate species-specific standard deviations for shell $\delta^{18}O$, vertical bars on black dots show exemplarily average uncertainties in calcification depth derived by projecting shell $\delta^{18}O$ with added/subtracted standard deviations on the $\delta^{18}O_C$ profiles. The uncertainty of the $\delta^{18}O_C$ profiles arising from the average standard deviation between measured and calculated $\delta^{18}O_{SW}$ is 0.05‰ (not shown). Colored shading indicates calcification depth ranges for the individual species in the study area. The average calcification depth is highlighted by colored horizontal bars. Note the different scaling of the axes in different panels. Individual data points, which are shown outside the range of predicted $\delta^{18}O_C$ do not match any profile (see text).

Table 4.4. Calcification depth and temperatures. The calcification depth of each species and core site was estimated by comparing shell $\delta^{18}O$ to depth profiles of predicted $\delta^{18}O$ calcite. Predicted $\delta^{18}O_C$ was calculated from CTD salinity applying the $\delta^{18}O_{SW}$-salinity equations of this study and the $\delta^{18}O$-temperature equation of *Bemis et al.* [1998] using CTD temperature. We assigned a depth of 0 m to samples that did not match any profile. Calcification temperatures are CTD temperatures at depth corresponding to the estimated calcification depths.

Core	*G. ruber* (250-355 µm)		*G. elongatus* (250-355 µm)		*G. sacculifer* (250-355 µm)		*P. obliquiloculata* (355-425 µm)		*N. dutertrei* (355-425 µm)		*G. tumida* (355-425 µm)		*G. tumida* (>425 µm)	
	Depth (m)	Temp. (°C)	Depth (m)	Temp. (°C)	Depth (m)	Temp. (°C)	Depth (m)	Temp. (°C)	Depth (m)	Temp. (°C)	Depth (m)	Temp. (°C)	Depth (m)	Temp. (°C)
Philippines														
RR1313-24 50MC	7	29.8	0	29.6	85	28.4	0	29.8	140	24.3	-	-	-	-
RR1313-25 53MC	77	28.3	0	28.8	-	-	-	-	-	-	-	-	-	-
GeoB 17404-2	47	28.9	57	28.5	83	27.8	-	-	-	-	-	-	-	-
GeoB 17410-3	22	29.3	0	29.9	70	28.2	-	-	-	-	-	-	-	-
GeoB 17414-2	25	29.2	37	28.7	45	28.2	88	25.8	94	25.3	-	-	-	-
Papua New Guinea														
GeoB 17419-2	32	29.7	40	29.8	60	29.6	147	24.6	150	24.2	200	18.8	175	20.9
RR1313-12 30MC	0	29.7	-	-	0	29.7	114	27.5	-	-	-	-	-	-
GeoB 17421-2	0	29.7	0	29.7	77	28.3	117	26.7	157	23.1	240	17.7	-	-
GeoB 17429-1	60	29.0	67	28.6	72	27.9	125	25.8	123	25.8	248	16.4	250	15.9
GeoB 17430-2	42	29.2	63	28.7	68	28.5	108	26.3	153	24.7	252	15.8	230	17.6
GeoB 17432-3	0	29.4	66	28.6	75	27.5	103	26.2	107	26.0	-	-	263	15.6
GeoB 17435-2	0	28.9	40	28.9	45	26.7	90	26.9	97	26.2	258	16.6	238	17.7

4.4.2.1. Mixed layer species: *G. ruber*, *G. elongatus* and *G. sacculifer*

Average shell $\delta^{18}O$ values are very similar for *G. ruber* and *G. elongatus* (–3.19 and –3.11‰, Table 4.1). This implies very similar calcification depths for both species in the WPWP. Depending on the selected $\delta^{18}O$-temperature equation, shell $\delta^{18}O$ derived mean calcification depths range from 0 to 45–105 m (Figures 4.4 and A1.4). Applying the $\delta^{18}O$-temperature equations of *Bemis et al.* [1998] and *Shackleton* [1974] the estimated depth range is within the upper 80 m of the water column for both, *G. ruber* and *G. elongatus*. By applying the equations of *Kim and O'Neil* [1997] and *Farmer et al.* [2007] calcification depths shoal to 0–45 m and 0–65 m, respectively, while the application of the species-specific equation of *Mulitza et al.* [2003] results in a slightly deeper depth range (0–105 m) (Figure A1.5a).

Shell $\delta^{18}O$ of *G. sacculifer* varies around –2.73‰ (excluding RR1313-12 30MC) (Table 4.1). Applying different $\delta^{18}O$-temperature equations, the mean calcification depth varies between 45 and 95 m. It ranges from 45 to 85 m using the equation of *Bemis et al.* [1998] (Figure 4.4c) and from 55 to 95 m applying the $\delta^{18}O$-temperature equations of *Shackleton* [1974] and *Spero et al.* [2003]. The equations of *Farmer et al.* [2007] and *Kim and O'Neil* [1997] lead to slightly shallower calcification depths (0–70 m) and the equation of *Mulitza et al.* [2003] to deeper calcification depths (70–110 m) (Figure A1.5). Note that sample RR1313-12 30MC shows an extremely low $\delta^{18}O$ value (–3.39‰), which does not match any profile.

4.4.2.2. Upper thermocline species: *P. obliquiloculata* and *N. dutertrei*

Shell $\delta^{18}O$ of *P. obliquiloculata* varies around –2.15‰ (excluding RR1313-24 50MC) (Table 4.1). For the majority of the samples this indicates a calcification depth between 90 and 125 m when applying the $\delta^{18}O$-temperature equation of *Bemis et al.* [1998] (Figure 4.4d). Applying the equations of *Shackleton* [1974] or *Bouvier-Soumagnac and Duplessy* [1985] leads to very similar calcification depths (85–120 and 90–130 m), and the equations of *Kim and O'Neil* [1997] and *Farmer et al.* [2007] leads to slightly shallower calcification depths (70–105 and 40–75 m) (Figure A1.6). Our foraminifera tests from site GeoB 17419-2 record exceptionally high $\delta^{18}O$ values resulting in, compared to the other core sites, relatively deeper (20–40 m) calcification depths. With a $\delta^{18}O$ value of –3.47‰ (Table 4.1), sample RR1313-24 50MC does not match any $\delta^{18}O_C$ profile.

The *N. dutertrei* average shell $\delta^{18}O$ of –1.88‰ is slightly higher than that of *P. obliquiloculata*. By using the equations of *Bemis et al.* [1998], *Shackleton* [1974] or *Farmer et al.* [2007] shell derived calcification depths vary between around 90 and 160 m (Figures 4.4e and A1.5). The application of the $\delta^{18}O$-temperature equation from *Kim and O'Neil* [1997] or *Bouvier-Soumagnac and Duplessy* [1985] results in slightly shallower or deeper depth ranges (80–150 or 95–155 m) (Figure A1.6).

4.4.2.3. Lower thermocline species: *G. tumida*

Average shell $\delta^{18}O$ of *G. tumida* is –0.15‰ for the 355–425 µm size fraction and –0.14‰ for the >425 µm size fraction (excluding GeoB 17419-2) (Table 4.1). Shell $\delta^{18}O$ of individual samples differ by maximal 0.3‰. Hence, under the restriction of the small set of samples, our data indicate, that there is no major size effect on the calcification depths of *G. tumida*. Based on the equation of *Bemis et al.* [1998] the calcification depth of *G. tumida* at most sites is between 230 and 265 m water depth (Figure 4.4f). The application of the equations from *Shackleton* [1974] and *Kim and O'Neil* [1997] results in slightly shallower calcification depths, ranging between 195 and 235 m. Based on the species-specific equation of *Farmer et al.* [2007] the estimated calcification depths are slightly deeper, ranging between 255 and 310 m (Figure A1.7). Exceptionally low $\delta^{18}O$ in *G. tumida* shells from GeoB 17419-2 indicates up to 70 m shallower calcification depth at this site, independent of the size fraction used.

4.4.3. Shell Mg/Ca

Mg/Ca ratios recorded in the Philippines and PNG samples are very similar. *G. ruber* and *G. elongatus* record highest Mg/Ca, averaging 5.26 and 5.37 mmol/mol, respectively. Shell Mg/Ca in *G. sacculifer* varies around 3.85 mmol/mol. *N. dutertrei* and *P. obliquiloculata* show similar shell Mg/Ca varying around 2.60 and 2.66 mmol/mol, respectively. *G. tumida* shows lowest Mg/Ca ratios around 1.88 mmol/mol (355–425 µm) and 1.69 mmol/mol (>425 µm). Hence, average Mg/Ca of the different species confirms the results obtained from oxygen isotope ratios with calcification depths being shallowest for *G. ruber*, *G. elongatus* and *G. sacculifer*, intermediate for *P. obliquiloculata* and *N. dutertrei* and deepest for *G. tumida*. Mg/Ca ratios of *P. obliquiloculata* in RR1313-24 50MC, *N. dutertrei* in RR1313-53MC, and *G. tumida* in GeoB 17410-3 are exceptionally high (3.17 mmol/mol, 4.23 mmol/mol, and 3.27 mmol/mol) (Table 4.1). The high Mg/Ca value of *P. obliquiloculata* in RR1313-24 50MC goes along with exceptionally low $\delta^{18}O$ and could therefore indicate an extremely shallow calcification depth at this site. Due to the limited number of specimens of *N. dutertrei* in RR1313-25 53MC and *G. tumida* in GeoB 17410-3, we could not measure the oxygen isotope composition in these samples.

4.5. Discussion

4.5.1. Water column data and $\delta^{18}O_{SW}$-salinity regressions

Generally, our surface and subsurface $\delta^{18}O_{SW}$-salinity regressions are within the range of published WPWP regressions [*Fairbanks et al.*, 1997; *Leech et al.*, 2013; *LeGrande and Schmidt*, 2011; *Morimoto*, 2002]. However, slope and/or intercept differ from previous regression lines. Especially the regressions of *Fairbanks et al.* [1997] and *LeGrande and Schmidt* [2011] and the surface regression of [*Leech et al.*, 2013]show shallower slopes (around 0.3) and accordingly, larger intercepts (between –10.47 and –9.14)

than our regressions. The regression of [*Morimoto*, 2002] is almost identical to our PNG surface equation ($\delta^{18}O_{SW}$ = 0.42 * S − 14.3). Since $\delta^{18}O_{SW}$-salinity relations depend on local environmental conditions, deviations are most probably due to different sampling sites, water depths and periods.

For the first time, we generated equations for individual water masses (surface waters, NPTW and SPTW). Our results reveal that for both, WPWP wide and regional regressions, the ratio between $\delta^{18}O_{SW}$ and salinity is higher in surface than in subsurface waters. Therefore, it appears reasonable to use different $\delta^{18}O_{SW}$-salinity regressions for surface and subsurface water masses. The regression coefficients of our regression lines (Figure 4.3) indicate that the application of a more general, WPWP wide regression for combined NPTW and SPTW is more robust than individual regressions for the NPTW and SPTW. This is due to the very small salinity range within the NPTW offshore the Philippines and the SPTW offshore PNG.

4.5.2. Calcification depths and temperatures

Accurate calcification depth estimates are indispensable to deduce precise calcification temperatures for each species. The accuracy of the depth estimates depends on the precision of the $\delta^{18}O_{SW}$-salinity equation applied, the choice of the $\delta^{18}O$-temperature equation, the availability of local water column data, the seasonal and interannual variations in local hydrography and possible shell disequilibrium effects [see *Regenberg et al.*, 2009; *Steph et al.*, 2009].

A comparison between predicted $\delta^{18}O_C$ calculated using discrete $\delta^{18}O_{SW}$ measured in water samples and predicted $\delta^{18}O_C$ using $\delta^{18}O_{SW}$ calculated from CTD salinity shows that the calculated values reproduce measured $\delta^{18}O$ precisely (Figure A1.8). The average deviation between calculated and measured $\delta^{18}O_{SW}$ is ± 0.07‰, the maximal deviation is ± 0.35‰ and only 6 out of 98 samples yielded $\delta^{18}O_{SW}$ differences larger than 0.20‰ (see Table A1.2). The comparison provides reliability to the accuracy of the $\delta^{18}O_{SW}$-salinity equations for our sampling period and sites.

For the following analyses we use calcification depth estimates based on the $\delta^{18}O$-temperature equation that was generated by *Bemis et al.* [1998] in a culture experiment for *O. universa*. Although it has been obtained on a single species not used in our study, this equation is commonly used for other planktic foraminiferal species [e.g. *Mohtadi et al.*, 2014; *Spero et al.*, 2003; *Thunell et al.*, 1999] and its application gives realistic results for all species used here. The equations of *Shackleton* [1974], *Bouvier-Soumagnac and Duplessy* [1985], and *Spero et al.* [2003] lead to similar calcification depths. The quadratic equation of *Kim and O'Neil* [1997] results in marginally shallower depths for surface and similar depths for subsurface dwellers. The application of the equations of *Farmer et al.* [2007] result in slightly shallower calcification depths. The equations of *Farmer et al.* [2007] are based on sample material from much greater water depths (mostly 3000–4000 m) where carbonate is affected by dissolution [*Hertzberg and*

Schmidt, 2013] which would increase $\delta^{18}O$ in foraminiferal tests. Consequently, the application of these equations would underestimate calcification depths. The equations proposed by *Mulitza et al.* [2003] result in deeper calcification depths. These equations are based on plankton tow studies and might overestimate calcification depths due to lower $\delta^{18}O$ in shells of living foraminifera [see *Regenberg et al.*, 2009 and references therein].

Based on the assumption that planktic foraminifera calcify perennially in the WPWP we assume that our $\delta^{18}O$ data represent mean annual conditions. However, we note that data from individual samples might be biased and reflect other than normal conditions (e.g. a single season or El Niño/La Niña conditions). We are well aware that our hydrographic data show a snapshot and therefore do not necessarily represent mean annual hydrography. However, seasonal temperature and salinity variations are very small in our study area and mostly restricted to the mixed layer (see section 4.2). Interannual variations in ocean hydrography are mainly caused by ENSO variability. Our water column data were collected during a normal year and are thus, not biased to El Niño or La Niña conditions. Considering the paucity of continuous subsurface temperature, salinity and especially $\delta^{18}O_{SW}$ data from the WPWP, our work provides the first simultaneous measurements on these parameters at different water depths at stations in close proximity to our core sites and thus the hitherto most suitable hydrographic estimates for the determination of calcification depths and temperatures.

Nonetheless, we also compared shell $\delta^{18}O$ with depth-profiles of $\delta^{18}O_C$ calculated by using mean annual temperature and salinity data from the World Ocean Atlas 13 (WOA13) [*Locarnini et al.*, 2013; *Zweng et al.*, 2013]. Shell $\delta^{18}O$ of most *G. ruber* and *G. elongatus* samples do not match the WOA13 $\delta^{18}O_C$ profiles. WOA13 derived calcification depths of *G. sacculifer* extent over a larger depth range than SO-228 and RR-1313 CTD (from here on referred to as CTD) calcification depths. WOA13 depth estimates of *P. obliquiloculata, N. dutertrei* and *G. tumida* differ only slightly from CTD derived depth estimates (maximal 35 m) with a tendency to shallower depths. Overall, for our study, the application of CTD data gives more realistic results than the application of WOA13 data.

Previous studies have shown that many species do not calcify in isotopic equilibrium with seawater [see *Ravelo and Hillaire-Marcel*, 2007 and references therein]. Potential reasons are the photosynthetic activity of symbionts, incorporation of low $\delta^{18}O$ metabolic CO_2, species-specific calcification rates, the addition of gametogenic calcite, and possibly carbonate ion concentrations of the ambient seawater [see *Ravelo and Hillaire-Marcel*, 2007 and references therein]. Disequilibrium effects depend on local conditions and the sample material used. For most species used in our study, negative disequilibrium effects ranging between 0.0 and 1.0‰ are presumed [see *Lončarić et al.*, 2006; *Niebler et al.*, 1999 and references therein]. No vital effects are reported for *G. tumida.* Correcting for negative disequilibrium effects would increase shell

$\delta^{18}O$, and subsequently result in deeper calcification depths and colder calcification temperatures [see discussion in *Regenberg et al.*, 2009]. However, the large variety of factors that could possibly influence shell $\delta^{18}O$ makes it difficult to correct $\delta^{18}O$ for disequilibrium effects precisely. In addition, most published $\delta^{18}O$-temperature equations do not take into account biological disequilibrium effects on $\delta^{18}O$. Therefore, we did not correct $\delta^{18}O$ values for disequilibrium effects.

Overall, our results show that *G. ruber* and *G. elongatus* calcify within the mixed layer (0–80 m) and *G. sacculifer* calcifies at the bottom of the mixed layer (45–85 m). *P. obliquiloculata* and *N. dutertrei* calcify within the upper thermocline, whereby our $\delta^{18}O$ values indicate that *N. dutertrei* calcifies within a larger depth range (90–160 m) than *P. obliquiloculata* does (90–125 m). *G. tumida* seems to calcify well below *P. obliquiloculata* and *N. dutertrei* within the lower thermocline at depth between 230 and 265 m. In relation to water masses, this means that *G. ruber*, *G. elongatus* and *G. sacculifer* calcify in surface waters. *P. obliquiloculata*, and *N. dutertrei* calcify predominantly within the NPTW offshore the Philippines and within the SPTW offshore PNG. *G. tumida* calcifies within the transition between NPTW/SPTW and NPIW or AAIW. Our depth estimates generally agree with results from sediment traps and plankton tows in the central equatorial Pacific, North Pacific and Indian Oceans [*Kuroyanagi and Kawahata*, 2004; *Mohtadi et al.*, 2009; *Peeters et al.*, 2002; *Rippert et al.*, 2016; *Watkins et al.*, 1996]. However, our data show a tendency to somewhat deeper absolute calcification depths and wider depth ranges for most species, probably owing to a generally thick mixed layer and deep thermocline in the WPWP. Recent results from the eastern WPWP indicate even deeper habitat depths of planktic foraminifera [*Rippert et al.*, 2016]. Such differences in absolute calcification depths are likely related to the specific regional hydrographic conditions in each study area. For *G. ruber* and *G. elongatus,* our data imply very similar calcification depths. This is in sharp contrast to studies from the South China Sea and North Pacific Ocean that suggest a deeper habitat depth for *G. elongatus* [*Kawahata*, 2005; *Steinke et al.*, 2005; *Wang*, 2000] but in agreement with studies from the eastern Indian Ocean and the Caribbean Sea, which suggest the same habitat depth for both species [*Mohtadi et al.*, 2009; *Thirumalai et al.*, 2014].

4.5.3. Mg/Ca versus calcification temperatures

A large number of studies revealed that Mg/Ca in planktic foraminiferal tests show an exponential relationship with ocean temperatures [e.g. *Anand et al.*, 2003; *Cléroux et al.*, 2008; *Dekens et al.*, 2002; *Elderfield and Ganssen*, 2000; *McConnell and Thunell*, 2005; *Mohtadi et al.*, 2009; *Mohtadi et al.*, 2011; *Nürnberg et al.*, 1996; *Regenberg et al.*, 2009]. Some culture and core top studies also described a positive salinity effect on shell Mg/Ca of planktic foraminifera [*Arbuszewski et al.*, 2010; *Ferguson et al.*, 2008; *Kısakürek et al.*, 2008; *Mathien-Blard and Bassinot*, 2009; *Nürnberg et al.*, 1996]. However, studies suggesting a significant salinity influence have been criticized due to substantial dissolution effects, seasonality [*Arbuszewski et al.*, 2010] or diagenetic alteration [*Ferguson et al.*, 2008] on the sample

material [*Hertzberg and Schmidt*, 2013; *Hönisch et al.*, 2013]. However, in our study area the salinity range is rather small (between 33.9 and 35.6 psu). Variations between stations at water depths that correspond to the calcification depth of individual foraminifera species at the corresponding core sites are below 1.2 psu. There is no significant correlation between Mg/Ca and salinity (R-values range between 0.00 and 0.35 for individual species). Besides, shell Mg/Ca in samples from offshore the Philippines and PNG are very similar, although these areas are influenced by water masses characterized by different salinities (Figure 4.2). Therefore, we argue that shell Mg/Ca in our samples is not biased by salinity. Some studies also indicate a negative effect of pH or [CO_3^{2-}] on Mg/Ca [*Evans et al.*, 2016; *Kısakürek et al.*, 2008; *Lea et al.*, 1999; *Russell et al.*, 2004; *Spero et al.*, 2015]. To date, it is not clear whether pH or [CO_3^{2-}] exert a dominant control on Mg/Ca [*Allen et al.*, 2016; *Evans et al.*, 2016]. Moreover, the effect is neither constant over temperature [*Spero et al.*, 2015], nor the same for different planktic foraminifera species [e.g. *Allen et al.*, 2016] and some studies provide confidence that the effect is negligible for ambient seawater conditions [*Kısakürek et al.*, 2008; *Russell et al.*, 2004]. Since pH or [CO_3^{2-}] were not measured during both SO-228 and RR-1313 expeditions, we cannot estimate the range of these parameters over the study area. We do not apply any corrections for possible effects of carbonate chemistry on shell Mg/Ca, while we cannot fully exclude such effect on our samples. More extensive culture and/or sediment trap studies are required to quantify the effect pH or [CO_3^{2-}] on Mg/Ca of the various planktic foraminifera species.

Mg/Ca to temperature calibrations are usually expressed as Mg/Ca = B exp (A*Temperature). We combined data of all species and compared shell Mg/Ca to CTD temperature at $\delta^{18}O$-derived calcification depths in a multispecies approach (Figure 4. 5). A depth of 0 m was assigned to samples, where shell $\delta^{18}O$ did not match the $\delta^{18}O_C$. Mg/Ca and temperature show a clear exponential relationship (Figure 4.5). Previous studies suggest that this relationship is best described by a reduced major axis (or geometric mean) regression (RMA) of the natural Log of (Mg/Ca) against calcification temperature [*Anand et al.*, 2003; *Rosenthal and Lohmann*, 2002]. An advantage of the RMA is that it accounts for both, uncertainties in Mg/Ca and calcification temperatures. Especially in field studies, calcification temperatures inherit an intrinsic scatter that arises from a range of different factors including uncertainties in the depth estimates or seasonality for example.

Using the RMA approach, the multispecies Mg/Ca-temperature relation is described by the following equation:

$$Mg/Ca = 0.26\ (\pm 0.04)\ \exp\ 0.097 * T\ (\pm 0.006) \qquad (4.3)$$

The calculation followed *Isobe et al.* [1990]. The uncertainties of the slope and intercept are given as standard deviations assuming that the intrinsic scatter of the data dominates any errors of the measurement

process. For comparison, we also calibrated shell Mg/Ca against WOA13 mean annual temperatures. Despite the differences in estimated calcification depths, WOA13 derived calcification temperatures are very similar to CTD derived calcification temperatures. The reason is that temperatures of the WOA13 climatology are generally lower than our CTD temperatures at the same depth levels. Due to the similarity of the calcification temperatures, the WOA13 derived regression is within the error range of the regression based on CTD derived calcification temperatures. (A = 0.101, B = 0.24).

Our multispecies Mg/Ca-temperature relation is in good agreement with previously published multispecies and species-specific temperature calibrations (Figure 4.5 and Table 4.5). However, comparing our calibration to published ones, it has to be noted that our calibration is based on samples that were treated by reductive cleaning, whereas most published calibrations are based on samples cleaned without a reductive step. Previous studies indicate that the reductive cleaning leads to a decrease in Mg/Ca [e.g. *Barker et al.*, 2003; *Xu et al.*, 2010]. To estimate the effects on the Mg/Ca-temperature relations, we applied a correction assuming that the Mg/Ca relations were reduced by about 10% in all samples [e.g. *Barker et al.*, 2003; *Martin and Lea*, 2002; *Rosenthal et al.*, 2004]. We note that some studies suggest different values for individual species [e.g. *Xu et al.*, 2010], but since exact rates of Mg/Ca loss are unknown for most species, we presume a constant rate of 10% for all species. The resulting regression line shows the same slope as the original calibration (0.097) and an only slightly modified intercept (0.24). Thus, the modified calibration is within the error range of the original one.

A multispecies equation does not seem accurate enough to describe the Mg/Ca-temperature relation of individual species in the WPWP. For example, all the *G. ruber* and *G. elongatus* samples fall above, and all the *P. obliquiloculata* and *N. dutertrei* samples fall below the regression line. That means that calcification temperatures of *G. ruber* and *G. elongatus* are overestimated, and those of *P. obliquiloculata* and *N. dutertrei* are underestimated by the multispecies regression. For that reason, species-specific regression lines are additionally required to reconstruct calcification temperatures for individual species precisely. Since the temperature range between the sites in our study area is very narrow, it is difficult to determine the temperature sensitivity for individual species unequivocally. Hence, we calculated regional species-specific regressions by assuming the same temperature sensitivity, A = 0.097, as it was calculated by the multispecies approach, for all species (Figure 4.5). The resulting regression lines for *G. ruber* and *G. elongatus* are very similar to the multispecies and species-specific regression published by *Anand et al.* [2003] or *Dekens et al.* [2002], respectively (Mg/Ca = 0.39 exp 0.09 * T). For the temperature range relevant for this study the regression lines of *G. tumida* fall next to the multispecies regression lines of *Anand et al.* [2003] and *Sagawa et al.* [2012]. However, especially slope and intercept of the *Sagawa et al.* [2012] regression differ from those of our species-specific regression (Table 4.5) and it is important to note that the slope affects the amplitude of temperature variations in paleorecords. The regression lines of

G. sacculifer, *P. obliquiloculata* and *N. dutertrei* deviate from previously published correlations (Figure 4.5). Calcification temperatures of these species are exceptionally warm in the western tropical Pacific Ocean despite deeper calcification depths and thus, *G. sacculifer*, *P. obliquiloculata* and *N. dutertrei* require regional, species-specific Mg/Ca-temperature calibrations. Assuming the temperature sensitivity calculated by the multispecies approach (A = 0.097) our data indicate an intercept of B = 0.24 for *G. sacculifer* and an intercept of B = 0.21 for both *P. obliquiloculata* and *N. dutertrei* (4.5).

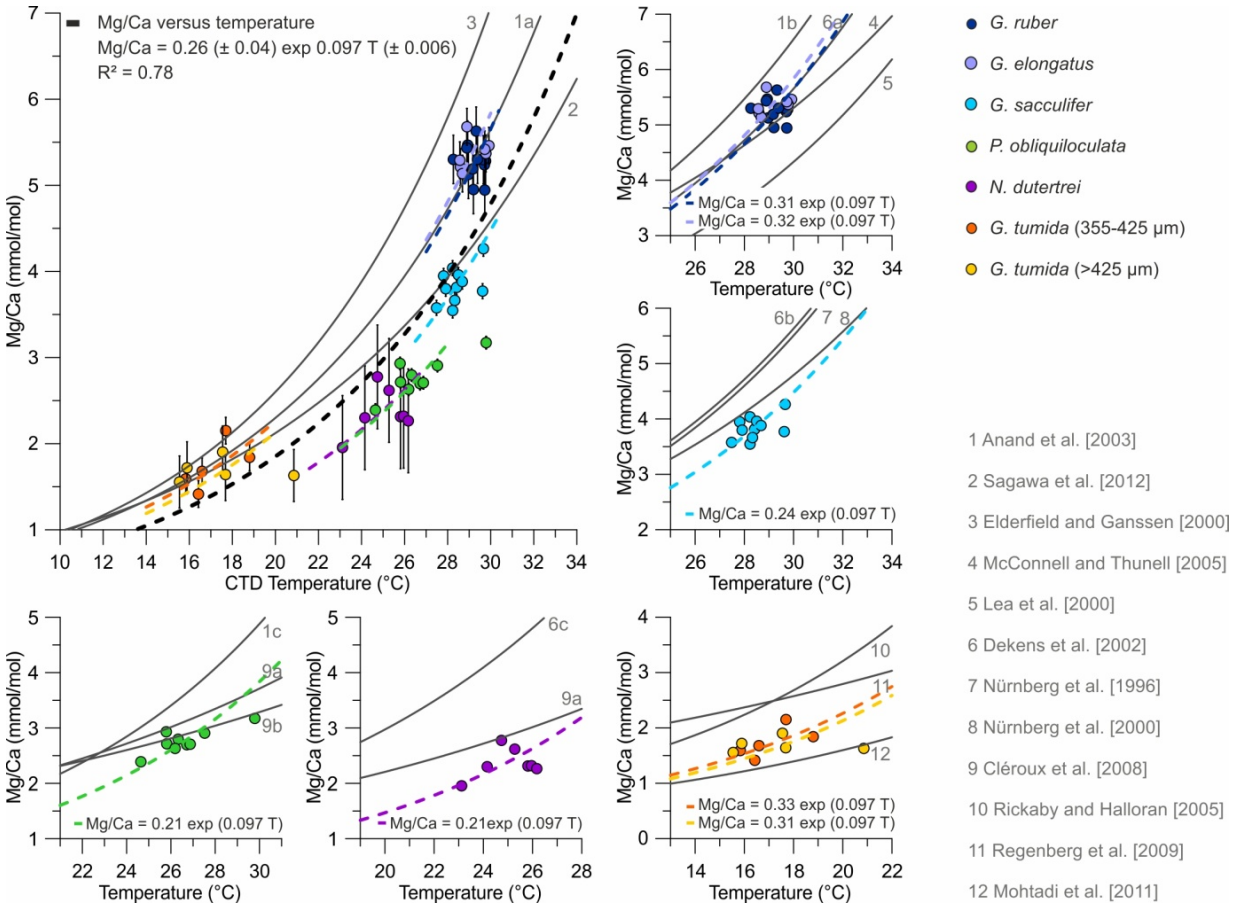

Figure 4.5. Shell Mg/Ca versus calcification temperature for different planktic foraminifera species. Black bars indicate species-specific standard deviations of Mg/Ca. Black and colored dashed lines indicate regional multispecies and species-specific regressions calculated with a RMA regression (this study). Gray solid lines show published multispecies (large graph) and species-specific (small graphs) regression lines. Numbers denote published calibrations (see also Table 4.5). Note that a, b and c refer to different calibrations in the same publication.

Table 4.5. Multispecies and species-specific Mg/Ca temperature in comparison to previously published relations. Calibration numbers introduced in Figure 4.5 are given in gray.

Reference	Species	Exponential relation Mg/Ca = B exp (A*Temperature)	
		A	B
Anand et al. [2003] (1a)	multispecies	0.09	0.38
Sagawa et al. [2011] (2)	multispecies	0.077	0.455
Elderfield and Ganssen [2000] (3)	multispecies	0.1	0.352
This study	multispecies	0.097	0.26
Anand et al. [2003] (1b)	*G. ruber*	0.09	0.44
McConnell and Thunell [2005] (4)	*G. ruber*	0.068	0.69
Lea et al. [2000] (5)	*G. ruber*	0.089	0.3
Dekens et al [2002] (6a)	*G. ruber*	0.09	0.38
This study	*G. ruber*	0.097	0.31
This study	*G. elongatus*	0.097	0.32
Dekens et al. [2002] (6b)	*G. sacculifer*	0.09	0.37
Nürnberg et al. [1996] (7)	*G. sacculifer*	0.089	0.39
Nürnberg et al. [2000] (8)	*G. sacculifer*	0.076	0.49
This study	*G. sacculifer*	0.097	0.24
Anand et al. [2003] (1c)	*P. obliquiloculata*	0.09	0.328
Cléroux et al. [2008] (9b)	*P. obliquiloculata*	0.039	1.02
This study	*P. obliquiloculata*	0.097	0.21
Dekens et al. [2002] (6c)	*N. dutertrei*	0.08	0.6
This study	*N. dutertrei*	0.097	0.21
Cléroux et al. [2008] (9a)	Deep dwelling species	0.052	0.78
Rickaby and Halloran [2005] (10)	*G. tumida*	0.09	0.53
Regenberg et al. [2009] (11)	*G. tumida*	0.041	1.23
Mohtadi et al. [2011] (12)	*G. tumida*	0.068	0.41
This study	*G. tumida* (355-425 µm)	0.097	0.33
This study	*G. tumida* (>425 µm)	0.097	0.31

A comparison of Mg/Ca-temperatures and calcification temperatures gives a measure of the uncertainty inherent in the Mg/Ca-temperature calibrations [*Anand et al.*, 2003]. We compared Mg/Ca-temperatures calculated by the application of species-specific calibrations to $\delta^{18}O$-derived calcification temperatures (4.6). The average standard error between Mg/Ca and $\delta^{18}O$-derived calcification temperatures is 0.5°C. The consistency of Mg/Ca and $\delta^{18}O$-derived calcification temperatures validates our previous steps and assumptions, and gives further evidence that Mg/Ca and $\delta^{18}O$ data are not influenced by secondary effects.

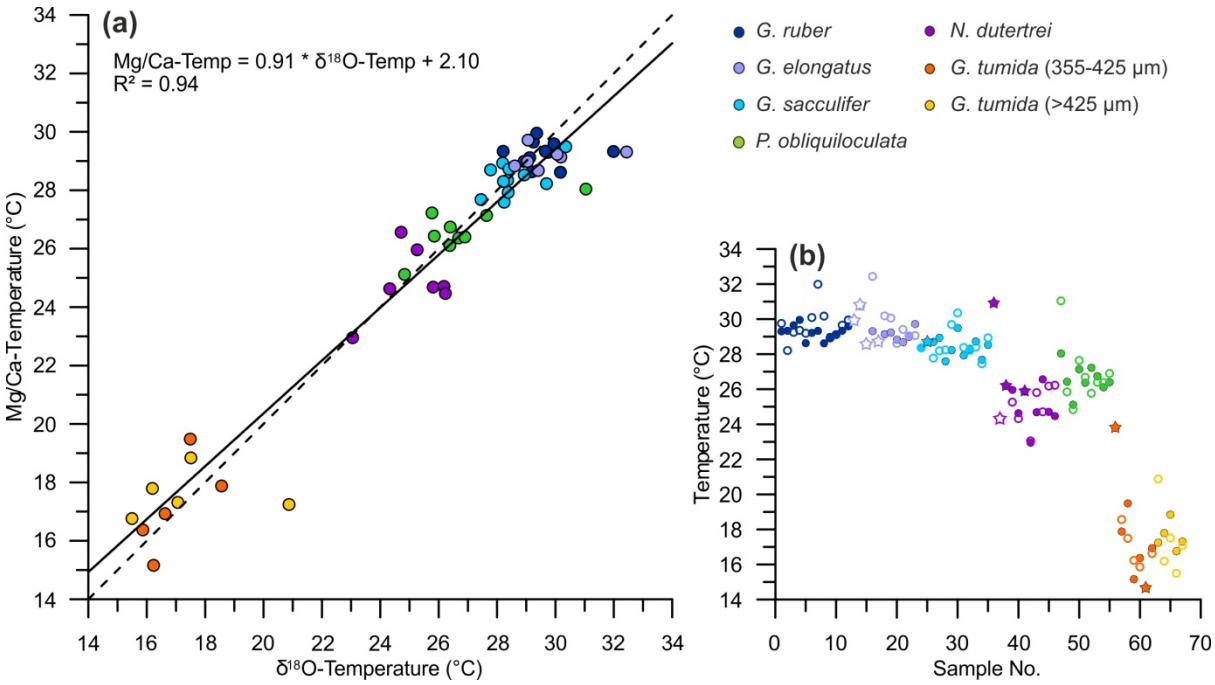

Figure 4.6. Consistency of temperature estimates. (a) Mg/Ca- versus $\delta^{18}O$-derived calcification temperatures. Mg/Ca-temperatures are based on species-specific regressions; $\delta^{18}O$-temperatures were calculated with the equation of *Bemis et al.* [1998]. The black solid line shows the correlation between Mg/Ca- and $\delta^{18}O$-temperatures. For comparison, the 1:1 relationship is shown (stippled line). (b) Comparison of Mg/Ca-temperatures (filled symbols) and $\delta^{18}O$-temperatures (open symbols). Note that (a) includes only samples with paired $\delta^{18}O$ and Mg/Ca measurements, whereas (b) includes all samples where $\delta^{18}O$ or Mg/Ca measurements are available. Samples where only $\delta^{18}O$ or Mg/Ca measurements are available are marked with stars. Sample numbers are related to cores as defined in Table A1.3.

4.5.4. Application of our Mg/Ca-temperature regression

Our species-specific equations were applied to convert Mg/Ca into temperature (Figure 4.7). While our regional Mg/Ca to temperature relations were established on the basis of only samples for which we have $\delta^{18}O$ measurements and thereby direct estimates of foraminiferal calcification depths at the respective core site, we applied the equations to all samples where we measured Mg/Ca ratios (see Table 4.1). Temperatures obtained from *G. ruber* and *G. elongatus* match mixed layer temperatures. Mg/Ca temperatures of *G. sacculifer* correspond to temperatures from the mixed layer bottom and uppermost thermocline. Mg/Ca temperatures calculated from *P. obliquiloculata* and *N. dutertrei* reflect upper and those calculated from *G. tumida* lower thermocline conditions. *P. obliquiloculata* and *N. dutertrei* are most suitable to track changes in NPTW and SPTW since they calcify at water depths corresponding to the core of these water masses.

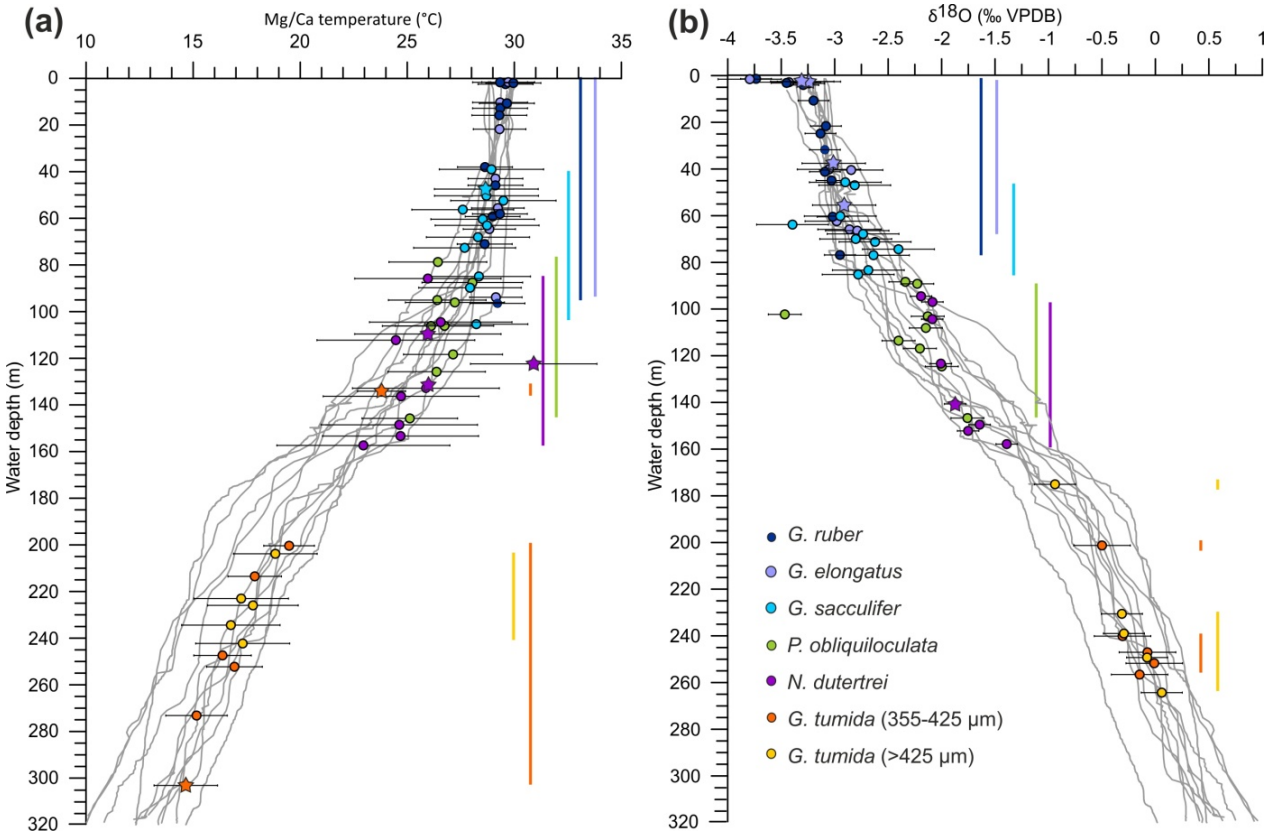

Figure 4.7. (a) Mg/Ca temperatures calculated by applying the newly established species-specific calibrations projected on CTD temperature profiles (gray lines). Horizontal bars denote temperature errors, calculated following the method described in *Mohtadi et al.* [2014]. Colored vertical bars indicate calcification depth ranges resulting from the application of our species-specific Mg/Ca-temperature calibrations. (b) For comparison, we show shell $\delta^{18}O$-derived calcification depth estimates for all species in combination. Gray lines indicate depth profiles of predicted $\delta^{18}Oc$ calculated from CTD casts. Samples where only Mg/Ca or $\delta^{18}O$ measurements are available are marked with stars.

4.6. Conclusions

We presented novel, paired Mg/Ca and $\delta^{18}O$ measurements on multispecies planktic foraminifera tests from accurately dated modern surface sediments in combination with water column data (CTD and $\delta^{18}O_{SW}$) from the WPWP. Based on CTD salinity and $\delta^{18}O_{SW}$, we establish new $\delta^{18}O_{SW}$-salinity regressions for surface (mixed layer) and subsurface (thermocline) waters (NPTW and SPTW) in the WPWP. Our data imply that it is reasonable to apply different $\delta^{18}O_{SW}$-salinity regressions for surface and thermocline water masses. Due to very similar regression lines for the Philippines and PNG areas, individual regressions for sub(surface) waters from both areas can be combined into more robust equations representing the entire study area. These equations are $\delta^{18}O_{SW} = 0.37 * S - 12.4$ for surface and $\delta^{18}O_{SW} = 0.33 * S - 11.0$ for thermocline waters.

Shell $\delta^{18}O$-derived estimates reveal that the calcification depths of planktic foraminifera offshore the Philippines and offshore PNG are very similar. Our estimates match results from other areas, and reveal that also in the WPWP, *G. ruber* and *G. elongatus* reflect mixed layer conditions (0–80 m) and *G. sacculifer* reflects bottom of mixed layer and uppermost thermocline conditions (45–85 m). *P. obliquiloculata* and *N. dutertrei* preserve upper (90–160 m) and *G. tumida* lower thermocline conditions (230–265 m). Hence, our data imply that these species are the best choice to reconstruct thermocline conditions in the WPWP. *N. dutertrei* inhabits a slightly larger depth range than *P. obliquiloculata* in the WPWP. Therefore, *P. obliquiloculata* might be more suitable to reconstruct the upper thermocline. Previous thermocline reconstructions that are based on other species need to be reconsidered in face of the new results. For example, shell $\delta^{18}O$ does not indicate different habitat depths for *G. ruber* and *G. elongatus*. Hence, for the WPWP, the data do not support the use of *G. ruber – G. elongatus* records to reconstruct variations in the vertical structure of the upper water column.

Our newly established regional multispecies Mg/Ca-temperature regression is within the range of published multispecies and species-specific Mg/Ca-temperature calibrations (Mg/Ca = 0.26 exp 0.097 * T as calculated using reduced major axis regression). However, the Mg/Ca temperature relation of most individual species is more accurately described by species-specific calibrations. We find that the regional regressions for *G. ruber*, *G. elongatus* and *G. tumida* are similar to the species-specific or multispecies equations published by *Dekens et al.* [2002] and *Anand et al.* [2003]. Calcification temperatures of *G. sacculifer*, *P. obliquiloculata* and *N. dutertrei* are exceptionally warm in the western tropical Pacific and thus, require regional, species-specific calibrations. The application of previously published calibrations would underestimate the calcification temperatures of these species. Using a reduced major axis regression we calculate the species-specific calibration Mg/Ca = 0.24 exp 0.097 * T for *G. sacculifer* and Mg/Ca = 0.21 exp 0.097 * T for *P. obliquiloculata* and *N. dutertrei*. Nevertheless, further studies are needed to confirm the applicability of these calibrations for the open Pacific Ocean and for paleo-reconstructions.

Acknowledgments

We would like to thank the captains, crews, and the scientific shipboard parties of expeditions SO–228 and RR–1313. We thank Henning Kuhnert, Birgit Meyer-Schack and Ryan Bu for technical assistance. John Southon (UC Irvine) is acknowledged for performing radiocarbon measurements. GeoB sample material was stored, curated and supplied by the GeoB Core Repository at the MARUM – Center for Marine Environmental Sciences, University of Bremen, Germany. RR samples were provided by the Rutgers Core Repository. We thank two anonymous reviewers for their constructive comments, which

helped to improve the quality of our manuscript. The work is funded by the DFG-Research Center / Cluster of Excellence “The Ocean in the Earth System”, the BMBF project 03G0228A (EISPAC) and by the NSF project OCE1131371. The data reported in this paper will be made available on Pangaea (www.pangaea.de) and WDS (www.icsu-wds.org).

Chapter 5.
Variations in Western Pacific Warm Pool surface and thermocline conditions over the past 110,000 years: Forcing mechanisms and implications for the glacial Walker circulation

Martina Hollstein[1], Mahyar Mohtadi[1], Yair Rosenthal[2], Matthias Prange[1], Delia Oppo[3], Gema Martínez Méndez[1], Kazuyo Tachikawa[4], Paola Moffa Sanchez[5], Stephan Steinke[6], Dierk Hebbeln[1]

[1]MARUM – Center for Marine Environmental Sciences, University of Bremen, Bremen, Germany

[2]Institute of Marine and Coastal Sciences, Rutgers, State University of New Jersey, USA.

[3]Department of Geology and Geophysics, Woodshole Oceanographic Institution, Massachusetts, USA

[4]Aix Marseille University, CNRS, IRD, Coll France, CEREGE, Aix-en-Provence, France

[5]School of Earth and Ocean Sciences, Cardiff University, Cardiff, UK

[6]Department of Geological Oceanography, Xiamen University, Xiamen, China

Submitted to *Quaternary Science Reviews*

Abstract

The Western Pacific Warm Pool (WPWP) plays a key role within the global atmospheric and ocean circulation systems. Previous studies suggest that a range of forcing mechanisms influence the WPWP on different timescales. We combine new and published sediment records from offshore Papua New Guinea(PNG) to reconstruct WPWP surface and thermocline conditions over the past 110 kyr. Mg/Ca and oxygen isotope records of surface and thermocline-dwelling planktic foraminifera reflect variations in temperature, thermocline depth and oxygen isotope composition of seawater (δ^{18}Osw) and illustrate the impact of local and remote drivers on the WPWP. Thermocline temperature variations coincide with variations in the Earth's obliquity with warmer temperatures when obliquity is high. This is attributed to variations in subduction and advection of the source waters, namely the South Pacific Tropical Water. The surface δ^{18}Osw displays cyclic variations of precessional duration, likely reflecting rainfall variations with enhanced precipitation under high precession. This pattern is linked to meridional migrations of the Intertropical Convergence Zone (ITCZ). Finally, a decreased surface-thermocline temperature gradient (ΔT) indicates a thermocline deepening during the Last Glacial Maximum (LGM). A compilation of available ΔT records illustrates a dipole-like pattern of LGM thermocline depth anomalies with a shoaling (deepening) in the northern (southern) WPWP. A comparison of the proxy compilation to the output of

Paleoclimate Model Intercomparison Project (PMIP) climate model simulations reveals that the spatial pattern of LGM thermocline depth anomalies is mainly attributable to wind-field anomalies and associated Sverdrup dynamics, and suggests a contraction of the Pacific Walker circulation on its western side during the LGM.

5.1. Introduction

The Western Pacific Warm Pool (WPWP) is a critical element within the global climate and ocean system. It is a major source of heat and moisture to the global atmosphere [e.g. *Gagan et al.*, 2004] with potentially far-reaching climate impacts. Its present climate is linked to the Austral-Asian monsoon system and the seasonally migrating Intertropical Convergence Zone (ITCZ), and other large-scale climate phenomena, such as the El Niño–Southern Oscillation (ENSO), which affects climate worldwide. In addition, the equatorial current system of the WPWP links the equatorial Pacific Ocean to the Indonesian Throughflow, which is an important component of the global ocean circulation [e.g. *Gordon*, 1986].

Due to its significant influence on global climate and ocean conditions, over the past years a growing body of studies have focused on the reconstruction of past WPWP climate and ocean dynamics. Previous studies proposed that the long-term climate variability and ocean dynamics of the WPWP are influenced by a range of factors, such as variations in the state of ENSO and the Walker circulation [e.g. *Bolliet et al.*, 2011; *Sagawa et al.*, 2012], changes in the Austral-Asian monsoon system and the Hadley circulation [e.g. *Dang et al.*, 2012; *Tachikawa et al.*, 2011], and a possible remote effect of southern hemisphere mid and high latitudes [e.g. *Rosenthal et al.*, 2013] in response to various forcing mechanisms.

Astronomical forcing and changing glacial–interglacial boundary conditions impact WPWP climate and ocean dynamics. The Earth's orbital precession controls the seasonal distribution of the incoming solar radiation in the northern and southern hemisphere tropics. It therefore has a strong influence on the latitudinal position of the ITCZ and the Austral-Asian monsoon and may affect the WPWP hydroclimate through interhemispheric alternating rainfall variations with high (low) precipitation in the southern hemisphere when precession is high (low) [e.g. *Merlis et al.*, 2013]. Accordingly, proxy records indicated that the rainfall around Papua New Guinea (PNG) is stronger (weaker) when precession is high (low) [e.g. *Dang et al.*, 2015; *Tachikawa et al.*, 2011]. Records from Indonesia and numerical simulations suggest that the WPWP hydroclimate is additionally controlled by complex changes in the Walker circulation that might be directly tied to insolation or to glacial–interglacial boundary conditions [*Cheng et al.*, 2012 and references therein].

The impact of obliquity (the Earth's axial tilt) on the WPWP is elusive. Obliquity only has a very small influence on low-latitude insolation. Nonetheless, various records from the tropical Pacific include a strong 41-kyr signal [e.g. *Beaufort et al.*, 2001; *de Garidel-Thoron et al.*, 2005; *Lea et al.*, 2000]. During the Holocene many temperature records from the tropical Pacific and Indian Ocean show a cooling, which has been related to the remote influence of insolation changes at mid- and high-latitudes [e.g. *Rosenthal et al.*, 2013; *Rosenthal et al.*, 2017]. Numerical studies additionally indicate a more direct influence of obliquity on tropical Pacific climate via reorganizations in the Hadley circulation [*Bosmans et al.*, 2015; *Mantsis et al.*, 2011; *Mantsis et al.*, 2014]. This is supported by proxy records, which indicate enhanced (decreased) rainfall over PNG when obliquity is low (high) [*Liu et al.*, 2015].

On glacial–interglacial timescales, changing boundary conditions such as atmospheric CO_2, extent of ice sheets in northern high latitudes and sea level additionally control the climate and ocean conditions in the WPWP, probably affecting both, Hadley and Walker circulation. Due to its global influence and consequences on the society, understanding past variations in the state and activity of ENSO raise particular interest of the scientific community. However, proxy records and numerical models that focus on past variations in the Walker circulation and the state of ENSO provide conflicting evidence for both a weaker Walker circulation and more El Niño-like conditions (or an enhanced ENSO activity) [e.g. *Koutavas et al.*, 2002; *Sadekov et al.*, 2013; *Sagawa et al.*, 2012] or a stronger Walker circulation and more La Niña-like conditions (or a reduced ENSO activity) [e.g. *Andreasen and Ravelo*, 1997; *Ford et al.*, 2015; *Zhu et al.*, 2017] during the Last Glacial Maximum (LGM).

Many previous reconstructions focus on the LGM, the deglaciation and/or the Holocene, and thus limit a comprehensive view on the driving forces and mechanisms that control climate and ocean conditions in the WPWP. Thermocline reconstructions are particularly sparse, thus limiting our understanding of the links between the WPWP thermocline and extratropical climate variability, and their influence on the equatorial Pacific climate. The state of the thermocline is also closely linked to the prevailing climate conditions. For example, variations in ENSO and the Pacific Walker circulation affect the depth and tilt of the thermocline leading to a thermocline shoaling (deepening) during El Niño (La Niña). Conversely, thermocline waters and conditions potentially influence equatorial surface ocean conditions and ENSO [e.g. *Gu and Philander*, 1997] and might therefore have a direct impact on the WPWP climate conditions.

Here, we present surface and thermocline records from offshore PNG (Figure 5.1), which span the past 110 kyr to reconstruct surface and thermocline conditions in the WPWP over the last glacial–interglacial cycle. Specifically, we combined new and published Mg/Ca and $\delta^{18}O$ records of the planktic foraminifera *Globigerinoides ruber* and *Pulleniatina obliquiloculata* from cores GeoB17419-1 and MD05-2920 [*Tachikawa et al.*, 2014] to estimate the past evolution of surface and thermocline temperatures and the

oxygen isotope composition of seawater ($\delta^{18}O_{SW}$). Moreover, we calculated the difference between SST and thermocline temperatures (ΔT), which allows reconstructing variations in the vertical structure of the upper water column. We discuss potential forcing mechanisms for changes in WPWP thermocline depth and use available PMIP (Paleoclimate Model Intercomparison Project) climate model output to infer features of the glacial tropical atmosphere circulation from the LGM thermocline structure.

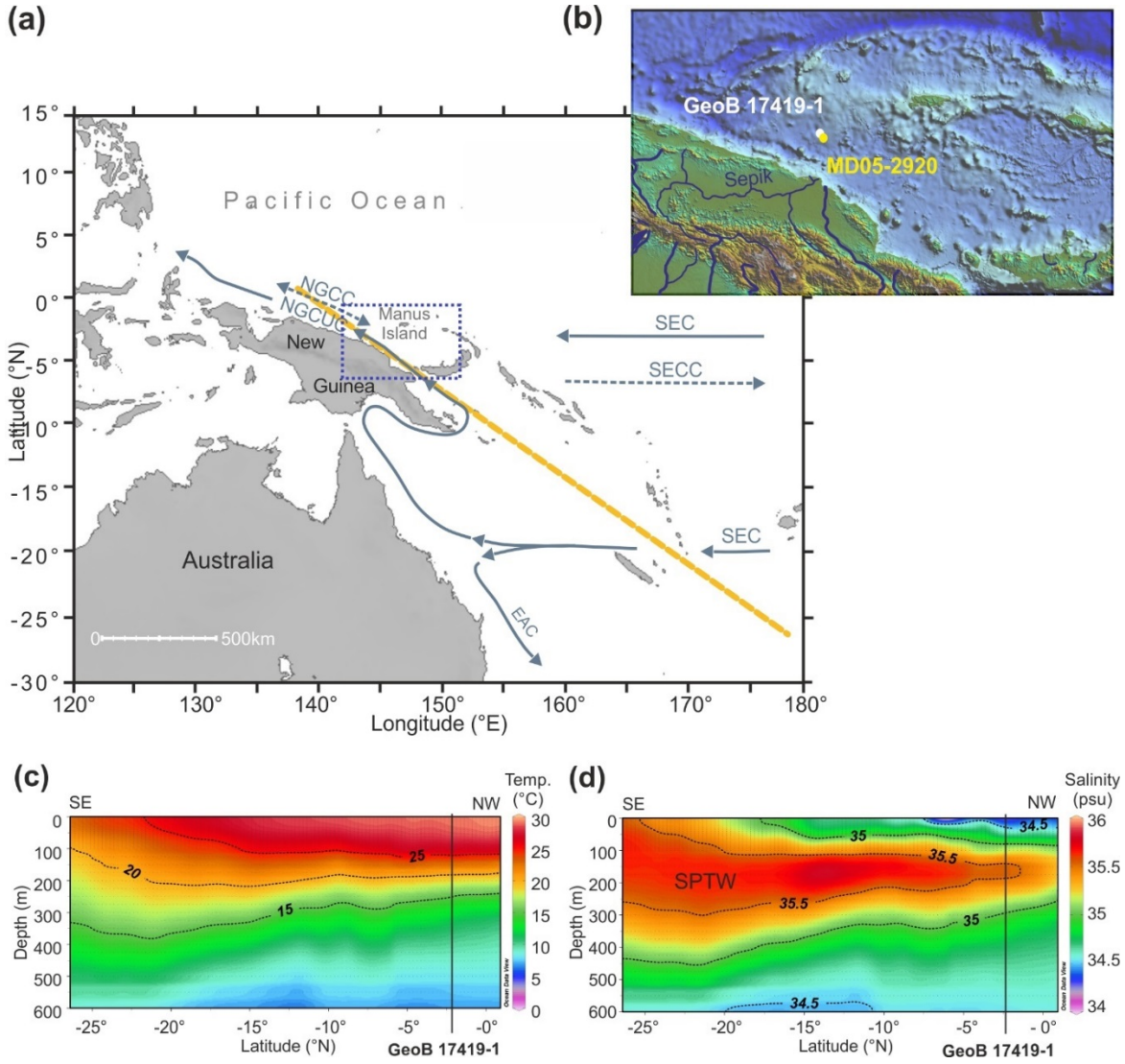

Figure 5.1. (a) Schematic map of the study area. Dashed and solid arrows indicate surface and subsurface currents, respectively. SEC – South Equatorial Current, SECC – South Equatorial Counter Current, NGCC – New Guinea Coastal Current, NGCUC – New Guinea Coastal Undercurrent, EAC – East Australian Current. The blue stippled rectangle denotes a close-up of the study area presented in (b). The yellow stippled line indicates the location of the temperature and salinity sections shown in (c) and (d). (b) Bathymetric map of the study area. White and yellow dots show the positions of cores GeoB 17419-1 (this study) and MD05-2920 [*Tachikawa et al.*, 2014]. (c) Temperature and (d) salinity sections along the profile indicated on the map (yellow line). Vertical black bars mark the latitude of site GeoB 17419-1. Temperature and salinity data are from WOA13 [*Locarnini et al.*, 2013; *Zweng et al.*, 2013]. The sections were created with the Ocean data view software [*Schlitzer*, 2014]. Note that the thermocline is influenced by the high salinity South Pacific Tropical Water (SPTW).

5.2. Study area

The core site GeoB 17419-1 is located in the center of the WPWP offshore PNG, approximately 100–150 km offshore the Sepik River mouth. Sea surface temperatures (SST) within the study area exceed 28°C year-round and sea surface salinity varies around 34.0–34.5 psu (Figure 5.2) [*Carton and Giese*, 2008; *Locarnini et al.*, 2013; *Zweng et al.*, 2013]. The mixed layer is between 50 and 100 m deep [*Locarnini et al.*, 2013].

The seasonal climate is controlled by the Austral-Asian monsoon, which is connected to the migration of the ITCZ and associated precipitation patterns. During the southeast monsoon season (austral winter), southeast winds dominate and the ITCZ is located to the north of the equator. During the northwest monsoon season (austral summer) winds reverse and the ITCZ is located to the south of the equator, which leads to increased precipitation over the study area and PNG (Figure 5.2a). Average seasonal variations in surface temperature and salinity are very small and within the range of 1–2 °C for temperature and below 1 psu for salinity (Figure 5.2) [*Carton and Giese*, 2008; *Locarnini et al.*, 2013; *Zweng et al.*, 2013]. Nonetheless, increased (decreased) precipitation over the Sepik catchment area generally goes along with a decrease (increase) in sea surface salinity in the study area (Figures 5.2 and A2.3). Seasonal variations in winds lead to only minor changes in the thermal stratification of the upper water column [*Carton and Giese*, 2008]. On interannual timescales, the regional climate is influenced by ENSO. The state of ENSO affects surface and particularly thermocline ocean conditions as well as the vertical structure of the water column. El Niño (La Niña) is characterized by cooler (warmer) sub(surface) temperatures, a shallower (deeper) thermocline at the core site and drier (wetter) conditions (Figure 5.2). According to the SODA dataset, interannual SST variations do not exceed 2–3 °C, while thermocline temperatures vary up to 7–8 °C [*Carton and Giese*, 2008]. Thermocline depth anomalies in the study area are in the order of several tens of meters. For example, the 20°C isotherm, often used as an indicator for the thermocline depth in the WPWP, varied up to 40 m in relation to ENSO between 1986 and 1998 [*Harrison and Vecchi*, 2001]. Interannual rainfall variations do not have a clear influence on salinity at the core site (Figure 5.2). Overall, regional rainfall and salinity variations are dominated by seasonal variations, while temperature and thermocline depth variations are mainly ENSO controlled.

The thermocline waters within the study area are marked by high salinity with a maximum around 35.5 psu that characterizes the South Pacific Tropical Water (SPTW). The SPTW is produced by subduction of surface waters within the South Pacific subtropical Gyre [e.g. *Qu et al.*, 2013; *Tsuchiya et al.*, 1989] and transported into the study area within the regional sub(surface) circulation system (Figure 5.1). The (sub)surface circulation is dominated by the westward flowing South Equatorial Current (SEC) and by western boundary currents that flow equatorward along the northern east coast of Australia and New

Guinea (Figure 5.1). The core sites are located within the flow path of the New Guinea Coastal Current (NGCC) and the New Guinea Coastal Undercurrent (NGCUC). Driven by trade winds, the NGCC underlies seasonal reversals flowing westward along the coast of PNG during austral winter and eastward during austral summer. The NGCUC does not reverse seasonally, but the westward flow is weaker during austral summer [e.g. *Cresswell*, 2000; *Kuroda*, 2000].

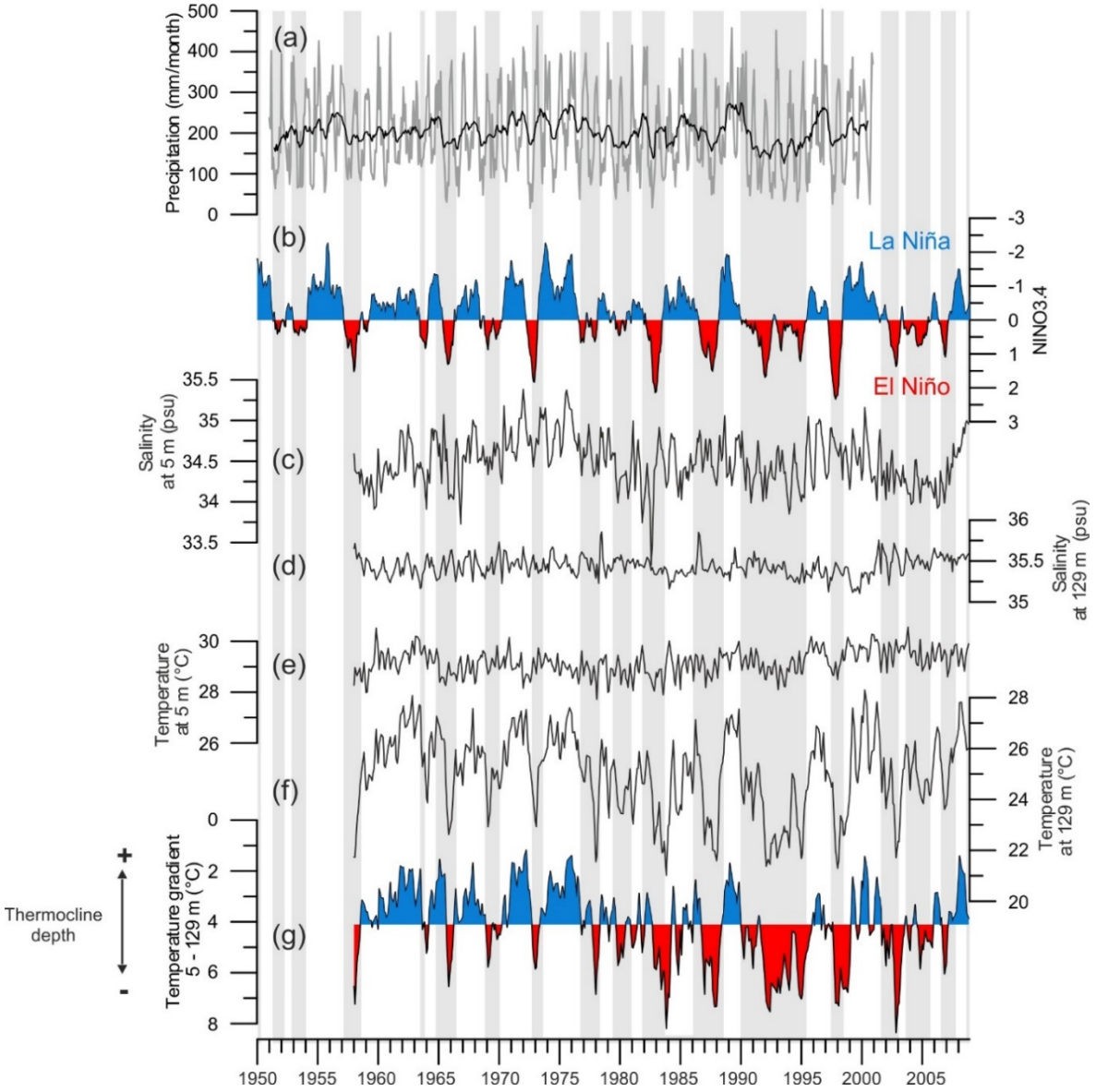

Figure 5.2. Monthly climatology of the study area. (a) Monthly precipitation rate above the catchment area of the Sepik River (gray) (143.50 – 144.50 °E, 3.50 – 4.50 °S) [*Beck et al.*, 2005] with an 11-point running mean (black). (b) Niño3.4 index (http://www.cpc.ncep.noaa.gov/data/indices/). (c, d) Surface (5 m) and thermocline (129 m) salinity and (e, f) temperature at the study site from SODA 2.1.6 at 144.25 °E and 2.25 °S [*Carton and Giese*, 2008]. (g) Difference between surface and subsurface temperatures used as an indicator for thermocline depth. Gray bars indicate El Niño periods. Note that rainfall and salinity variations are dominated by seasonal variations, while temperature and thermocline depth variations are mainly ENSO controlled.

5.3. Material and methods

5.3.1. Material

Gravity core GeoB 17419-1 was retrieved during R/V *Sonne* cruise SO–228 offshore PNG (2.81 °S, 144.50 °E, 1883 m water depth, 914 cm length) [*Mohtadi et al.*, 2013]. Samples for geochemical analyses were taken at 4 cm intervals throughout the core. All samples were freeze dried, washed over 150 µm sieves and dried. Since the core site is located well above the modern position of the calcite lysocline (at about 3300 m water depth [see *Berger et al.*, 1982 and references therein]) the carbonate preservation is expected to be good.

Our reconstructions are based on proxy records of benthic and planktic foraminifera. The benthic foraminifera *Cibicides wuellerstorfi* $\delta^{18}O$ record is used to establish the age model of core GeoB 17419-1 in addition to radiocarbon dates in planktic foraminifera. *G. ruber* is used as an indicator for surface, and *P. obliquiloculata* for upper thermocline conditions. The choice of species is based on $\delta^{18}O$-derived calcification depth estimates for site GeoB 17419-1, which indicate that *G. ruber* calcifies within the upper 60 m of the water column (mixed layer) and *P. obliquiloculata* inhabits the depth range between 110 and 150 m (upper thermocline) [*Hollstein et al.*, 2017]. Previous studies indicate that both species calcify perennially in the study area [*Kawahata et al.*, 2002; *Yamasaki et al.*, 2008].

For our study, we generated new Mg/Ca and $\delta^{18}O$ records of *P. obliquiloculata* of core GeoB 17419-1. Additionally, we measured the $\delta^{18}O$ of the surface-dwelling planktic foraminifera *G. ruber*. We then combined the surface $\delta^{18}O$ and the thermocline Mg/Ca record with the published Mg/Ca-based SST record of MD05-290 [*Tachikawa et al.*, 2014] to estimate the surface $\delta^{18}O_{SW}$ and surface-thermocline ΔT, respectively. Core MD05-2920 is located in close proximity to GeoB 17419-1. Coherent variations of Ti/Ca records of the two cores provide confidence that the Mg/Ca and $\delta^{18}O$ records can be combined (appendix A2.1).

5.3.2. Age model

Between 6 and 414 cm core depth, the age model of GeoB 17419-1 is based on 26 accelerator mass spectrometry (AMS) ^{14}C ages (Table 5.1). Radiocarbon ages were measured either on *G. sacculifer* or on mixed *G. ruber, G. elongatus* and *G. sacculifer* samples. The measurements were performed at the Keck Carbon Cycle Accelerator Mass Spectrometry Laboratory at the University of California, Irvine (UCI). The age-depth relation was modelled with a Bayesian approach using the software BACON R 2.2 [*Blaauw and Christen*, 2011]. Radiocarbon ages were converted to calendar ages using the Marine13 calibration curve [*Reimer et al.*, 2013] and applying a local reservoir age correction of $\Delta R = 70 \pm 60$ yrs [*McGregor et al.*, 2008]. We used the default settings of BACON, with the following adjustments: We decreased the memory (*mem.mean = 0.4*) to increase the flexibility of the age-depth model, section

thickness was set to *res = 2*, to calibrate the dates, we used a student-t distribution with 9 degrees of freedom (*t.a = 9, t.b = 10*). However, due to the high amount of radiocarbon ages, differences between age-depth relations computed with varying parameter settings are negligible. A total of 10000 Monte-Carlo runs (*ssize = 10000*) were extracted to calculate mean ages and uncertainties for each sample. The age uncertainty given as 95% confidence interval ranges between 145 and 1365 yrs.

Table 5.1. AMS-^{14}C ages and calibrated calendar ages of core GeoB 17419-1 as well as tie points used to construct the age model of GeoB 17419-1. For the radiocarbon dated part of the core weighted mean ages are given as estimated by the BACON run.

Lab-ID	Sample depth (cm)	Foraminifera species	^{14}C age ± 1σ error (years BP)	Cal. age (years BP)	95% confidence interval (years)
142706	6	*G. sacculifer*	1515 ± 20	1033	246 – 1117
156177	14	*G. ruber + G. sacculifer*	2385 ± 25	1923	1727 – 2115
150149	38	*G. sacculifer*	4505 ± 20	4607	4378 – 4810
142707	58	*G. sacculifer*	6395 ± 20	6788	6640 – 6931
142708	58	*G. sacculifer*	6365 ± 20	6788	6640 – 6931
150150	66	*G. sacculifer*	7235 ± 20	7260	6982 – 7568
150151	74	*G. sacculifer*	6625 ± 20	7391	7138 – 7711
156178	82	*G. ruber + G. sacculifer*	7415 ± 25	7724	7468 – 7956
156179	90	*G. ruber + G. sacculifer*	8810 ± 25	9266	9009 – 9525
156180	98	*G. ruber + G. sacculifer*	9245 ± 25	9975	9740 – 10193
146301	106	*G. ruber + G. sacculifer*	9490 ± 30	10304	10138 – 10448
156181	114	*G. ruber + G. sacculifer*	9530 ± 25	10512	10354 – 10688
156182	122	*G. ruber + G. sacculifer*	10880 ± 35	12210	11754 – 12583
156183	130	*G. ruber + G. sacculifer*	11520 ± 30	12928	12723 – 13143
150152	138	*G. sacculifer*	11900 ± 30	13365	13177 – 13553
156184	142	*G. ruber + G. sacculifer*	12270 ± 30	13634	13433 – 13850
156185	148	*G. ruber + G. sacculifer*	12730 ± 30	14191	13927 – 14564
146302	156	*G. ruber + G. sacculifer*	13175 ± 40	15059	14724 – 15315
156203	164	*G. ruber + G. sacculifer*	13565 ± 40	15646	15378 – 15905
156186	172	*G. ruber + G. sacculifer*	13705 ± 35	15986	15754 – 16194
156187	180	*G. ruber + G. sacculifer*	13760 ± 35	16218	16026 – 16421
150153	192	*G. sacculifer*	14730 ± 45	17276	16751 – 17682
146303	208	*G. ruber + G. sacculifer*	16145 ± 45	18909	18475 – 19210
156188	228	*G. ruber + G. sacculifer*	16990 ± 50	20035	19696 – 20343
146304	256	*G. ruber + G. sacculifer*	19060 ± 60	22471	22099 – 22757
156189	268	*G. ruber + G. sacculifer*	19600 ± 60	23147	22855 – 23470
150154	288	*G. sacculifer*	20290 ± 100	24052	23690 – 24409
146940	308	*G. ruber + G. sacculifer*	21760 ± 160	25575	25001 – 26051
146941	356	*G. ruber + G. sacculifer*	26210 ± 260	29769	28922 – 30561
146942	412	*G. ruber + G. sacculifer*	30340 ± 440	33568	32249 – 34563
-	748	-	-	66000	-
-	836	-	-	87000	-
-	904	-	-	110000	-

Below 414 cm the age model is based on visual correlation of the benthic $\delta^{18}O$ (*C. wuellerstorfi,* see section 5.3.4 for details on isotope measurements) to the global benthic stack LR04 [*Lisiecki and Raymo*, 2005]. The correlation was done with the software AnalySeries 1.6 [*Paillard et al.*, 1996]. We defined tie points at the core bottom, which is associated with the onset of Marine Isotope Stage (MIS) 5c and at maxima in $\delta^{18}O$ associated with MIS 5b and MIS 4 (Table 5.1, Figure 5.3). Between the tie points set to correlate the $\delta^{18}O$ records, the chronology was inferred by linear interpolation. To extend the gravity core GeoB 17419-1 to present, we use $\delta^{18}O$ and Mg/Ca values measured on the core top of the multi core (MUC) GeoB 17419-2, which was retrieved at the same location as the gravity core. The core top is radiocarbon dated and reflects modern ocean conditions [*Hollstein et al.*, 2017]. All ages are given in calendar years before present (BP).

Since we combine temperature and $\delta^{18}O$ records from GeoB 17419-1 with the published SST record of MD05-2920 to calculate a surface $\delta^{18}O_{SW}$ and ΔT, having thorough age models for both cores is critical. We therefore revised the age model of MD05-2920 and used Ti/Ca elemental ratios that were measured in high resolution in both cores to validate the age models (see appendix A2.1).

5.3.3. X-Ray Fluorescence (XRF) core scanner analyses

Ti and Ca intensities in GeoB 17419-1 were measured with an X-Ray Fluorescence (XRF) Core Scanner at the MARUM, University of Bremen, Germany. Data were collected every 2 cm down-core over a 1.2 cm^2 area with a down-core slit size of 10 mm using generator settings of 10 kV, a current of 0.02 mA, and a sampling time of 20 seconds directly at the split core surface of the archive half with XRF Core Scanner III (AVAATECH Serial No. 12). Prior to core scanning, the split core surface was covered with a 4 µm thin SPEXCerti Prep Ultralene1 foil to avoid contamination of the XRF measurement unit and desiccation of the sediment. The data have been acquired by a Canberra X-PIPS Silicon Drift Detector (SDD; Model SXD 15C-150-500) with 150eV X-ray resolution, the Canberra Digital Spectrum Analyzer DAS 1000 and an Oxford Instruments 100W Neptune X-ray tube with rhodium (Rh) target material. Raw data spectra were processed by the Analysis of X-ray spectra by Iterative Least square software (WIN AXIL) package from Canberra Eurisys.

5.3.4. Isotope, Mg/Ca and Nd/Ca analyses

In order to establish an age model for core GeoB17419-1 (section 5.3.2) we measured the oxygen isotope composition ($\delta^{18}O$) of the benthic foraminifera *C. wuellerstorfi* (size fraction 250–425 µm). For reconstructing $\delta^{18}O_{SW}$ we measured $\delta^{18}O$ of the planktic foraminifera *G. ruber* (size fraction 250–355 µm) and *P. obliquiloculata* (size fraction 355–425 µm). Identification of *G. ruber* followed the species concept of *Aurahs et al.* [2011]. Hence, only individuals which were previously referred to as *G. ruber* s.s. were included.

Isotope analyses were performed at MARUM, University of Bremen on Finnigan MAT 251 mass spectrometers with Kiel I or Kiel III devices. Isotope values were calibrated against the international Vienna Pee Dee Belemnite (VPDB) standard. The internal carbonate standard is a Solnhofen Limestone, which is calibrated to the National Bureau of Standards (NBS) 19 standard. The long-term analytical precision was better than ± 0.07‰. Replicate measurements on 10% of the samples indicate an average standard deviation of 0.12‰ for *G. ruber* (n = 22) and 0.14‰ for *P. obliquiloculata* (n = 22). As an indicator for surface water stratification we calculate differences between the $\delta^{18}O$ of *G. ruber* and *P. obliquiloculata* ($\Delta\delta^{18}O$).

We measured Mg/Ca ratios on *P. obliquiloculata* for reconstructing the thermocline conditions and Nd/Ca to estimate variations in continental precipitation above PNG. For our measurements, we used about 20 specimens of *P. obliquiloculata* per sample. Foraminifera tests were weighed to estimate a potential influence of test dissolution on the Mg/Ca records and gently crushed to open the chambers. We applied a full trace metal cleaning including a reductive step [*Boyle and Keigwin*, 1985] as modified by *Rosenthal et al.* [1997] and *Rosenthal et al.* [1999]. The cleaned samples were dissolved in 0.065N HNO_3. After centrifuging the samples for 10 min at 10000 rpm, the solution was diluted with 0.5 N HNO_3. The final calcium concentration of the samples averaged 5.5 mM (between 1.0 and 9.7 mM). The samples were analyzed at Rutgers University, New Jersey using a Thermo Fisher/Finnigan Element XR sector-field inductively coupled mass spectrometer (ICP-MS). Measured ratios were blank corrected. The long term reproducibility of the data, drift and matrix effects were controlled by repeated measurements of in house consistency standards [*Rosenthal et al.*, 1999]. The long-term precision of the instrument was about of ± 1% and <2.5% for Mg/Ca and Nd/Ca, respectively. All Mg/Ca ratios are given in mmol/mol, Nd/Ca is reported in µmol/mol. Replicates indicate a sample reproducibility of ± 0.3 mmol/mol for Mg/Ca (n = 22). We monitored the cleaning efficacy by measuring Al/Ca, Fe/Ca and Mn/Ca alongside with Mg/Ca. None of these ratios co-vary with Mg/Ca. Thus, we assume that the Mg/Ca ratios are not affected by contaminant phases. Mg/Ca values do not correlate to shell normalized weights (Figure A2.2), suggesting that shell Mg/Ca is not substantially affected by carbonate dissolution.

To convert the Mg/Ca ratios of *P. obliquiloculata* to temperature, we applied the species-specific equation established for the modern WPWP by [*Hollstein et al.*, 2017]:

$$Mg/Ca = 0.21 \exp 0.097 * T \qquad (5.1)$$

For the surface, we used the published Mg/Ca-based temperature record on mixed *G. ruber* and *G. elongatus* (previously referred to as *G. ruber* s.s. and s.l., respectively) from the nearby core site MD05-2920 [*Tachikawa et al.*, 2014] (see appendix 2 details). To estimate the oxygen isotope composition of

seawater ($\delta^{18}O_{SW}$) from Mg/Ca-based temperatures and shell $\delta^{18}O$ of *G. ruber* and *P. obliquiloculata*, we applied the high-light $\delta^{18}O$-temperature equation of *Bemis et al.* [1998]:

$$T(°C) = 14.9 – 4.8 (\delta^{18}O – \delta^{18}O_{SW}) \qquad (5.2)$$

The resulting values were converted to Vienna Standard Mean Ocean Water (VSMOW) by adding 0.27‰ [*Hut*, 1987] and corrected for changes in global ice volume following *Waelbroeck et al.* [2002].

In order to track changes in the stratification of the upper water column, we calculate the difference between *G. ruber* and *P. obliquiloculata*-based temperatures (ΔT). Since Mg/Ca and $\delta^{18}O$ of *G. ruber* are from different cores (MD05-2920 and GeoB 17419-1), the age scales of the relevant records were aligned prior to the calculation of $\delta^{18}O_{SW}$ and ΔT. To this end, we linearly resampled the relevant records on intervals of 500 years using the software AnalySeries [*Paillard et al.*, 1996].

The estimation of temperature and $\delta^{18}O_{SW}$ uncertainties followed the conservative approach described in *Mohtadi et al.* [2014] and is based on propagation of uncertainties introduced by Mg/Ca and $\delta^{18}O$ measurements (see previous sections), the Mg/Ca-temperature calibration (equation 5.1) and/or the $\delta^{18}O$-temperature equation (equation 5.2) as well as the global ice volume estimate (± 0.09‰) [*Waelbroeck et al.*, 2002]. We also estimated the uncertainties of the already published surface temperatures to calculate uncertainties in ΔT. Here, the mean external reproducibility as reported by *Tachikawa et al.* [2014] was assumed as uncertainty estimate for Mg/Ca. Estimates of $\Delta\delta^{18}O$ and ΔT uncertainties are based on propagation of $\delta^{18}O$ and temperature uncertainties. Resulting temperature uncertainties average about 1 °C for SST, 2 °C for thermocline temperatures and about 2 °C for ΔT. For $\delta^{18}O_{SW}$ uncertainties average 0.3‰ for the surface and 0.5‰ for the thermocline.

5.4. Results

5.4.1. Benthic $\delta^{18}O$ and age model

Benthic $\delta^{18}O$ (*C. wuellerstorfi*) reveals that core GeoB 17419-1 covers the last 110 kyr (Figure 5.3). The average temporal resolution of the records is about 0.5 kyr/sample. The record is characterized by glacial–interglacial variations representing Marine Isotope Stages (MIS) with higher $\delta^{18}O$ values during MIS 2 and 4 and lower values during MIS 1, 3 and 5 (Figure 5.3). The substages MIS 5a, b and c are clearly recognizable (Figure 5.3).

To estimate changes in temperature and local $\delta^{18}O_{SW}$ we corrected the record for changes in global ice volume following *Waelbroeck et al.* [2002]. During MIS 5 the ice volume corrected $\delta^{18}O$ ($\delta^{18}O_{IVC}$) fluctuates between 2.6 and 3.0‰. During MIS 4 the $\delta^{18}O_{IVC}$ slightly increases to values around 3.2‰. During MIS 3 the record is characterized by oscillations of millennial duration. During MIS 2 $\delta^{18}O_{IVC}$

varies around 3.1‰ before it exhibits an abrupt decrease of about 1.4‰ starting at 16.9 ka. The decrease is interrupted by a plateau that lasts from around 15.6 to 12.6 ka.

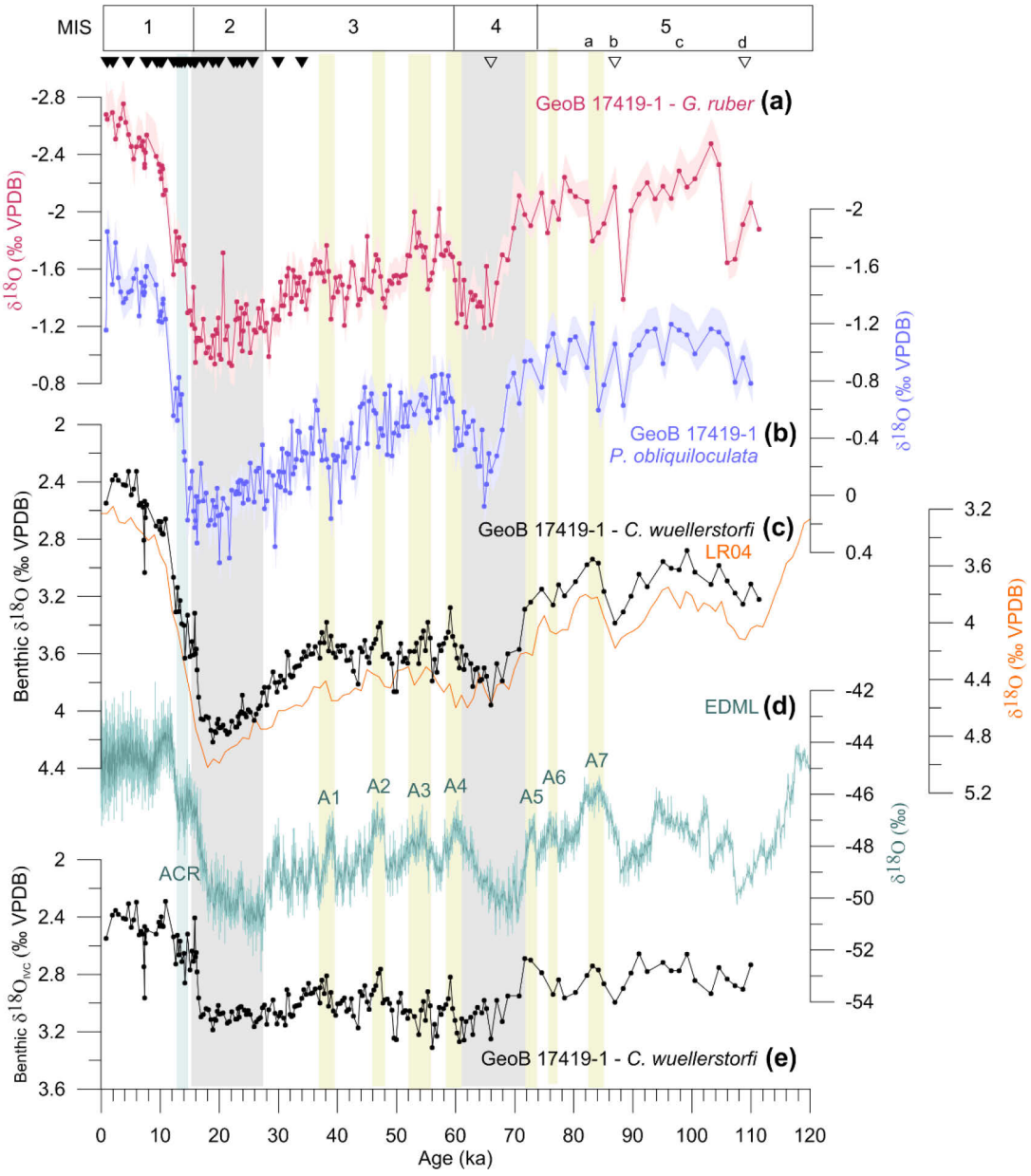

Figure 5.3. Planktic and benthic $\delta^{18}O$ and age model of core GeoB 17419-1. Shell $\delta^{18}O$ of *G. ruber* (a) and *P. obliquiloculata* (b). Shadings represent 1σ-uncertainties (see section 5.3.4). (c) Benthic $\delta^{18}O$ of GeoB 17419-1 (black line) compared to the LR04 benthic $\delta^{18}O$ stack of *Lisiecki and Raymo* [2005] (orange line). (d) EDML ice core $\delta^{18}O$ on the AICC12 chronology [*Bazin et al.*, 2013]. (e) Ice volume corrected benthic $\delta^{18}O$ of GeoB 17419-1. Filled and open triangles indicate radiocarbon dates of GeoB 17419-1 and tie points to LR04, respectively. Marine isotopes stages (MIS) 1–5 as dated by *Sanchez Goñi and Harrison* [2010] are indicated at the top. Gray shadings mark MIS 2 and 4. Yellow and blue shadings mark Antarctic millennial events A1 to A7 and the Antarctic Cold Reversal (ACR) as indicated by the EDML record.

5.4.2. Planktic $\delta^{18}O$ and Mg/Ca temperatures

Shell $\delta^{18}O$ of *G. ruber* varies between −2.75 and −0.92‰ (Figure 5.3a), $\delta^{18}O$ of *P. obliquiloculata* varies between -1.84 and 0.47‰ (Figure 5.3b). Both records follow the MIS and show $\delta^{18}O$ maxima during MIS 2 and minima during the Holocene.

The shell Mg/Ca record of *P. obliquiloculata* varies between 1.63 and 3.57 mmol/mol, which converts into temperatures of ~21.1 and 28.4 °C (Figure 5.4b). Minimum temperatures (21.1 °C) occur during MIS 4, maximum temperatures (28.4 °C) during the early Holocene. With ~25.1°C, modern temperatures are only slightly warmer than during the LGM (~24.2 °C) and temperatures during MIS 3–4 and MIS 5a–d are comparable. The record indicates slightly increasing temperatures during MIS 5c and declining temperatures during MIS 5a, interrupted by a single data point that marks cooler temperatures during MIS 5b. The interval between 69.8 and 65.2 ka (within MIS 4) is marked by cool temperatures averaging 22.2 °C. Then the record depicts an abrupt temperature increase of about 2–3 °C that is followed by a declining trend until approximately 30 ka. Afterwards, temperatures rise to maximal values of ~28.4 °C during the early Holocene (~10.5 ka). The warming trend is interrupted by a temperature plateau during the LGM. The Holocene is characterized by a cooling trend of about 2 to 2.5 °C. The ΔT record (*G. ruber* - *P. obliquiloculata*) shows a stepwise decreasing trend towards the LGM and an increase afterwards (Figure 5.4c). Maximal values up to ~5.0 °C are measured between 110 and 65–66 ka. Coeval with the abrupt warming indicated by *P. obliquiloculata* at 65/66 ka, the ΔT estimates reveal a decrease with an amplitude of 3.2 °C. ΔT remains relatively constant during MIS 3 and reaches minimum values averaging ~1.3 °C during MIS 2. Afterwards it increases towards the present.

The *G. ruber* $\delta^{18}O_{SW}$ record is characterized by high frequency oscillations with values ranging between −0.09 and 1.00‰ (Figure 5.4d). *G. ruber* indicates exceptionally low $\delta^{18}O_{SW}$ from 74 to 66 ka and from about 28 to 18 ka. The $\delta^{18}O_{SW}$ of *P. obliquiloculata* ranges between 0.14 and 2.05‰ (Figure 5.4e). The record depicts glacial–interglacial variations with lower (higher) values during interglacial (glacial) periods, superimposed by higher frequency oscillations.

Figure 5.4. Mg/Ca derived temperature and $\delta^{18}O_{SW}$ records of core GeoB17419-1. For comparison we also show the sea surface temperature record of MD05-2920 [*Tachikawa et al.*, 2014] that was used to estimate the surface $\delta^{18}O_{SW}$ and ΔT. (a) Sea surface temperature estimates of MD05-2920 on a revised age scale. (b) Thermocline temperature estimates from GeoB 17419-1. The dark blue line shows the bandpass-filtered thermocline temperature signal (see section 5.5.2). The gray solid line indicates variations in the Earth's obliquity [*Laskar*, 1990]. (c) Surface-thermocline temperature gradient (ΔT*; G. ruber* − *P. obliquiloculata*). (d) Surface $\delta^{18}O_{SW}$ calculated from *G. ruber*-based temperatures of MD05-2920 and and $\delta^{18}O$ of GeoB17419-1. (e) *P. obliquiloculata*-based thermocline $\delta^{18}O_{SW}$ of GeoB17419-1. Triangles depict dating points of GeoB 17419-1 (black) and MD05-2920 (gray). Shadings represent 1σ-uncertainties (see section 5.3.4). Black dots reflect modern conditions as indicated by core top data from the multi core GeoB 17419-2 [*Hollstein et al.*, 2017]. Marine Isotope stages (MIS) 1–5 as dated by *Sanchez Goñi and Harrison* [2010] are indicated at the top. Gray shadings additionally indicate MIS 2 and 4.

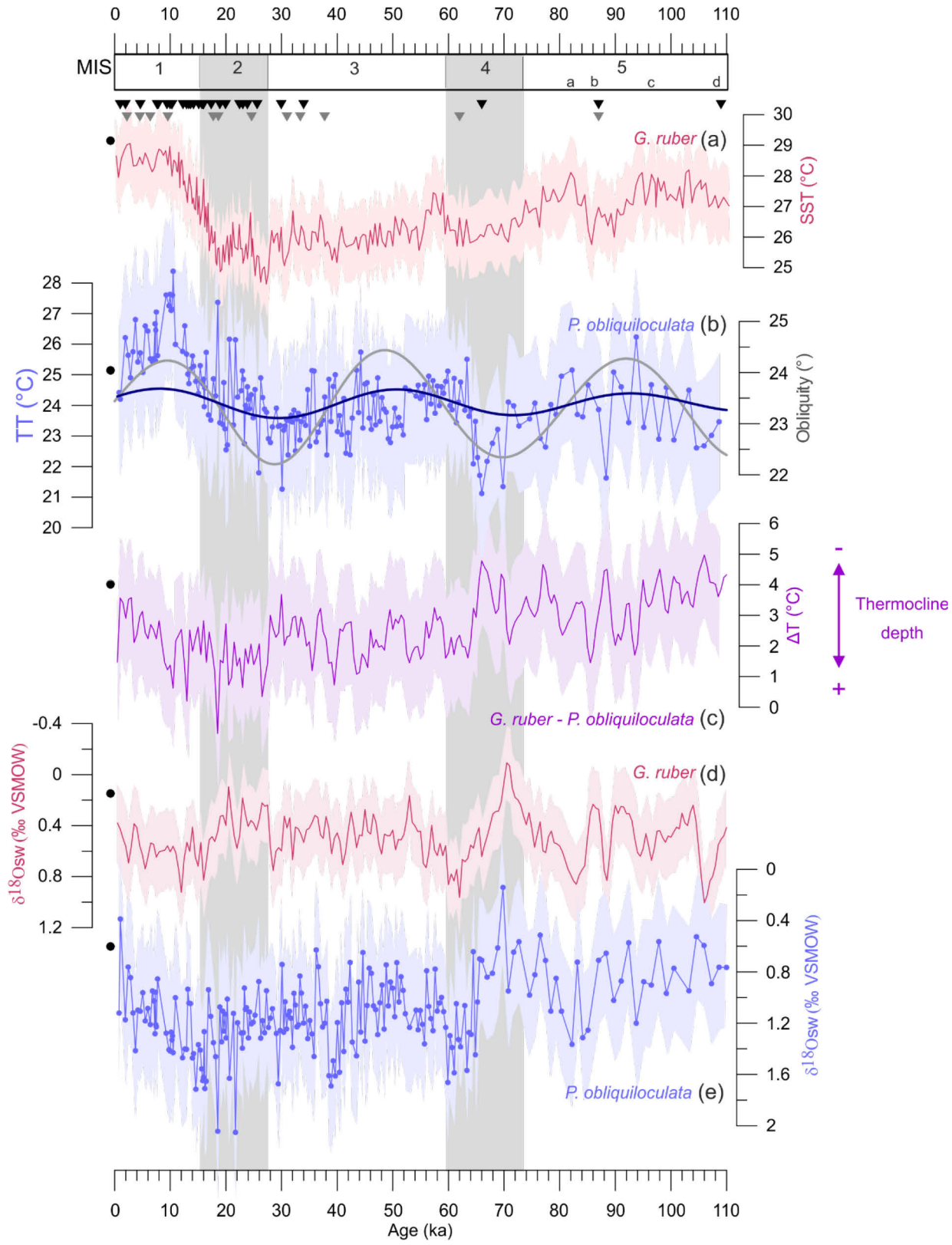
MIS
1
2
3
4
5
a
b
c
d
G. ruber (a)
SST (°C)
P. obliquiloculata (b)
TT (°C)
Obliquity (°)
ΔT (°C)
Thermocline depth
G. ruber - P. obliquiloculata (c)
G. ruber (d)
P. obliquiloculata (e)
δ18Osw (‰ VSMOW)
Age (ka)

5.5. Discussion

5.5.1. Southern Ocean influence on West Pacific deep waters

The benthic $\delta^{18}O$ record exhibits variations similar to those of $\delta^{18}O$ in Antarctic ice cores and appears to resolve Antarctic warm events A1 to A7 as well as the Antarctic cold reversal (Figure 5.3). Today, site GeoB 17419-1 is bathed by Pacific Deep Water (PDW), which is ultimately fed by waters coming from the Southern Ocean [e.g. *Bostock et al.*, 2010]. We thus infer that changes in the benthic $\delta^{18}O$ at this site reflect changes in $\delta^{18}O_{SW}$ and/or temperature of the Southern Ocean, where the source waters of PDW originate. Deviations between the peaks of our benthic $\delta^{18}O$ record and EDML are likely due to uncertainties in the age model. Note that, for the radiocarbon-dated part of the record, we did not apply age corrections to account for the travel time of the deep water from the Southern Ocean to the WPWP.

In the $\delta^{18}O_{IVC}$ record, the events A4 to A1 are marked by peaks of decreasing $\delta^{18}O_{IVC}$ with amplitudes of 0.28 to 0.49‰. During the deglaciation, $\delta^{18}O_{IVC}$ decreased by about 0.7‰. These magnitudes are consistent with estimates reported earlier by *Saikku et al.* [2009] and *Stott et al.* [2007] on the basis of benthic $\delta^{18}O$ of core MD98-2181 located in the northern WPWP. Assuming that the changes in $\delta^{18}O_{IVC}$ were solely related to temperature, the AA events during MIS 3 would be characterized by a warming of between 1.0 and 2.5 °C (depending on the $\delta^{18}O$-temperature equation chosen) and the deglaciation by a warming of 2.6 to 3.3 °C.

5.5.2. Obliquity-controlled variations of WPWP thermocline temperatures

The Mg/Ca-derived thermocline temperature record of GeoB17419-1 depicts quasi-cyclic variations, which appear to co-vary with variations in Earth's obliquity. Visual inspection indicates that *P. obliquiloculata* records higher (lower) temperatures during periods of increased (decreased) obliquity (Figure 5.4b). For example, the exceptionally early onset of deglacial warming (starting around 30 ka) reflected by the *P. obliquiloculata* temperature estimates are unlikely to be due to changes in the glacial–interglacial boundary conditions but coincides with an increase in obliquity. In addition, the record indicates a 2 to 2.5 °C cooling of thermocline temperatures throughout the Holocene, which is coeval with a decrease in obliquity. Such a Holocene cooling trend was already observed in other thermocline temperature records from the western Pacific and Indonesian seas [e.g. *Bolliet et al.*, 2011; *Dang et al.*, 2012; *Rosenthal et al.*, 2013].

We filtered the temperature record with a Gaussian band-pass filter centered at a frequency of 0.02439 ± 0.007 (corresponding to periods of 31.5 – 58.6 kyr) (Figure 5.4b) to emphasize cyclic variations on the obliquity band of 41 kyr within the temperature record. Filtering was done with Astrochron (R package for astrochronology) [*Meyers*, 2014]. The specific shape of the resulting curve (amplitude and exact phase) varies with the chosen filter parameters. However, independent of the parameters the filtered signal co-

varies with obliquity. Additionally, we performed a spectral analysis to assess the statistical significance of cyclic variations on the obliquity band. In order to exclude long-term (glacial–interglacial) variations from the spectral analysis we eliminated frequencies below 0.018 kyr^{-1} from the temperature record. The spectral analysis was performed with REDFIT [*Schulz and Mudelsee*, 2002]. The results confirm that the thermocline temperature record is characterized by cyclic variations that correspond to the periodicity of obliquity (Figure 5.5a). The power spectrum depicts a statistically significant peak at a frequency of 0.024 kyr^{-1}, which corresponds to a period of 41 kyr. We thus infer that obliquity has a significant impact on WPWP thermocline temperatures. This is also in accordance with modeling studies, which demonstrate that an increase (decrease) in obliquity leads to a warming (cooling) of tropical Pacific subsurface temperatures [*Lee and Poulsen*, 2005; *Mantsis et al.*, 2011].

Variations in the Earth's obliquity only have a very small influence on low-latitude insolation, and neither SSTs of MD05-2920 [see also *Tachikawa et al.*, 2014] nor ΔTs between GeoB 17419-1 and MD05-2920 show a dominating influence of obliquity (Figure A2.3). Thus, we suggest that obliquity-related thermocline temperature fluctuations are caused by remote forcing on southern mid-latitude climate variations. Most likely a warming (cooling) of thermocline waters at the core site during periods of increased (decreased) obliquity is caused by a reduced (intensified) ventilation and advection of the SPTW [*Lee and Poulsen*, 2005]. Similar mechanisms have been proposed earlier to explain the temperature drops observed in many Holocene records from the WPWP and the Indonesian Seas [*Dang et al.*, 2012; *Rosenthal et al.*, 2013; *Rosenthal et al.*, 2017]. Indeed, numerical simulations indicate a weakening of subtropical trades and mid-latitude westerlies that is associated with a reduction in meridional (equator-pole) insolation and surface pressure gradients during periods of increased obliquity and which causes a weakening of the subtropical gyre circulation [*Lee and Poulsen*, 2005; *Mantsis et al.*, 2011; *Timmermann et al.*, 2014]. A weakening in the subtropical gyre circulation could diminish both, the subduction and advection of relatively cool waters from the subtropical Pacific and the heat export from the tropical Pacific and thus, lead to a warming of subsurface temperatures in the WPWP [*Lee and Poulsen*, 2005; *Mantsis et al.*, 2011; *Qu et al.*, 2013].

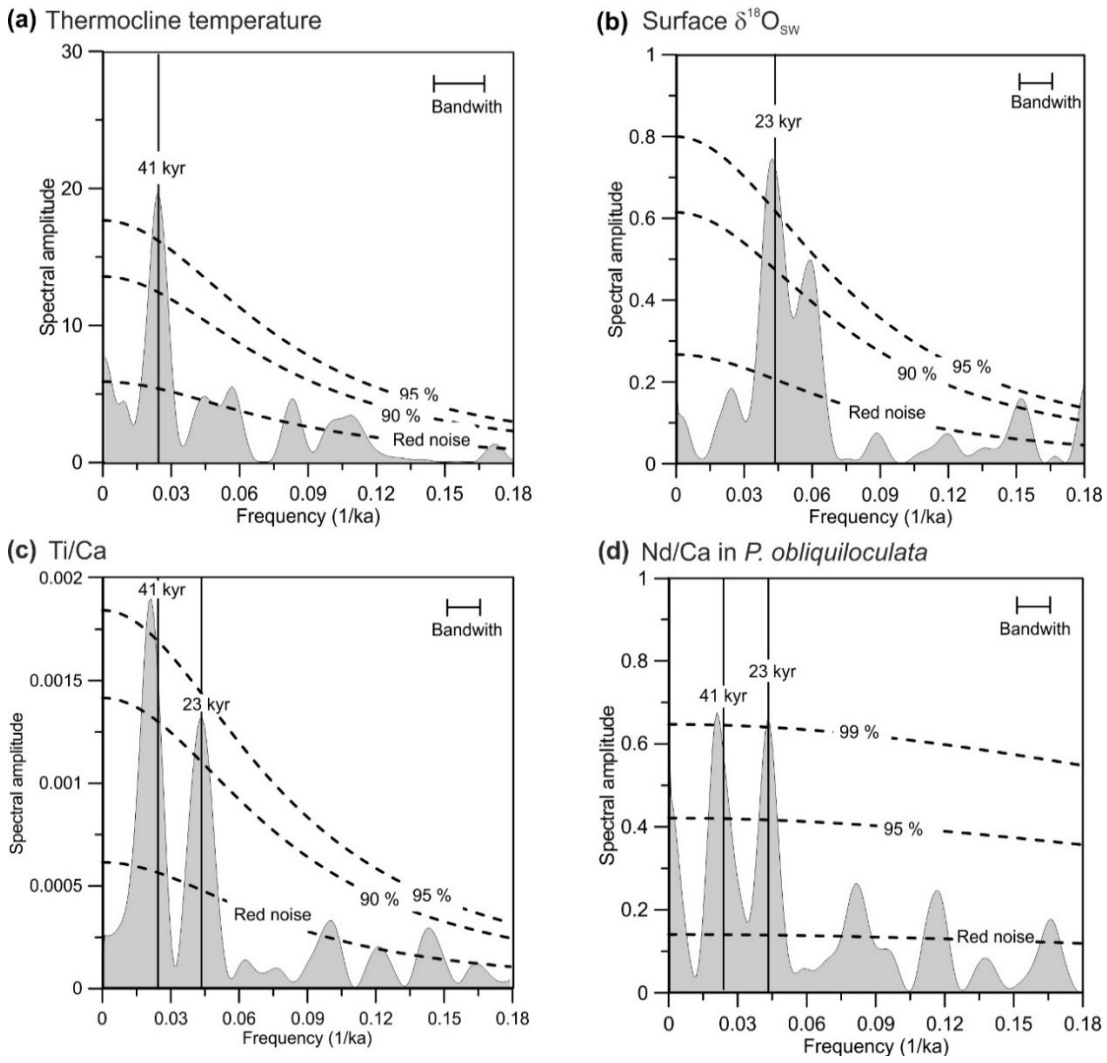

Figure 5.5. Spectral analysis of thermocline temperature (a), surface $\delta^{18}O_{SW}$ (b), Ti/Ca (c) and *P. obliquiloculata* Nd/Ca (d) of GeoB 17419-1 and MD05-2920. The analyses were performed with REDFIT [*Schulz and Mudelsee*, 2002]. An oversampling factor of 9 was chosen to increase the resolution of samples frequencies. The bandwidth is 6 dB. We used a Welch type spectral window. Dashed lines indicate the red-noise spectrum as well as 90 and 95% confidence levels. Solid vertical lines denote frequencies that correspond to obliquity (41 kyr) or precession (23 and 19 kyr) periodicities.

Numerical modeling simulations provide conflicting results regarding how far the equatorial atmospheric and ocean circulation systems are affected by these processes. However, they consistently show that the warming observed in the WPWP thermocline during periods of high obliquity does not penetrate to the sea surface [*Lee and Poulsen*, 2005; *Mantsis et al.*, 2011]. This is in agreement with the SST and ΔT records from MD05-2920 and GeoB17419-1, which, as noted above, do not show dominant variations at the obliquity periodicity. It is however possible that obliquity-related thermocline temperature anomalies in upwelling areas reach the sea surface. In addition, many Holocene temperature records from the Indonesian Seas and the eastern Indian Ocean show a Holocene cooling trend as it is observed in our

thermocline record [see compilations by *Linsley et al.*, 2010; *Rosenthal et al.*, 2013; *Rosenthal et al.*, 2017]. Previously, the gradual cooling during the Holocene observed in thermocline temperature records from the Timor Sea has been related to an intensification of a cool thermocline-dominated ITF [e.g. *Xu et al.*, 2008]. Opposing this view, we suggest that the temperature signal observed in records from the Indonesian Seas and the ITF outflow area originates in the western Pacific Ocean [see also *Dang et al.*, 2012].

5.5.3. Precession-controlled variations in regional precipitation

The *G. ruber* $\delta^{18}O_{SW}$ reveals cyclic variations with low (high) $\delta^{18}O_{SW}$ corresponding to precession maxima (minima) (Figure 5.6a). A spectral analysis performed with REDFIT [*Schulz and Mudelsee*, 2002] confirms that the record is dominated by cyclic variations on the precession band (Figure 5.5b). The power spectrum depicts a statistically significant peak at a frequency of 0.042 kyr^{-1}, which matches the precession periodicity of 23 kyr.

We interpret variations in $\delta^{18}O_{SW}$ to be primarily controlled by variations in the amount of precipitation within the marine environment. A time series of $\delta^{18}O_{SW}$ data from Manus Island (PNG, Figure 5.1) shows that variations in the oxygen isotopic composition of seawater closely correlate with variations in salinity, evaporation and precipitation with lower $\delta^{18}O_{SW}$ corresponding to less saline conditions, but enhanced evaporation and precipitation, and vice versa [*Conroy et al.*, 2017] indicating that $\delta^{18}O_{SW}$ in the study area is predominantly controlled by local precipitation. Continental precipitation over PNG and river runoff could additionally influence the $\delta^{18}O_{SW}$ record, since the sites GeoB 17419-1 and MD05-2920 are located in close proximity to the Sepik river mouth (Figure 5.1) [see also *Tachikawa et al.*, 2011]. A provenance study based on the composition of Rare Earth Elements in bulk sediments of MD05-2920 and a nearby core showed that the terrigenous fraction of these cores are dominated by river particles from the Sepik and Ramu river systems [*Tachikawa et al.*, 2011]. Moreover, precipitation over PNG and salinity at the study site are in general agreement (see Figures 5.2 and A2.4). We hence infer that the observed variations in surface $\delta^{18}O_{SW}$ are primarily driven by variations in local precipitation and potentially also influenced by river runoff from PNG. Nonetheless, we cannot fully exclude that source effects and/or variations in oceanic advection or upwelling have an additional influence on the surface $\delta^{18}O_{SW}$ at the study site. We will address this issue further below.

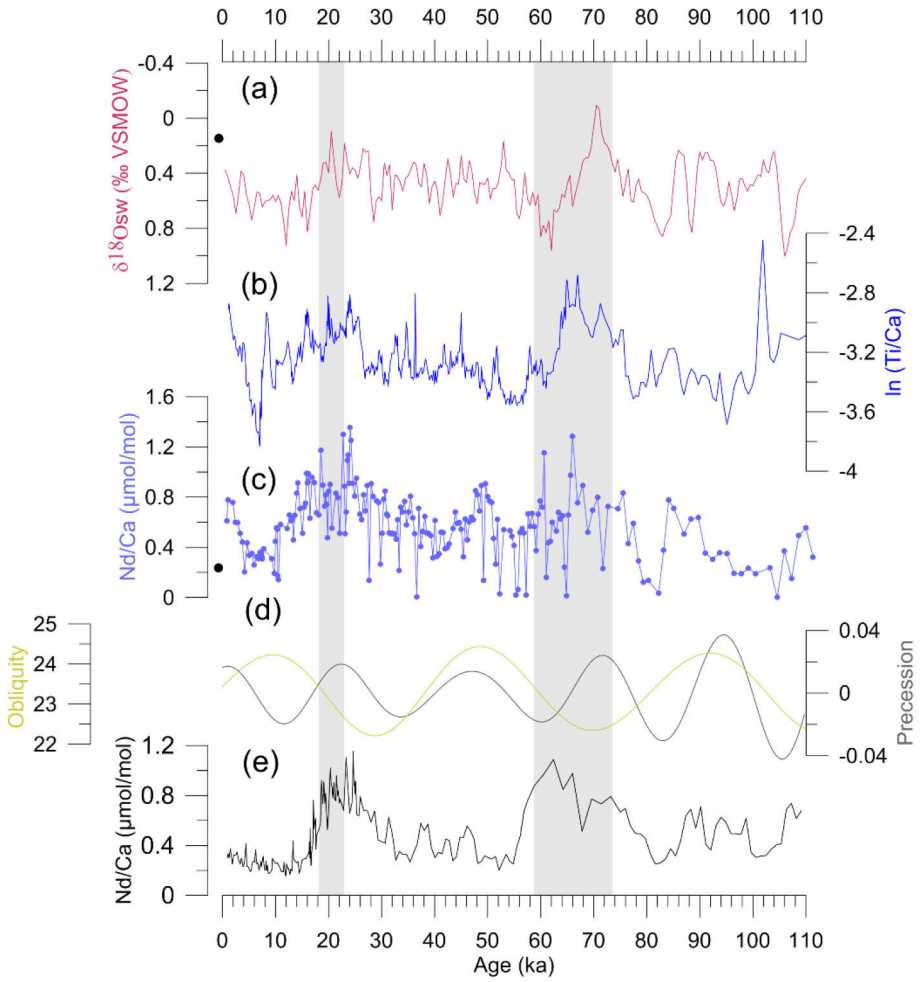

Figure 5.6. Comparison of WPWP precipitation records. (a) *G. ruber* $\delta^{18}O_{SW}$, (b) ln(Ti/Ca), (c) *P. obliquiloculata* Nd/Ca of GeoB 17419-1 and (e) *G. ruber* Nd/Ca record of MD05-2925 [*Liu et al.*, 2015]. (d) Variations in the Earth's obliquity (yellow) and orbital precession (gray) [*Laskar*, 1990]. Black dots reflect modern conditions as indicated by core top data from the multi core GeoB 17419-2 [*Hollstein et al.*, 2017]. Gray shadings mark MIS 2 and 4.

Modern precipitation over the study area is mainly controlled by the Austral-Asian monsoon system and the seasonal migration of the ITCZ. Enhanced precipitation is recorded during the northwest monsoon season in austral summer, when the ITCZ is located to the south of the equator above PNG. An increase in precipitation is therefore most probably linked to a shift in the position of the ITCZ, an intensification of its rainfall intensity [*Merlis et al.*, 2013], and potentially by an increase of the Austral-Asian monsoon during periods of increased precession. Presently, with precession being near its maximum, seasonal variations in salinity are relatively small (below 1 psu, Figure A2.4) [*Carton and Giese*, 2008; *Zweng et al.*, 2013]. Assuming a constant $\delta^{18}O_{SW}$-salinity relation of $\delta^{18}O_{SW} = 0.37*S - 12.4$ [*Hollstein et al.*, 2017], salinity must have been up to about 2 psu higher during the last precession minimum to account for the observed $\delta^{18}O_{SW}$ increase in our record. As mentioned, changes in the isotopic composition of rainfall caused by shifts in the source area, and variations in oceanic advection or upwelling could influence the

surface $\delta^{18}O_{SW}$ at the study site. As we assume that the water vapor, over the past glacial–interglacial cycle, has been constantly sourced from the nearby ocean, associated variations in the $\delta^{18}O_{SW}$ are expected to be negligible. In analogy to seasonal changes observed in the modern ocean, the NGCC would be expected to strengthen when precession is low, and the core sites would be more strongly affected by freshwater from PNG. Precession-related alterations in oceanic advection would thus counteract the precession signal observed in the $\delta^{18}O_{SW}$ record. Likewise, the effect of wind-driven upwelling would counteract the observed signal. If upwelling affected the core site, it is expected to be stronger, when precession is high. We therefore assume that the $\delta^{18}O_{SW}$ record predominantly reflects rainfall variations.

To assess past variations in continental rainfall, we additionally use Ti/Ca ratios in GeoB 17419-1 as well as Nd/Ca ratios that were measured along with Mg/Ca on *P. obliquiloculata* samples of GeoB 17419-1 (Figure 5.6). As discussed in detail in *Tachikawa et al.* [2011], element ratios such as Ti/K or Ti/Ca in core MD05-2920 reflect past rainfall variations over PNG and continental runoff, and indicate that rainfall above PNG predominantly varies in response to precession. The Ti/Ca record of GeoB 17419-1 is in close correlation to the Ti/Ca record of MD05-2920 and thus shows comparable variations (Figures 5.6 and A2.1). High (low) Ti/Ca ratios indicate an increased (decreased) terrigenous input and reflect enhanced (decreased) precipitation over PNG when precession is high (low). A spectral analysis confirms that the Ti/Ca varies on the precession band (Figure 5.5c). A similar pattern is also observed in Nd/Ca (Figures 5.5d and 5.6). Most likely, Nd is delivered by fine particles originating from PNG. Elevated Nd concentrations are reported within the Bismarck Sea downstream the Sepik River [*Grenier et al.*, 2013]. Provenance studies consistently indicate that increased particulate concentrations of REEs in the western equatorial Pacific are river-derived [*Sholkovitz et al.*, 1999; *Tachikawa et al.*, 2011]. We therefore assume enhanced Nd concentrations to be associated with increased precipitation and Sepik River discharge from PNG. However, an additional dust input of Nd from volcanic sources is possible [*Grenier et al.*, 2013]. Nd particles could either be incorporated into the foraminifera tests within the water column [*Liu et al.*, 2015; *Martínez-Botí et al.*, 2009] or added as secondary calcite overgrowth on the foraminifera tests after deposition [*Roberts et al.*, 2012, Rosenthal, unpublished data; *Tachikawa et al.*, 2013]. Taken together, the Ti/Ca and Nd/Ca records reflect an increase (decrease) in terrigenous runoff from PNG when precession is high (low) suggesting an intensification (reduction) of the Austral-Asian monsoon during these periods. Our reconstruction is in agreement with previous proxy-based and numerical modeling studies that indicate an overriding control of precession on the tropical monsoon system, the position of the ITCZ, and ultimately on precipitation over PNG [*Dang et al.*, 2015; *Kutzbach et al.*, 2008; *Liu et al.*, 2015; *Tachikawa et al.*, 2011]. Evidence for precession-induced migrations of the ITCZ also comes from speleothem records from caves in eastern China that indicate increased (decreased) precipitation when precession is low (high) [see e.g. *Cheng et al.*, 2012; *Wang et al.*, 2014].

Recent modeling studies suggest that obliquity exerts an additional influence on tropical Pacific precipitation via reorganizations of the Hadley circulation [*Bosmans et al.*, 2015; *Mantsis et al.*, 2011; *Mantsis et al.*, 2014; *Rachmayani et al.*, 2016]. More specifically, the studies proposed that high obliquity corresponds to a weakening in the zonal mean Hadley circulation and a reduced ITCZ rainfall intensity. An obliquity control on PNG precipitation is also supported by a record of Nd/Ca measured on *G. ruber* from a core off southern PNG [*Liu et al.*, 2015], and by modeling studies that indicate less precipitation over PNG during periods of high obliquity [*Mohtadi et al.*, 2016].

In consistency with this, our Ti/Ca and Nd/Ca records show a significant obliquity influence with low Ti/Ca and Nd/Ca corresponding to high obliquity and vice versa (Figure 5.6). This is also confirmed by spectral analyses. Both records depict statistically significant peaks on the obliquity band (Figure 5.5c,d). However, the surface $\delta^{18}O_{SW}$ record does not reflect significant variations at the obliquity frequency. This divergence either indicates a decoupling between continental and oceanic rainfall, or secondary effects on the Ti/Ca and Nd/Ca records on the obliquity band. For Ti/Ca, the obliquity-related variability could be attributed to variations in the carbonate contribution [*Tachikawa et al.*, 2011]. Similarly, variations in the carbonate contribution could also affect the Nd/Ca ratios of *P. obliquiloculata* from GeoB 17419-1. In addition, the Ti/Ca and Nd/Ca variations could be caused by obliquity-driven variations in the strength of the NGCC and NGCUC. As explained in section 5.5.2, the NGCC and NGCUC, and hence the transport of Ti and Nd particles to the core site, might have been weaker during periods of high obliquity. It appears therefore likely, that the obliquity-driven variations in Ti/Ca and Nd/Ca of GeoB 17419-1 are caused by secondary effects.

5.5.4. Glacial thermocline depth and implications for the Pacific Walker circulation

Variations in the ΔT (*G. ruber – P. obliquiloculata*) are interpreted as changes in the thermocline depth with a large (small) ΔT corresponding to a shallow (deep) thermocline [*Bolliet et al.*, 2011; *Steinke et al.*, 2010; *Xu et al.*, 2008]. Our ΔT record reflects a stepwise thermocline deepening at the core location towards the LGM and a shoaling afterwards (Figure 5.4c). During the last interglacial period (MIS 5) the thermocline was relatively shallow. The strong decrease in ΔT starting around 66–65 ka indicates a deepening of the thermocline during MIS 4. The LGM is characterized by a minimum in ΔT indicating the weakest thermal stratification during the past 110 kyr. From the LGM until the present an increasing ΔT denotes a gradual thermocline shoaling. However, the apparent glacial–interglacial variability is superimposed by other variations. The beginning of MIS 4 for instance is characterized by a very shallow thermocline, and during the early Holocene, the thermocline is as deep as during MIS 3. This is reasonable because variations in ΔT are associated with both variations in surface and thermocline temperatures, and are thus not only controlled by glacial–interglacial boundary conditions but presumably also by obliquity, which has a strong influence on the thermocline temperature record (see section 5.5.2.), and by precession,

which has a clear influence on the surface temperature record [*Tachikawa et al.*, 2014]. As inferred from $\delta^{18}O_{SW}$ of *P. obliquiloculata*, the thermocline deepening coincides with more saline conditions within the upper thermocline (Figure 5.4b and e).

Previously published reconstructions from the western equatorial Pacific and Indian Ocean based on a wide range of proxies show an inconsistent pattern indicating either a thermocline deepening [e.g. *Andreasen and Ravelo*, 1997; *Patrick and Thunell*, 1997] or shoaling [e.g. *Leech et al.*, 2013; *Regoli et al.*, 2015; *Sagawa et al.*, 2012] during the LGM. To analyze the spatial pattern of thermocline depth anomalies during the LGM relative to the present we compile ΔT records from the WPWP (Table A2.1 and Figure A2.5). We exclusively use Mg/Ca-based ΔT records as this proxy has been shown to be a robust indicator of relative thermocline depth (TCD) in previous studies [e.g. *Mohtadi et al.*, 2017]. This way we also avoid potential discrepancies associated with the use of different proxies. The compilation of the hitherto available proxy records illustrates a dipole-like pattern with a LGM thermocline shoaling in the northern WPWP [*Sagawa et al.*, 2012], no change within the equatorial WPWP [*Ford et al.*, 2015] and a deepening in the southern WPWP (this study) (Figure 5.7a). We do not include the ΔT records published by *de Garidel-Thoron et al.* [2007], *Regoli et al.* [2015] and *Seo et al.* [2016], because these records are all based on foraminifera species that presumably calcify within the mixed layer [*Hollstein et al.*, 2017]. The ΔT record of MD06-3067 (from offshore Mindanao) [*Bolliet et al.*, 2011] has to be considered with caution, since it does not cover the late Holocene.

We compared the reconstructed LGM thermocline depth pattern with the output of 14 available PMIP2 and PMIP3/CMIP5 climate model simulations of the LGM [*Braconnot et al.*, 2007; *Harrison et al.*, 2015]. All models consider LGM boundary conditions, such as reduced greenhouse gas concentrations, altered astronomical parameters and ice sheet extent. The specifications of the individual models are provided in the appendix (Table A2.2). We identify MRI-CGCM3 as the only model that captures the asymmetric TCD anomaly pattern that we inferred from the ΔT records (Table A2.2). In this model, changes in vertical temperature gradients are close to the reconstructed values at the core sites (Figure 5.7a). The TCD anomaly pattern is to a large extent attributable to glacial wind-field anomalies (Figure 5.7b and c) and associated Sverdrup dynamics [*DiNezio et al.*, 2011; *Leech et al.*, 2013], through which the western Pacific TCD becomes a function of wind stress and curl, integrated from the eastern side of the basin towards west. A large region of positive wind-stress curl in the southeastern equatorial Pacific (Figure 5.7d) creates Ekman convergence, which sets the stage for an overall deepening of the thermocline in the glacial tropical Pacific south of the equator. Regions of glacial wind-stress anomalies with an easterly component in the tropical West Pacific (Figure 5.7b) further tend to deepen the thermocline there. In addition, particularly large glacial thermocline deepening off the coast of New Guinea, which also affects the TCD at site GeoB 17419-1, is favored by strong along-shore southeasterly wind anomalies (Figure

5.7b). Glacial thermocline shoaling in the northern tropical West Pacific is associated with strong westerly wind-stress anomalies and a positive anomalous wind-stress curl north of about 10 °N (Figure 5.7b and d).

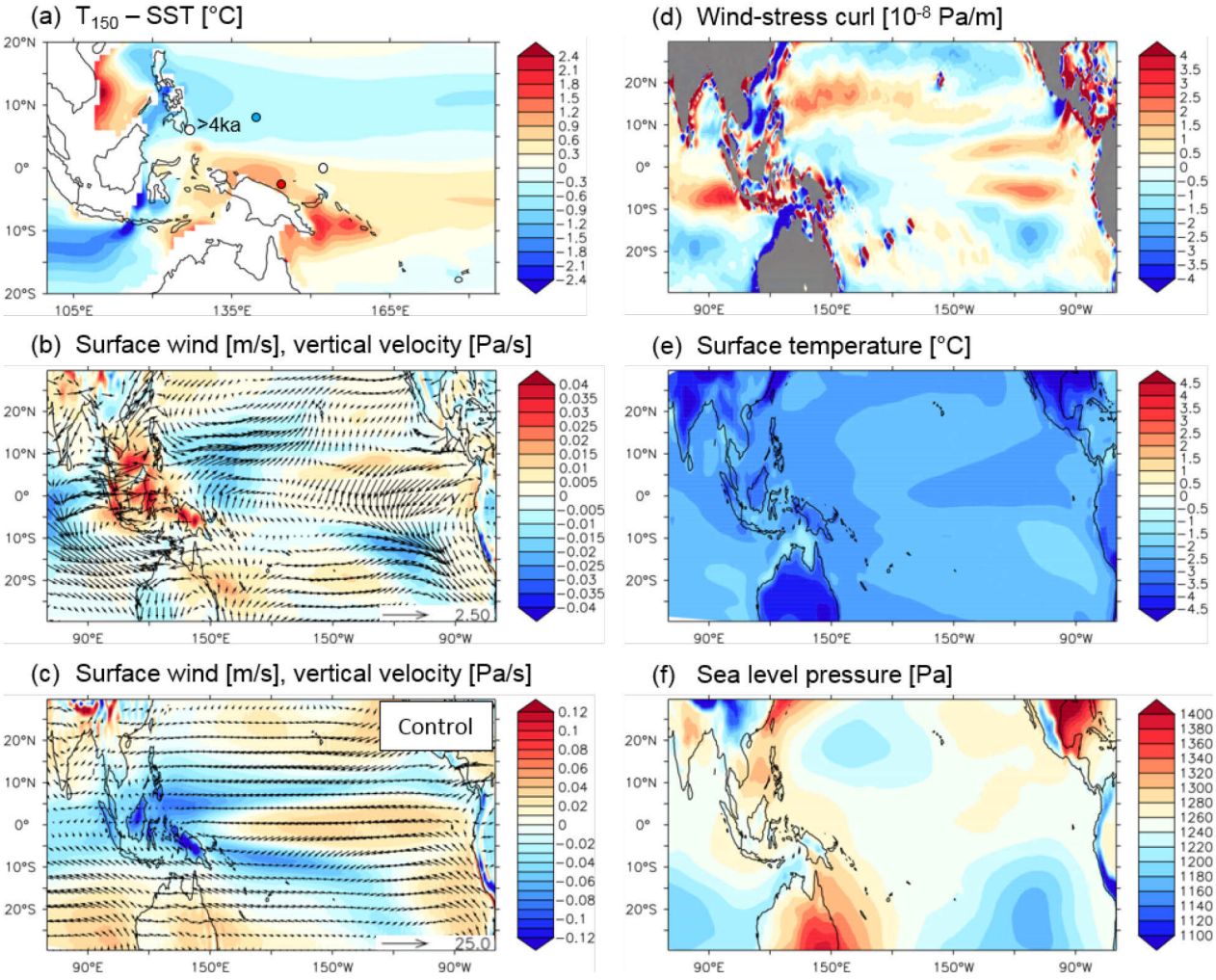

Figure 5.7. Tropical Pacific (annual mean) thermocline and climate conditions as simulated by the MRI-CGCM3 coupled general circulation model (PMIP3/CMIP5 simulations). All panels show LGM anomalies relative to the pre-industrial control run, except for panel (c) which shows pre-industrial control run fields. (a) Ocean subsurface (150 m) minus surface temperature difference in the WPWP as a measure for thermocline depth (red and blue colors indicate thermocline deepening and shoaling, respectively); colored dots represent proxy records discussed in this study, from which LGM thermocline depth changes have been inferred (red and blue indicate thermocline deepening and shoaling, white indicates a comparable thermocline depth). (b) Surface (925 hPa) winds and mid-troposphere (500 hPa) vertical velocity (red and blue colors indicate descent/ascent). Note that the field of wind-stress anomaly shows major structures almost identical to the field of surface wind anomaly and is therefore not shown here. (c) Same as (b) but for control to help interpret the LGM circulation anomaly pattern. (d) Wind-stress curl over the ocean. (e) Surface land and ocean temperature. (f) Sea level pressure (Pa). Note the different map section in (a) and (b–f).

In MRI-CGCM3, the LGM annual-mean wind system over the tropical West Pacific, which shapes the TCD anomaly pattern, is characterized by reduced convection over the Maritime Continent, whereas enhanced ascent takes place over the western Pacific (Figure 5.7b). The associated change in the equatorial wind circulation can be interpreted as a contraction of the Pacific Walker cell on its western side (Figures 5.7b and A2.6) compared to the modern situation (Figure 5.7c). In contrast to what would be expected from simple hydrologic-thermodynamic considerations [*Soden and Held*, 2006; *Vecchi et al.*, 2006] the strength of the Pacific Walker circulation does not increase in the colder climate. Reduced convection over the Maritime Continent is attributable to the relatively strong (compared to the surrounding sea surface) land surface cooling (Figure 5.7e), which is primarily related to the different evaporation response of land and ocean to the glacial cooling as well as to land–surface feedbacks [*Braconnot et al.*, 2012].

Around Indonesia, a Gill-type circulation response results from the reduced convection, with anomalous surface wind divergence over the Maritime continent (Figure 5.7b) and two areas of anomalous high sea-level pressure (SLP) centered north and south of the equator (Figure 5.7f) [*Gill*, 1980]. The location of these highs is modified by the continental configuration, with one anticyclone over the South China Sea and the other one shifted over Australia and substantially strengthened probably due to substantial surface cooling there (Figure 5.7e and f). As a result of this hemispherically asymmetric SLP distribution, anomalous cross-equatorial southerly wind occurs east of the Maritime Continent (Figure 5.7b). Over the South China Sea, the wind-stress curl associated with the high pressure anomaly causes the thermocline to deepen, consistent with regional TCD reconstructions (Figure 5.7a and d) [*Xu et al.*, 2010 and references therein]. We note that MRI-CGCM3 suggests a decrease in precipitation over PNG during the LGM in comparison to the preindustrial period (cf. Figure 5.7b), while the precipitation records (Ti/Ca and *P. obliquiloculata* Nd/Ca) indicate similar to enhanced precipitation over PNG during the same period (see section 5.5.3). This discrepancy may be related to the fact that the model does not resolve regional topographic features of PNG.

In summary, our model–data comparison suggests a substantial change in the Pacific Walker circulation during the LGM compared to the modern one with enhanced ascent over the western equatorial Pacific, and drastically reduced convection over the Maritime Continent. A recent study by [*Mohtadi et al.* [2017]] suggests a stronger-than-today glacial Indian Walker circulation with enhanced ascent over the eastern equatorial Indian Ocean. Taken together, and in view of the weakened ascending branch over the Maritime Continent, these results suggest a weaker coupling between the Indian and Pacific Walker cells during the last glacial than today.

5.6. Summary and conclusions

Combined Mg/Ca-derived temperature and $\delta^{18}O$ records of planktic foraminifera from GeoB 17419-1 and MD05-2920 were used to reconstruct variations in WPWP surface and thermocline conditions and the vertical stratification of the upper water column over the past 110 kyr. The records reflect a complex pattern of astronomically driven and glacial–interglacial variations in (sub)surface temperature, $\delta^{18}O_{SW}$ (salinity) and the water column structure allowing the following conclusions.

The benthic $\delta^{18}O$ record appears to resolve Antarctic warm events and the Antarctic cold reversal. The finding suggests that changes in the benthic $\delta^{18}O$ at this site reflect changes in $\delta^{18}O_{SW}$ and/or temperature of the Southern Ocean. Assuming that the changes in $\delta^{18}O_{IVC}$ were solely related to temperature, the AA events during MIS 3 would be characterized by a warming of between 1.0 and 2.5 °C and the deglaciation by a warming of 2.6 to 3.3 °C.

The thermocline temperatures exhibit a close connection to variations in the Earth's obliquity with warmer (colder) temperatures during periods of high (low) obliquity. This indicates that obliquity controlled variations in southern hemisphere mid-latitude climate and ocean conditions have a strong impact on the thermocline off PNG, likely via variations in the subduction and lateral advection of source waters (SPTW). Specifically, a warming of thermocline waters in the WPWP might be caused by a reduced subduction and advection of relatively cool waters from the subtropical Pacific along with a reduced export of warm waters from the tropical Pacific when obliquity is high. Our findings suggest that the WPWP thermocline temperature off PNG is remotely controlled by mid-latitude Pacific climate. The coherence of Holocene cooling trends observed in our WPWP thermocline temperature and temperature records of the Indonesian Seas and the eastern Indian Ocean suggests that the temperature signals observed in records of the Indonesian Seas and the ITF outflow region potentially originate in the western Pacific Ocean.

Our surface $\delta^{18}O_{SW}$ is interpreted to reflect local rainfall variations, while Ti/Ca and *P. obliquiloculata*-based Nd/Ca records of GeoB 17419-1 reflect variations in river discharge from PNG, which is linked to continental rainfall over PNG. The records imply that variations in the rainfall amount are mainly driven by variations in the Earth's precession with enhanced (decreased) precipitation when precession is high (low). An increase (decrease) in precipitation is most probably linked to an intensification (reduction) of the rainfall and/or a southward (northward) shift in the mean position of the ITCZ, and/or to an intensification (reduction) of the Austral-Asian monsoon.

A decreased ΔT is interpreted to reflect a thermocline deepening during the LGM in comparison to the last interglacial and present conditions. A compilation of available surface-thermocline ΔT records from the WPWP illustrates a dipole-like pattern of LGM thermocline depth anomalies (compared to the present)

with a thermocline shoaling in the northern, and a deepening in the southern WPWP. A comparison of the proxy compilation to the output of PMIP2 and PMIP3/CMIP5 LGM climate model simulations reveals that the spatial pattern of LGM thermocline depth anomalies is to a large extent attributable to glacial wind-field anomalies and associated Sverdrup dynamics that are related to a contracted Pacific Walker circulation during the LGM with enhanced ascent of the western equatorial Pacific, and reduced convection over the Maritime Continent. In conjunction with a strengthened glacial Indian Walker circulation with enhanced ascent over the eastern equatorial Indian Ocean and a weakened ascending branch over the Maritime Continent, our results suggest a weaker coupling between the Indian and Pacific Walker cells during the LGM than today.

Acknowledgements

We thank the captain, crew, and the scientific shipboard party of expeditions SO–228 and acknowledge technical assistance from Henning Kuhnert, Birgit Meyer-Schack, Vera Lukies and Ryan Bu. Discussions with Thomas Westerhold helped to improve parts of the manuscript. The sample material was stored and supplied by the GeoB Core Repository at the MARUM – Center for Marine Environmental Sciences, University of Bremen, Germany. XRF data were acquired at the XRF Core Scanner Lab at MARUM. We acknowledge the World Climate Research Programme's Working Group on Coupled Modeling, which is responsible for CMIP, and the climate modeling groups (listed in the supplementary Table A2.2) for producing and making available their model output. For CMIP the U.S. Department of Energy's Program for Climate Model Diagnosis and Intercomparison provides coordinating support and led development of software infrastructure in partnership with the Global Organization for Earth System Science Portals. The Laboratoire des Sciences du Climat et de l'Environnement (LSCE) is acknowledged for collecting and archiving the PMIP2 model data. The PMIP2 Data Archive is supported by CEA, CNRS and the Programme National d'Etude de la Dynamique du Climat (PNEDC). M.P. acknowledges support from the German PalMod initiative (BMBF). This work is funded by the DFG-Research Center / Cluster of Excellence "The Ocean in the Earth System" and the BMBF project 03G0228A (EISPAC). The data presented in this study are available on Pangaea (www.pangaea.de).

Chapter 6.
The impact of astronomical forcing on the surface and thermocline variability across the WPWP over the past 160 kyr

Martina Hollstein[1], Mahyar Mohtadi[1], Jeroen Groeneveld[1], Delia Oppo[2], Markus Kienast[3], Gema Martínez Méndez[1], Dierk Hebbeln[1]

[1]MARUM – Center for Marine Environmental Sciences, University of Bremen, Bremen, Germany

[2]Department of Geology and Geophysics, Woodshole Oceanographic Institution, Massachusetts, USA

[3]Department of Oceanography, Dalhousie University, Halifax, Canada

In preparation

Abstract

The Western Pacific Warm Pool (WPWP) is a key component within the global climate system by providing an enormous amount of latent and sensible heat to the global atmosphere. Nevertheless, past variability of oceanography and climate across the WPWP is largely unknown. Here, we compare newly generated and published surface and thermocline temperature and seawater stable oxygen isotopes ($\delta^{18}O_{SW}$) records from the northern (MD06-3067, offshore Mindanao) and southern (17419-1, Bismarck Sea and GeoB 17426-3, east of the Bismarck Archipelago) WPWP to monitor its variability over the last glacial–interglacial cycle. We find that the records of the three sites, to a first-order, varied coherently over the past 160 kyr. Our finding indicates that the (spatial structure of the) WPWP remained relatively stable during the investigated period. In addition, the sea surface temperature records indicate that during the last glacial period, cooling in the open ocean WPWP was smaller than the cooling within the coastal WPWP areas. The surface $\delta^{18}O_{SW}$ records, interpreted to mainly reflect variations in precipitation, show that the precipitation across the WPWP is uniformly driven by precession-controlled shifts of the Intertropical Convergence Zone (ITCZ) with a more northward (southward) position under low (high) precession. Differences between the thermocline temperature records from the three sites can be attributed to the differing influence of astronomical forcing on the thermocline water masses influencing the individual sites. While the thermocline temperature within the Bismarck Sea has been shown to be influenced by remote effects of obliquity on the South Pacific Tropical Water, the thermocline at the WPWP sites offshore Mindanao and east of the Bismarck Archipelago are influenced by precession. Cyclic variations of precessional duration are also inherent in the thermocline $\delta^{18}O_{SW}$ records of all sites.

These precession-related variations in the thermocline conditions could be either related to modification of the thermocline source waters that influence the individual core sits and/or to variations in the vertical structure of the water column.

6.1. Introduction

The Western Pacific Warm Pool (WPWP) is the largest warm water body on Earth. As such, it provides an enormous amount of latent and sensible heat to the global atmosphere, and influences climate worldwide. The WPWP thus constitutes a key component within the global climate system. Nonetheless, our knowledge on the long-term variability of surface and thermocline conditions across the WPWP is still limited. Previous studies focused exclusively on the spatial variability of surface ocean temperatures and hydrologic changes in the Indo-Pacific realm during the last deglaciation and Holocene [e.g. *Gibbons et al.*, 2014; *Linsley et al.*, 2010]. Compilations of longer records are needed to better understand the WPWP variability in response to astronomical forcing and varying glacial–interglacial boundary conditions. Studies that focus on the evolution of both, WPWP surface and thermocline conditions beyond the Last Glacial Maximum (LGM) are particularly sparse. So far, there is one study that focuses on the reconstruction of surface and thermocline conditions offshore Mindanao [*Bolliet et al.*, 2011], and two that reconstruct surface and thermocline conditions within the Bismarck Sea offshore Papua New Guinea (PNG) [*Hollstein et al.*, submitted; *Tachikawa et al.*, 2014]. WPWP thermocline waters link the extratropical and the equatorial Pacific Ocean. Thermocline reconstructions thus allow to examine the impact of remote forcings on the WPWP. Furthermore, variations in WPWP thermocline characteristics influence the eastern equatorial Pacific Ocean, the Indonesian Throughflow, and potentially affect the equatorial surface ocean conditions and climate [e.g. *Gu and Philander*, 1997]. Therefore, accurate thermocline reconstructions are needed to understand the processes that drive the Pacific Ocean and climate.

Bolliet et al. [2011] attribute glacial–interglacial changes observed in surface and thermocline temperature, $\delta^{18}O_{SW}$, and in paleoproductivity records of offshore Mindanao (MD06-3067) to local influences, specifically, variations in the Mindanao Dome upwelling. A generally strengthened dome during glacial intervals was inferred from cool thermocline temperatures and increased thermal surface-thermocline gradients. On the basis of a SST record from the Bismarck Sea (MD05-2920), *Tachikawa et al.* [2014] illustrate that greenhouse gas forcing is the main driver for WPWP surface ocean temperatures. In addition, the SST record and rainfall proxies of Bismarck Sea records (MD05-2920 and GeoB 17419-1) indicate that the regional hydroclimate is controlled by variations in the Earth's orbital precession such that precipitation over PNG and the Bismarck Sea is enhanced (weakened) when precession is high (low).

This pattern has been mainly linked a more southern (northern) position of the ITCZ [*Hollstein et al.*, submitted; *Tachikawa et al.*, 2014]. The thermocline temperature record of GeoB 17419-1 exhibits a close connection to variations in the Earth's obliquity with warmer temperatures when obliquity is high. This has been attributed to obliquity-driven variations in the subduction and lateral advection of the thermocline source waters [*Hollstein et al.*, submitted].

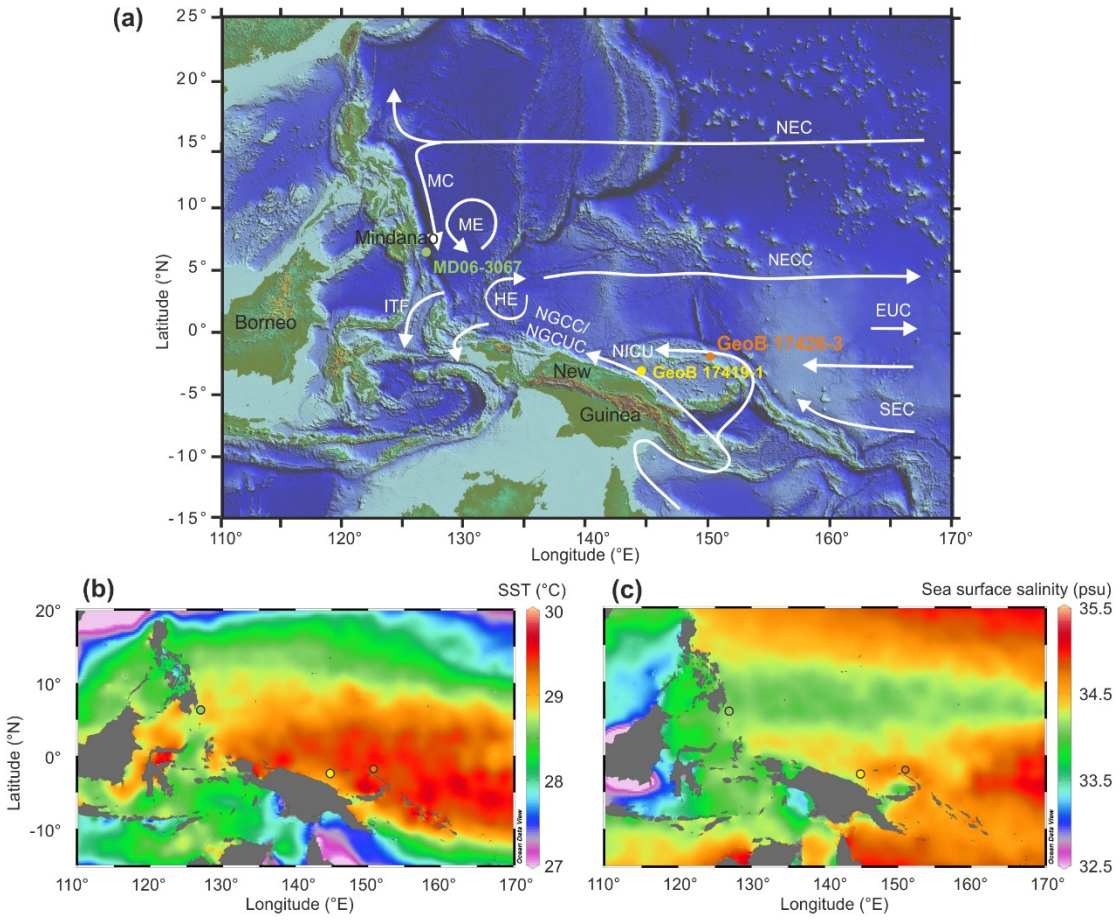

Figure 6.1. (a) Bathymetric map of the study area. White arrows schematically indicate the main (sub)surface currents that influence the WPWP. MC – Mindanao Current, NEC – North Equatorial Current, NECC – North Equatorial Counter Current, EUC – Equatorial Undercurrent, NGCC – New Guinea Coastal Current, NGCUC – New Guinea Coastal Undercurrent, SEC – South Equatorial Current, ITF – Indonesian Throughflow. The position of gravity core GeoB 17426-3 is indicated by an orange dot. The positions of Core GeoB 17419-1 [*Hollstein et al.*, submitted] and MD06-3067 [*Bolliet et al.*, 2011] are marked by a yellow and green dot, respectively. (b) Sea surface temperatures and (c) sea surface salinity across the WPWP [*Locarnini et al.*, 2013; *Zweng et al.*, 2013]. The temperature and salinity maps were created with the Ocean Data View software [*Schlitzer*, 2014].

Here, we present new surface and thermocline Mg/Ca and $\delta^{18}O$ records of planktic foraminifera from gravity core GeoB 17426-3, which was retrieved in the heart of the WPWP offshore the Bismarck Archipelago (Figure 6.1), to reconstruct variations in surface and thermocline temperatures and the oxygen isotope composition of seawater ($\delta^{18}O_{SW}$). The newly generated records are compared with the

existing surface and thermocline records from the Bismarck Sea (GeoB 17419-1 and MD05-2920) [*Hollstein et al.*, submitted; *Tachikawa et al.*, 2014] and the northern WPWP off Mindanao (MD06-3067) [*Bolliet et al.*, 2011] to investigate the temperature and $\delta^{18}O_{SW}$ (salinity) variability across the WPWP over the last glacial–interglacial cycle(s).

6.2. Modern setting

Core site GeoB 17426-3 is located east of New Hanover, offshore the Bismarck Archipelago, Papua New Guinea (PNG) (2.19 °S, 150.86 °E, 1368 m water depth) in the heart of the WPWP. The WPWP is marked by sea surface temperatures (SST) above 28–29 °C all year-round, with slightly cooler SST in the northern part of the WPWP and maximal temperatures around site GeoB 17426-3 (Figure 6.1) [*Locarnini et al.*, 2013]. The surface ocean is characterized by relatively low salinity around 34 psu, with slightly lower values in the northern, and slightly higher values in the southern WPWP (Figure 6.1) [*Zweng et al.*, 2013].

The thermoclines of the northern and southern WPWP are influenced by the North Pacific Tropical Water (NPTW) and South Pacific Tropical Water (SPTW), respectively. Both water masses originate in the extratropical Pacific Ocean and are transported into the WPWP by branches of the respective (North and South) Pacific Subtropical Gyres. The NPTW is formed within the North Pacific Subtropical Gyre by subduction relatively salty (~34.5–35.0 psu) surface water [e.g. *Fine et al.*, 1994]. The SPTW is produced by subduction of saltier (>35.5 psu) surface waters within the South Pacific Subtropical Gyre [e.g. *Qu et al.*, 2013; *Tsuchiya et al.*, 1989]. There are two branches of SPTW. The first branch, the South Pacific Equatorial Water (SPEW), is formed within the subtropical central South Pacific Ocean near the Polynesian islands (~20 °S) by subduction of surface waters that have become saltier (and denser) through evaporation [see *Grenier et al.*, 2013 and references therein]. It enters the WPWP from the east. The core of the SPEW is marked by highest salinities of ~35.6–35.8 psu [*Qu and Lindstrom*, 2002]. The second branch of the SPTW enters the WPWP from south of Vanuatu. Its formation is not completely understood but it appears to form by subduction of surface waters in the subtropical Pacific around 30 °S (Figure 6.2) [see *Grenier et al.*, 2013 and references therein]. The core of this SPTW branch has slightly lower salinity (~35.5 psu). The thermocline at core site GeoB 17426-3 is most influenced by the SPEW, site GeoB 17419-1 by the SPTW, and the northern WPWP site MD06-3067 by the NPTW (Figure 6.2).

The surface and subsurface currents that influence the WPWP include the North Equatorial Current (NEC) in the North, and the South Equatorial Current (SEC) in the South Pacific Ocean, as well as the tropical Western Boundary Currents (WBCs), namely the Mindanao Current (MC), the New Guinea Coastal Current (NGCC), New Guinea Coastal Undercurrent (NGCUC) and the New Ireland Coastal Undercurrent (NICU) (Figure 6.1) that are formed by bifurcation of the equatorial currents at the Philippine and

Australian coasts [e.g. *Gordon et al.*, 2014; *Kessler and Gourdeau*, 2007]. At the confluence zone of the MC and the SEC and NGCC/NGCUC near the equator, the currents feed the eastward flowing equatorial currents and the ITF [e.g. *Fine et al.*, 1994; *Gordon*, 1986]. The retroflection of the currents is also associated with the formation of the Mindanao and the Halmahera Eddies [e.g. *Firing et al.*, 2005; *Lukas et al.*, 1991]. The cyclonic Mindanao Eddy favors local and seasonal upwelling of waters, forming a dome, with maximal intensity during boreal winter [e.g. *Wijffels et al.*, 1996].

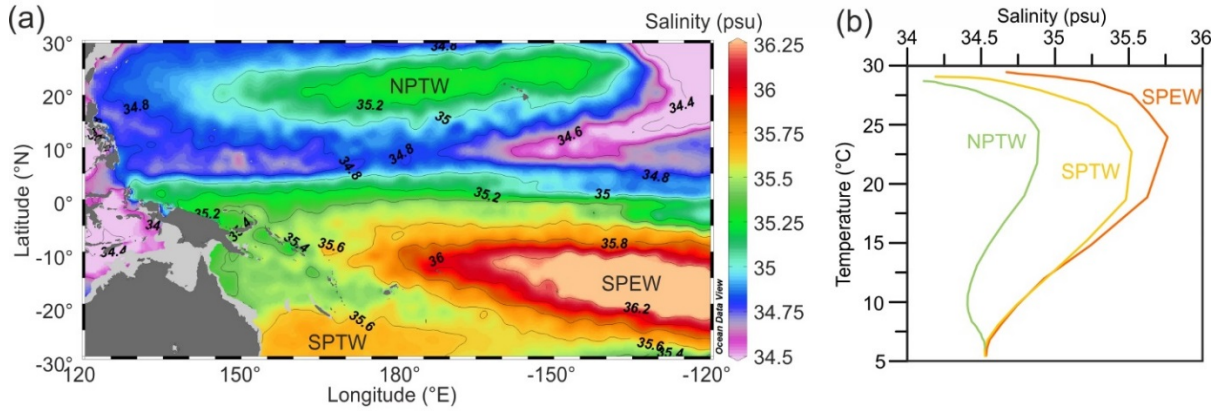

Figure 6.2. (a) Mean annual salinity at 100 m water depth derived from WOA13 [*Zweng et al.*, 2013]. The map was created with the Ocean data view software [*Schlitzer*, 2014]. (b) Temperature-salinity relations near stations MD06-3067, GeoB 17419-1 and GeoB 17426-3. NPTW – North Pacific Tropical Water, SPTW – South Pacific Tropical Water, SPEW – South Pacific Equatorial Water.

6.3. Material and methods

6.3.1. Material

Gravity core GeoB17426-3 was recovered during the R/V *Sonne* expedition SO–228 [*Mohtadi et al.*, 2013]. The core has a length of 1031 cm and was sampled at 4 cm intervals on board. All samples were freeze dried, washed over 150 µm sieves and dried in an oven at 40–60 °C. The core site is located far above the modern lysocline depth of 3300 m [see *Berger et al.*, 1982 and references therein]. This implies an overall good carbonate preservation, which is additionally indicated by the presence of aragonitic pteropod shells in many of our samples.

We use the planktic foraminifera *G. ruber* as an indicator for surface, and *P. obliquiloculata* as an indicator for upper thermocline conditions. The choice of species is consistent with results from a study on modern surface sediments from the WPWP that revealed that *G. ruber* calcifies at mixed layer (between 0 and 80 m) and *P. obliquiloculata* at upper thermocline depths within the NPTW/SPTW (between 90 and 125–150 m) [*Hollstein et al.*, 2017]. For *G. ruber*, we followed the species concept of *Aurahs et al.* [2011]. Thus, we used only individuals that were previously referred to as *G. ruber* s.s. Both *G. ruber* and

P. obliquiloculata appear to calcify perennially within the WPWP [*Kawahata et al.*, 2002; *Yamasaki et al.*, 2008].

6.3.2. Age model

The age model of core GeoB17426-3 is based on 9 AMS ^{14}C ages and alignment of benthic δ^{18}O (*C. wuellerstorfi*) to the global benthic LR04 stack (Table 6.1) [*Lisiecki and Raymo*, 2005]. The radiocarbon ages are based on monospecific or mixed *G. ruber*, *G. elongatus* and *G. sacculifer* carbonate samples and were measured at the Keck Carbon Cycle Accelerator Mass Spectrometry Laboratory at the University of California, Irvine (UCI). We applied a Bayesian approach to model the age-depth relation using BACON R 2.2 [*Blaauw and Christen*, 2011]. To convert radiocarbon ages into calendar ages the Marine13 calibration curve was used [*Reimer et al.*, 2013] with a local correction for reservoir ages of $\Delta R = 141 \pm 131$ yrs [*Petchey and Ulm*, 2016]. BACON was run using default settings with the following modifications: *mem.mean=0.4, res=2, t.a=9, t.b=10*. Age uncertainties estimated from 95% confidence intervals range between 271 and 3013 years. Below 206 cm, the age model is based on graphic correlation of benthic δ^{18}O to the LR04 stack. Tie points were defined at maxima in δ^{18}O that were associated with Marine Isotope Stages (MIS) 7a, 6e and a, 5d and b and 4 (Figure 6.3). Between the tie points the age-depth chronology was inferred by linear interpolation. All ages are given as calibrated calendar ages before present. According to our age model the core spans the last 209 kyr with a temporal resolution between 0.5 to 1.2 kyr.

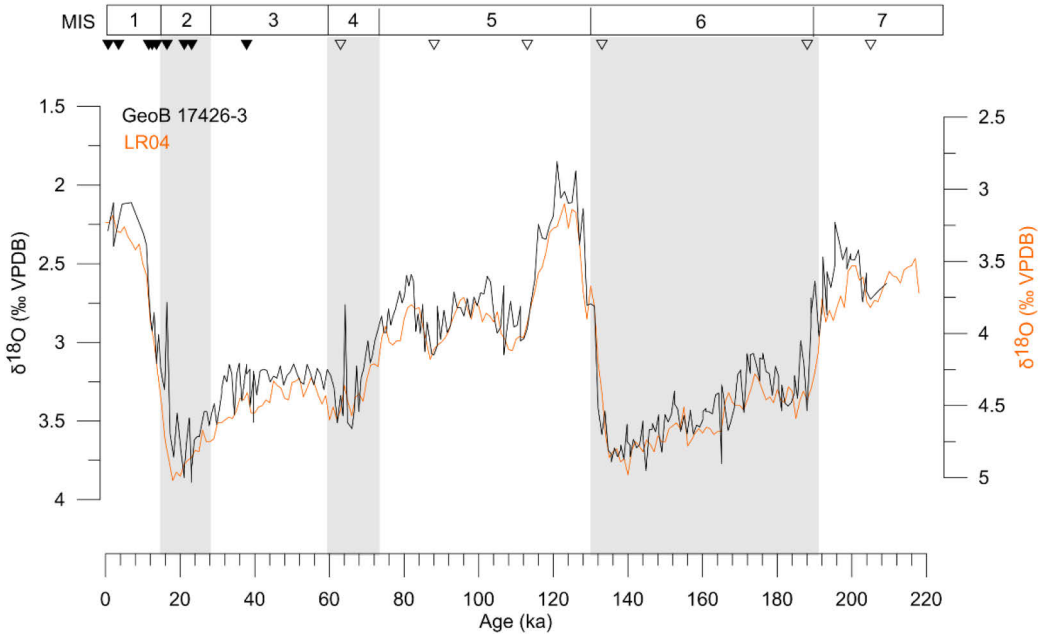

Figure 6.3. Age model of core GeoB 17426-3. Benthic δ^{18}O of GeoB 17426-3 (black line) compared to the LR04 benthic δ^{18}O stack (orange line) [*Lisiecki and Raymo*, 2005]. Filled and empty triangles indicate radiocarbon dates of GeoB 17426-3 and tie points to LR04, respectively. Marine isotopes stages (MIS) 1−7 are marked at the top [*Lisiecki and Raymo*, 2005; *Sanchez Goñi and Harrison*, 2010]. Gray shadings additionally mark MIS 2, 4 and 6.

Table 6.1. Radiocarbon ages with calibrated calendar ages of core GeoB 17426-3 and tie points set to construct the age model. Calibrated calendar ages are reported as weighted mean ages as estimated by BACON.

Lab-ID	Sample depth (cm)	Foraminifera species	^{14}C age ± 1σ error (years BP)	Cal. age (years BP)	95% confidence interval (years)
142709	2	*G. elongatus*	1340 ± 20	635	−837 – 1117
150627	10	*G. ruber*	3840 ± 15	3434	3146 – 3705
150128	10	*G. sacculifer*	3550 ± 20	3434	3146 – 3705
150629	50	*G. ruber* + *G. sacculifer*	10640 ± 25	11610	11198 – 12079
142710	58	*G. elongatus*	11075 ± 35	12462	12073 – 12766
150630	66	*G. ruber* + *G. sacculifer*	12305 ± 25	13623	13322 – 13941
150631	86	*G. ruber* + *G. sacculifer*	14110 ± 30	16427	15963 – 16929
146954	106	*G. sacculifer*	18030 ± 210	21074	20363 – 21768
150632	118	*G. ruber* + *G. sacculifer*	19740 ± 60	23778	22482 – 23762
146955	206	*G. sacculifer*	33400 ± 1400	37823	34884 – 40836
-	318	-	-	63000	-
-	482	-	-	88000	-
-	594	-	-	113000	-
-	674	-	-	133000	-
-	934	-	-	188000	-
-	998	-	-	205000	-

6.3.3. Stable oxygen isotope and Mg/Ca analyses

To generate the age model, we used the stable oxygen isotope composition of the benthic foraminifera *C. wuellerstorfi* (>250 µm). For further analysis, we measured the shell $\delta^{18}O$ and Mg/Ca on the planktic foraminifera *G. ruber* (250–355 µm) and *P. obliquiloculata* (355–425 µm). Isotope analyses were carried out by the isotope laboratory of MARUM, University of Bremen on Finnigan MAT 251 mass spectrometers, connected with automatic lines for carbonate preparation of type Kiel I or Kiel III. All isotope values were calibrated against the international Vienna Pee Dee Belemnite (VPDB) standard by using an in-house carbonate standard, which has been calibrated to the National Bureau of Standards (NBS) 19 standard. The long-term analytical standard deviation is below ± 0.07‰. To control the sample reproducibility we measured replicates on 10% of the samples. The results indicate a standard deviation of 0.15‰ for *G. ruber*, and 0.17‰ for *P. obliquiloculata.*

The cleaning procedure for Mg/Ca measurements followed the protocol of *Barker et al.* [2003]. It includes five water and two methanol washes, an oxidative step with 1% NaOH-buffered H_2O_2, and a weak acid leach using 0.001 M HNO_3. The cleaned samples were dissolved in 0.075 M HNO_3, centrifuged (10 min at 6000 rpm) and diluted with water. The samples were analysed at the Faculty of Geosciences, University of Bremen, on an Agilent Technologies 700 Series Inductively Coupled Plasma Optical Emission Spectrophotometer (ICP-OES), which is connected to a Cetax ASX 520 autosampler. The analytical

standard deviation was better than 0.01 mmol/mol. The instrumental drift and precision was controlled by using an in-house standard solution with a Mg/Ca of 2.93 mmol/mol, which was measured after every fifth sample and the international ECRM 752-1 standard with a reported Mg/Ca of 3.75 [*Greaves et al.*, 2008], typically measured after every fiftieth sample. The standard deviations were better than 0.045 mmol/mol (0.5%) for the in-house standard solution and 0.012 (0.07%) for ECRM. We corrected the Mg/Ca ratios of all samples for the reported ECRM value. Replicates indicate a reproducibility of ± 0.28 mmol/mol for *G. ruber* and ± 0.26 mmol/mol for *P. obliquiloculata*. Al/Ca, Fe/Ca and Mn/Ca were measured alongside with Mg/Ca to monitor the cleaning efficiency. None of these ratios shows a correlation to Mg/Ca and we therefore assume that the Mg/Ca is not affected by contamination.

The Mg/Ca ratios were converted to temperature by applying the multispecies Mg/Ca-temperature calibration of *Anand et al.* [2003]

$$Mg/Ca = 0.38 \exp 0.09 * T \qquad (6.1)$$

for *G. ruber*. The equation was shown to give reasonable results for the WPWP [*Hollstein et al.*, 2017]. For *P. obliquiloculata* we used the species-specific calibration of *Hollstein et al.* [2017] that was established for the WPWP

$$Mg/Ca = 0.21 \exp 0.097 * T \qquad (6.2)$$

but corrected it for differences in the cleaning procedure (reductive vs. non-reductive cleaning) by assuming a Mg/Ca loss of 10% [*Barker et al.*, 2003; *Martin and Lea*, 2002; *Rosenthal et al.*, 2004] is caused by reductive cleaning:

$$Mg/Ca = 0.23 \exp 0.097 * T \qquad (6.3)$$

Using $\delta^{18}O$ and Mg/Ca we estimated the oxygen isotope composition of seawater ($\delta^{18}O_{SW}$) by applying the high-light $\delta^{18}O$-temperature equation established by *Bemis et al.* [1998]:

$$T(°C) = 14.9 - 4.8 (\delta^{18}O - \delta^{18}O_{SW}) \qquad (6.4)$$

We converted the $\delta^{18}O_{SW}$ values from Vienna Pee Dee Belemnite (VPDB) into the Vienna Standard Mean Ocean Water (VSMOW) by adding 0.27‰ following *Hut* [1987] and corrected them for changes in global ice volume following *Waelbroeck et al.* [2002].

Uncertainties of temperature, ΔT, and $\delta^{18}O_{SW}$ were estimated by propagation of the uncertainties introduced by Mg/Ca and $\delta^{18}O$ measurements (see above), Mg/Ca-temperature calibrations (equations I–II) and/or the $\delta^{18}O$-temperature equation (equation IV) as well as the global ice volume estimate (± 0.09‰) [*Waelbroeck et al.*, 2002] as described in *Mohtadi et al.* [2014]. Resulting uncertainties average

about 1.3 °C for surface and 2.6 °C for thermocline temperatures, and about 0.3‰ for the surface and 0.6‰ for thermocline $\delta^{18}O_{SW}$. The unusually high uncertainties for thermocline temperature and $\delta^{18}O_{SW}$ are mainly due to slightly higher uncertainties within the temperature calibration in comparison to other calibrations.

6.4. Results

6.4.1. Mg/Ca temperatures

Shell Mg/Ca of *G. ruber* ranges between 3.8 and 5.9 mmol/mol, which converts to temperature estimates between 25.6 and 30.5 °C (Figure 6.4c). The calculated core top temperature of 28.7 °C agrees within error with the mean annual surface ocean temperature of around 29.0 °C reported by the World Ocean Atlas 13 (WOA 13) (2.5 °S, 151.5 °E) [*Locarnini et al.*, 2013]. The record depicts elevated temperatures during MIS7, MIS 5e and during the Holocene. During MIS 6, and from MIS 5d to 2, the record shows cooler and relatively constant temperatures.

Mg/Ca values of *P. obliquiloculata* range between 2.0 and 3.6 mmol/mol, equivalent to temperatures between 22.1 and 28.3 °C (Figure 6.4d). The core top value of 26.6 °C matches the mean annual upper thermocline temperature of 26.5 °C (75–150 m) [*Locarnini et al.*, 2013]. Generally, the record shows a higher variability than the *G. ruber* record. *P. obliquiloculata* records maximal temperatures during MIS 5e and the Holocene and minimal temperatures during the early MIS 6, MI4 and the LGM. The temperatures during MIS 5d–a are slightly cooler than temperatures during MIS 6 and 3. During MIS 3 the record shows a slight cooling trend. The shape of the surface and thermocline temperature records is very similar (Figure 6.4). Both records show exceptionally warm temperatures during the last peak interglacial and the Holocene and rather uniform temperatures from MIS 5 to 2.

6.4.2. $\delta^{18}O$ and $\delta^{18}O_{SW}$

The planktic $\delta^{18}O$ records of GeoB 17426-3 reflect glacial–interglacial variations and the corresponding MISs with higher $\delta^{18}O$ during MIS 2, 4 and 6 and lower values during MIS 1, 3 and 5. The $\delta^{18}O$ of *G. ruber* varies between −2.76 and −0.95‰ (Figure 6.4a). Due to its deeper calcification depth, the $\delta^{18}O$ of *P. obliquiloculata* is higher and varies between −1.66 and 0.23‰ (Figure 6.4b).

The sea level corrected $\delta^{18}O_{SW}$ record of *G. ruber* shows cyclic variations with values ranging between 0.1 and 1.4‰. The $\delta^{18}O_{SW}$ of *P. obliquiloculata* varies between 0.4 and 2.2‰. As the *G. ruber* record, it shows cyclic variations, but superimposed on long-term variations with decreased $\delta^{18}O_{SW}$ between about 130 to 70 ka.

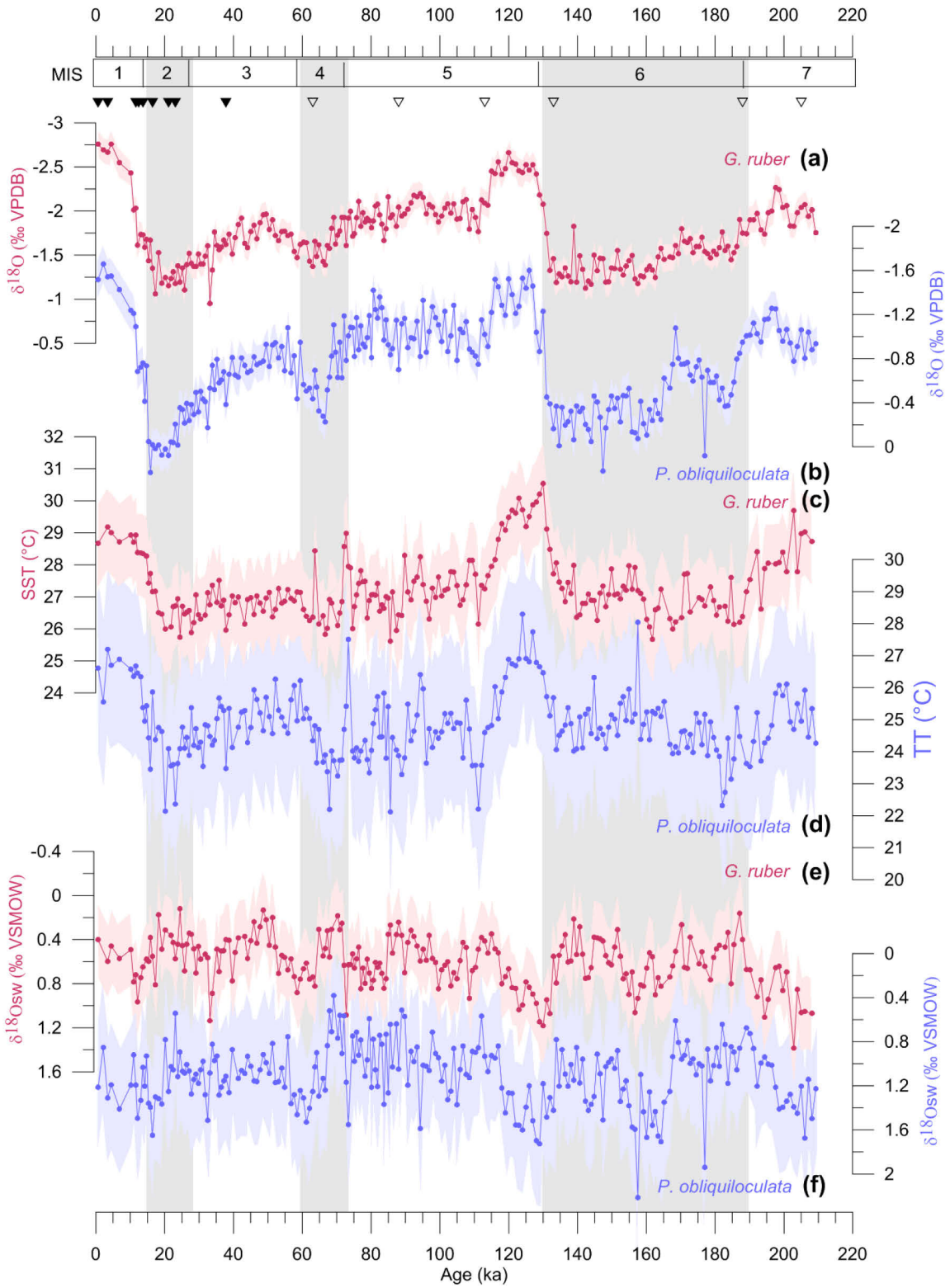

Figure 6.4. Surface and thermocline $\delta^{18}O$, temperature and $\delta^{18}O_{SW}$ records of core GeoB 17426-3. (a and b) Shell $\delta^{18}O$, (c and d) Mg/Ca temperature estimates and (e and f) ice volume corrected $\delta^{18}O_{SW}$ of *G. ruber* (surface indicator) and *P. obliquiloculata* (thermocline indicator). Colored shadings indicate 1σ-uncertainties (see text). Triangles on top mark dating points. MIS 1-7 are indicated at the top. MIS 2, 4 and 6 are additionally marked by gray bars.

6.5. Discussion

6.5.1. Comparison of temperature and $\delta^{18}O_{SW}$ variations across the WPWP

To assess the surface and thermocline variability across the WPWP we compare shell $\delta^{18}O$, temperature and $\delta^{18}O_{SW}$ records from GeoB 17426-3 to records from the Bismarck Sea (GeoB 17419-1 and MD05-2920) [*Hollstein et al.*, submitted; *Tachikawa et al.*, 2014] and published records from the northern WPWP offshore Mindanao (MD06-3067) [*Bolliet et al.*, 2011]. Considering the different cleaning methods used to prepare the samples for Mg/Ca measurements (non-reductive vs. reductive cleaning), the temperature and $\delta^{18}O_{SW}$ estimates of GeoB 17419-1 are based on the same equations used in this study [see *Hollstein et al.*, submitted]. We recalculated the temperature and $\delta^{18}O_{SW}$ of MD06-3067 accordingly, to allow a comparison of the temperature and $\delta^{18}O_{SW}$ data between the individual cores. The choice of the above mentioned Mg/Ca-temperature calibrations for all three sites is also in accordance with a study on modern surface sediments from the WPWP that indicated the applicability of the equations for the northern and southern WPWP [*Hollstein et al.*, 2017]. The resulting temperature and $\delta^{18}O_{SW}$ values are slightly higher than those presented by *Bolliet et al.* [2011]. The record of MD06-3067 does not cover the late Holocene. However, the Mg/Ca temperature of 26.4 °C estimated from a modern sediment sample collected in the nearby Davao Gulf (6.26 °N, 125.83 °E) matches the observed temperature of 26.4°C [*Locarnini et al.*, 2013] at an calcification depth of 88 m, which was estimated for *P. obliquiloculata* at the same core site [*Hollstein et al.*, 2017]. For consistency, we resampled all records on intervals of 0.5 ka. Since the southern WPWP records do not resolve millennial-scale events, we will focus on the influence of glacial–interglacial and astronomical forcing on the northern and southern WPWP in this study.

The comparison reveals that, over the past 160 kyr, to a first order, both, shell $\delta^{18}O$, temperature and $\delta^{18}O_{SW}$ varied coherently across the WPWP (Figures 6.5 and 6.6). This is true for both, the general shape of the records and the absolute values of surface and thermocline temperatures and $\delta^{18}O_{SW}$. The overall coherence of the records indicates that the spatial structure across the WPWP over the past 160 kyr remained relatively stable. This is surprising, given the fact that the sites underlie different local influences. For instance, the northern site MD06-3067 lies in the flow path of the Mindanao Current and is influenced by the NPTW, while the southern sites lie in the flow paths of the NGCC/NGCUC and NICU and are influenced by the SPTW and SPEW, respectively (Figures 6.1 and 6.2). Additionally, site MD06-3067 is affected by the Mindanao Dome. Indeed, glacial–interglacial and suborbital variations apparent in the surface and thermocline records of MD06-3067 over the past 160 kyr have been primarily related to local variations in the Mindanao Dome activity [*Bolliet et al.*, 2011]. In contrast, the overall coherence of the records presented here suggests that the overall WPWP temperature and $\delta^{18}O_{SW}$ variability is mainly governed by supra-regional forcings.

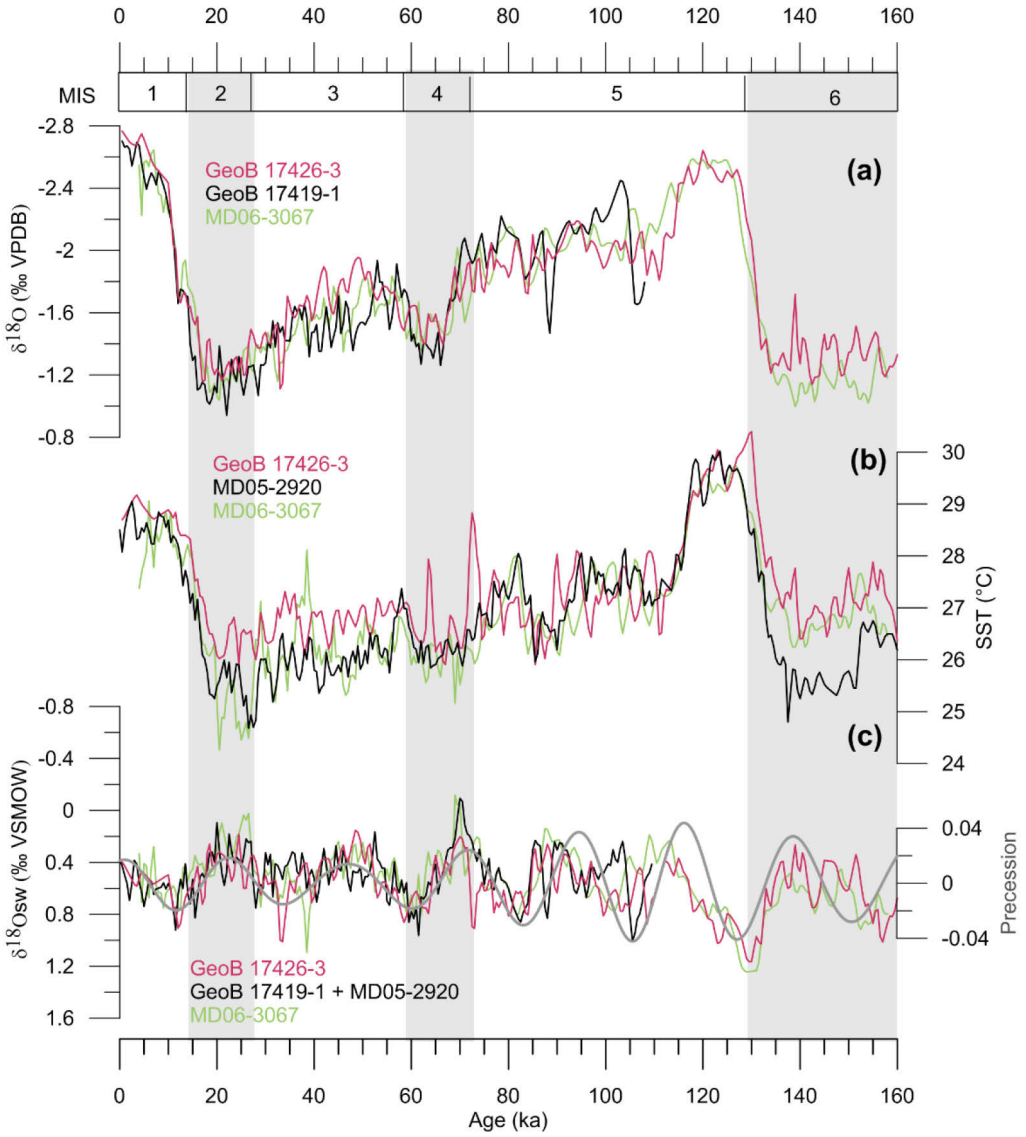

Figure 6.5. Comparison of surface $\delta^{18}O$, temperature and $\delta^{18}O_{SW}$ records from GeoB 17426-3 (this study), combined GeoB 17419-1 and MD05-2920 [see *Hollstein et al.*, submitted] and MD06-3067 [*Bolliet et al.*, 2011]. (a) Surface $\delta^{18}O$ of GeoB 17426-3 (red line), GeoB 17419-1 (black) and MD06-3067 (green). (b) Surface temperature of GeoB 17426-3 (red), MD05-2920 [*Tachikawa et al.*, 2014] on an updated age scale [see *Hollstein et al.*, submitted] (black) and MD06-3067 (green). (c) $\delta^{18}O_{SW}$ of GeoB 17426-3, combined MD05-2920 and GeoB17419, and MD06-3067. The gray solid lines indicate variations in the Earth's orbital precession [*Laskar*, 1990] For consistency, all records were resampled on intervals of 0.5 ka. Marine Isotope Stages are indicated at the top. MIS 6, 4 and 2 are marked by gray bars.

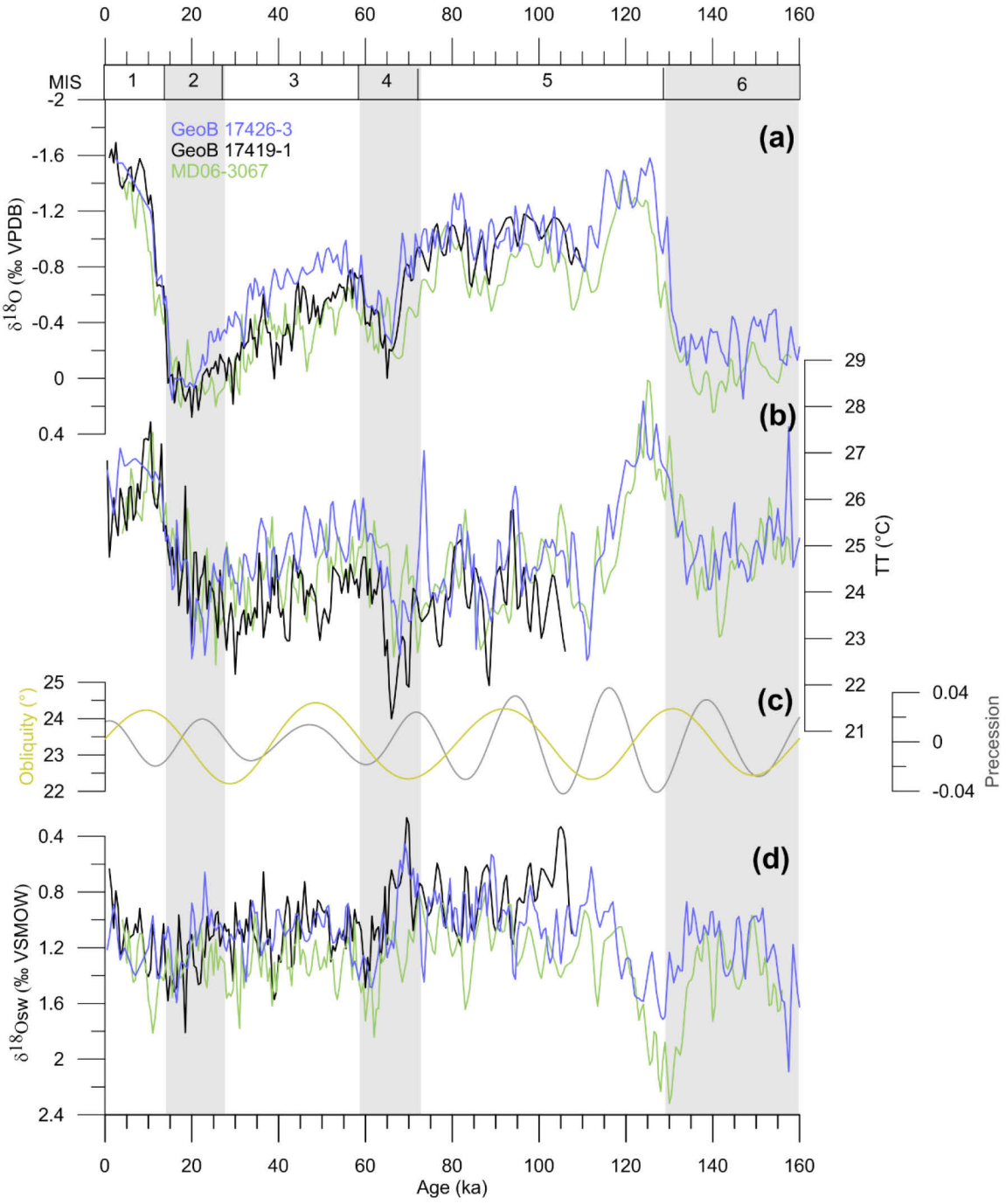

Figure 6.6. Comparison of thermocline $\delta^{18}O$, temperature and $\delta^{18}O_{SW}$ records from GeoB 17426-3 (this study), GeoB 17419-1 [*Hollstein et al.*, submitted] and MD06-3067 [*Bolliet et al.*, 2011]. (a) Shell $\delta^{18}O$ records of GeoB 17426-3 (blue), GeoB 17419-1 (black) and MD06-3067 (green). (b) Temperature of GeoB 17426-3 (blue), GeoB 17419-1 (black) and MD06-3067 (green). (c) Variations in the Earth's obliquity (yellow) and precession (gray) [*Laskar*, 1990]. (d) $\delta^{18}O_{SW}$ of GeoB 17426-3, GeoB17419, and MD06-3067. For consistency, all records were resampled on intervals of 0.5 ka. Marine Isotope Stages are indicated at the top. MIS 6, 4 and 2 are marked by gray bars.

6.5.2. SST variability

The SST record of GeoB 17426-3 is in general agreement with the SST records of MD05-2920 and MD06-3067. However, starting in MIS 4, SST estimates suggest slightly higher temperatures at site GeoB 17426-3 than at the other two sites. This slight temperature offset matches the present annual mean surface temperature distribution across the WPWP with higher SSTs east of the Bismarck Archipelago (GeoB 17426-3) in comparison to the Bismarck Sea (MD05-2920) and the northern WPWP (MD06-3067) (Figure 6.1). The offset is especially apparent during the last glacial period, where the SST record of GeoB 17426-3 indicates a smaller temperature cooling than MD05-2920 and MD06-3067. The glacial–interglacial variability depicted by the SST record of GeoB 17426-3 is comparable to the glacial–interglacial variability of other SST records from the central (open ocean) WPWP [*de Garidel-Thoron et al.*, 2005; *de Garidel-Thoron et al.*, 2007; *Lea et al.*, 2000]. The difference in the glacial temperature anomalies between the records from the open ocean WPWP and coastal WPWP regions suggests a general smaller LGM cooling of the open ocean WPWP compared to coastal WPWP regions.

6.5.3. Surface $\delta^{18}O_{SW}$ variability

The surface $\delta^{18}O_{SW}$ of all three cores shows a striking relation to precession, with $\delta^{18}O_{SW}$ minima corresponding to precession maxima and vice versa. The records hence indicate fresher conditions in the northern and southern WPWP when precession is high (Figure 6.5). Spectral analyses confirm the presence of statistical significant periodicities on the precession band of 23 kyr with power spectra peaking at 0.042 kyr^{-1} (GeoB 17426-3), 0.042 kyr^{-1} (GeoB 17419-1) [*Hollstein et al.*, submitted], and 0.044 kyr^{-1} (MD06-3067) (Figure 6.7).

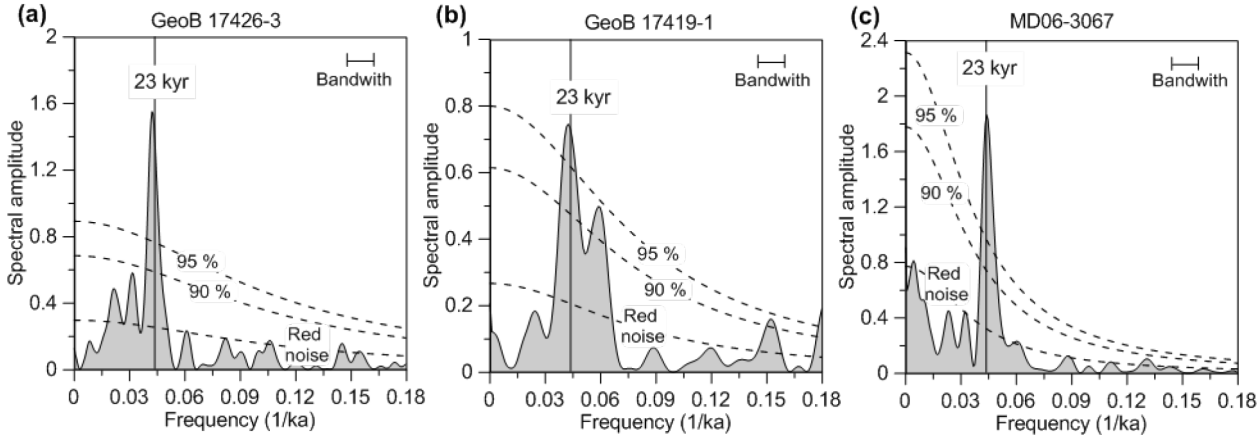

Figure 6.7. Spectra of surface $\delta^{18}O_{SW}$ of (a) GeoB 17426-3, (b) combined MD05-2920 and GeoB 17419-1 [see *Hollstein et al.*, submitted], and (c) MD06-3067. Spectral analyses were performed using REDFIT [*Schulz and Mudelsee*, 2002]. We chose a Welch type spectral window and used an oversampling factor of 9. The bandwidth is 6 dB. Dashed lines denote the red-noise spectrum and 90 and 95% confidence levels. Vertical black bars indicate the frequency that corresponds to the precession periodicity of 23 kyr.

The $\delta^{18}O_{SW}$ variations of core GeoB 17419-1 were interpreted to be primarily related to local variations in precipitation with enhanced (decreased) precipitation when precession is high (low) [*Hollstein et al.*, submitted]. The rainfall variability has been linked to variations in the rainfall intensity and/or position of the ITCZ with a more southern (northern position) when precession is high (low). Additionally, rainfall variations over PNG associated with variations in the Austral-Asian monsoon system could affect the $\delta^{18}O_{SW}$ at site GeoB 17419-1 [*Hollstein et al.*, submitted]. In contrast to GeoB 17419-1, site GeoB 17426-3 is located at an open WPWP site and not affected by continental climate variations and the Austral-Asian monsoon system. The coincidence of the $\delta^{18}O_{SW}$ records of the southern sites hence reveals that the $\delta^{18}O_{SW}$ variability observed in the southern WPWP records, reflects variations in the position or rainfall intensity of the ITCZ.

The surface $\delta^{18}O_{SW}$ of MD06-3067 is likely influenced by the evaporation-precipitation budget, the source of precipitation, as well as by continental runoff from Mindanao [*Bolliet et al.*, 2011]. Attributed solely to variations in precipitation and continental runoff, the $\delta^{18}O_{SW}$ record indicates an increase (decrease) in local and continental precipitation, when precession is high (low). Support for respective rainfall variations comes from proxies of sedimentary discharge from Mindanao that indicate an increase in continental rainfall during high precession [*Fraser et al.*, 2014; *Kissel et al.*, 2010]. The consistency of the absolute $\delta^{18}O_{SW}$ values of the three cores suggests that any changes in the moisture source can only have a limited effect on the $\delta^{18}O_{SW}$ across the WPWP. Additionally, the surface $\delta^{18}O_{SW}$ record of MD06-3067 could be affected by upwelling of saltier thermocline waters associated with the Mindanao Dome. Though the upwelled waters, presently, do not reach the surface, they might have affected the mixed layer isotopic composition. If so, the $\delta^{18}O_{SW}$ record points to an enhanced (reduced) dome intensity when precession is low (high). However, the Mindanao Dome strongly depends on the local wind system. Today, the Mindanao Dome activity is closely related to the Austral-Asian monsoon, with increasing upwelling during boreal winter (austral summer), when northeast winds prevail [*Wijffels et al.*, 1996]. By analogy to modern seasonal variations, one would therefore expect a weaker dome intensity when precession is low. Upwelling related variations in $\delta^{18}O_{SW}$ would thus counteract the observed variations. For this reason, it appears less likely that the surface $\delta^{18}O_{SW}$ record of MD06-3067 is driven by the Mindanao Dome intensity.

We thus infer that the coherent $\delta^{18}O_{SW}$ variations at the GeoB 17426-3, GeoB 17419-1/MD05-2920 and MD06-3067 sites reflect precession-controlled rainfall variation with enhanced (reduced) rainfall, when precession is high (low). The coherence of the surface $\delta^{18}O_{SW}$ records from the northern and southern WPWP suggests a uniform response of rainfall across the WPWP to precession. A northward shift of the ITCZ would be accompanied by decrease in mean annual rainfall over the WPWP relative to periods of high precession. A northward shift of the ITCZ during periods of low precession was also proposed on the

basis of southern Asian speleothem records that reflect an increase in monsoon rainfall during these periods [*Cheng et al.*, 2012; *Wang et al.*, 2014].

We note that precipitation indices from the maritime continent show a different phasing than the WPWP records described above [*Carolin et al.*, 2013; *Dang et al.*, 2015; *Partin et al.*, 2007], suggesting different controls on continental and oceanic precipitation [*Fraser et al.*, 2014]. While the rainfall over the Pacific Ocean is assumed to be mainly controlled by the ITCZ, continental rainfall records are strongly modulated by local boundary conditions (e.g. glacial–interglacial sea level variations).

6.5.3. Thermocline temperature and $\delta^{18}O_{SW}$ variability

The thermocline temperatures of GeoB 17426-3 and MD06-3067 agree well until MIS 4, whereas the GeoB 17419-1 record suggests somewhat lower temperatures than the other two sites. During MIS3, GeoB 17426-3 indicates highest, and GeoB 17419-1 lowest temperatures. While GeoB 17426-3 and MD06-3067 show coolest temperatures during the LGM and a warming thereafter, the thermocline warming at site GeoB 17419-1 starts earlier, around 30 ka. In contrast to MD06-3067 and GeoB 17419-1 and other records from the region [*Stott et al.*, 2002], the temperature record of GeoB 17426-3 does not show a Holocene cooling.

We suggest that such differences between the records are related to the varying impact of astronomical forcing on the different water masses that influence the individual core sites as follows: On the basis of the thermocline temperature record of core GeoB 17419-1 it has been suggested [*Hollstein et al.*, submitted] that the thermocline offshore PNG is strongly influenced by obliquity controlled variations in southern hemisphere mid-latitude climate and ocean conditions. A warming of thermocline waters during periods of high obliquity was interpreted as resulting from reduced subduction and advection of cool waters from the subtropical Pacific along with a reduced export of warm waters from the tropical Pacific [*Hollstein et al.*, submitted]. The obliquity influence is less apparent in GeoB 17426-3. For instance, as mentioned, the thermocline temperature record of GeoB 17426-3 does not show a Holocene cooling trend. The power spectrum of the GeoB 17426-3 confirms that obliquity related 41 kyr cycles are not statistically significant in the temperature record (Figure 6.8). Instead, the spectrum depicts statistically significant peaks at frequencies that correspond to periodicities of about 35 kyr and 23 kyr (Figure 6.8). While the 35 kyr signals cannot be clearly assigned to orbital forcing (it might be a blurred 41 kyr signal though), the presence of 23 kyr cycles in the thermocline temperature demonstrates the influence of precession on the thermocline offshore the Bismarck Archipelago. Generally, thermocline temperatures are warmer (cooler) when precession is low (high).

This discrepancy in the spectra of the thermocline temperature records of the two southern WPWP sites (which are located close to each other) is likely related to the differing origin of the SPTW branches

influencing the two sites. As described in section 6.2, site GeoB 17419-1 is influenced by a SPTW branch that originates in the subtropical South Pacific Ocean and enters the WPWP from the south, whereas site GeoB 17426-3 is influenced by the SPEW that forms in the subtropical central Pacific Ocean and enters the WPWP from the east. Due to its formation at lower latitudes, the SPEW might be less sensitive to obliquity forcing. The different origin of the thermocline water masses influencing sites GeoB 17426-3 and GeoB 17419-1 could also explain the offsets in absolute thermocline temperatures observed during the last glacial period, with cooler temperatures at GeoB 17419-1 and warmer temperatures at GeoB 17426-3. Similar to the temperature record of GeoB 17426-3, the thermocline temperature record of MD06-3067 shows cyclic variations of precessional duration (Figure 6.8). We will discuss the precession-related variability in the thermocline temperature records of GeoB 17426-3 and MD06-3067 further below.

The thermocline $\delta^{18}O_{SW}$ records of GeoB 17426-3, GeoB 17419-1 and MD06-3067 agree well in both absolute $\delta^{18}O_{SW}$ values and pattern. The coherence of the thermocline records is especially surprising, given the fact that the northern and southern WPWP sites are influenced by different water masses. Nowadays, NPTW and SPTW are marked by different salinities with a higher salinity in the SPTW (Figure 6.2b). Although the difference is rather small (~1 psu), we would therefore expect a slightly lower $\delta^{18}O_{SW}$ at the northern site in comparison to the southern sites. However, the record of MD 06-3067 rather indicates that the thermocline $\delta^{18}O_{SW}$ off Mindanao was slightly higher than at the southern sites until the LGM and comparable from the LGM to the late Holocene. If our $\delta^{18}O_{SW}$ estimates are correct, this implies that the salinity at the northern site (relative to the southern sites) must have been relatively higher over the past 160 kyr than it is today. The reason for this shift in the absolute values of the thermocline $\delta^{18}O_{SW}$ of MD06-3067 cannot be clarified on the basis of our data.

The $\delta^{18}O_{SW}$ records are marked by peaks of increasing $\delta^{18}O_{SW}$ around ~130 and ~60 ka, and decreased values between ~120 and ~70 ka. Furthermore, the records depict cyclic variations of precessional duration (Figure 6.8) with generally decreased (increased) $\delta^{18}O_{SW}$ when precession is high (low) (Figure 6.6). Specifically, the $\delta^{18}O_{SW}$ of GeoB 17426-3 is characterized by cyclic variations of 35 kyr and 21 kyr duration (Figure 6.8d), in coherence with the cyclic variations in the thermocline temperature record of the core. The coincidence of thermocline temperature and $\delta^{18}O_{SW}$ variations at site GeoB 17426-3 suggests that the two parameters are controlled by the same forcing. The same pattern is also inherent in the thermocline temperature and $\delta^{18}O_{SW}$ records of MD06-3067, which consistently depict cyclic variations with periodicities around 23 kyr (Figures 6.6 and 6.8). In contrast, the thermocline $\delta^{18}O_{SW}$ record of GeoB 17419-1 shows cyclic variations of precessional duration, while the thermocline temperature record of the core is controlled by obliquity, suggesting a decoupling of thermocline temperature and $\delta^{18}O_{SW}$ within the

Bismarck Sea. Alternatively, the influence of precession on the thermocline temperature at site GeoB 17419-1 could be masked by obliquity-related and glacial–interglacial variations.

It remains unclear whether cyclic variations in the thermocline records are driven by precession controlled variations in the source regions of the NPTW and SPTW/SPEW, or by local processes, such as thermocline ventilation. While the NPTW forms by subduction of surface waters during boreal winter (austral summer) [*Katsura et al.*, 2013], the SPTW/SPEW forms by subduction of surface waters during boreal summer (austral winter) [*Qu et al.*, 2013]. Climate model simulations show that during boreal winter (austral summer), the surface ocean temperature at the northern hemisphere mid-latitudes, where the NPTW is formed, is lower when precession is low [*Rachmayani et al.*, 2016]. During boreal summer (austral winter), the surface ocean temperature at the southern hemisphere mid-latitudes, where the SPTW/SPEW forms, is similar to the preindustrial period with a tendency to somewhat cooler temperatures [*Rachmayani et al.*, 2016]. While it is difficult to assess the variability of the $\delta^{18}O_{SW}$ in the NPTW and SPTW/SPEW source areas, precession-related variations in surface ocean temperature in the source areas of the WPWP thermocline water masses would counteract the temperature variability observed in our records. Potentially, the effect could be outweighed by shifts in the source areas of the SPTW/SPEW and NPTW. For instance, at site GeoB 17426-3, decreasing (increasing) temperature and $\delta^{18}O_{SW}$ values could be explained by the intrusion of cooler (warmer) and more depleted (less depleted) waters during periods of high (low) precession that might be associated with a more southward (northward) position of the Hadley cells and vice versa [*Varma et al.*, 2012].

Precession-controlled variations in the WPWP atmospheric circulation and rainfall could additionally affect the stratification of the upper water column. Recent observations indicate that thermocline mixing along the northern western boundary currents is generally weak [*Liu et al.*, 2017]. However, enhanced mixing is found to be associated with the Mindanao Dome. In contrast to the precession related variations in surface $\delta^{18}O_{SW}$, the variations in thermocline temperature and $\delta^{18}O_{SW}$ observed in MD06-3067 could be related to the local influence of the Mindanao Dome activity, provided that the Mindanao Dome has been stationary over the past 160 kyr. A stronger (reduced) Mindanao Dome intensity during periods of increased (decreased) precession would cause a concomitant cooling and freshening of the thermocline at the core site. In the southern WPWP upward mixing is expected to be smaller.

In addition, enhanced (reduced) rainfall over the WPWP during periods of high (low) precession could affect the stratification of the water column by causing a deepening (lifting) of the pycnocline, and a thermocline shoaling (deepening) and hence favoring a decrease (increase) in both, thermocline $\delta^{18}O_{SW}$ and temperature, when precession is high (low). However, taking present-day seasonal and interannual

variations in WPWP hydrography as a modern analogue such effects are expected to have only a limited influence on the thermocline waters [*Carton and Giese*, 2008; *Locarnini et al*., 2013; *Zweng et al*., 2013].

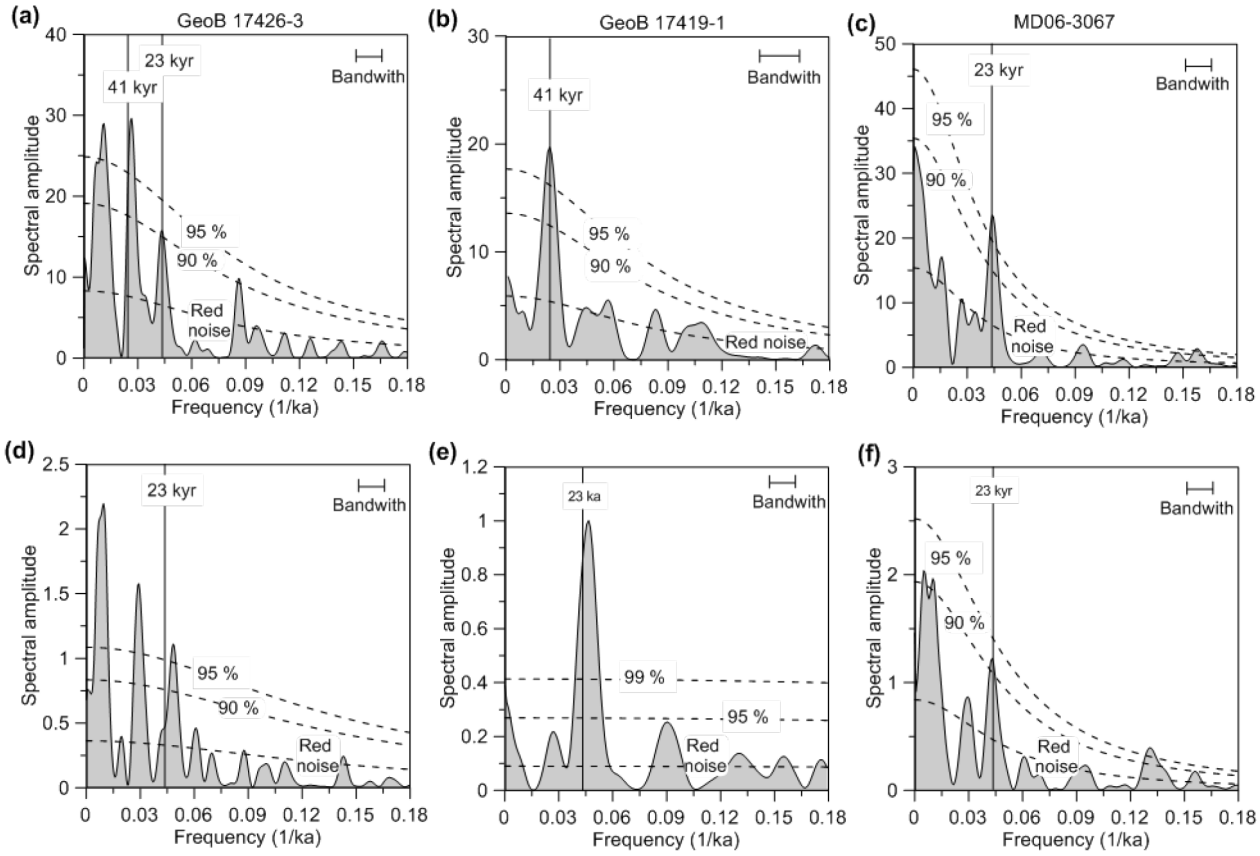

Figure 6.8. Spectra of thermocline temperature (a-c) and $\delta^{18}O_{SW}$ (d-e) of GeoB 17426-3 (a and d), GeoB 17419-1 (b and e), and MD06-3067 (c and f). Spectral analyses were performed using REDFIT [*Schulz and Mudelsee*, 2002]. Outlier of the individual records were eliminated prior to the analyses to avoid a possible control on the outliers on the analyses. We chose a Welch type spectral window and used an oversampling factor of 9. The bandwidth is 6 dB. Dashed lines denote the red-noise spectrum and 90 and 95% confidence levels. Vertical black bars indicate the frequency that corresponds to the precession periodicity of 23 kyr.

6.6. Summary and conclusions

We compile newly generated surface and thermocline shell $\delta^{18}O$, temperature and $\delta^{18}O_{SW}$ records from the southern WPWP offshore the Bismarck Archipelago (GeoB 17426-3) with records from the Bismarck Sea (MD05-2920 and GeoB 17419-1) and the northern WPWP offshore Mindanao (MD06-3067). The compilation indicates that the spatial structure across the WPWP, despite the influence of many different local forcings affecting the individual core sites, remained relatively stable over the past 160 kyr.

A comparison of the SST records suggests a lower glacial cooling of the open ocean WPWP in comparison to coastal WPWP areas.

Records of surface $\delta^{18}O_{SW}$ are interpreted to mainly reflect variations in the amount of rainfall and suggest that precipitation across the WPWP varied uniformly in response to precession with enhanced (decreased) precipitation when precession is high (low). Likely, the ITCZ was located further north during periods of low precession and had a smaller impact on the WPWP.

The thermocline temperature records illustrate the role of the thermocline water masses (NPTW and SPTW/SPEW) in modifying the WPWP. While the Bismarck Sea record shows cyclic variations on the obliquity band, the thermocline temperature records from the area east of the Bismarck Archipelago and the northern WPWP depict cyclic variations of precessional duration. We suggest that such differences between the records are related to the varying impact of astronomical forcing on the individual water masses that influence the core sites. A precession cyclicity is also inherent in the thermolicne $\delta^{18}O_{SW}$ at all three sites. The signal might be related to modifications in the thermocline source waters and/or variations in the stratification of the upper water column.

Acknowledgements

The sample material was collected during the expedition SO-228. We acknowledge the captain, crew, and the scientific shipboard party for their support during the expedition. Henning Kuhnert, Birgit Meyer-Schack and Silvana Pape are acknowledged for technical assistance. The sample material was stored and supplied by the GeoB Core Repository at the MARUM – Center for Marine Environmental Sciences, University of Bremen, Germany. This study is funded by the DFG-Research Center / Cluster of Excellence “The Ocean in the Earth System” and the BMBF project 03G0228A (EISPAC).

Chapter 7.
Synthesis and perspective

7.1. Synthesis

This thesis aims to reconstruct surface and especially thermocline conditions of the Western Pacific Warm Pool (WPWP) during the last (two) glacial–interglacial cycle(s). Presented results are largely based on geochemical proxy records, such as stable isotopes and trace element ratios in planktic foraminifera tests of marine sediment cores from offshore Papua New Guinea (PNG) and the Philippines.

In a first step, a study on **modern** surface sediment samples and water column data was performed to assess the regional calcification depth and temperature of various planktic foraminifera species and to establish regional multispecies and species-specific Mg/Ca-temperature calibrations. The study provides valuable information for the paleo-community working in the tropical Pacific Ocean, allowing the following implications:

- The species *G. ruber* and *G. elongatus* calcify within (~0–80 m), and *G. sacculifer* at the bottom (~45–85 m) of the mixed layer. *P. obliquiloculata* and *N. dutertrei* preserve upper (~90–160 m), and *G. tumida* lower (~230–265 m) thermocline conditions and are therefore appropriate species to reconstruct upper and lower thermocline conditions. Previously published thermocline reconstructions that are based on species should be reconsidered with respect to the new results.
- The Mg/Ca-temperature dependencies of *G. ruber*, *G. elongatus* and G. *tumida* are well described by the previously published multispecies Mg/Ca-temperature calibration of *Anand et al.* [2003]. The calcification temperatures of *G. sacculifer*, *P. obliquiloculata* and *N. dutertrei* in the WPWP, are exceptionally warm and therefore underestimated by published calibrations from other areas. The regional Mg/Ca-temperature relations are best described by Mg/Ca = 0.24 exp 0.097 * T for *G. sacculifer* and by Mg/Ca = 0.21 exp 0.097 * T for *P. obliquiloculata* and *N. dutertrei*.

These results are of key importance aiming at the reconstruction of the paleoconditions in the WPWP. On their basis, *G. ruber* and *P. obliquiloculata* are chosen as suitable indicators for surface and thermocline conditions, respectively. The regional, species-specific Mg/Ca-temperature calibrations set the basis for accurate paleotemperature estimates. Subsequently, in a second step, WPWP surface and thermocline conditions over the **past** (two) glacial–interglacial cycle(s) were reconstructed by analyzing $\delta^{18}O$ values and Mg/Ca ratios in tests of *G. ruber* and *P. obliquiloculata* of sediments retrieved within the Bismarck Sea and east of the Bismarck Archipelago offshore PNG. The reconstructions demonstrate the potential and significance of WPWP thermocline records to better understand ocean and climate dynamics of the

Pacific Ocean and reveal a complex pattern of astronomically driven and glacial–interglacial variations in temperature, salinity and the vertical water column structure:

- Precipitation over the WPWP is mainly controlled by variations in the Earth's orbital precession. Enhanced (decreased) precipitation when precession is high (low) is likely linked to a more southern (northern) position of the Intertropical Convergence Zone (ITCZ).

- The thermocline temperature record of gravity core GeoB 17419-1 (Bismarck Sea) shows warmer (colder) temperatures during periods of high (low) obliquity. This is attributed to obliquity-driven variations in subduction and lateral advection of the source waters, the South Pacific Tropical Water (SPTW) and indicates that the thermocline temperature at the core site is critically influenced by climate variations in the South Pacific mid-latitudes. Specifically, a warming (cooling) of thermocline waters is likely caused by a reduced (enhanced) subduction and advection of cool waters from the subtropical Pacific along with a reduced (increased) export of warm waters from the tropical Pacific. This obliquity-relation is less apparent in the thermocline temperature records of GeoB 17426-3 (east of the Bismarck Archipelago) and published records from the northern WPWP. This discrepancy is likely related to the differing influence of astronomical forcing on the thermocline water masses influencing the individual core sites.

  The thermocline temperature record of GeoB 17419-1 reveals that striking features observed within records from the Indonesian Seas and the Indonesian Troughflow (ITF) outflow region are also recorded off PNG. Specifically, many Holocene surface and thermocline temperature records from the Indonesian Seas and the Timor Sea outflow region show a gradual cooling [see e.g. *Linsley et al.*, 2010; *Rosenthal et al.*, 2013; *Xu et al.*, 2008], as it is also evident in the thermocline temperature record of GeoB 17419-1 and other WPWP records [e.g. *Stott et al.,* 2002; *Dang et al*., 2012]. Previously, the gradual cooling during the Holocene observed in thermocline temperature records from the Timor Sea has been related to an intensification of a cool, thermocline-dominated ITF [*Xu et al.*, 2008]. However, the similarities between western Pacific, Indonesian and Timor Sea records suggest that the observed temperature signal originates in the western Pacific Ocean [see also *Dang et al*., 2012; *Rosenthal et al*., 2013; *Rosenthal et al*., 2017].

- The thermocline temperature and $\delta^{18}O_{SW}$ at the southern and northern WPWP sites are also influenced by precession, with generally cooler (warmer) temperatures at site GeoB 17426-3 and the northern WPWP and depleted (enriched) $\delta^{18}O_{SW}$ at both PNG and northern WPWP sites when precession is high (low). It remains unclear whether these precession-related variations are related to modifications of the thermocline source waters (e.g., by shifts in the formation areas) and/or to local variations in the stratification of the upper water column.

- The *G. ruber* – *P. obliquiloculata* ΔT record of GeoB 17419-1 indicates a thermocline deepening during the LGM in comparison to the present and the last interglacial. A compilation of Mg/Ca-based ΔT records from the WPWP indicates a dipole-like pattern of LGM thermocline depth anomalies with a thermocline shoaling in the northern and a deepening in the southern WPWP. Using the output of Paleoclimate Model Intercomparison Project (PMIP) climate model simulations, the dipole-like pattern is mainly attributed to LGM wind-field anomalies and associated Sverdrup dynamics that are related to a contraction of the Pacific Walker cell, with enhanced ascend over the western Pacific Ocean and reduced convection over Indonesia. In conjunction with alterations in the Indian Walker circulation marked by anomalous ascend over the eastern Indian Ocean and reduced convection over Indonesia [*Mohtadi et al.*, 2017] the results suggest a weaker coupling between the Indian and Pacific Walker cells during the LGM.

  The proxy-model comparison adds an important piece to the ongoing discussion about past variations in the state of the Pacific Ocean and the Pacific Walker circulation. As soon as we better understand the dynamics that controlled the equatorial Pacific Ocean and the Walker circulation during the past, we will be able to better assess future changes of the Walker circulation and potentially the El Niño Southern–Oscillation (ENSO), and its impact on the global climate. The analysis provides further evidence that a modern ENSO analogue is not appropriate to explain long-term variations in the state of the Pacific Ocean and atmosphere.

7.2. Outlook

Several questions of topical interes arise from the hypotheses and conclusions presented above. For instance, the influence of obliquity on WPWP climate and ocean conditions remains an unresolved issue. While proxy records of GeoB 17419-1 and GeoB 17426-3 clearly indicate a precession control on WPWP precipitation, the impact of obliquity on the tropical Pacific atmospheric circulation and WPWP hydroclimate remains enigmatic. Climate model simulations suggest a direct influence of obliquity on the tropical Pacific precipitation via reorganizations of the Hadley circulation [*Bosmans et al.*, 2015; *Mantsis et al.*, 2011; *Mantsis et al.*, 2014; *Rachmayani et al.*, 2016]. This suggestion is further supported by previously published [*Liu et al.*, 2015; *Tachikawa et al.*, 2011] and newly established (this study, chapter 5) proxy records used to reconstruct variations in sediment discharge and continental precipitation above PNG (Ti/Ca and Nd/Ca on planktic foraminifera) that depict significant variations on the obliquity band. However, the proxy records are potentially biased by secondary influences (e.g. variations in the advection of terrigenous material or calcareous productivity) on the obliquity band (chapter 5). It might therefore be valuable to analyze records that unambiguously reflect rainfall variations (e.g. compound-specific leaf

wax δD, $\delta^{13}C$, or lacustrine records) in order to investigate a direct influence of obliquity on WPWP precipitation.

While the thermocline temperature record of core GeoB 17419-1 suggests that the thermocline off PNG is affected by obliquity-driven climate variations of the southern hemisphere mid-latitudes via variations in subduction and lateral advection of the thermocline source waters (the South Pacific Tropical Water) this hypothesis needs to be tested. The GeoB 17419-1 record only covers two and a half obliquity cycles. Thus, longer records, e.g. cores taken within the Bismarck Sea during the IODP expedition 363 [*Rosenthal et al*., 2016] may provide the potential to verify the robustness of the obliquity signal over a few glacial–interglacial cycles. More importantly, a meridional transect of sediment cores from the southern hemisphere mid-latitudes to the WPWP along the East Australian and PNG margins could be used to test the hypothesis that the South Pacific Subtropical Gyre, and hence the advection of thermocline waters, was weaker (stronger) when obliquity was high (low). Obliquity presumably has a strong influence on the meridional (equator–pole) insolation and surface pressure gradients, which are expected to affect the atmospheric and South Pacific Subtropical Gyre circulation [*Lee and Poulsen*, 2005; *Mantsis et al.*, 2011; *Timmermann et al.*, 2014]. A meridional transect of sediment cores could thus be used to reconstruct variations in meridional temperature gradients and consequently provide clues about variations in the strength of the South Pacific Subtropical Gyre circulation in response to obliquity.

Beyond that, future studies should investigate the potential influence of obliquity-controlled variations in the SPTW on the thermocline depth and the surface of the equatorial Pacific and, subsequently, on the state of ENSO and the atmospheric circulation under varying glacial–interglacial boundary conditions. This could be achieved by using a fully coupled climate model able to simulate ocean and atmosphere dynamics under varying obliquity and glacial–interglacial boundary conditions. Inter alia, 10 ka and 30 ka runs in comprehensive Earth system models could provide this option. Alternatively, transient models could enlighten the respective variations in the ocean–atmosphere dynamics. However, these models are much more elaborately and not necessarily needed in this case.

The formation of WPWP thermocline waters masses is tightly coupled to the position of the northern and southern westerly wind belts and the descending branches of the Hadley circulation. The reconstruction of shifts in the westerly wind belts could thus help to reconstruct variations in the atmospheric circulation and potential shifts in the source regions of WPWP thermocline and intermediate water masses.

While coherent variations (e.g. Holocene cooling trends) observed in thermocline temperature records from the WPWP compared to temperature records from the Indonesian Seas and the ITF outflow region suggest that the temperature signals observed in the records originates in the western Pacific Ocean, this hypothesis needs to be proofed in future studies. With respect to this, records from the Indonesian Seas,

along the main ITF pathways, that extend beyond the LGM, are a missing link. In relation to this, it also remains a pending question how source waters of South Pacific origin influenced the ITF during the past. Especially thermocline and intermediate-depth records of gravity cores from the ITF entrances (Molucca, Halmahera or Ceram Sea) could help to reconstruct the water masses that enter the eastern ITF route over time. While Mg/Ca and $\delta^{18}O$ records provide valuable insights into the evolution of temperature and conservative water mass tracers (e.g. $\delta^{18}O_{SW}$ or $\delta^{13}C$) would be additionally useful to follow the water masses entering the ITF from the North and South Pacific Ocean over time.

Finally, the compilation of hitherto available surface-thermocline ΔT records of the WPWP suggest a dipole-like pattern of LGM thermocline depth anomalies with a thermocline shoaling (deepening) in the northern (southern) WPWP. However, so far there are only very few robust ΔT records from the WPWP available. To verify the spatial pattern of LGM thermocline depth anomalies it would therefore be useful to investigate glacial–interglacial (LGM-Holocene) thermocline variations in a meridional transect of gravity cores across the WPWP. Overall, these approaches will further improve our understanding about, how the WPWP and the ITF reacted to various forcings in the past, and how the ocean and climate in this area might behave in response to future climate change.

References

Allen, K. A., B. Hönisch, S. M. Eggins, L. L. Haynes, Y. Rosenthal, and J. Yu (2016), Trace element proxies for surface ocean conditions: A synthesis of culture calibrations with planktic foraminifera, *Geochimica et Cosmochimica Acta*, *193*, 197-221, https://doi.org/10.1016/j.gca.2016.08.015.

An, Z. (2000), The history and variability of the East Asian paleomonsoon climate, *Quaternary Science Reviews*, *19*, 171-187, https://doi.org/10.1016/S0277-3791(99)00060-8.

Anand, P., H. Elderfield, and M. H. Conte (2003), Calibration of Mg/Ca thermometry in planktonic foraminifera from a sediment trap time series, *Paleoceanography*, *18*(2), https://doi.org/10.1029/2002PA000846.

Andreasen, D. J., and A. C. Ravelo (1997), Tropical Pacific Ocean thermocline depth reconstructions for the Last Glacial Maximum, *Paleoceanography*, *12*(3), 395-413, https://doi.org/10.1029/97PA00822.

Arbuszewski, J., P. deMenocal, A. Kaplan, and E. C. Farmer (2010), On the fidelity of shell-derived $\delta^{18}O_{seawater}$ estimates, *Earth and Planetary Science Letters*, *300*(3-4), 185-196, https://doi.org/10.1016/j.epsl.2010.10.035.

Arnold, A. J., and W. C. Parker (2003), Biogeography of planktonic foraminifera, in *Modern foraminifera*, edited by A. Sen Gupta, pp. 103-122, Kluwer Academic Publishers, Dordrecht.

Arz, H., J. Pätzold, and G. Wefer (1998), Correlated millennial-scale changes in surface hydrography and terrigenous sediment yield inferred from Last-Glacial marine deposits off northeastern Brazil, *Quaternary Research*, *50*, 157-166.

Aurahs, R., Y. Treis, K. Darling, and M. Kucera (2011), A revised taxonomic and phylogenetic concept for the planktonic foraminifer species *Globigerinoides ruber* based on molecular and morphometric evidence, *Marine Micropaleontology*, *79*(1-2), 1-14, https://doi.org/10.1016/j.marmicro.2010.12.001.

Bard, E. (1988), Correction of accelerator mass spectrometry ^{14}C ages measured in planktonic foraminifera: Paleoceanographic implications, *Paleoceanography*, *3*, 635-645.

Barker, S., M. Greaves, and H. Elderfield (2003), A study of cleaning procedures used for foraminiferal Mg/Ca paleothermometry, *Geochemistry Geophysics Geosystems*, *4*(9), https://doi.org/10.1029/2003GC000559.

Bazin, L., et al. (2013), An optimized multi-proxy, multi-site Antarctic ice and gas orbital chronology (AICC2012): 120-800 ka, *Climate of the Past*, *9*(4), 1715-1731, https://doi.org/10.5194/cp-9-1715-2013.

Beaufort, L., T. de Garidel-Thoron, A. C. Mix, and N. G. Pisias (2001), ENSO-like forcing on oceanic primary production during the Late Pleistocene, *Science*, *293*(5539), 2440-2444, https://doi.org/10.1126/science.293.5539.2440.

Beck, C., J. Grieser, and B. Rudolf (2005), A new monthly precipitation climatology for the global land areas for the period 1951 to 2000. DWD, Klimastatusbericht KSB 2004.

Bemis, B. E., H. J. Spero, J. Bijma, and D. W. Lea (1998), Reevaluation of the oxygen isotopic composition of planktonic foraminifera: Experimental results and revised paleotemperature equations, *Paleoceanography*, *13*(2), 150-160, https://doi.org/10.1029/98pa00070.

Berger, W. H., M. C. Bonneau, and F. L. Parker (1982), Foraminifera on the deep-sea floor: Lysocline and dissolution rate, *Oceanologica Acta*, *5*, 249-258.

Bjerknes, J. (1969), Atmospheric teleconnections from the equatorial Pacific, *Monthly Weather Review*, *97*(3), 163-172.

Blaauw, M., and J. A. Christen (2011), Flexible Paleoclimate Age-Depth Models Using an Autoregressive Gamma Process, *Bayesian Analysis*, *6*, 457-474, https://doi.org/10.1214/11-ba618.

Böhlke, J. K., J. R. de Laeter, P. De Bièvre, H. Hidaka, H. S. Peiser, K. J. R. Rosman, and P. D. P. Taylor (2005), Isotopic Compositions of the Elements, 2001, *Journal of Physical and Chemical Reference Data*, *34*(1), 57-67, https://doi.org/10.1063/1.1836764.

Böhm, F., M. M. Joachimski, H. Lehnert, G. Morgenroth, W. Kretschmer, J. Vacelet, and W.-C. Dullo (1996), Carbon isotope records from extant Caribbean and South Pacific sponges: Evolution of $\delta^{13}C$ in surface

water DIC, *Earth and Planetary Science Letters*, *139*(1), 291-303, https://doi.org/10.1016/0012-821X(96)00006-4.

Bolliet, T., A. Holbourn, W. Kuhnt, C. Laj, C. Kissel, L. Beaufort, M. Kienast, N. Andersen, and D. Garbe-Schonberg (2011), Mindanao Dome variability over the last 160 kyr: Episodic glacial cooling of the West Pacific Warm Pool, *Paleoceanography*, *26*(1), https://doi.org/10.1029/2010pa001966.

Bosmans, J. H. C., F. J. Hilgen, E. Tuenter, and L. J. Lourens (2015), Obliquity forcing of low-latitude climate, *Climate of the Past*, *11*(10), 1335-1346, https://doi.org/10.5194/cp-11-1335-2015.

Bostock, H. C., B. N. Opdyke, and M. J. M. Williams (2010), Characterising the intermediate depth waters of the Pacific Ocean using $\delta^{13}C$ and other geochemical tracers, *Deep Sea Research Part I: Oceanographic Research Papers*, *57*(7), 847-859, https://doi.org/10.1016/j.dsr.2010.04.005.

Bostock, H. C., et al. (2013), A review of the Australian–New Zealand sector of the Southern Ocean over the last 30 ka, *Quaternary Science Reviews*, *74*, 35-57, https://doi.org/10.1016/j.quascirev.2012.07.018.

Bouvier-Soumagnac, Y., and J. C. Duplessy (1985), Carbon and oxygen isotopic composition of planktonic foraminifera from laboratory culture, plankton tows and Recent sediment: implications for the reconstruction of paleoclimatic conditions and of the global carbon cycle, *Journal of Foraminiferal Research*, *15*, 302-320.

Boyle, E. A., and L. D. Keigwin (1985), Comparison of Atlantic and Pacific paleochemical records for the last 215,000 years: changes in deep ocean circulation and chemical inventories, *Earth and Planetary Science Letters*, *76*, 135-150.

Braconnot, P., S. P. Harrison, M. Kageyama, P. J. Bartlein, V. Masson-Delmotte, A. Abe-Ouchi, B. Otto-Bliesner, and Y. Zhao (2012), Evaluation of climate models using palaeoclimatic data, *Nature Climate Change*, *2*(6), 417-424, https://doi.org/10.1038/nclimate1456.

Braconnot, P., et al. (2007), Results of PMIP2 coupled simulations of the Mid-Holocene and Last Glacial Maximum – Part 1: experiments and large-scale features, *Climate of the Past*, *3*, 261-277, 10.5194/cp-3-261-2007.

Brown, S. J., and H. Elderfield (1996), Variations in Mg/Ca and Sr/Ca ratios of planktonic foraminifera caused by postdepositional dissolution: Evidence of shallow Mg-dependent dissolution, *Paleoceanography*, *11*, 543-551.

Carolin, S. A., K. M. Cobb, J. F. Adkins, B. Clark, J. L. Conroy, S. Lejau, J. Malang, and A. A. Tuen (2013), Varied response of western Pacific hydrology to climate forcings over the last glacial period, *Science*, *340*(6140), 1564-1566, https://doi.org/10.1126/science.1233797.

Carton, J. A., and B. S. Giese (2008), A reanalysis of ocean climate using simple ocean data assimilation (SODA). , *Monthly Weather Review*, *136*, 2999-3017.

Chang, C.-P., Z. Wang, J. McBride, C.-H. Liu (2005), Annual cycle of Southeast Asia-Maritime Continent rainfall and the asymmetric monsoon transition, *Journal of Climate*, *18*, 287-301.

Cheng, H., A. Sinha, X. Wang, F. Cruz, and R. Edwards (2012), The Global Paleomonsoon as seen through speleothem records from Asia and the Americas, *Climate Dynamics*, *39*(5), 1045-1062, https://doi.org/10.1007/s00382-012-1363-7.

Clement, A. C., R. Seager, and M. A. Cane (1999), Orbital controls on the El Niño/Southern Oscillation and the tropical climate, *Paleoceanography*, *14*(4), 441-456, https://doi.org/10.1029/1999pa900013.

Cléroux, C., E. Cortijo, P. Anand, L. Labeyrie, F. Bassinot, N. Caillon, and J.-C. Duplessy (2008), Mg/Ca and Sr/Ca ratios in planktonic foraminifera: Proxies for upper water column temperature reconstruction, *Paleoceanography*, *23*(3), PA3214, doi:10.1029/2007pa001505.

Collins, M., et al. (2010), The impact of global warming on the tropical Pacific Ocean and El Niño, *Nat Geosci*, *3*(6), 391-397, 10.1038/ngeo868.

Conroy, J. L., D. M. Thompson, K. M. Cobb, D. Noone, S. Rea, and A. N. Legrande (2017), Spatiotemporal variability in the $\delta^{18}O$-salinity relationship of seawater across the tropical Pacific Ocean, *Paleoceanography*, https://doi.org/10.1002/2016pa003073.

Coplen, T. B. (1996), More uncertainty than necessary, *Paleoceanography*, *11*, 369-370.

Craig, H., and L. I. Gordon (1965), Deuterium and oxygen-18 variations in the ocean and the marine atmosphere, in *Stable isotope in oceanographic studies and paleotemperatures*, edited by E. Tongiorgi, pp. 9-130, Spoleto, Pisa (Consiglio Nazionale delle Ricerche, Laboratorio di Geologia Nucleare).

Cresswell, G. R. (2000), Coastal currents of northern Papua New Guinea, and the Sepik River outflow, *Marine and Freshwater Research*, *51*(6), 553, https://doi.org/10.1071/mf99135.

Dang, H., C. Kissel, and F. Bassinot (2015), Precessional changes in the western equatorial Pacific hydroclimate: A 240 kyr marine record from the Halmahera Sea, East Indonesia, *Geochemistry Geophysics Geosystems*, *16*, 148-164, https://doi.org/10.1002/2014GC005550.

Dang, H., Z. Jian, F. Bassinot, P. Qiao, and X. Cheng (2012), Decoupled Holocene variability in surface and thermocline water temperatures of the Indo-Pacific Warm Pool, *Geophysical Research Letters*, *39*(1), https://doi.org/10.1029/2011gl050154.

de Garidel-Thoron, T., Y. Rosenthal, F. Bassinot, and L. Beaufort (2005), Stable sea surface temperatures in the western Pacific warm pool over the past 1.75 million years, *Nature*, *433*(7023), 294-298, https://doi.org/10.1038/nature03189.

de Garidel-Thoron, T., Y. Rosenthal, L. Beaufort, E. Bard, C. Sonzogni, and A. C. Mix (2007), A multiproxy assessment of the western equatorial Pacific hydrography during the last 30 kyr, *Paleoceanography*, *22*, https://doi.org/10.1029/2006PA001269.

Dekens, P. S., D. W. Lea, D. K. Pak, and H. J. Spero (2002), Core top calibration of Mg/Ca in tropical foraminifera: Refining paleotemperature estimation, *Geochemistry, Geophysics, Geosystems*, *3*(4), https://doi.org/10.1029/2001GC000200.

DiNezio, P. N., and J. E. Tierney (2013), The effect of sea level on glacial Indo-Pacific climate, *Nat Geosci*, *6*(6), 485-491, 10.1038/ngeo1823.

DiNezio, P. N., A. Clement, G. A. Vecchi, B. Soden, A. J. Broccoli, B. L. Otto-Bliesner, and P. Braconnot (2011), The response of the Walker circulation to Last Glacial Maximum forcing: Implications for detection in proxies, *Paleoceanography*, *26*(3), https://doi.org/10.1029/2010PA002083.

Ding, X., F. Bassinot, F. Guichard, and N. Q. Fang (2013), Indonesian Throughflow and monsoon activity records in the Timor Sea since the last glacial maximum, *Marine Micropaleontology*, *101*, 115-126, https://doi.10.1016/j.marmicro.2013.02.003.

Donohoe, A., J. Marshall, D. Ferreira, and D. McGee (2013), The Relationship between ITCZ Location and Cross-Equatorial Atmospheric Heat Transport: From the Seasonal Cycle to the Last Glacial Maximum, *Journal of Climate*, *26*(11), 3597-3618, https://doi.org/10.1175/jcli-d-12-00467.1.

Elderfield, H., and G. Ganssen (2000), Past temperature and $\delta^{18}O$ of surface ocean waters inferred from foraminiferal Mg/Ca ratios, *Nature*, *405*(6785), 442-445, https://doi.org/10.1038/35013033.

Emile-Geay, J., et al. (2015), Links between tropical Pacific seasonal, interannual and orbital variability during the Holocene, *Nat Geosci*, *9*(2), 168-173, 10.1038/ngeo2608.

Epstein, S., and T. Mayeda (1953), Variation of O^{18} content of waters from natural sources, *Geochimica et Cosmochimica Acta*, *4*, 213-224.

Evans, D., B. S. Wade, M. Henehan, J. Erez, and W. Müller (2016), Revisiting carbonate chemistry controls on planktic foraminifera Mg/Ca: implications for sea surface temperature and hydrology shifts over the Paleocene–Eocene Thermal Maximum and Eocene–Oligocene transition, *Climate of the Past*, *12*(4), 819-835, https://doi.org/10.5194/cp-12-819-2016.

Fairbanks, R. G. (1982), The origin of Continental Shelf and Slope Water in the New York Bight of Maine: Evidence from $H_2{}^{18}O/H_2{}^{16}O$ Ratio Measurements, *Journal of Geophysical Research*, *87*(C8), 5796-5808.

Fairbanks, R. G. (1989), A 17,000 year glacio-eustratic sea level record: influence of glacial melting rate on the Younger Dryas event and deep-ocean circulation, *Nature*, *342*, 637-642.

Fairbanks, R. G., C. D. Charles, and J. D. Wright (1992), Origin of global meltwater pulses, in *Radiocarbon after four decades*, edited by R. E. Taylor, pp. 473-500, Springer Verlag.

Fairbanks, R. G., M. N. Evans, J. L. Rubenstone, R. A. Mortlock, K. Broad, M. D. Moore, and C. D. Charles (1997), Evaluating climate indices and their geochemical proxies measured in corals, *Coral Reefs*, *16*, 93-100.

Farmer, E. C., A. Kaplan, P. B. de Menocal, and J. Lynch-Stieglitz (2007), Corroborating ecological depth preferences of planktonic foraminifera in the tropical Atlantic with the stable oxygen isotope ratios of core top specimens, *Paleoceanography*, *22*(3), https://doi.org/10.1029/2006PA001361.

Ferguson, J. E., G. M. Henderson, M. Kucera, and R. E. M. Rickaby (2008), Systematic change of foraminiferal Mg/Ca ratios across a strong salinity gradient, *Earth and Planetary Science Letters*, *265*(1-2), 153-166, https://doi.org/10.1016/j.epsl.2007.10.011.

Fine, R. A., R. Lukas, F. M. Bingham, M. J. Warner, and R. H. Gammon (1994), The western equatorial Pacific: A water mass crossroads, *Journal of Geophysical Research*, *99*(C12), 63-80, https://doi.org/10.1029/94jc02277.

Firing, E., Y. Kashino, and P. Hacker (2005), Energetic subthermocline currents observed east of Mindanao, *Deep-Sea Res*, *52*(3-4), 605-613, https://doi.org/10.1016/j.dsr2.2004.12.007.

Ford, H. L., A. C. Ravelo, and P. J. Polissar (2015), Reduced El Nino-Southern Oscillation during the Last Glacial Maximum, *Science*, *347*(6219), 255-258, https://doi.org/10.1126/science.1258437.

Fraser, N., W. Kuhnt, A. Holbourn, T. Bolliet, N. Andersen, T. Blanz, and L. Beaufort (2014), Precipitation variability within the West Pacific Warm Pool over the past 120 ka: Evidence from the Davao Gulf, southern Philippines, *Paleoceanography*, *29*(11), 1094-1110, https://doi.org/10.1002/2013pa002599.

Friedli, H., H. Lötscher, H. Oeschger, U. Siegenthaler, and B. Stauffer (1986), Ice core record of the $^{13}C/^{12}C$ ratio of atmospheric CO_2 in the past two centuries, *Nature*, *324*, 237-238.

Gagan, M. K., E. J. Hendy, S. G. Haberle, and W. S. Hantoro (2004), Post-glacial evolution of the Indo-Pacific Warm Pool and El Niño-Southern oscillation, *Quaternary International*, *118-119*, 127-143, https://doi.org/10.1016/s1040-6182(03)00134-4.

Gasparin, F., A. Ganachaud, C. Maes, F. Marin, and G. Eldin (2012), Oceanic transports through the Solomon Sea: The bend of the New Guinea Coastal Undercurrent, *Geophysical Research Letters*, *39*(15), https://doi.org/10.1029/2012gl052575.

Gasparin, F., C. Maes, J. Sudre, V. Garcon, and A. Ganachaud (2014), Water mass analysis of the Coral Sea through an Optimum Multiparameter method, *Journal of Geophysical Research: Oceans*, *119*, 7229-7244, https://doi.10.1002/2014JCO10246.

Gibbons, F. T., D. W. Oppo, M. Mohtadi, Y. Rosenthal, J. Cheng, Z. Liu, and B. K. Linsley (2014), Deglacial δ18O and hydrologic variability in the tropical Pacific and Indian Oceans, *Earth and Planetary Science Letters*, *387*, 240-251, 10.1016/j.epsl.2013.11.032.

Gill, A. E. (1980), Some simple solutions for heat-induced tropical circulation, *Quarterly Journal of the Royal Meteorological Society*, *106*, 447-462, https://10.1002/qj.49710644905.

Godwin, H. (1962), Half-life of radiocarbon, *Nature*, *195*, 984.

Goodman, P. J., W. Hazeleger, P. De Vries, and M. Cane (2005), Pathways into the Pacific Equatorial Undercurrent: A trajectory analysis, *Journal of Physical Oceanography*, *35*(11), 2134-2151, https://doi.org/10.1175/Jpo2825.1.

Gordon, A. L. (1986), Interocean exchange of thermocline water, *Journal of Geophysical Research*, *91*(C4), 5037, doi:10.1029/JC091iC04p05037.

Gordon, A. L., P. Flament, C. Villanoy, and L. Centurioni (2014), The nascent Kuroshio of Lamon Bay, *J Geophys Res-Oceans*, *119*(7), 4251-4263, https://doi.org/10.1002/2014jc009882.

Greaves, M., et al. (2008), Interlaboratory comparison study of calibration standards for foraminiferal Mg/Ca thermometry, *Geochemistry Geophysics Geosystems*, *9*, Q08010, doi:08010.01029/02008GC001974, Artn Q08010, https://doi.org/ 10.1029/2008gc001974.

Grenier, M., C. Jeandel, F. Lacan, D. Vance, C. Venchiarutti, A. Cros, and S. Cravatte (2013), From the subtropics to the central equatorial Pacific Ocean: Neodymium isotopic composition and rare earth element concentration variations, *Journal of Geophysical Research: Oceans*, *118*(2), 592-618, https://doi.org/10.1029/2012jc008239.

Grenier, M., S. Cravatte, B. Blanke, C. Menkes, A. Koch-Larrouy, F. Durand, A. Melet, and C. Jeandel (2011), From the western boundary currents to the Pacific Equatorial Undercurrent: Modeled pathways and water mass evolutions, *Journal of Geophysical Research*, *116*(C12), https://doi.org/10.1029/2011jc007477.

Griffiths, M. L., et al. (2009), Increasing Australian–Indonesian monsoon rainfall linked to early Holocene sea-level rise, *Nat Geosci*, *2*(9), 636-639, 10.1038/ngeo605.

Gu, D., and S. G. H. Philander (1997), Interdecadal climate fluctuations that depend on exchanges between the tropics and extratropics, *Science*, *275*(5301), 805-807, https://doi.org/10.1126/science.275.5301.805

Hanawa, K., and L. D. Talley (2001), Mode Waters, in *Ocean circulation and climate: Observing and modeling the global ocean*, edited by G. Siedler, J. Church and J. L. A. Gould, pp. 373-386, Academic, London.

Harrison, D. E., and G. A. Vecchi (2001), El Niño and La Niña - Equatorial Pacific thermocline depth and sea surface temperature anomalies, 1986-98, *Geophysical Research Letters*, *28*(6), 1051-1054, https://doi.org/10.1029/1999GL011307.

Harrison, S. P., P. J. Bartlein, K. Izumi, G. Li, J. Annan, J. Hargreaves, P. Braconnot, and M. Kageyama (2015), Evaluation of CMIP5 palaeo-simulations to improve climate projections, *Nature Clim. Change*, *5*, 735-743, https://doi.org/10.1038/nclimate2649.

Hartin, C. A., R. A. Fine, B. M. Sloyan, L. D. Talley, T. K. Chereskin, and J. Happell (2011), Formation rates of Subantarctic mode water and Antarctic intermediate water within the South Pacific, *Deep Sea Research Part I: Oceanographic Research Papers*, *58*(5), 524-534, https://doi.org/10.1016/j.dsr.2011.02.010.

Hertzberg, J. E., and M. W. Schmidt (2013), Refining *Globigerinoides ruber* Mg/Ca paleothermometry in the Atlantic Ocean, *Earth and Planetary Science Letters*, *383*, 123-133, https://doi.org/10.1016/j.epsl.2013.09.044.

Higgins, H. W., D. J. Mackey, and L. Clementson (2006), Phytoplankton distribution in the Bismarck Sea north of Papua New Guinea: The effect of the Sepik River outflow, *Deep-Sea Research Part I: Oceanographic Research Papers*, *53*(11), 1845-1863, doi:10.1016/j.dsr.2006.09.001.

Holbourn, A., A. S. Henderson, and N. MacLeod (2013), *Atlas of benthic foraminifera*, Wiley-Blackwell, London.

Hollstein, M., M. Mohtadi, Y. Rosenthal, P. Moffa Sanchez, D. Oppo, G. Martínez-Méndez, S. Steinke, and D. Hebbeln (2017), Stable oxygen isotopes and Mg/Ca in planktic foraminifera from modern surface sediments of the Western Pacific Warm Pool: Implications for thermocline reconstructions, *Paleoceanography*, https://doi.org/10.1002/2017PA003122.

Hollstein, M., M. Mohtadi, Y. Rosenthal, M. Prange, D. Oppo, K. Tachikawa, G. Martínez-Méndez, S. Steinke, P. Moffa Sanchez, and D. Hebbeln, Glacial-interglacial and astronomically driven variations in Western Pacific Warm Pool surface and thermocline conditions over the past 110,000 years, submitted to *Quaternary Science Reviews*.

Hönisch, B., K. A. Allen, D. W. Lea, H. J. Spero, S. M. Eggins, J. Arbuszewski, P. deMenocal, Y. Rosenthal, A. D. Russell, and H. Elderfield (2013), The influence of salinity on Mg/Ca in planktic foraminifers – Evidence from cultures, core-top sediments and complementary $\delta^{18}O$, *Geochimica et Cosmochimica Acta*, *121*, 196-213, https://doi.org/10.1016/j.gca.2013.07.028.

Hu, D., et al. (2015), Pacific western boundary currents and their roles in climate, *Nature*, *522*(7556), 299-308, https://doi.org/10.1038/nature14504.

Hughen, K. A. (2007), Chapter Five Radiocarbon Dating of Deep-Sea Sediments, *1*, 185-210, https://doi.org/10.1016/s1572-5480(07)01010-x.

Hut, G. (1987), Consultants group meeting on stable isotopic reference samples for geochemical and hydrological investigations, edited, p. 42, International Atomic Energy Agency, Vienna.

IAEA (2000), Stable isotope processes in the water cycle, paper presented at International Atomic Energy Agency, www.iaea.or.at/programmes/ripc/ih/volumes/vol_two/cht_ii_03.pdf, Vienna.

Imbrie, J., J. D. Hays, D. G. Martinson, A. McIntyre, A. C. Mix, J. J. Morley, N. G. Pisias, W. L. Prell, and N. J. Shackleton (1984), The orbital theory of Pleistocene climate: support from a revised chronology of the marine $\delta^{18}O$ record, in *Milankovitch and Climate, Part 1*, edited by A. L. Berger, et al., pp. 269-305, D. Reidel Publishing Company, Hingham.

Isobe, T., E. D. Feigelson, M. G. Akritas, and G. J. Babu (1990), Linear Regression in Astronomy I., *The Astrophysical Journal*, *364*, 104-113.

Jourdain, N. C., A. S. Gupta, A. S. Taschetto, C. C. Ummenhofer, A. F. Moise, and K. Ashok (2013), The Indo-Australian monsoon and its relationship to ENSO and IOD in reanalysis data and the CMIP3/CMIP5 simulations, *Climate Dynamics*, *41*(11-12), 3073-3102, 10.1007/s00382-013-1676-1.

Katsura, S., E. Oka, B. Qui, and N. Schneider (2013), Formation and subduction of North Pacific Tropical Water and their interannual variability, *Journal of Physical Oceanography*, *43*, 2400-2415, https://doi.org/10.1175/JPO-D-13-031.1.

Kawahata, H. (2005), Stable isotopic composition of two morphotypes of Globigerinoides ruber (white) in the subtropical gyre in the North Pacific, *Paleontological Research*, *9*(1), 27-35.

Kawahata, H., A. Nishimura, and M. K. Gagan (2002), Seasonal change in foraminiferal production in the western equatorial Pacific warm pool: evidence from sediment trap experiments, *Deep-Sea Research Part II: Topical Studies in Oceanography*, *49*(13-14), 2783-2800, https://doi.org/10.1016/S0967-0645(02)00058-9.

Kennett, J. P. (1976), Phenotypic variation in some recent and late Cenozoic planktonic foraminifera. , in *Foraminifera*, edited by R. H. Hedley and C. G. Adams, pp. 111-170, Academic Press, New York.

Kessler, W. S., and L. Gourdeau (2007), The annual cycle of circulation of the southwest subtropical pacific, analyzed in an ocean GCM, *Journal of Physical Oceanography*, *37*(6), 1610-1627, https://doi.org/10.1175/Jpo3046.1.

Kim, S.-T., and J. R. O'Neil (1997), Equilibrium and nonequilibrium oxygen isotope effects in synthetic carbonates, *Geochimica et Cosmochimica Acta*, *61*(16), 3461-3475, 10.1016/s0016-7037(97)00169-5.

Kısakürek, B., A. Eisenhauer, F. Böhm, D. Garbe-Schönberg, and J. Erez (2008), Controls on shell Mg/Ca and Sr/Ca in cultured planktonic foraminiferan, *Globigerinoides ruber* (white), *Earth and Planetary Science Letters*, *273*(3-4), 260-269, https://doi.org/10.1016/j.epsl.2008.06.026.

Kissel, C., C. Laj, M. Kienast, T. Bolliet, A. Holbourn, P. Hill, W. Kuhnt, and P. Braconnot (2010), Monsoon variability and deep oceanic circulation in the western equatorial Pacific over the last climatic cycle: Insights from sedimentary magnetic properties and sortable silt, *Paleoceanography*, *25*(3), 10.1029/2010pa001980.

Koutavas, A., J. Lynch-Stieglitz, T. M. Marchitto, and J. P. Sachs (2002), El Nino-like pattern in ice age tropical Pacific sea surface temperature, *Science*, *297*, 226-230.

Kucera, M. (2007), Chapter Six Planktonic Foraminifera as Tracers of Past Oceanic Environments, *1*, 213-262, https://doi.org/10.1016/s1572-5480(07)01011-1.

Kuroda, Y. (2000), Variability of currents off the northern coast of New Guinea, *Journal of Oceanography*, *56*, 103-116, https://doi.org/10.1023/A:1011122810354.

Kuroyanagi, A., and H. Kawahata (2004), Vertical distribution of living planktonic foraminifera in the seas around Japan, *Marine Micropaleontology*, *53*(1-2), 173-196, https://doi.org/10.1016/j.marmicro.2004.06.001.

Kutzbach, J. E., X. Liu, Z. Y. Liu, and G. Chen (2008), Simulation of the evolutionary response of global summer monsoons to orbital forcing over the past 280,000 years, *Climate Dynamics*, *360*, 567-579, https://doi.org/10.1007/s00382-007-0308-z.

Laskar, J. (1990), The chaotic motion of the solar system: a numerical estimate of the size of the chaotic zones, *Icarus*, *88*, 266-291.

Lea, D. W. (2014), Elemental and Isotopic Proxies of Past Ocean Temperatures, 373-397, https://doi.org/10.1016/b978-0-08-095975-7.00614-8.

Lea, D. W., T. A. Mashiotta, and H. J. Spero (1999), Controls on magnesium and strontium uptake in planktonic foraminifera determined by live culturing, *Geochimica et Cosmochimica Acta*, *63*(16), 2369-2379, https://doi.org/10.1016/S0016-7037(99)00197-0.

Lea, D. W., D. K. Pak, and H. J. Spero (2000), Climate impact of late quaternary equatorial pacific sea surface temperature variations, *Science*, *289*(5485), 1719-1724.

Lee, S. Y., and C. J. Poulsen (2005), Tropical Pacific climate response to obliquity forcing in the Pleistocene, *Paleoceanography*, *20*(4), https://doi.org/10.1029/2005PA001161.

Leech, P. J., J. Lynch-Stieglitz, and R. Zhang (2013), Western Pacific thermocline structure and the Pacific marine Intertropical Convergence Zone during the Last Glacial Maximum, *Earth and Planetary Science Letters*, *363*, 133-143, https://doi.org/10.1016/j.epsl.2012.12.026.

LeGrande, A. N., and G. A. Schmidt (2006), Global gridded data set of the oxygen isotopic composition in seawater, *Geophysical Research Letters*, *33*(12), https://doi.org/10.1029/2006gl026011.

LeGrande, A. N., and G. A. Schmidt (2011), Water isotopologues as a quantitative paleosalinity proxy, *Paleoceanography*, *26*(3), https://doi.org/10.1029/2010pa002043.

Libby, W. F. (1955), *Radiocarbon dating*, University of Chicago Press, Chicago.

Linsley, B. K., Y. Rosenthal, and D. W. Oppo (2010), Holocene evolution of the Indonesian throughflow and the western Pacific warm pool, *Nat Geosci*, *3*(8), 578-583, https://doi.org/10.1038/Ngeo920.

Lisiecki, L. E., and M. E. Raymo (2005), A Pliocene-Pleistocene stack of 57 globally distributed benthic $\delta^{18}O$ records, *Paleoceanography*, *20*(1), https://doi.org/10.1029/2004pa001071.

Liu, Z. Y., J. Kutzbach, and L. X. Wu (2000), Modeling climate shift of El Niño variability in the Holocene, *Geophysical Research Letters*, *27*(15), 2265-2268.

Liu, Z., Q. Lian, F. Zhang, L. Wang, M. Li, X. Bai, J. Wang, and F. Wang (2017), Weak Thermocline Mixing in the North Pacific Low-Latitude Western Boundary Current System, *Geophysical Research Letters*, *44*(20), 10,530-510,539, 10.1002/2017gl075210.

Liu, Y., et al. (2015), Obliquity pacing of the western Pacific Intertropical Convergence Zone over the past 282,000 years, *Nature communications*, *6*, 10018, https://doi.org/10.1038/ncomms10018.

Locarnini, R. A., et al. (2013), *World Ocean Atlas 2013, Volume 1: Temperature.*, U.S. Government Printing Office, Washington, D.C.

Lončarić, N., F. J. C. Peeters, D. Kroon, and G.-J. A. Brummer (2006), Oxygen isotope ecology of recent planktic foraminifera at the central Walvis Ridge (SE Atlantic), *Paleoceanography*, *21*(3), https://doi.org/10.1029/2005pa001207.

Lückge, A., M. Mohtadi, C. Rühlemann, G. Scheeder, A. Vink, L. Reinhardt, and M. Wiedicke (2009), Monsoon versus ocean circulation controls on paleoenvironmental condition off southern Sumatra during the past 300,000 years, *Paleoceanography*, *24*, https://doi.org/10.1029/2008PA001627.

Lukas, R., E. Firing, P. Hacker, P. L. Richardson, C. A. Collins, R. Fine, and R. Gammon (1991), Observations of the Mindanao Current during the Western Equatorial Pacific-Ocean Circulation Study, *J Geophys Res-Oceans*, *96*(C4), 7089-7104, Doi 10.1029/91jc00062.

Mantsis, D. F., A. C. Clement, A. J. Broccoli, and M. P. Erb (2011), Climate Feedbacks in Response to Changes in Obliquity, *Journal of Climate*, *24*(11), 2830-2845, https://doi.org/10.1175/2010jcli3986.1.

Mantsis, D. F., B. R. Lintner, A. J. Broccoli, M. P. Erb, A. C. Clement, and H.-S. Park (2014), The Response of Large-Scale Circulation to Obliquity-Induced Changes in Meridional Heating Gradients, *Journal of Climate*, *27*(14), 5504-5516, https://doi.org/10.1175/jcli-d-13-00526.1.

Martin, P. A., and D. W. Lea (2002), A simple evaluation of cleaning procedures on fossil benthic foraminiferal Mg/Ca, *Geochemistry Geophysics Geosystems*, *3*(10), 1-8, https://doi.org/10.1029/2001gc000280.

Martínez-Botí, M. A., D. Vance, and P. G. Mortyn (2009), Nd/Ca ratios in plankton-towed and core top foraminifera: Confirmation of the water column acquisition of Nd, *Geochemistry, Geophysics, Geosystems*, *10*(8), https://doi.org/10.1029/2009gc002701.

Mathien-Blard, E., and F. Bassinot (2009), Salinity bias on the foraminifera Mg/Ca thermometry: Correction procedure and implications for past ocean hydrographic reconstructions, *Geochemistry, Geophysics, Geosystems*, *10*(12), https://doi.org/10.1029/2008gc002353.

McCartney, M. S. (1977), Subantarctic Mode Water, in *A voyage of discovery: George Deacon 70th Anniversary Volume*, edited by M. V. Angel, pp. 103-119, Pergamon Press, Oxford.

McConnell, M. C., and R. C. Thunell (2005), Calibration of the planktonic foraminiferal Mg/Ca paleothermometer: Sediment trap results from the Guaymas Basin, Gulf of California, *Paleoceanography*, *20*(2), https://doi.org/10.1029/2004pa001077.

McGregor, H. V., M. K. Gagan, M. T. McCulloch, E. Hodge, and G. Mortimer (2008), Mid-Holocene variability in the marine ^{14}C reservoir age for northern coastal Papua New Guinea, *Quaternary Geochronology*, *3*, 213-225, https://doi.org/10.1016/j.quageo.2007.11.002.

Merlis, T. M., T. Schneider, S. Bordoni, and I. Eisenman (2013), The Tropical Precipitation Response to Orbital Precession, *Journal of Climate*, *26*(6), 2010-2021, https://doi.org/10.1175/jcli-d-12-00186.1.

Meyers, S. R. (2014), Astrochron: An R Package for Astrochronology., edited, http.//cran.r-project.org/packaeg=astrochron.

Mohtadi, M., M. Prange, and S. Steinke (2016), Palaeoclimatic insights into forcing and response of monsoon rainfall, *Nature*, *533*(7602), 191-199, https://doi.org/10.1038/nature17450.

Mohtadi, M., M. Prange, E. Schefuß, and T. C. Jennerjahn (2017), Late Holocene slowdown of the Indian Ocean Walker circulation, *Nature communications*, *8*(1), https://doi.org/10.1038/s41467-017-00855-3.

Mohtadi, M., S. Steinke, J. Groeneveld, H. G. Fink, T. Rixen, D. Hebbeln, B. Donner, and B. Herunadi (2009), Low-latitude control on seasonal and interannual changes in planktonic foraminiferal flux and shell geochemistry off south Java: A sediment trap study, *Paleoceanography*, *24*(1), https://doi.org/10.1029/2008pa001636.

Mohtadi, M., D. W. Oppo, A. Lückge, R. DePol-Holz, S. Steinke, J. Groeneveld, N. Hemme, and D. Hebbeln (2011), Reconstructing the thermal structure of the upper ocean: Insights from planktic foraminifera shell chemistry and alkenones in modern sediments of the tropical eastern Indian Ocean, *Paleoceanography*, *26*(3), https://doi.org/10.1029/2011pa002132.

Mohtadi, M., M. Prange, D. W. Oppo, R. De Pol-Holz, U. Merkel, X. Zhang, S. Steinke, and A. Luckge (2014), North Atlantic forcing of tropical Indian Ocean climate, *Nature*, *509*(7498), 76-80, https://doi.org/10.1038/nature13196.

Mohtadi, M., et al. (2013), Report and preliminary results of RV SONNE cruise SO-228, Kaohsiung-Townsville, 04.05.2013- 23.06.2013, EISPAC-WESTWIND-SIODP. Berichte aus dem MARUM und dem Fachbereich Geowissenschaften der Universität Bremen, 295, 110 pp. urn:nbn:de:gbv:46-00103343-13.

Morimoto, M. (2002), Salinity records for the 1997–98 El Niño from Western Pacific corals, *Geophysical Research Letters*, *29*(11), https://doi.org/10.1029/2001gl013521.

Mulitza, S., D. Boltovskoy, B. Donner, H. Meggers, A. Paul, and G. Wefer (2003), Temperature:$\delta^{18}O$ relationships of planktonic foraminifera collected from surface waters, *Palaeogeography, Palaeoclimatology, Palaeoecology*, *202*(1-2), 143-152, https://doi.org/10.1016/s0031-0182(03)00633-3.

Niebler, H.-S., H.-W. Hubberten, and G. Gersonde (1999), Oxygen isotope values of planktic foraminifera: a tool for the reconstruction of surface water stratification, in *Use of Proxies in Paleoceanography: Examples from the South Atlantic*, edited by G. Fischer and G. Wefer, pp. 165-189, Springer-Verlag, Berlin, Heidelberg.

Nürnberg, D., J. Bijma, and C. Hemleben (1996), Assessing the reliability of magnesium in foraminiferal calcite as a proxy for water mass temperatures, *Geochimica et Cosmochimica Acta*, *60*(5), 803-814.

Nürnberg, D., A. Müller, and R. R. Schneider (2000), Paleo-sea surface temperature calculations in the equatorial east Atlantic from Mg/Ca ratios in planktic foraminifera: A comparison to sea surface temperature estimates from Uk37, oxygen isotopes, and foraminiferal transfer function, *Paleoceanography*, *15*(1), 124-134, https://doi.org/10.1029/1999PA000370.

Paillard, D., L. Labeyrie, and P. Yiou (1996), Macintosh program performs time-series analysis, *Eos Trans. AGU*, *77*, 379.

Partin, J. W., K. M. Cobb, J. F. Adkins, B. Clark, and D. P. Fernandez (2007), Millennial-scale trends in West Pacific Warm Pool hydrology since the Last Glacial Maximum, *Nature*, *449*(7161), 452-455, https://doi.org/10.1038/nature06164.

Patrick, A., and R. C. Thunell (1997), Tropical Pacific sea surface temperatures and upper water column thermal structure during the Last Glacial Maximum, *Paleoceanography*, *12*(5), 649-657, https://doi.org/10.1029/97pa01553.

Peeters, F. J. C., G.-J. A. Brummer, and G. Ganssen (2002), The effect of upwelling on the distribution and stable isotope composition of *Globigerina bulloides* and *Globigerinoides ruber* (planktic foraminifera) in modern

surface waters of the NW Arabian Sea, *Global and Planetary Change*, *34*(3-4), 269-291, https://doi.org/10.1016/S0921-8181(02)00120-0.

Peltier, W. R., and R. G. Fairbanks (2006), Global glacial ice volume and Last Glacial Maximum duration from an extended Barbados sea level record, *Quaternary Science Reviews*, *25*, 3322-3337, https://doi.org/10.1016/j.quascirev.2006.04.010.

Pena, L. D., I. Cacho, P. Ferretti, and M. A. Hall (2008), El Niño-Southern Oscillation-like variability during glacial terminations and interlatitudinal teleconnections, *Paleoceanography*, *23*(3). https://doi.org/10.1029/2008pa001620.

Pena, L. D., E. Calvo, I. Cacho, S. Eggins, and C. Pelejero (2005), Identification and removal of Mn-Mg-rich contaminant phases on foraminiferal tests: Implications for Mg/Ca past temperature reconstructions, *Geochemistry Geophysics Geosystems*, *6*(9), n/a-n/a, https://doi.org/10.1029/2005gc000930.

Petchey, F., and S. Ulm (2016), Marine Reservoir Variation in the Bismarck Region: An Evaluation of Spatial and Temporal Change in ΔR and R Over the Last 3000 Years, *Radiocarbon*, *54*(01), 45-58, https://doi.org/10.2458/azu_js_rc.v54i1.13050.

Philander, S. G. H. (1985), El Niño and La Niña, *Journal of the atmospheric sciences*, *42*, 2652-2662, https://doi.org/10.1175/1520-0469(1985)042<2652:ENALN>2.0.CO;2.

Qiu, B., and S. C. Chen (2010), Interannual-to-decadal variability in the bifurcation of the North Equatorial Current off the Philippines, *Journal of Physical Oceanography*, *40*(11), 2525-2538, https://doi.org/10.1175/2010jpo4462.1.

Qu, T., and E. J. Lindstrom (2002), A Climatological Interpretation of the Circulation in the Western South Pacific, *Journal of Physical Oceanography*, *32*(9), 2492-2508, 10.1175/1520-0485(2002)032<2492:ACIOTC>2.0.CO;2.

Qu, T., S. Gao, and R. A. Fine (2013), Subduction of South Pacific Tropical Water and its equatorward pathways as shown by a simulated passive tracer, *Journal of Physical Oceanography*, *43*(8), 1551-1565, https://doi.org/doi:10.1175/jpo-d-12-0180.1.

Qu, T., S. Gao, I. Fukumori, R. A. Fine, and E. J. Lindstrom (2009), Origin and pathway of equatorial 13°C water in the Pacific identified by a simulated passive tracer and its adjoint, *Journal of Physical Oceanography*, *39*(8), 1836-1853, 10.1175/2009jpo4045.1.

Rachmayani, R., M. Prange, and M. Schulz (2016), Intra-interglacial climate variability: model simulations of Marine Isotope Stages 1, 5, 11, 13, and 15, *Climate of the Past*, *12*(3), 677-695, https://doi.org/10.5194/cp-12-677-2016.

Radenac, M.-H., and M. Rodier (1996), Nitrate and chlorophyll distributions in relation to thermohaline and current structures in the western tropical Pacific during 1985-1989, *Deep Sea Research Part II: Topical Studies in Oceanography*, *4-6*, 725-752.

Radenac, M. H., F. Leger, M. Messie, P. Dutrieux, C. Menkes, and G. Eldin (2016), Wind-driven changes of surface current, temperature, and chlorophyll observed by satellites north of New Guinea, *J Geophys Res-Oceans*, *121*(4), 2231-2252, https://doi.org/10.1002/2015JC011438.

Rasmussen, E. M., and T. H. Carpenter (1982), Variations in tropical sea surface temperature and surface wind fields associated with the Southern Oscillation/El Niño, *Monthly Weather Review*, *354*, 354-384, https://doi.org/10.1175/1520-0493(1982)110<0354:VITSST>2.0.CO;2.

Ravelo, A. C., and R. G. Fairbanks (1992), Oxygen isotopic composition of multiple species of planktonic foraminifera: Recorders of the modern photic zone temperature gradient, *Paleoceanography*, *7*(6), 815-831.

Ravelo, A. C., and C. Hillaire-Marcel (2007), The use of oxygen and carbon isotopes of foraminifera in paleoceanography, in *Developments in marine geology - Proxis in late Cenozoic Paleoceanography*, edited by C. Hillaire-Marcel and A. de Vernal, pp. 735-764, Elsevier, https://doi.org/10.1016/s1572-5480(07)01023-8.

Regenberg, M., A. Regenberg, D. Garbe-Schönberg, and D. W. Lea (2014), Global dissolution effects on planktonic foraminiferal Mg/Ca ratios controlled by the calcite-saturation state of bottom waters, *Paleoceanography*, *29*(3), 127-142, 10.1002/2013pa002492.

Regenberg, M., S. Steph, D. Nürnberg, R. Tiedemann, and D. Garbe-Schönberg (2009), Calibrating Mg/Ca ratios of multiple planktonic foraminiferal species with $\delta^{18}O$-calcification temperatures: Paleothermometry for the upper water column, *Earth and Planetary Science Letters*, *278*(3-4), 324-336, https://doi.org/10.1016/j.epsl.2008.12.019.

Regoli, F., T. de Garidel-Thoron, K. Tachikawa, Z. Jian, L. Ye, A. W. Droxler, G. Lenoir, M. Crucifix, N. Barbarin, and L. Beaufort (2015), Progressive shoaling of the equatorial Pacific thermocline over the last eight glacial periods, *Paleoceanography*, *30*(5), 439-455, https://doi.org/10.1002/2014pa002696.

Reimer, P. J., et al. (2013), IntCal13 and Marine13 Radiocarbon Age Calibration Curves 0–50,000 Years cal BP, *Radiocarbon*, *55*(4), 1869-1887, https://doi.org/10.2458/azu_js_rc.55.16947.

Rhein, M., et al. (2013), Observations: Ocean, in *Climate Change 2013: The physical science basis. Contribution of working goup I to the fifth assessment report of the Intergovernmental Panel on Climate Change*, edited by T. F. Stocker, D. Qin, G.-K. Plattner, M. Tignor, S. K. Allen, J. Boschung, A. Nauels, Y. Xia, V. Bex and P. M. Midgley, Cambridge University Press, Cambridge, United Kingdom and New York, USA.

Rickaby, R. E. M., and P. Halloran (2005), Cool La Niña During the Warmth of the Pliocene?, *Science*, *307*(5717), 1948-1952, https://doi.org/10.1126/science.1104666.

Rippert, N., D. Nürnberg, J. Raddatz, E. Maier, E. Hathorne, J. Bijma, and R. Tiedemann (2016), Constraining foraminiferal calcification depths in the western Pacific warm pool, *Marine Micropaleontology*, *128*, 14-27, https://doi.org/10.1016/j.marmicro.2016.08.004.

Roberts, N. L., A. M. Piotrowski, H. Elderfield, T. I. Eglinton, and M. W. Lomas (2012), Rare earth element association with foraminifera, *Geochimica et Cosmochimica Acta*, *94*, 57-71, https://doi.org/10.1016/j.gca.2012.07.009.

Rosenthal, Y. (2007), Elemental proxies for reconstructing Cenozoic seawater paleotemperatures from calcareous fossils, *1*, 765-797, https://doi.org/10.1016/s1572-5480(07)01024-x.

Rosenthal, Y., and G. P. Lohmann (2002), Accurate estimation of sea surface temperatures using dissolution-corrected calibrations for Mg/Ca paleothermometry, *Paleoceanography*, *17*(3), 16-11-16-16, https://doi.org/10.1029/2001pa000749.

Rosenthal, Y., A. E. Holbourn, D. K. Kulhanek, and the Expedition 363 Scientists, 2016. *Expedition 363 preliminary report: Western Pacific Warm Pool.* International Ocean Discovery Program, http://dx.doi.org/10.14379/iodp.pr.363.2017.

Rosenthal, Y., E. A. Boyle, and N. Slowey (1997), Temperature control on the incorporation of magnesium, strontium, fluorine, and cadmium into benthic foraminiferal shells from Little Bahama Bank: Prospects for thermocline paleoceanography, *Geochimica et Cosmochimica Acta*, *61*(17), 3633-3643, https://doi.org/10.1016/S0016-7037(97)00181-6.

Rosenthal, Y., M. P. Field, and R. M. Sherrell (1999), Precise determination of element/calcium ratios in calcareous samples using sector field inductively coupled plasma mass spectrometry, *Anal Chem*, *71*(15), 3248-3253, https://doi.org/10.1021/AC981410x.

Rosenthal, Y., D. W. Oppo, and B. K. Linsley (2003), The amplitude and phasing of climate change during the last deglaciation in the Sulu Sea, western equatorial Pacific, *Geophysical Research Letters*, *30*(8), https://doi.org/10.1029/2002gl016612.

Rosenthal, Y., B. K. Linsley, and D. W. Oppo (2013), Pacific Ocean heat content during the past 10,000 years, *Science*, *342*(6158), 617-621, https://doi.org/10.1126/science.1240837.

Rosenthal, Y., G. Lohmann, K. C. Lohmann, and R. M. Sherrell (2000), Incorporation and preservation of Mg in *G. sacculifer:* Implications for reconstructing sea surface temperatures and the oxygen isotopic composition of seawater., *Paleoceanography*, *15*, 135-145.

Rosenthal, Y., J. Kalansky, A. Morley, and B. K. Linsley (2017), A paleo-perspective on ocean heat content: Lessons from the Holocene and Common Era, *Quaternary Science Reviews*, *155*, 1-12, https://doi.org/10.1016/j.quascirev.2016.10.017.

Rosenthal, Y., et al. (2004), Interlaboratory comparison study of Mg/Ca and Sr/Ca measurements in planktonic foraminifera for paleoceanographic research, *Geochemistry Geophysics Geosystems*, *5*, doi:10.1029/2003GC000650.

Russell, A. D., B. Hönisch, H. J. Spero, and D. W. Lea (2004), Effects of seawater carbonate ion concentration and temperature on shell U, Mg, and Sr in cultured planktonic foraminifera, *Geochimica et Cosmochimica Acta*, *68*(21), 4347-4361, https://doi.org/10.1016/j.gca.2004.03.013.

Russell, A. D., S. Emerson, B. K. Nelson, J. Erez, and D. W. Lea (1994), Uranium in foraminiferal calcite as a recorder of seawater uranium concentrations, *Geochimica et Cosmochimica Acta*, *58*, 671-681.

Sadekov, A. Y., R. Ganeshram, L. Pichevin, R. Berdin, E. McClymont, H. Elderfield, and A. W. Tudhope (2013), Palaeoclimate reconstructions reveal a strong link between El Nino-Southern Oscillation and Tropical Pacific mean state, *Nature communications*, *4*, 2692, https://doi.org/10.1038/ncomms3692.

Sagawa, T., Y. Yokoyama, M. Ikehara, and M. Kuwae (2012), Shoaling of the western equatorial Pacific thermocline during the last glacial maximum inferred from multispecies temperature reconstruction of planktonic foraminifera, *Palaeogeography, Palaeoclimatology, Palaeoecology*, *346–347*, 120-129, https://doi.org/10.1016/j.palaeo.2012.06.002.

Saikku, R., L. Stott, and R. Thunell (2009), A bi-polar signal recorded in the western tropical Pacific: Northern and Southern Hemisphere climate records from the Pacific warm pool during the last Ice Age, *Quaternary Science Reviews*, *28*(23-24), 2374-2385, https://doi.org/10.1016/j.quascirev.2009.05.007.

Sanchez Goñi, M. F., and S. P. Harrison (2010), Millennial-scale climate variability and vegetation changes during the Last Glacial: Concepts and terminology, *Quaternary Science Reviews*, *29*(21-22), 2823-2827, https://doi.org/10.1016/j.quascirev.2009.11.014.

Sarmiento, J. L., N. Gruber, M. A. Brzezinski, and J. P. Dunne (2004), High-latitude controls of thermocline nutrients and low latitude biological productivity, *Nature*, *427*, 56-59, https://doi.org/10.1038/nature02204.

Schlitzer, R. (2014), Ocean Data View, odv.awi.de, edited.

Schneider, T., T. Bischoff, and G. H. Haug (2014), Migrations and dynamics of the intertropical convergence zone, *Nature*, *513*(7516), 45-53, https://doi.org/10.1038/nature13636.

Schrag, D. P., J. F. Adkins, K. McIntyre, J. L. Alexander, D. A. Hodell, C. D. Charles, and J. F. McManus (2002), The oxygen isotopic composition of seawater during the Last Glacial Maximum, *Quaternary Science Reviews*, *21*(1-3), 331-342.

Schulz, M., and M. Mudelsee (2002), REDFIT: estimatingred-noise spectra directly from unevenly spaced paleoclimatic time series, *Computers & Geosciences*, *28*, 421-426.

Sen Gupta, B. K. (2003), *Modern foraminifera*, Kluver Academic Publishers, New York.

Seo, I., Y. Lee, Y. I. Lee, C. M. Yoo, and K. Hyeong (2016), Climatic evolution of the central equatorial Pacific since the Last Glacial Maximum, *Geochemistry, Geophysics, Geosystems*, *17*(8), 3454-3468, https://doi.org/10.1002/2016gc006371.

Shackleton, N. J. (1967), Oxygen isotope analysis and Pleistocene temperatures re-assessed, *Nature*, *215*, 15-17.

Shackleton, N. (1974), Attainment of isotopic equilibrium between ocean water and the benthonic foraminifera genus *Uvigerina*: Isotopic changes in the ocean during the last glacial, in *Les méthodes quantitatives d'étude des variations du climat au cours du Pléistocène*, edited by L. Labeyrie, pp. 203-209, CNRS, Paris.

Shcherbina, A. Y., L. D. Talley, and D. L. Rudnick (2003), Direct observations of North Pacific ventilation: Brine rejection in the Okhotsk Sea, *Science*, *302*(5652), 1952-1955, https://doi.10.1126/science.1088692.

Sholkovitz, E. R., H. Elderfield, R. Szymczak, and K. Casey (1999), Island weathering: river sources of rare earth elements to the Western Pacific Ocean, *Marine Chemistry*, *68*, 39-57.

Simon, Q., N. Thouveny, D. L. Bourles, J. P. Valet, F. Bassinot, L. Menabreaz, V. Guillou, S. Choy, and L. Beaufort (2016), Authigenic 10Be/9Be ratio signatures of the cosmogenic nuclide production linked to geomagnetic dipole moment variation since the Brunhes/Matuyama boundary, *Journal of geophysical research. Solid earth*, *121*(11), 7716-7741, 10.1002/2016JB013335.

Soden, B. J., and I. M. Held (2006), An assessment of climate feedbacks in coupled ocean-atmosphere models, *Journal of Climate*, *19*, 3354-3360, https://doi.org/10.1175/JCLI3799.1.

Spero, H. J., K. M. Mielke, E. M. Kalve, D. W. Lea, and D. K. Pak (2003), Multispecies approach to reconstructing eastern equatorial Pacific thermocline hydrography during the past 360 kyr, *Paleoceanography*, *18*(1), https://doi.org/10.1029/2002PA000814.

Spero, H. J., S. M. Eggins, A. D. Russell, L. Vetter, M. R. Kilburn, and B. Hönisch (2015), Timing and mechanism for intratest Mg/Ca variability in a living planktic foraminifer, *Earth and Planetary Science Letters*, *409*, 32-42, https://doi.org/10.1016/j.epsl.2014.10.030.

Steinke, S., H.-Y. Chiu, P.-S. Yu, C.-C. Shen, L. Löwemark, H.-S. Mii, and M.-T. Chen (2005), Mg/Ca ratios of two *Globigerinoides ruber* (white) morphotypes: Implications for reconstructing past tropical/subtropical surface water conditions, *Geochemistry, Geophysics, Geosystems*, *6*(11), https://doi.org/10.1029/2005gc000926.

Steinke, S., M. Mohtadi, J. Groeneveld, L.-C. Lin, L. Löwemark, M.-T. Chen, and R. Rendle-Bühring (2010), Reconstructing the southern South China Sea upper water column structure since the Last Glacial Maximum: Implications for the East Asian winter monsoon development, *Paleoceanography*, *25*(2), https://doi.org/10.1029/2009pa001850.

Steph, S., M. Regenberg, R. Tiedemann, S. Mulitza, and D. Nürnberg (2009), Stable isotopes of planktonic foraminifera from tropical Atlantic/Caribbean core-tops: Implications for reconstructing upper ocean stratification, *Marine Micropaleontology*, *71*(1-2), 1-19, https://doi.org/10.1016/j.marmicro.2008.12.004.

Stott, L., A. Timmermann, and R. Thunell (2007), Southern Hemisphere and deep-sea warming led deglacial atmospheric CO_2 rise and tropical warming, *Science*, *318*(5849), 435-438, https://doi.org/10.1126/science.1143791.

Stuiver, M., and H. A. Polach (1977), Discussion, Reporting of ^{14}C data, *Radiocarbon*, *19*(3), 355-363.

Tachikawa, K., T. Toyofuku, I. Basile-Doelsch, and T. Delhaye (2013), Microscale neodymium distribution in sedimentary planktonic foraminiferal tests and associated mineral phases, *Geochimica et Cosmochimica Acta*, *100*, 11-23, https://doi.org/10.1016/j.gca.2012.10.010.

Tachikawa, K., A. Timmermann, L. Vidal, C. Sonzogni, and O. E. Timm (2014), CO_2 radiative forcing and Intertropical Convergence Zone influences on western Pacific warm pool climate over the past 400 ka, *Quaternary Science Reviews*, *86*(0), 24-34, https://doi.org/10.1016/j.quascirev.2013.12.018.

Tachikawa, K., O. Cartapanis, L. Vidal, L. Beaufort, T. Barlyaeva, and E. Bard (2011), The precession phase of hydrological variability in the Western Pacific Warm Pool during the past 400 ka, *Quaternary Science Reviews*, *30*(25-26), 3716-3727, https://doi.org/10.1016/j.quascirev.2011.09.016.

Talley, L. D. (1993), Distribution and formation of North Pacific Intermediate Water, *Journal of Physical Oceanography*, *23*, 517-537, https://doi.org/10.1175/1520-0485(1993)023<0517:DAFONP>2.0.CO;2.

Thirumalai, K., J. N. Richey, T. M. Quinn, and R. Z. Poore (2014), Globigerinoides ruber morphotypes in the Gulf of Mexico: a test of null hypothesis, *Scientific reports*, *4*, 6018, https://doi.org/10.1038/srep06018.

Thunell, R., E. Tappa, C. Pride, and E. Kincaid (1999), Sea-surface temperature anomalies associated with the 1997/1998 El Niño recorded in the oxygen isotope composition of planktonic foraminifera, *Geology*, *27*(9), 843-846.

Timmermann, A., J. Sachs, and O. E. Timm (2014), Assessing divergent SST behavior during the last 21 ka derived from alkenones and *G. ruber*-Mg/Ca in the equatorial Pacific, *Paleoceanography*, *29*(6), 680-696, https://doi.org/10.1002/2013pa002598.

Timmermann, A., T. Friedrich, O. E. Timm, M. O. Chikamoto, A. Abe-Ouchi, and A. Ganopolski (2014), Modeling obliquity and CO_2 effects on southern hemisphere climate during the Past 408 ka, *Journal of Climate*, *27*(5), 1863-1875, https://doi.org/10.1175/jcli-d-13-00311.1.

Tomczak, M., and J. S. Godfrey (2003), *Regional oceanography: an introduction*, 391 pp., Daya Publishing House.

Toole, J. M., R. C. Millard, Z. Wang, and S. Pu (1990), Oservations of the Pacific North Equatorial Current Bifurcation at the Philippine Coast, *Journal of Physical Oceanography*, 307-318, https://doi.org/10.1175/1520-0485(1990)020.

Tsuchiya, M., R. Lukas, and R. Fine (1989), Source Waters of the Pacific Equatorial Undercurrent, *Progress in Oceanography*, *23*, 46.

Tudhope, A. W., C. P. Chilcott, M. T. McCulloch, E. R. Cook, J. Chappell, R. M. Ellam, D. W. Lea, J. M. Lough, and G. B. Shimmield (2001), Variability in the El Niño - Southern Oscillation through a glacial-interglacial cycle, *Science*, *291*, 1511-1517.

Turney, C. S. M., A. P. Kershaw, S. C. Clemens, N. Branch, P. T. Moss, and L. Keith Fifield (2004), Millennial and orbital variations of El Niño/Southern Oscillation and high-latitude climate in the last glacial period, *Nature*, *428*(6980), 306-310.

van Geldern, R., and J. A. C. Barth (2012), Optimization of instrument setup and post-run corrections for oxygen and hydrogen stable isotope measurements of water by isotope ratio infrared spectroscopy (IRIS), *Limnology and Oceanography: Methods*, *10*(12), 1024-1036, https://doi.org/10.4319/lom.2012.10.1024.

Vecchi, G. A., B. J. Soden, A. T. Wittenberg, I. M. Held, A. Leetmaa, and M. J. Harrison (2006), Weakening of tropical Pacific atmospheric circulation due to anthropogenic forcing, *Nature*, *441*(7089), 73-76, https://doi.org/10.1038/nature04744.

Waelbroeck, C., L. Labeyrie, E. Michel, J. C. Duplessy, J. F. McManus, K. Lambeck, E. Balbon, and M. Labracherie (2002), Sea-level and deep water temperature changes derived from benthic foraminifera isotopic records, *Quaternary Science Reviews*, *21*(1-3), 295-305, https://doi.org/10.1016/S0277-3791(01)00101-9.

Wang, L. J. (2000), Isotopic signals in two morphotypes of *Globigerinoides ruber* (white) from the South China Sea: implications for monsoon climate change during the last glacial cycle, *Palaeogeography Palaeoclimatology Palaeoecology*, *161*(3-4), 381-394, https://doi.org/10.1016/S0031-0182(00)00094-8.

Wang, Y. J., H. Cheng, R. L. Edwards, Z. S. An, J. Y. Wu, C. C. Shen, and J. A. Dorale (2001), A high-resolution absolute-dated late Pleistocene Monsoon record from Hulu Cave, China, *Science*, *294*(5550), 2345-2348, https://doi.org/10.1126/science.1064618.

Wang, P. X., B. Wang, H. Cheng, J. Fasullo, Z. T. Guo, T. Kiefer, and Z. Y. Liu (2014), The global monsoon across timescales: coherent variability of regional monsoons, *Climate of the Past*, *10*(6), 2007-2052, https://doi.org/10.5194/cp-10-2007-2014.

Watkins, J. M., A. C. Mix, and J. Wilson (1996), Living planktic foraminifera: Tracers of circulation and productivity regimes in the central equatorial Pacific, *Deep Sea Research Part II: Topical Studies in Oceanography*, *43*(4-6), 26.

Wijffels, S. E., J. M. Toole, H. L. Bryden, R. Fine, W. J. Jenkins, and J. L. Bullister (1996), The water masses and circulation at 10°N in the Pacific, *Deep Sea Research Part I: Oceanographic Research Papers*, *43*(4), 501-544.

Wyrtki, K. (1961), Physical Oceanography of the Southeast Asian Waters, Scripps Institute of Oceanography NAGA Rep. 2, 195 pp.

Xu, J., A. Holbourn, W. Kuhnt, Z. Jian, and H. Kawamura (2008), Changes in the thermocline structure of the Indonesian outflow during Terminations I and II, *Earth and Planetary Science Letters*, *273*(1-2), 152-162, https://doi.org/10.1016/j.epsl.2008.06.029.

Xu, J. A., W. Kuhnt, A. Holbourn, M. Regenberg, and N. Andersen (2010), Indo-Pacific Warm Pool variability during the Holocene and Last Glacial Maximum, *Paleoceanography*, *25*(4), PA4230, https://doi.org/10.1029/2010PA001934.

Yamasaki, M., A. Sasaki, M. Oda, and H. Domitsu (2008), Western equatorial Pacific planktic foraminiferal fluxes and assemblages during a La Niña year (1999), *Marine Micropaleontology*, *66*(3-4), 304-319, https://doi.org/10.1016/j.marmicro.2007.10.006.

Zenk, W., G. Siedler, A. Ishida, J. Holfort, Y. Kashino, Y. Kuroda, T. Miyama, and T. J. Müller (2005), Pathways and variability of the Antarctic Intermediate Water in the western equatorial Pacific Ocean, *Progress in Oceanography*, *67*, 245-281, https://doi.org/10.1016/j.pocean.2005.05.003.

Zhu, J., et al. (2017), Reduced ENSO Variability at the LGM Revealed by an Isotope-enabled Earth System Model, *Geophysical Research Letters*, https://doi.org/10.1002/2017gl073406.

Zweng, M. M., et al. (2013), *World Ocean Atlas 2013, Volume 2: Salinity*, Washington, D.C.

Appendix 1

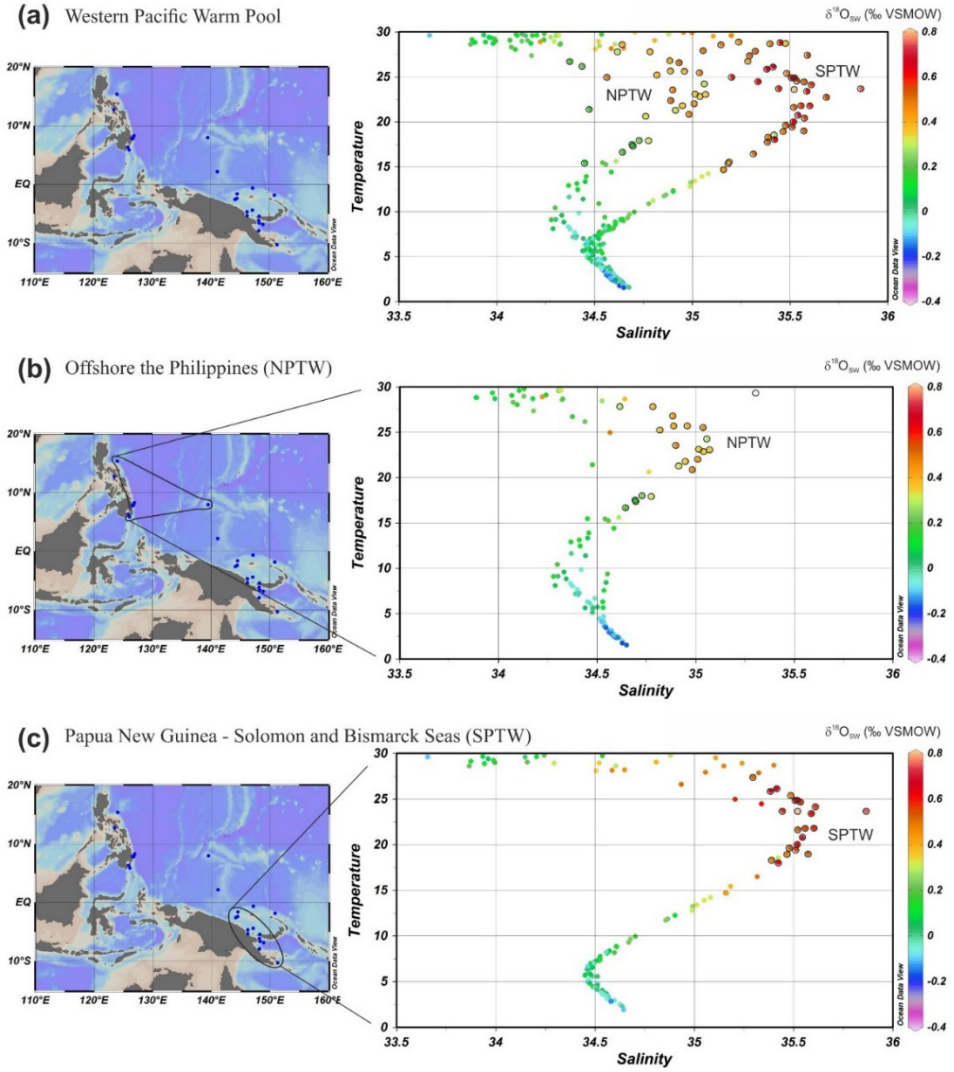

Figure A1.1. Temperature-salinity diagrams for SO-228 and RR-1313 stations. Colors represent $\delta^{18}O_{SW}$. Black surrounded dots indicate samples used to calculate the $\delta^{18}O_{SW}$-salinity regressions of subsurface of (a) the Western Pacific Warm Pool, (b) offshore the Philippines, (c) offshore Papua New Guinea.

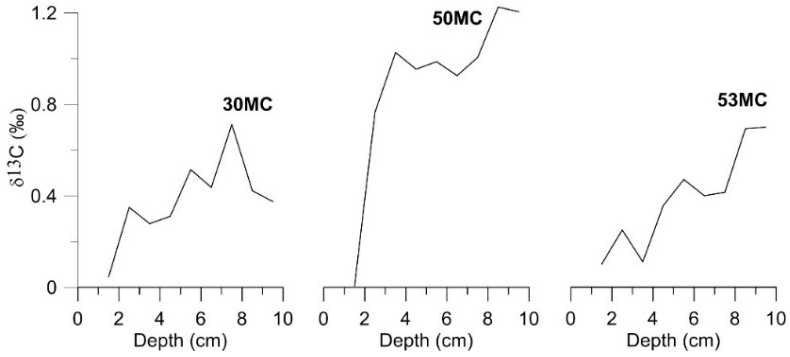

Figure A1.2. Shell $\delta^{13}C$ of *G. ruber* in samples from RR-1313 multicores. Rapid drops in $\delta^{13}C$ are indicative for the Suess effect.

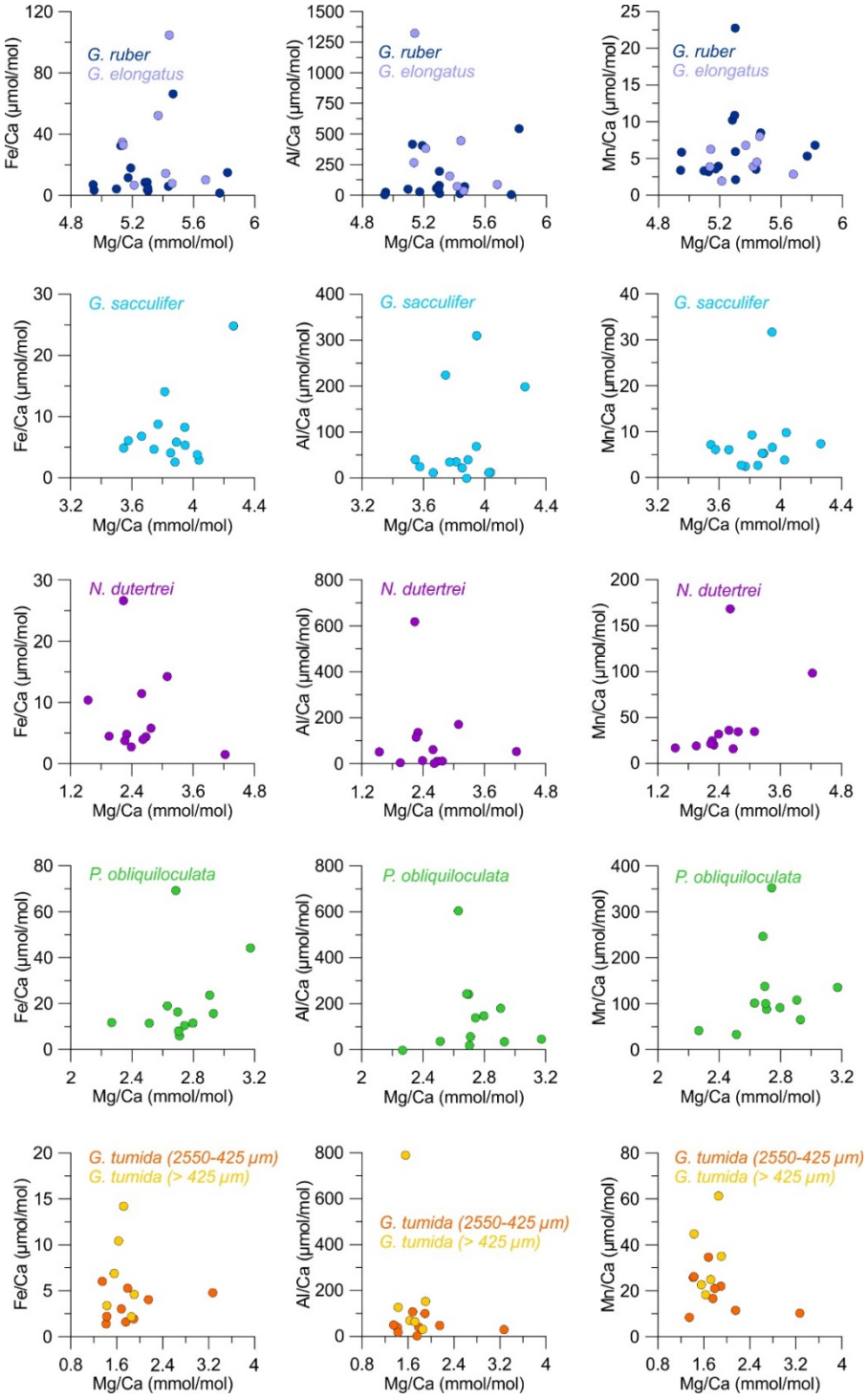

Figure A1.3. Fe/Ca (left), Al/Ca (middle) and Mn/Ca (right) of each species and sample versus Mg/Ca. Note the different scaling of the axes for individual species. Results from replicate measurements are shown separately.

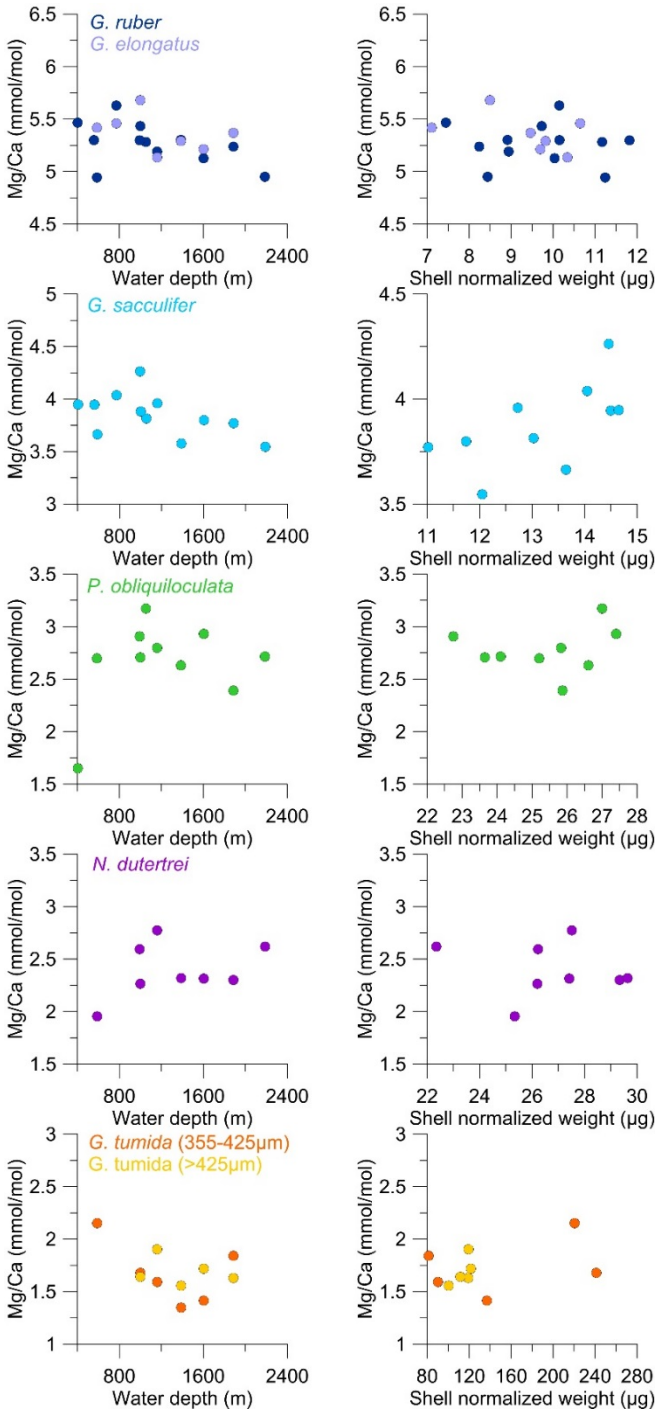

Figure A1.4. Shell Mg/Ca of each species and sample versus water depth at the respective core sites (left) and shell normalized weight (right).

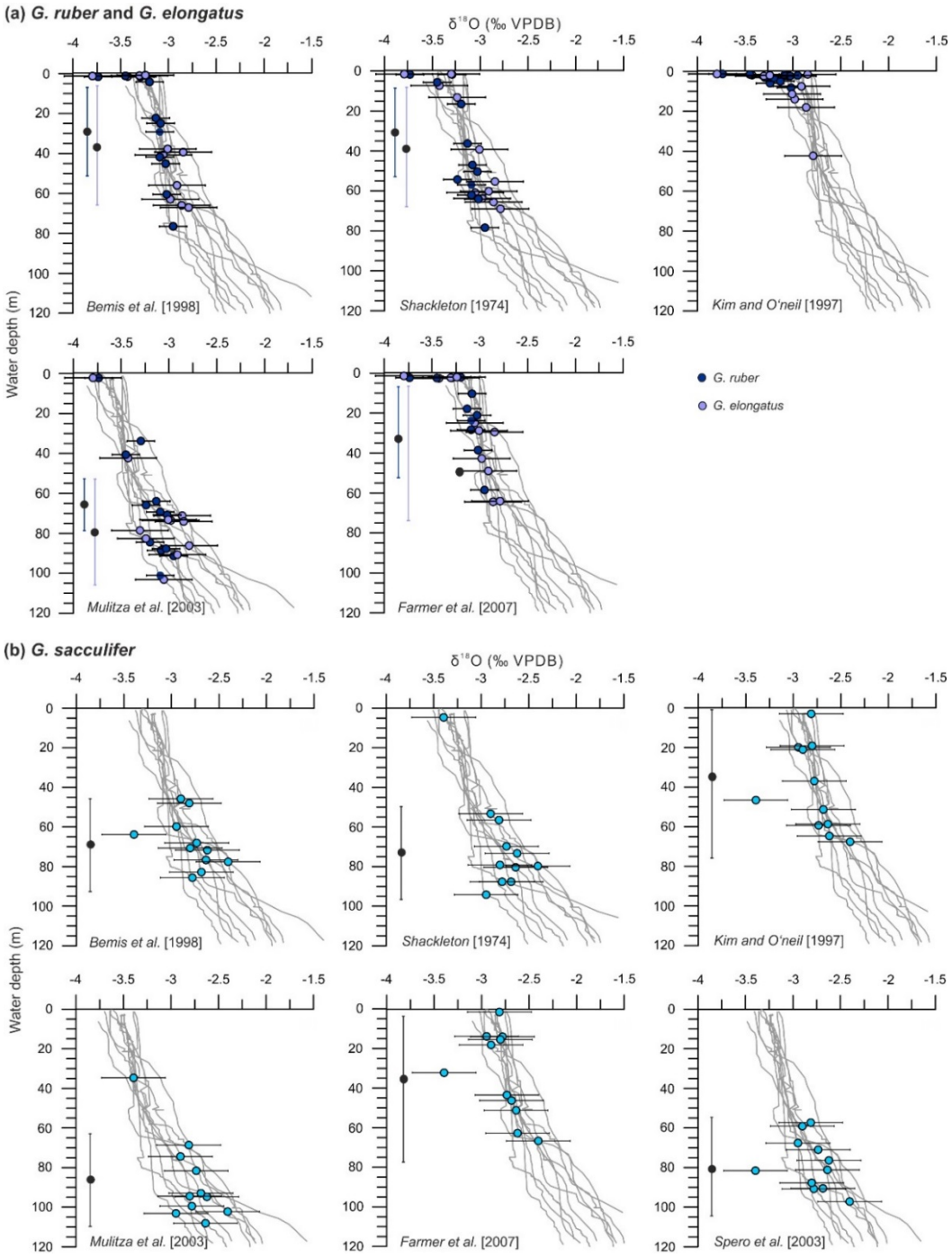

Figure A1.5. Shell $\delta^{18}O$ derived calcification depth estimates for (a) *G. ruber*, *G. elongatus* and (b) *G. sacculifer*. Colored dots show shell $\delta^{18}O$. Gray lines indicate depth profiles of predicted $\delta^{18}O$ calcite using the noted paleotemperature equations. CTD temperature and seawater $\delta^{18}O$ calculated from salinity via $\delta^{18}O$-salinity regressions from the study area were implemented in the equations. Horizontal bars indicate 1σ error ranges for shell $\delta^{18}O$, vertical bars on black dots show exemplarily average uncertainties in calcification depth derived by projecting shell $\delta^{18}O$ with added/subtracted standard deviations on an average $\delta^{18}O$ calcite profile.

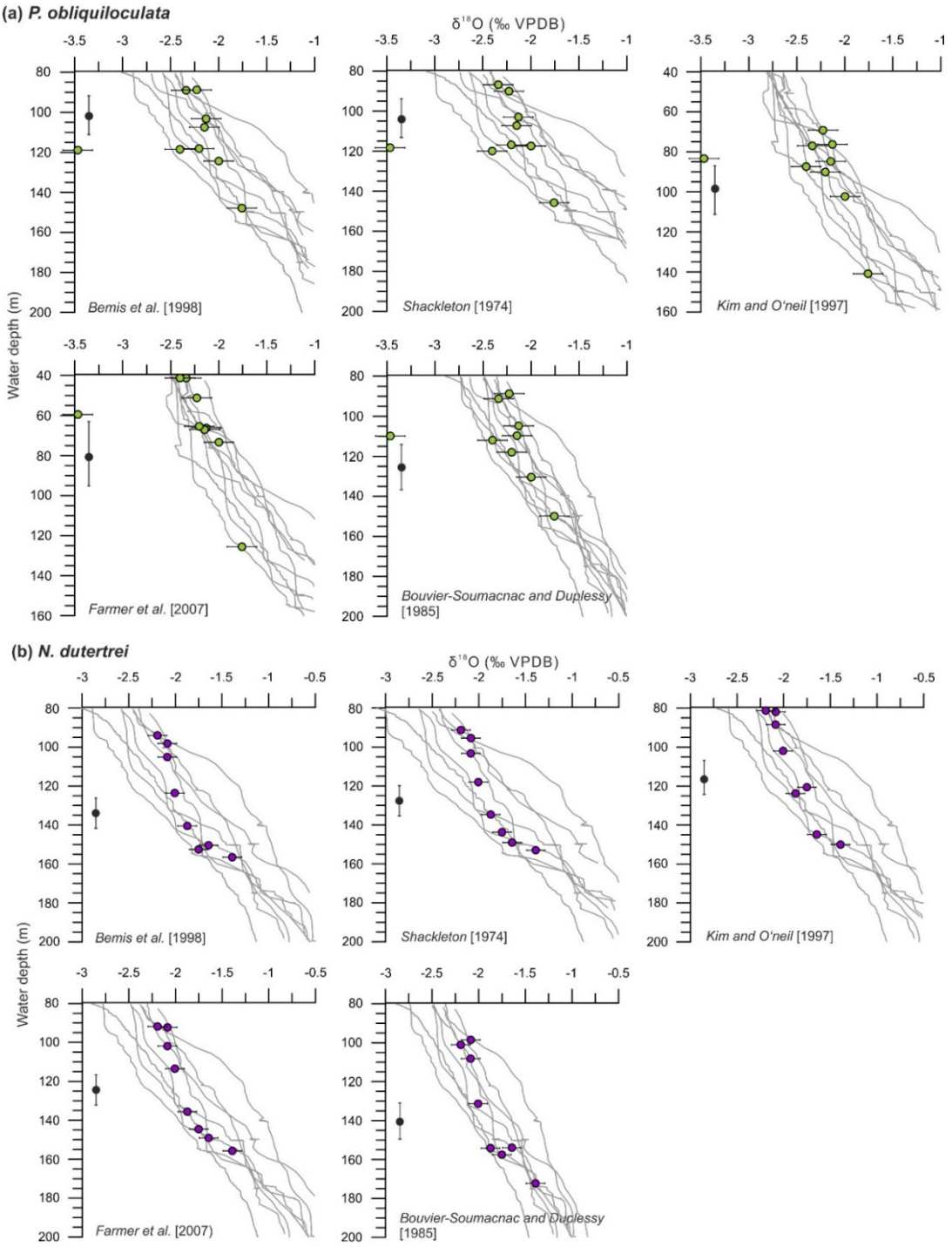

Figure A1.6. Shell $\delta^{18}O$ derived calcification depth estimates for (a) *P. obliquiloculata* and (b) *N. dutertrei*. Colored dots show shell $\delta^{18}O$. Gray lines indicate depth profiles of predicted $\delta^{18}O$ calcite using the noted paleotemperature equations. CTD temperature and seawater $\delta^{18}O$ calculated from salinity via $\delta^{18}O$-salinity regressions from the study area were implemented in the equations. Horizontal bars indicate 1σ error ranges for shell $\delta^{18}O$, vertical bars on black dots show exemplarily average uncertainties in calcification depth derived by projecting shell $\delta^{18}O$ with added/subtracted standard deviations on an average $\delta^{18}O$ calcite profile.

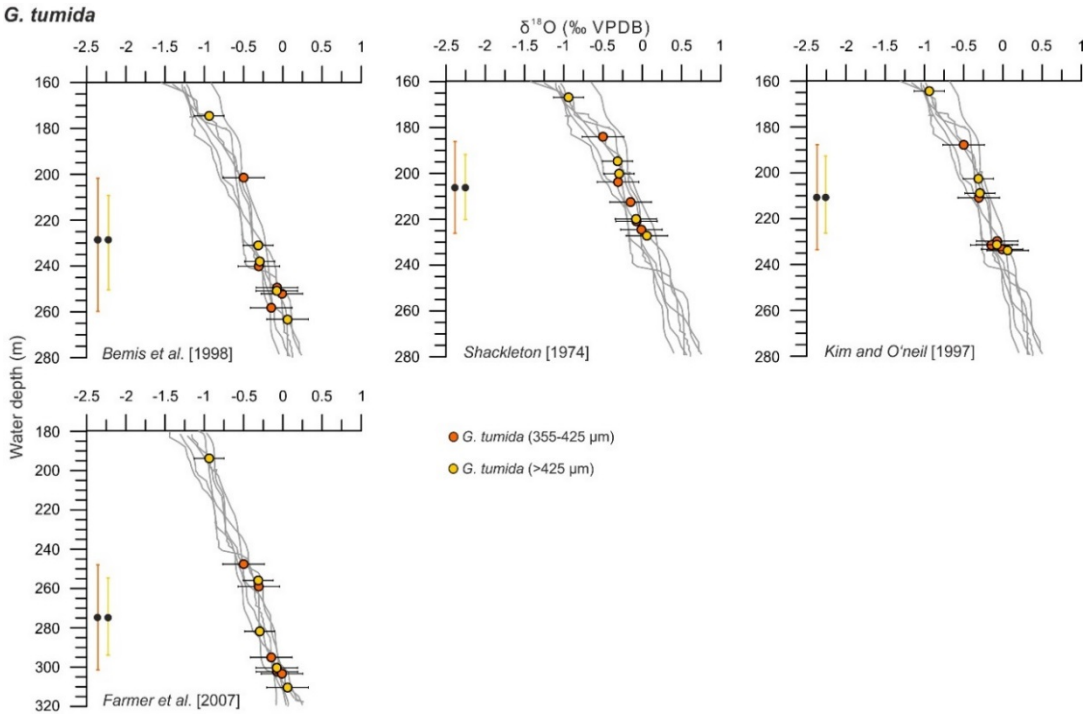

Figure A1.7. Shell $\delta^{18}O$ derived calcification depth estimates for *G. tumida*. Colored dots show shell $\delta^{18}O$. Gray lines indicate depth profiles of predicted $\delta^{18}O$ calcite using the noted paleotemperature equations. CTD temperature and seawater $\delta^{18}O$ calculated from salinity via $\delta^{18}O$-salinity regressions from the study area were implemented in the equations. Horizontal bars indicate 1σ error ranges for shell $\delta^{18}O$, vertical bars on black dots show exemplarily average uncertainties in calcification depth derived by projecting shell $\delta^{18}O$ with added/subtracted standard deviations on an average $\delta^{18}O$ calcite profile.

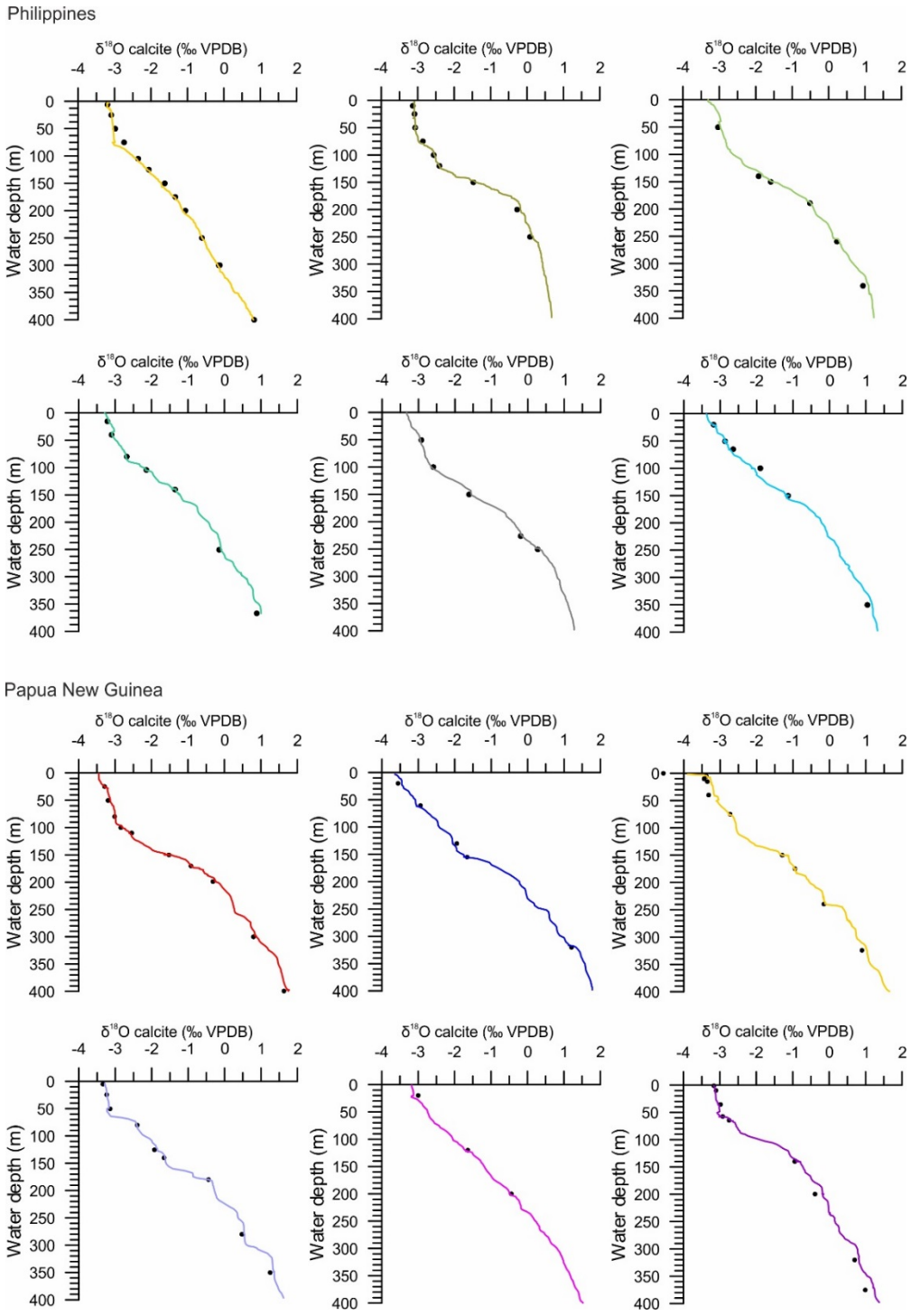

Figure A1.8. Comparison of $\delta^{18}O$ predicted calcite calculated from $\delta^{18}Osw$ measured in water samples (dots) and from CTD salinity (colored lines) at different stations offshore the Philippines and Papua New Guinea. $\delta^{18}O$ values were converted to the VPDB scale by subtracting 0.27‰ [*Hut*, 1987]. The temperature equation of *Bemis et al.,* [1998] was used to predict equilibrium $\delta^{18}O$ calcite. Profiles from all stations used to estimate foraminiferal calcification depths are shown. The standard deviation for $\delta^{18}O_{SW}$ measurements is smaller than the symbol size and therefore error bars are not shown in the figure.

Table A1.1. SO-228 and RR-1313 CTD temperature, salinity and $\delta^{18}O_{SW}$

Station	Longitude (°E)	Latitude (°N)	Depth (m)	Temperature (°C)	Salinity (psu)	$\delta^{18}O_{SW}$ (‰ VSMOW)
GeoB 17401-1	126.91	8.33	50.2	28.7	34.18	0.09
			150.8	23.13	35.02	0.35
			259.4	13.35	34.45	0.06
			310.2	11.41	34.44	0.03
			349.9	9.85	34.42	-0.06
GeoB 17403-1	126.68	7.82	50.2	28.66	34.33	0.1
			140	24.23	35.06	0.29
			150.3	22.87	35.04	0.34
			189.3	17.32	34.7	0.26
			259.5	13.12	34.41	0.13
			340.6	9.12	34.3	0.01
GeoB 17404-1	126.54	7.9	15.2	29.62	34.1	0.12
			39.9	29.11	34.24	0.13
			79.9	27.86	34.62	0.29
			104.4	25.71	34.89	0.38
			140.3	21.78	34.95	0.35
			250.6	15.26	34.56	0.2
			366.9	9.59	34.33	0.05
GeoB 17407-1	126.76	7.94	50.5	28.59	34.32	0.2
			100	27.82	34.79	0.37
			150.2	23.02	35.07	0.35
			226.5	15.45	34.54	0.19
			250.7	12.92	34.37	0.13
GeoB 17412-1	126.07	5.93	49.3	28.46	34.53	0.26
			100.1	25.49	35.04	0.45
			150	17.96	34.73	0.23
			200.3	17.5	34.69	0.12
			220.4	16.64	34.65	0.18
			259.9	12.46	34.41	0.1
			285.9	11.64	34.37	-0.01
GeoB 17413-2	125.85	6.35	20.1	29.36	33.97	0.1
			50.5	28.04	34.1	0.14
			65.1	27.35	34.18	0.22
			100	24.97	34.57	0.47
			150.3	20.63	34.76	0.33
			350.3	8.84	34.34	0.05
GeoB 17417-1	144.5	-1.58	24.8	29.79	34.24	0.2
			50.4	29.77	34.88	0.29
			79.9	29.52	35.11	0.41
			100	28.92	35.24	0.43
			110	27.92	35.06	0.48
			150.1	24.16	35.61	0.56
			170.3	21.82	35.6	0.58
			198.8	18.95	35.47	0.47
			300.1	13.91	35.05	0.32
			399.3	9.96	34.7	0.17
GeoB 17420-1	144.48	-2.36	20	29.61	33.66	
			20	29.61	33.66	-0.11
			60.6	28.94	34.52	0.34
			130	26.15	35.41	0.64
			154.9	24.9	35.53	0.61
			320.3	11.88	34.87	0.22
GeoB 17424-1	147.17	-0.62	4.8	29.97	34.71	0.35
			20.6	29.93	34.96	0.45
			49.8	29.58	35.2	0.46
			78.5	28.83	35.45	0.6
			170	24.45	35.57	0.51
			300.9	11.24	34.8	0.29
GeoB 17426-1	150.86	-1.81	1.2	29.95	35	0.37
			4.9	29.89	35	0.44
			45.2	29.69	35.2	0.3
			70	28.72	35.48	0.36
			119.9	27.41	35.59	0.54
			169.6	22.74	35.69	0.54
			198.9	20.46	35.58	0.55
			223	17.78	35.39	0.5

Appendix 1

Station	Longitude (°E)	Latitude (°N)	Depth (m)	Temperature (°C)	Salinity (psu)	$\delta^{18}O_{SW}$ (‰ VSMOW)
			257.8	15.54	35.19	0.36
			273.7	12.35	34.9	0.49
			298.5	10.88	34.78	0.22
GeoB 17428-1	144.15	-2.54	0.1	29.31	29.48	-1.19
			5.3	29.66	33.93	0.08
			10.2	29.59	34.15	0
			15.2	29.63	34.2	0.1
			39.8	29.73	34.54	0.16
			75	28.61	35.15	0.47
			150	23.4	35.59	0.6
			175	21.8	35.56	0.55
			239.5	18.32	35.39	0.47
			324.3	13.25	34.99	0.25
GeoB 17432-1	146.2	-4.66	5.2	29.39	33.96	0.05
			24.5	29.22	33.99	0.11
			50.4	28.99	34	0.15
			80.1	27.4	35.3	0.5
			125.5	25.41	35.49	0.47
			140.2	24.62	35.54	0.54
			180	19.67	35.48	0.52
			280.1	15.43	35.18	0.38
			350.3	11.74	34.86	0.23
GeoB 17433-1	147.13	-4.38	1.1	29.14	33.87	0.14
			6.9	29.13	33.87	0.12
			30.9	29.01	33.99	0.2
			60.6	28.61	34.6	0.28
			91	27.86	35.32	0.5
			149	23.64	35.52	0.8
			194.7	19.49	35.51	0.55
			319	13.41	35.01	0.32
GeoB 17434-1	148.27	-5.41	19.9	28.62	33.87	0.2
			120	24.89	35.51	0.63
			200	20.03	35.52	0.61
GeoB 17436-2	148.2	-6.11	1.3	28.88	33.94	0.1
			9.9	29.05	34.16	0.2
			35.6	28.92	34.29	0.29
			57.5	29.04	34.81	0.38
			64.5	28.69	35.4	0.47
			140	21.65	35.52	0.51
			199.6	18.54	35.42	0.29
			320.3	14.23	35.08	0.3
			375.3	12.26	34.9	0.1
RR1313-01 01CTD/HC	151.31	-10.25	5	26.6	34.93	0.49
			25	26.61	34.93	0.51
			65	24.98	35.2	0.58
			75	24.48	35.34	0.6
			100	23.72	35.45	0.57
			150	20.77	35.54	0.69
			200	18.06	35.42	0.62
			300	14.71	35.16	0.46
			400	12.8	34.99	0.3
RR1313-05 13CTD/HC	148.91	-6.82	5	28.09	34.51	0.34
			25	28.15	34.59	0.46
			50	28.19	34.65	0.44
			100	25.89	35.38	0.65
			130	23.69	35.86	0.75
			190	19.01	35.57	0.51
			250	16.49	35.32	0.5
			300	14.7	35.16	0.43
RR1313-15 38CTD/HC	141.14	2.22	5	29.73	34.1	0.19
			26	29.62	34.18	0.15
			51	29.42	34.28	0.27
			101	26.78	35.29	0.41
			151	22.37	34.89	0.49
			231	10.91	34.52	0.17
RR1313-19 42CTD/HC	139.5	8	10	29.59	34.3	0.18
			25	29.6	34.3	0.25
			50	29.62	34.32	0.3

Station	Longitude (°E)	Latitude (°N)	Depth (m)	Temperature (°C)	Salinity (psu)	$\delta^{18}O_{SW}$ (‰ VSMOW)
			75	28.66	34.64	0.37
			75	28.66	34.64	0.39
			120	25.68	34.96	0.38
			150	21.3	34.92	0.31
			200	14.4	34.59	0.13
			300	9.39	34.55	0.17
			400	8.44	34.55	0.06
RR1313-21 42CTD/HC	124	15.4	6	29.77	34.13	0.17
			25	29.07	34.07	0.13
			50	28.96	34.13	0.22
			75	28.89	34.22	0.44
			105	26.81	34.89	0.4
			125	25.24	34.82	0.37
			150	23.54	34.9	0.45
			175	21.99	35.01	0.42
			200	20.84	34.98	0.45
			250	17.94	34.78	0.3
			300	15.62	34.61	0.28
			300	15.62	34.61	0.31
			400	10.44	34.3	0.17
RR1313-25 56CTD/HC	123.48	12.78	10	28.83	33.89	0.04
			25	28.83	33.89	0.09
			50	28.71	33.98	0.08
			75	28.3	34.08	0.2
			100	26.72	34.38	0.17
			120	26.17	34.44	0.21
			150	21.42	34.48	0.16
			200	15.48	34.45	0.12
			250	13.9	34.46	0.14

Table A1.2. Measured $\delta^{18}O_{SW}$ versus $\delta^{18}O_{SW}$ calculated from CTD salinity. Results for all stations where vertical profiles of $\delta^{18}O$ were used to estimate the calcification depth of several planktic foraminifera are shown.

Station	Longitude (°E)	Latitude (°N)	Measured $\delta^{18}O_{SW}$ (‰ VSMOW)	Calculated $\delta^{18}O_{SW}$ (‰ VSMOW)	Difference between measured and calculated $\delta^{18}O_{SW}$ (‰ VSMOW)
GeoB 17401-1	126.91	8.33	0.09	0.12	-0.03
			0.35	0.40	-0.05
			0.06	0.21	-0.15
			0.03	0.21	-0.18
			-0.06	0.20	-0.26
GeoB 17403-1	126.68	7.82	0.10	0.17	-0.07
			0.29	0.41	-0.12
			0.34	0.40	-0.06
			0.26	0.29	-0.03
			0.13	0.20	-0.07
			0.01	0.16	-0.15
GeoB 17404-1	126.54	7.9	0.12	0.16	-0.04
			0.13	0.14	-0.01
			0.29	0.27	0.02
			0.38	0.35	0.03
			0.35	0.37	-0.02
			0.20	0.25	-0.05
			0.05	0.17	-0.12
GeoB 17407-1	126.76	7.94	0.20	0.17	0.03
			0.37	0.32	0.05
			0.35	0.41	-0.06
			0.19	0.24	-0.05
			0.13	0.18	-0.05
GeoB 17413-2	125.85	6.35	0.10	0.11	-0.01
			0.14	0.10	0.04
			0.22	0.12	0.10
			0.47	0.25	0.22

Appendix 1

Station	Longitude (°E)	Latitude (°N)	Measured $\delta^{18}O_{SW}$ (‰ VSMOW)	Calculated $\delta^{18}O_{SW}$ (‰ VSMOW)	Difference between measured and calculated $\delta^{18}O_{SW}$ (‰ VSMOW)
			0.33	0.31	0.02
			0.05	0.18	-0.13
GeoB 17417-1	144.5	-1.58	0.20	0.21	-0.01
			0.29	0.35	-0.06
			0.41	0.42	-0.01
			0.43	0.47	-0.04
			0.48	0.41	0.07
			0.56	0.59	-0.03
			0.58	0.59	-0.01
			0.47	0.54	-0.07
			0.32	0.41	-0.09
			0.17	0.29	-0.12
GeoB 17420-1	144.48	-2.36	-0.11	-0.01	-0.10
			0.34	0.23	0.11
			0.64	0.52	0.12
			0.61	0.56	0.05
			0.22	0.35	-0.13
GeoB 17428-1	144.15	-2.54	-1.19	-1.54	0.35
			0.08	0.09	-0.01
			0.00	0.17	-0.17
			0.10	0.19	-0.09
			0.16	0.32	-0.16
			0.47	0.44	0.03
			0.60	0.58	0.02
			0.55	0.57	-0.02
			0.47	0.52	-0.05
			0.25	0.39	-0.14
GeoB 17432-1	146.2	-4.66	0.05	0.10	-0.05
			0.11	0.11	0.00
			0.15	0.06	0.09
			0.50	0.49	0.01
			0.47	0.55	-0.08
			0.54	0.56	-0.02
			0.52	0.55	-0.03
			0.38	0.45	-0.07
			0.23	0.34	-0.11
GeoB 17434-1	148.27	-5.41	0.20	0.07	0.13
			0.63	0.56	0.07
			0.61	0.56	0.05
GeoB 17436-2	148.2	-6.11	0.10	0.10	0.00
			0.20	0.18	0.02
			0.29	0.23	0.06
			0.38	0.33	0.05
			0.47	0.52	-0.05
			0.51	0.56	-0.05
			0.29	0.53	-0.24
			0.30	0.42	-0.12
			0.10	0.36	-0.26
RR1313-21 42CTD/HC	124	15.4	0.17	0.17	0.00
			0.13	0.14	-0.01
			0.22	0.17	0.05
			0.44	0.14	0.30
			0.40	0.35	0.05
			0.37	0.33	0.04
			0.45	0.36	0.09
			0.42	0.39	0.03
			0.45	0.38	0.07
			0.30	0.32	-0.02
			0.28	0.26	0.02
			0.31	0.26	0.05
			0.17	0.16	0.01
RR1313-25 56CTD/HC	123.48	12.78	0.04	0.08	-0.04
			0.09	0.08	0.01
			0.08	0.06	0.02
			0.20	0.09	0.11
			0.17	0.19	-0.02

Station	Longitude (°E)	Latitude (°N)	Measured $\delta^{18}O_{SW}$ (‰ VSMOW)	Calculated $\delta^{18}O_{SW}$ (‰ VSMOW)	Difference between measured and calculated $\delta^{18}O_{SW}$ (‰ VSMOW)
			0.21	0.21	0.00
RR1313-25 56CTD/HC	123.48	12.78	0.16	0.22	-0.07
			0.12	0.21	-0.09
			0.15	0.21	-0.07

Table A1.3. Mg/Ca versus $\delta^{18}O$-derived calcification temperatures. Mg/Ca-temperatures are based on our newly established species-specific regressions; $\delta^{18}O$-temperatures were calculated with the equation of *Bemis et al*. [1998].

Sample No.	Core	Latitude (°N)	Longitude (°E)	Species	Mg/Ca-temperature (°C)	$\delta^{18}O$-temperature (°C)
1	RR1313-24 50 MC	13.57	123.73	*G. ruber*	29.30	29.75
2	RR1313-25 53 MC	12.78	123.48	*G. ruber*	29.33	28.21
3	GeoB 17404-2	7.90	126.54	*G. ruber*	29.65	29.24
4	GeoB 17410-3	7.87	126.59	*G. ruber*	29.95	29.36
5	GeoB 17414-2	6.26	125.83	*G. ruber*	28.63	29.19
6	GeoB 17419-2	-2.81	144.50	*G. ruber*	29.21	30.09
7	RR1313-12 30 MC	-3.13	142.76	*G. ruber*	29.33	31.99
8	GeoB 17421-2	-3.55	144.20	*G. ruber*	28.62	30.17
9	GeoB 17429-1	-4.10	145.20	*G. ruber*	28.99	28.92
10	GeoB 17430-2	-4.22	145.03	*G. ruber*	29.12	29.12
11	GeoB 17432-3	-5.34	146.20	*G. ruber*	29.34	29.65
12	GeoB 17435-2	-7.27	147.34	*G. ruber*	29.59	29.95
13	RR1313-24 50 MC	13.57	123.73	*G. elongatus*	-	29.91
14	RR1313-25 53 MC	12.78	123.48	*G. elongatus*	-	30.74
15	GeoB 17404-2	7.90	126.54	*G. elongatus*	-	28.55
16	GeoB 17410-3	7.87	126.59	*G. elongatus*	29.31	32.44
17	GeoB 17414-2	6.26	125.83	*G. elongatus*	-	28.71
18	GeoB 17419-2	-2.81	144.50	*G. elongatus*	29.14	30.19
19	GeoB 17421-2	-3.55	144.20	*G. elongatus*	29.23	30.06
20	GeoB 17429-1	-4.10	145.20	*G. elongatus*	28.83	28.61
21	GeoB 17430-2	-4.22	145.03	*G. elongatus*	28.68	29.41
22	GeoB 17432-3	-5.34	146.20	*G. elongatus*	28.99	29.04
23	GeoB 17435-2	-7.27	147.34	*G. elongatus*	29.72	29.06
24	RR1313-24 50 MC	13.57	123.73	*G. sacculifer*	28.34	28.36
25	RR1313-25 53 MC	12.78	123.48	*G. sacculifer*	28.69	-
26	GeoB 17404-2	7.90	126.54	*G. sacculifer*	28.70	27.78
27	GeoB 17410-3	7.87	126.59	*G. sacculifer*	28.93	28.19
28	GeoB 17414-2	6.26	125.83	*G. sacculifer*	27.59	28.24
29	GeoB 17419-2	-2.81	144.50	*G. sacculifer*	28.23	29.69
30	RR1313-12 30 MC	-3.13	142.76	*G. sacculifer*	29.49	30.35
31	GeoB 17421-2	-3.55	144.20	*G. sacculifer*	27.93	28.38
32	GeoB 17429-1	-4.10	145.20	*G. sacculifer*	28.30	28.22
33	GeoB 17430-2	-4.22	145.03	*G. sacculifer*	28.73	28.40
34	GeoB 17432-3	-5.34	146.20	*G. sacculifer*	27.68	27.45
35	GeoB 17435-2	-7.27	147.34	*G. sacculifer*	28.52	28.93
36	RR1313-25 53 MC	12.78	123.48	*N. dutertrei*	30.91	-
37	RR1313-24 50 MC	13.57	123.73	*N. dutertrei*	-	24.30
38	GeoB 17410-3	7.87	126.59	*N. dutertrei*	26.19	-
39	GeoB 17414-2	6.26	125.83	*N. dutertrei*	25.96	25.26
40	GeoB 17419-2	-2.81	144.50	*N. dutertrei*	24.63	24.32
41	RR1313-12 30 MC	-3.13	142.76	*N. dutertrei*	25.87	-
42	GeoB 17421-2	-3.55	144.20	*N. dutertrei*	22.95	23.05
43	GeoB 17429-1	-4.10	145.20	*N. dutertrei*	24.69	25.81
44	GeoB 17430-2	-4.22	145.03	*N. dutertrei*	26.56	24.71
45	GeoB 17432-3	-5.34	146.20	*N. dutertrei*	24.71	26.18
46	GeoB 17435-2	-7.27	147.34	*N. dutertrei*	24.47	26.23
47	RR1313-24 50 MC	13.57	123.73	*P. obliquiloculata*	28.04	31.04
48	GeoB 17414-2	6.26	125.83	*P. obliquiloculata*	26.43	25.85
49	GeoB 17419-2	-2.81	144.50	*P. obliquiloculata*	25.12	24.83
50	RR1313-12 30 MC	-3.13	142.76	*P. obliquiloculata*	27.14	27.64
51	GeoB 17421-2	-3.55	144.20	*P. obliquiloculata*	26.37	26.68
52	GeoB 17429-1	-4.10	145.20	*P. obliquiloculata*	27.22	25.77
53	GeoB 17430-2	-4.22	145.03	*P. obliquiloculata*	26.74	26.40

Appendix 1

Sample No.	Core	Latitude (°N)	Longitude (°E)	Species	Mg/Ca-temperature (°C)	$\delta^{18}O$-temperature (°C)
54	GeoB 17432-3	-5.34	146.20	*P. obliquiloculata*	26.11	26.38
55	GeoB 17435-2	-7.27	147.34	*P. obliquiloculata*	26.40	26.90
56	GeoB 17410-3	7.87	126.59	*G. tumida* (355-425 µm)	23.80	-
57	GeoB 17419-2	-2.81	144.50	*G. tumida* (355-425 µm)	17.88	18.56
58	GeoB 17421-2	-3.55	144.20	*G. tumida* (355-425 µm)	19.48	17.49
59	GeoB 17429-1	-4.10	145.20	*G. tumida* (355-425 µm)	15.16	16.23
60	GeoB 17430-2	-4.22	145.03	*G. tumida* (355-425 µm)	16.37	15.87
61	GeoB 17432-3	-5.34	146.20	*G. tumida* (355-425 µm)	14.66	-
62	GeoB 17435-2	-7.27	147.34	*G. tumida* (355-425 µm)	16.93	16.62
63	GeoB 17419-2	-2.81	144.50	*G. tumida* (>425 µm)	17.24	20.87
64	GeoB 17429-1	-4.10	145.20	*G. tumida* (>425 µm)	17.79	16.19
65	GeoB 17430-2	-4.22	145.03	*G. tumida* (>425 µm)	18.84	17.51
66	GeoB 17432-3	-5.34	146.20	*G. tumida* (>425 µm)	16.76	15.49
67	GeoB 17435-2	-7.27	147.34	*G. tumida* (>425 µm)	17.31	17.06

Appendix 2

A2.1. Age model of MD05-2920

The age model of MD05-2920 is based on radiocarbon dates and correlation of benthic $\delta^{18}O$. Originally, the calibration of radiocarbon dates was based on the Marine04 calibration curve and the chronology between dating points was inferred by linear interpolation. For consistency reasons, we revised the chronology for the radiocarbon dated part of core MD05-2920 following the approach described above for GeoB17419-1. We also included two additional radiocarbon dates that were recently published by *Simon et al.* [2016]. For the lower part of the core we adopted the tie points that were used in the original publication of *Tachikawa et al.* [2014] which had been selected by aligning benthic $\delta^{18}O$ to the LR04 stack. An additional tie point at 41.3 ka was defined by *Simon et al.* [2016] on the basis of $^{9}Be/^{10}Be$ and associated with the Laschamp event. A tie point at 108.5 ka was defined for this study. Differences between the previous [*Tachikawa et al.*, 2014] and the revised age model are generally negligible. Only during MIS 3 the revised chronology indicates ages that are up to 2 ka younger than indicated by the original age model in *Tachikawa et al.* [2014]. Since we combine temperature records from GeoB 17419-1 and MD05-2920, having thorough age models for both cores is of utmost importance. To validate the age models, we use Ti/Ca elemental ratios that were measured in high resolution on both cores. The benthic $\delta^{18}O$ records of GeoB 17419-1 and MD05-2920 are in good agreement and the comparison of the Ti/Ca records from the two cores provide additional confidence that the temperature records can be combined (Figure A2.1). An exception is the period before ~95 ka, where the Ti/Ca records and/or benthic $\delta^{18}O$ records show offsets. This inconsistency in the age-models cannot be resolved with the benthic isotope and Ti/Ca records alone. However, modifications of the age models in this part of the cores would not affect any major outcome or conclusion of this study.

A2.2. Isotope and Mg/Ca analyses

To convert the Mg/Ca of *G. ruber* to temperature, *Tachikawa et al.* [2014] used the multispecies equation of *Anand et al.* [2003]:

$$Mg/Ca = 0.38 \exp 0.09 * T$$

A study on modern WPWP sediments indicated that this equation is suitable for *G. ruber* in the WPWP [*Hollstein et al.*, 2017]. Data from modern WPWP sediments indicate that there is no clear difference between $\delta^{18}O$ and Mg/Ca of *G. ruber* and *G. elongatus* [*Hollstein et al.*, 2017] and we therefore combine the *G. ruber* $\delta^{18}O$ record with the Mg/Ca record of combined *G. ruber* and *G. elongatus*. For simplicity, in the following, we will denote the record as *G. ruber* record.

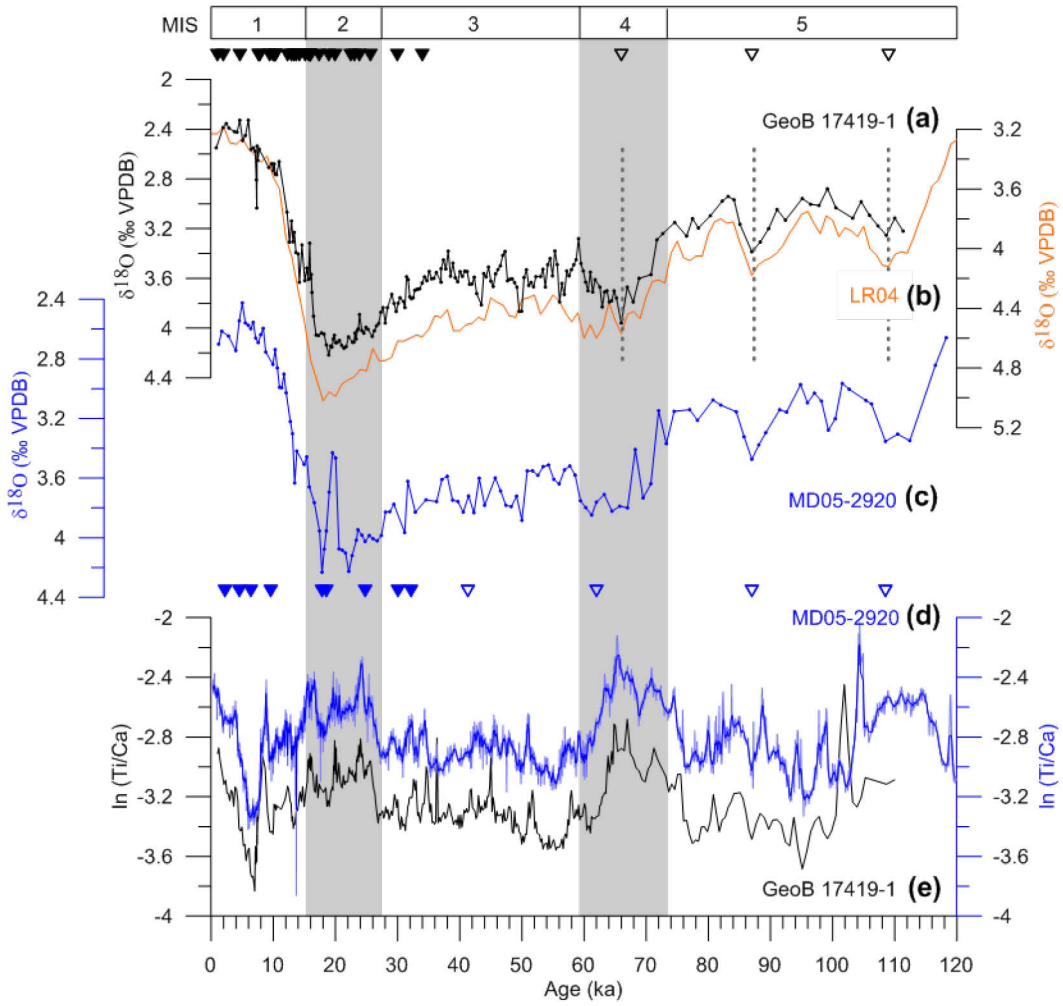

Figure A2.1. Age models of core GeoB 17419-1 and MD05-2920. (a) Benthic $\delta^{18}O$ of GeoB 17419-1 compared to the LR04 benthic $\delta^{18}O$ stack of *Lisiecki and Raymo* [2005] (b) and to benthic $\delta^{18}O$ of core MD05-2920 (c). (d) Ti/Ca of GeoB 17419-1 (black) and MD05-2920 (blue). Filled triangles indicate radiocarbon dates of GeoB 17419-1 (black) and MD05-2920 (blue). Empty triangles indicate tie points to LR04. Dashed vertical lines indicate the tie points between GeoB 17419-1 and the benthic stack. Marine isotopes stages (MIS) 1–5 as dated by *Sanchez Goñi and Harrison* [2010] are indicated at the top. Gray shadings mark MIS 2 and 4.

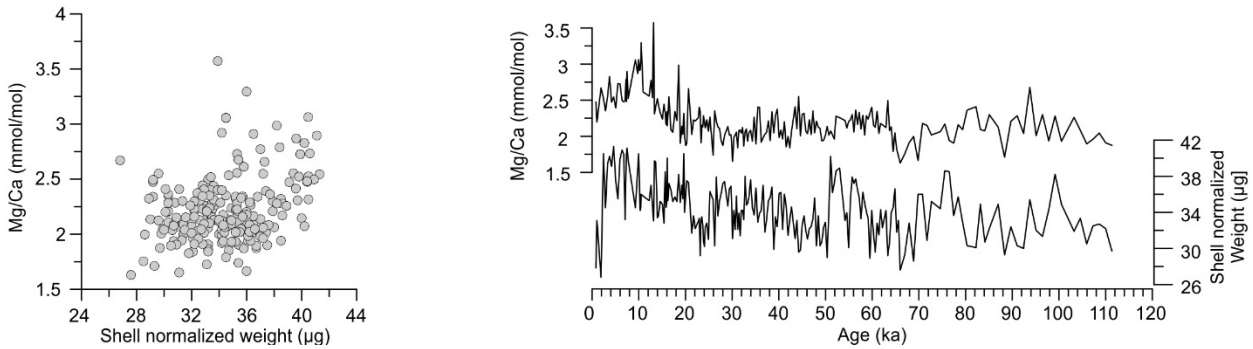

Figure A2.2. Shell Mg/Ca of *P. obliquiloculata* from GeoB 17419-1 compared to shell normalized weight.

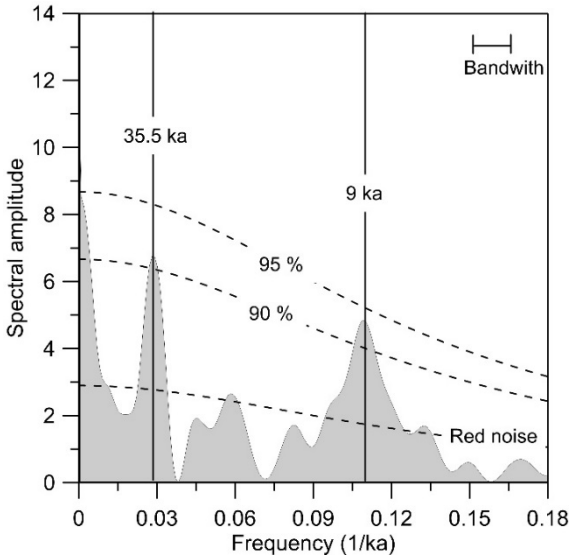

Figure A2.3. Spectral analysis of ΔT (*G. ruber – P. obliquiloculata*). The analysis was performed with REDFIT [*Schulz and Mudelsee*, 2002]. An oversampling factor of 9 was used to increase the resolution of samples frequencies. The bandwidth is 6 dB. We used a Welch type spectral window. Dashed lines indicate the red-noise spectrum as well as 90 and 95% confidence levels. Solid vertical lines denote periods that correspond to frequencies exceeding the 90% confidence levels.

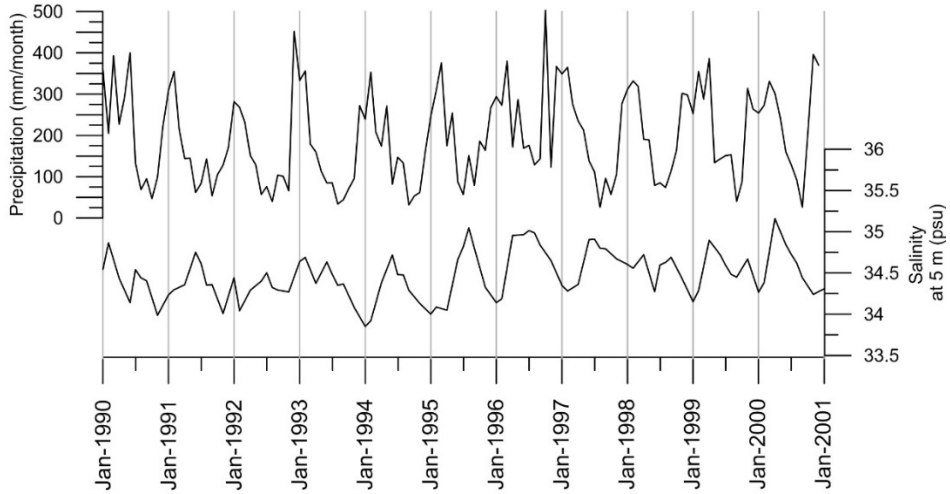

Figure A2.4. Precipitation rate above the catchment area of the Sepik River (143.50 – 144.50 °E, 3.50 – 4.50 °S) [*Beck et al.*, 2005] compared to surface (5 m) salinity near site GeoB 17419-1 from SODA 2.1.6. at 144.25 °E and 2.25 °S [*Carton and Giese*, 2008].

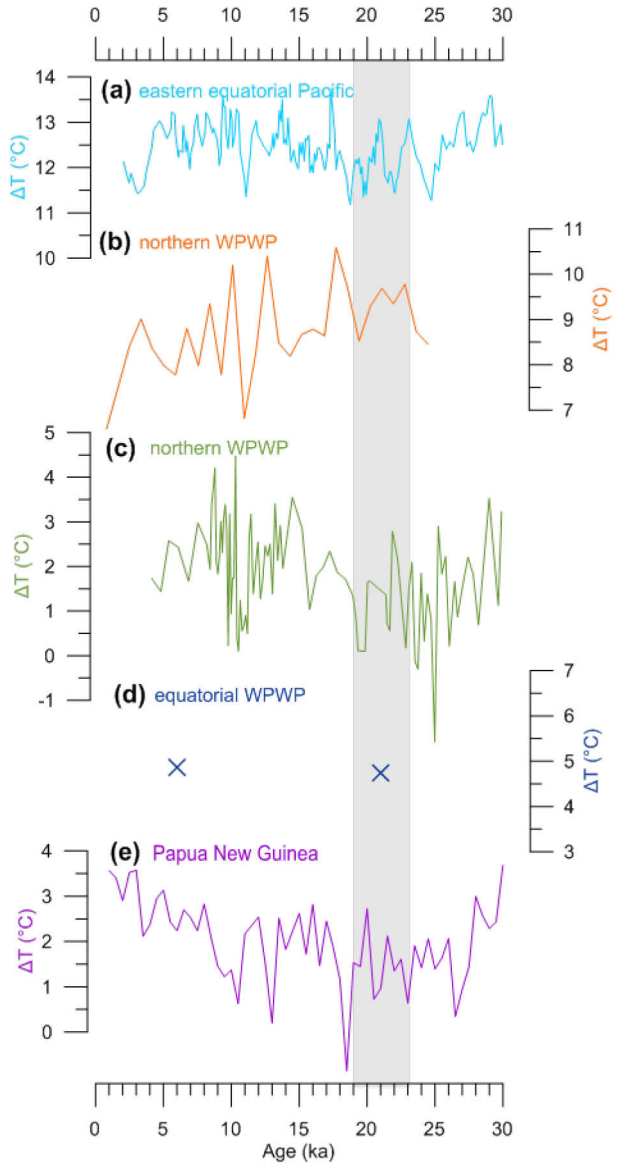

Figure A2.5. Mg/Ca-based ΔT reconstructions for the tropical Indo-Pacific region. (a) *G. ruber – N. dutertrei* ΔT of ODP 1240 [*Pena et al.*, 2008], (b) *G. ruber – P. obliquiloculata* ΔT of 3cBx [*Sagawa et al.*, 2012], (c) *G. ruber – P. obliquiloculata* ΔT of MD06-3067 [*Bolliet et al.*, 2011] and (d) late Holocene and LGM *G. sacculifer – G. tumida* ΔT of ODP 806 [*Ford et al.*, 2015] in comparison to (e) *G. ruber – P. obliquiloculata* ΔT of GeoB 17419-1 (this study). The ΔT estimate of site ODP806 is based on an average of Mg/Ca-temperature estimates on individual foraminifera samples. The samples are not accurately dated, but correspond to the late Holocene and the LGM. The LGM is marked by a gray bar.

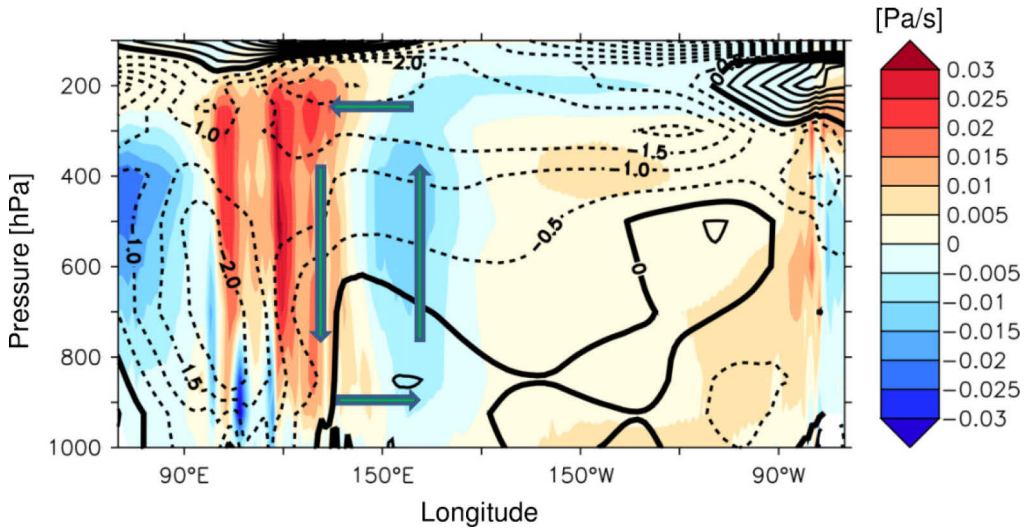

Figure A2.6. Annual mean atmospheric circulation anomaly (LGM minus pre-industrial) over the equatorial Pacific (5 °S – 5 °N) in a longitude-height plot as simulated by the MRI-CGCM3 coupled general circulation model (PMIP3/CMIP5 simulations). Colors show change in vertical velocity (red and blue colors indicate anomalous descent and ascent, respectively), contour lines show change in zonal wind (positive/negative is eastward/westward) in units of m/s. Arrows indicate an "anti-Walker cell" which is associated with reduced ascent over the Maritime Continent and enhanced ascent over the western equatorial Pacific during the LGM.

Table A2.1. Source and location of Mg/Ca-based temperature and ΔT records compiled in this study

Core	Location	Source	Longitude	Latitude	Water depth (m)	LGM anomaly
ODP 1240	Eastern eq. Pacific	*Peña et al*., 2008	86°28'W	0°02'N	2921	no change
3cBX	Northern WPWP	*Sagawa et al*., 2012	139°38′E	8°01'N	2829	shoaling
MD06-3067	Northern WPWP	*Bolliet et al*., 2011	126°30′E	6°31′N	1575	unclear
ODP806	Eq. WPWP	*Ford et al*., 2015	152°E	0°N	2520	no change
GeoB 17419-1 MD05-2920	WPWP	This study *Tachikawa et al*., 2014	144°30'E 144°32'E	2°48'S 2°52'S	1883	deepening

Table A2.2. Specifications of PMIP2 and PMIP3/CMIP5 climate models and simulated patterns of LGM thermocline depth (TCD) in the tropical Pacific relative to modern conditions.

No	Model	Institute	Resolution	PMIP phase	TCD pattern (LGM anomaly in WPWP)
1	MRI-CGCM3	Meteorological Research Institute, Japan	Atm: 320 x 160 x L48 Ocn: 364 x 368 x L51	3	Dipole with shoaling in the northern and deepening in the southern WPWP
2	ECHAM5-MPIOM	Max Planck Institute for Meteorology, Germany	Atm: 96 x 48 x L19 Ocn: 120 x 101 x L40	2	Overall thermocline deepening
3	FGOALS-g1.0	LASG/Institute of Atmospheric Physics, China	Atm: 128 x 60 x L26 Ocn: 360 x 180 x L33	2	Overall thermocline deepening
4	IPSL-CM4	Institut Pierre Simon Laplace, France	Atm: 96 x 72 x L19 Ocn: 182 x 149 x L31	2	Overall thermocline deepening
5	CCSM4	National Center for Atmospheric Research, USA	Atm: 288 x 192 x L26 Ocn: 320 x 384 x L60	3	Overall thermocline deepening
6	GISS-E2-R	NASA Goddard Institute for Space Studies, USA	Atm: 144 x 90 x L40 Ocn: 288 x 180 x L32	3	Overall thermocline deepening
7	HadCM3	UK Met Office Hadley Centre, UK	Atm: 96 x 72 x L19 Ocn: 288 x 144 x L20	2	Overall thermocline shoaling
8	CNRM-CM5	Centre National de Recherches Meteorologiques, France	Atm: 256 x 128 xL31 Ocn: 362 x 292 x L42	3	Overall thermocline shoaling
9	CCSM3	National Center for Atmospheric Research, USA	Atm: 128 x 64 x L26 Ocn: 320 x 384 x L40	2	Deepening in the northern and shoaling in the southern WPWP
10	MIROC3.2	Center for Climate System Research (University of Tokyo), JAMSTEC, Japan	Atm: 128 x 64 x L20 Ocn: 256 x 192 x L43	2	Deepening in the northern and shoaling in the southern WPWP
11	IPSL-CM5A	Institut Pierre Simon Laplace, France	Atm: 96 x 96 x L39 Ocn: 182 x 149 x L31	3	Deepening in the northern and shoaling in the southern WPWP
12	MIROC-ESM	JAMSTEC, University of Tokyo, National Inst. for Environmental Studies, Japan	Atm: 128 x 64 x L80 Ocn: 256 x 192 x L44	3	Deepening in the northern and shoaling in the southern WPWP
13	MPI-ESM	Max Planck Institute for Meteorology, Germany	Atm: 196 x 98 x L47 Ocn: 256 x 220 x L40	3	Deepening in the northern and shoaling in the southern WPWP
14	FGOALS-g2.0	LASG/Institute of Atmospheric Physics, China	Atm: 128 x 60 x L26 Ocn: 360 x 180 x L30	3	Deepening, but shoaling offshore PNG

Versicherung an Eides Statt / *Affirmation in lieu of an oath*

gem. § 5 Abs. 5 der Promotionsordnung vom 15.07.2015 /
according to § 5 (5) of the Doctoral Degree Rules and Regulations of 15 July, 2015

Ich / I, _____
(Vorname / First *Name*, Name / *Name*, Anschrift / *Address*, ggf. Matr.-Nr. / *student ID no., if applicable)*

versichere an Eides Statt durch meine Unterschrift, dass ich die vorliegende Dissertation selbständig und ohne fremde Hilfe angefertigt und alle Stellen, die ich wörtlich dem Sinne nach aus Veröffentlichungen entnommen habe, als solche kenntlich gemacht habe, mich auch keiner anderen als der angegebenen Literatur oder sonstiger Hilfsmittel bedient habe und die zu Prüfungszwecken beigelegte elektronische Version (PDF) der Dissertation mit der abgegebenen gedruckten Version identisch ist. / *With my signature I affirm in lieu of an oath that I prepared the submitted dissertation independently and without illicit assistance from third parties, that I appropriately referenced any text or content from other sources, that I used only literature and resources listed in the dissertation, and that the electronic (PDF) and printed versions of the dissertation are identical.*

Ich versichere an Eides Statt, dass ich die vorgenannten Angaben nach bestem Wissen und Gewissen gemacht habe und dass die Angaben der Wahrheit entsprechen und ich nichts verschwiegen habe*. / I affirm in lieu of an oath that the information provided herein to the best of my knowledge is true and complete.*

Die Strafbarkeit einer falschen eidesstattlichen Versicherung ist mir bekannt, namentlich die Strafandrohung gemäß § 156 StGB bis zu drei Jahren Freiheitsstrafe oder Geldstrafe bei vorsätzlicher Begehung der Tat bzw. gemäß § 161 Abs. 1 StGB bis zu einem Jahr Freiheitsstrafe oder Geldstrafe bei fahrlässiger Begehung. / *I am aware that a false affidavit is a criminal offence which is punishable by law in accordance with § 156 of the German Criminal Code (StGB) with up to three years imprisonment or a fine in case of intention, or in accordance with § 161 (1) of the German Criminal Code with up to one year imprisonment or a fine in case of negligence.*

_____ _____
Ort / *Place*, Datum / *Date* Unterschrift / *Signature*